Proceedings of the 30th Nordic Seminar on Computational Mechanics (NSCM-30)

Høgsberg, Jan Becker; Pedersen, Niels Leergaard

Publication date:
2017

Document Version
Publisher's PDF, also known as Version of record

NSCM 30

The 30th Nordic Seminar on Computational Mechanics

Proceedings

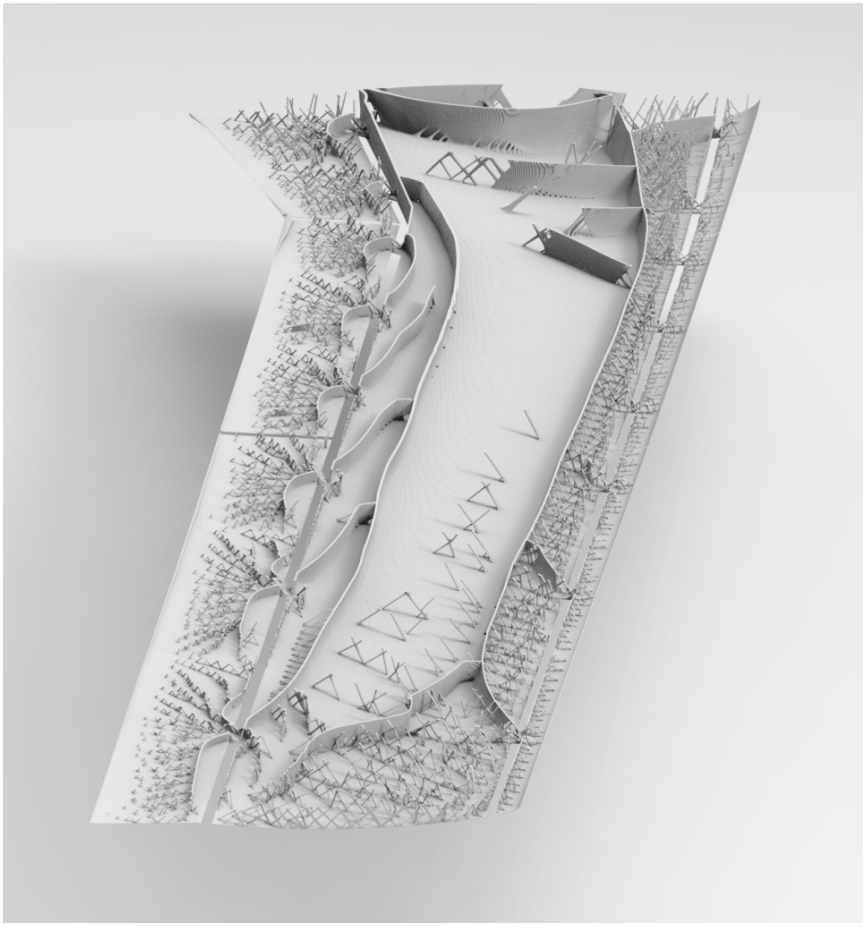

J. Høgsberg
N. L. Pedersen
(editors)

25-27 October, 2017
Kgs. Lyngby, Denmark

DTU Mechanical Engineering

Section of Solid Mechanics
Technical University of Denmark

Proceedings of NSCM 30: The 30th Nordic Seminar on Computational Mechanics 25-27 October 2017

Jan Høgsberg and Niels L. Pedersen (editors)

Front picture: Giga voxel optimization of wing, courtesy Niels Aage et al.

Sponsors:


DCAMM


DTU

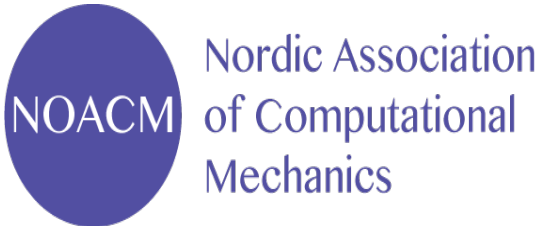
NOACM
Nordic Association
of Computational
Mechanics


DYNA
MORE
NORDIC

Preface

These proceedings contain the papers presented at the 30th Nordic Seminar on Computational Mechanics (NSCM30), held at The Technical University of Denmark (DTU), 25-27 October 2017.
In order to celebrate the anniversary of NSCM, the seminar is this year extended by a half day of plenary lectures, including presentations from outside the Nordic community and a historical overview of NSCM and its association. As a new contribution, this year's conference also introduces a poster session.

The Nordic Association for Computational Mechanics (NoACM) was founded in October 1988 by a group of people from university and industry in the Nordic countries, and in 1991 the Baltic countries joined NoACM. Its objective is to stimulate and promote research and applications within computational mechanics, to foster the interchange of ideas among the various fields contributing to computational mechanics, and to provide a forum for personal contacts and dissemination of knowledge about computational mechanics. In addition, NoACM represents the interests of its members in the International Association for Computational Mechanics (IACM).

The organizers wish to thank all the invited lectures and the contributors for their effort in preparing their presentations, posters and manuscripts in these proceedings. The financial support from DCAMM, The Department of Mechanical Engineering, NoACM and DYNAmore Nordic is gratefully acknowledged.

Kgs. Lyngby, 12 October, 2017

Jan Høgsberg and Niels L. Pedersen

Table of contents

Plenary Lectures

Contributed papers

Posters

BLENDING OF FEM AND PARTICLE-BASED TECHNIQUES FOR ANALYSIS OF PARTICULATE FLOWS AND THEIR INTERACTION WITH STRUCTURES

EUGENIO OÑATE[1] , MIGUEL ANGEL CELIGUETA[1], JOSEP MA CARBONELL[1], ALESSANDRO FRANCI[1] ,GUILLERMO CASAS[1] AND SERGIO R. IDELSOHN[1*]

[1]International Center for Numerical Methods in Engineering (CIMNE),
Universitat Politècnica de Catalunya (UPC), Barcelona, Spain
[*]*ICREA Research Professor at CIMNE*
e-mail: onate@cimne.upc.edu

Abstract

We present advances in the development and application of a new particle-discrete-finite element method based on the blending of an enhanced discrete element method (DEM, www.cimne.com/dempack) [1] for non-cohesive and cohesive materials and an extension of an innovative combination of particle-based techniques and the finite element method (the PFEM, www.cimne.com/pfem/) [2]. The hereafter called PDFEM allows the study of flows incorporating particles of different sizes and their interaction with structures. The goal is to solve particulate fluid-solid-structure interaction problems at the scales that are necessary for predicting the response and safety of structures under water hazards with accuracy and reliability.
The PDFEM uses a Lagrangian description to model the motion of discrete physical particles within a fluid and nodes (viewed as "virtual particles") in both the fluid and the solid domains. These "continuum" domains are discretized with a mesh in which the governing equations for the corresponding continuum problem (i.e. a fluid or a solid) are solved using the FEM. The analysis mesh is re-generated at each time step in terms of the motion of the nodes belonging to the moving continua. The interaction between the discrete particles with the underlying fluid is modelled with an embedded technique. Structural failure is predicted using an innovative combination of FEM and DEM procedures [3].
In the paper we present advances in the PDFEM for studying the frictional contact between a particulate flow and deforming structures, surface erosion and multi-fracture situations in a structure under the effect of the forces induced by a particulate flow. We present applications of the PDFEM to several problems in civil, mechanical, marine and naval engineering.

Keywords: Particle Finite Element Method, Discrete Element Method, Finite Element Method, Particulate Flow, Fluid-Structure Interaction.

References

[1] Oñate E, Zárate F, Miquel J, Santasusana M, Celigueta MA, Arrufat F, Gandikota R, Valiullin K and Ring L, A local constitutive model for the discrete element method. Application to geomaterials and concrete, *Comput. Particle Mechanics.*,2,139-160, 2015.
[2] Oñate E, Celigueta MA, Latorre S, Casas G, Rossi R, Rojek J, Lagrangian analysis of multiscale particulate flows with the particle finite element method, *Comput. Particle Mechanics*,1,85-102, 2014
[3] Zarate F and Oñate E, A simple FEM–DEM technique for fracture prediction in materials and structures, *Comput. Particle Mechanics*, 2, 3, 301-314, 2015.

30th Nordic Seminar on Computational Mechanics
NSCM-30
J. Høgsberg. N.L. Pedersen (Eds.)
2017

COMPUTATIONAL MECHANICS-ON THE EVOLUTION OF A NEW SCIENTIFIC FIELD

NILS-ERIK WIBERG*

* Chalmers University of Technology
Department of Industrial and Materials Science
Division of material and computational mechanics
SE-41206 Gothenburg, Sweden
e-mail: new@chalmers.se, web page: http://www.chalmers.se

Key words: Computational Mechanics, Modelling, Simulation, Finite Elements

Summary. This paper is written on the occasion of the 30th anniversary of the Nordic Seminar on Computational Mechanics (NSCM). The development of the digital computers after the Second World War has dramatically changed the mathematical and numerical methods to solve problems in physics and mechanics. Due to this development a new scientific field called Computational Mechanics has evolved. It is then of interest to have a look at the evolution process of science as such and the joint efforts of researchers to support interchange of knowledge. The successive establishment of international as well as local associations as the Nordic Association on Computational Mechanics (NoACM) is described together with personal comments on the development of the scientific field.

1 INTRODUCTION

It has always been a need to understand nature and predict performance of for example structures to be built, and to create tools to achieve this. The use of mathematical models to describe physical and mechanical phenomena in nature has a long history. Modelling and simulation of problems in physics and mechanics have undergone a dramatic development since the 1950s. Due to the advent of the digital computer new mathematical and numerical techniques have developed to be an indispensable tool to better understand the physical and mechanical behavior and to make better “constructions”. This has meant that a new scientific field denoted Computational Mechanics or more generally Computational Methods in Applied Sciences has appeared. A new scientific field demands joint efforts and cooperation among the researchers on different levels. Associations on local, European and international levels have been established such as the Nordic Association on Computational Mechanics (NoACM).

A major effort of the associations is to arrange and coordinate seminars, conferences and congresses. This paper is written on the occasion of the 30th anniversary of the Nordic Seminar on Computational Mechanics (NSCM). At a jubilee like this, it can be appropriate to look back and see how it all developed and to put things in a longer perspective. It will deal with the evolution of the scientific field of Computational Mechanics in a general context, describing the establishment of Computational Mechanics Societies as well as to give some

brief comments to the evolution of the field with glimpses from personal experiences during a 50 year period. It is stressed that the young generation should be in focus in order to vitalize the whole society.

2 NORDIC SEMINARS ON COMPUTATIONAL MECHANICS (NSCM)

On the initiative of Alf Samuelsson, some scientists and engineers from the Nordic Countries (Denmark, Finland, Norway and Sweden) were personally invited to Chalmers University of Technology in Gothenburg, Sweden in October 1988 to the 1:st Nordic Seminar on Computational Mechanics (NSCM). The NSCM is after that organized annually by the Nordic Association for Computational Mechanics (NoACM). The hosting of the seminars is circulated among the member countries.

On certain occasions the seminar is extended with an additional day. An example of this was at the retirement of Alf Samuelsson at NSCM-8 at Chalmers in 1995. It is known as the snow conference with a warm farewell.

The effort of the NoACM-Seminars has been to encourage young people to meet, to present scientific work in a friendly atmosphere and to create a personal network early in life, which is invaluable. At the same time it makes it possible for more experienced researchers to meet and discuss common matters.

3 COMPUTATIONAL MECHANICS SOCIETIES

3.1 Computational mechanics-a new type of conferences

In the field of mechanics International Union of Theoretical and Applied Mechanics (IUTAM)) dates back to 1922 when the first International Conference in Mechanics took place in Innsbruck. It was arranged by Theodore von Karman, who wanted to bring scientists from all countries together after the First World War. After the Second World War applied mechanics changed drastically due to the development of fast computers. To promote this evolving field young scientists and engineers together with their mentors had a special need to come together, so a new type of conferences were arranged by Engineering Societies as AICE and by Engineering Departments as Civil Engineering in Swansea UK. In 1960s and 70s the development of computers and computer-based methods of analyses was very intensive and fast: new types of conferences, scientific journals and books appeared. Soon discussions appeared to bring the community of computational mechanics together.

3.2 IACM

In 1981, some individuals (R.H. Gallagher, T. Oden and O.C. Zienkiewicz) in the field of computational mechanics took the initiative and called to a meeting in Atlanta. At this meeting the International Association of Computational Mechanics (IACM) was established. The first World Congress was held in Austin 1986. The congresses were from start arranged

every 4th year but later every 2nd year. Alf Samuelsson from NoACM has in periods been its secretary as well as president. It was soon understood that the main work of IACM must be locally based, close to the roots of research. Therefore discussions came up that local Chapters/Associations should be created. Early associations of this kind were the US 1987, the Nordic 1988 and the Spanish 1989.

3.3 NoACM

At NSCM-1 in 1988 the Nordic Association of Computational Mechanics (NoACM) was established. In fact NoACM became one of the very first associations of this kind. The Nordic Seminar series NSCM was by that started and since then being held annually. At NSCM-3 1990, held in Helsinki, the question to invite the newly liberated Baltic countries (Estonia, Latvia and Lithuania) to join NoACM. This became a reality at the seminar in Lund in 1991.

Within the local associations in Europe the question then arose, that there should be some cooperation on European level, between the local Associations and with IACM to better match the larger US and Japanese Associations.

3.4 ECCOMAS

After some years of discussions in early 1990s between different local Associations mainly from the fields of Computational Solid and Structural Mechanics (CSM) and Computational Fluid Mechanics (CFD) a European Association was formed. It became a reality at the First European Congress in Brussels 1992, when the European Community of Computational Methods in Applied Sciences, (ECCOMAS) was born. Now it is a federation of 23 members in Europe to promote joint efforts of European associations with interests in the development and applications in science and technology. The main goal is to arrange and coordinate Congresses and conferences in Europe. To better promote science a number of Committees has been formed like Computational Applied Mathematics, Computational Fluid Mechanics, Computational Solid and Structural Mechanics. ECCOMAS has got strong administrative support from the international research center CIMNE in Barcelona, by managing the Secretariat.

A most successful initiative has been the “Thematic Conferences” that started in 2003 (held in every 2nd odd year). Now about 25 small/medium sized conferences are organized in these years. This really shows vitality and strength of the field and its organization. Examples of contributions started from NoACM are the ADMOS-conference now on its 8th edition and MARINE-conference on its 7th edition.

To recognize and encourage young researchers the “ECCOMAS PhD-Thesis Awards” is delivered every year since 2003. It is given to the two best theses in Europe Meaning: honor, prize money in cash, and a plenary lecture at an ECCOMAS conference. The competition is very strong with around 100 applications every year. Another initiative is the “Young Investigators Conference” which target is PhD students and young researchers under the age of 35. It is run mainly by the young researchers themselves.

.

4 COMPUTATIONAL MECHANICS - COMMENTS ON ITS EVOLUTION

4.1 Introduction

The development in the field of Computational Mechanics has been dramatic and never dreamed of since the advent of the digital computer. It paved the way for numerical approximation methods. Some notes on the development will be given together with comments related to the authors experience during a 50-year period.

4.2 Development of computational mechanics

Starting up period (1950-1980): With the digital computer the first systemized analysis were first made on beam-like structures with matrix manipulation methods. From mid 1950s pioneering work was made by J. Argyris on energy methods and by R. Clough on structural analysis of thin airplane wings. Clough coined the name "Finite Element Method" in 1960. My experience started in mid 1960s with matrix based sub-structuring techniques combining displacement and force methods. Solution with a skyline solver.

Approximation methods like FEM came into wide use. The first book on FEA by O.C. Zienkiewicz was published in 1967. General FEA codes like ASKA (by Stuttgart, J. Argyris), NASTRAN (by NASA) and SESAM69 (by DNV Oslo, P. Bergan) were released at the end of 1960s. Papers, journals and conferences appeared in different fields. Notable is the conference "Finite Elements in Nonlinear Mechanics" in Geilo 1977, a cooperation between NTNU and Chalmers, gathering the expertise of the field. Courses entered curriculums of universities.

Maturing period (1980-2010): Simulation techniques, more mature and in many new fields of applications, became a tool for daily use in simulation of large scale problems. Error control and improved solutions became new subjects. Input and output facilities such as CAD and VR were added to the analyses programs as it is of utmost importance for engineers in practice. To strengthen joint efforts, societies like IACM, NoACM and ECCOMAS were established. Examples from the authors own experience are: Adaptive methods, Wave propagation problems. Use of iterative methods for large scale indefinite problems appearing in analysis with constraint equations and in multi-physics.

Period without limits (2010- and forward): Although much have been achieved, there are many scientific challenges which need effective numerical procedures such as for: multi-physics problems, multi-scale problems, fluid flow, analysis in real time, automated adaptive models with error control in all fields. Lifelong education is a must on all levels in order to properly utilize new achievements in science and engineering.

5 CONCLUSIONS

Many challenges are waiting for us all to better understand and handle nature. We quote the vision of Astrid Lindgren, "Everything great that happened in the world, happened first in some human mind, and how the world of tomorrow will look like depends to a great extent on the amount of strength of imagination that exists in those who just now are learning to read". Thus let the young generation be in focus, and this is also the mission of NSCM. Computational Mechanics offers a great future for young scientists.

30th Nordic Seminar on Computational Mechanics
NSCM-30
J. Høgsberg. N.L. Pedersen (Eds.)
2017

STABILISED FINITE ELEMENT METHODS FOR VARIATIONAL INEQUALITIES

TOM GUSTAFSSON*, ROLF STENBERG* AND JUHA VIDEMAN†

*Department of Mathematics and Systems Analysis, Aalto University
P.O. Box 11100, 00076 Aalto, Finland
e-mail: tom.gustafsson@aalto.fi, rolf.stenberg@aalto.fi

†CAMGSD/Departamento de Matemática, Instituto Superior Técnico, Universidade de Lisboa
Av. Rovisco Pais 1, 1049-001 Lisboa, Portugal
e-mail: jvideman@math.tecnico.ulisboa.pt

Abstract. We survey our recent and ongoing work[1,2] on finite element methods for contact problems. Our approach is to first write the problem in mixed form, in which the contact pressure act as a Lagrange multiplier. In order to avoid the problems related to a direct mixed finite element discretisation, we use a stabilised formulation, in which appropriately weighted residual terms are added to the discrete variational forms. We prove that the formulation is uniformly stable, which implies an optimal a priori error estimate. Using the stability of the continuous problem, we also prove a posteriori estimates, the optimality of which is ensured by local lower bounds. In the implementation of the methods, the discrete Lagrange multiplier is locally eliminated, leading to a Nitsche-type method[3].

For the problems of a membrane and plate subject to solid obstacles, we present numerical results.

Keywords: Variational inequalities, Contact problems, Stabilised finite element methods, Nitsche's method, error analysis.

REFERENCES

[1] Tom Gustafsson, Rolf Stenberg, and Juha Videman, *Mixed and stabilized Finite Element Methods for the obstacle problem*, SIAM J. Numer. Anal. (to appear). arXiv preprint:1603.04257.

[2] Tom Gustafsson, Rolf Stenberg, and Juha Videman, *A stabilized finite element method for the plate obstacle problem*, In prepartation

[3] E. Burman, P. Hansbo, M. G. Larson, and R. Stenberg, *Galerkin least squares finite element method for the obstacle problem*, Computer Methods in Applied Mechanics and Engineering, 313 (2016), pp. 362–374.

30th Nordic Seminar on Computational Mechanics
NSCM-30
J. Høgsberg. N.L. Pedersen (Eds.)
2017

NUMERICAL STABILITY OF STRUCTURES

ANDERS ERIKSSON AND ARNE NORDMARK

KTH Mechanics
Royal Institute of Technology
Osquars backe 18, SE-10044 Stockholm, Sweden
e-mail: <anderi,nordmark>@kth.se, web page: http://www.mech.kth.se/

Abstract.

All structures — to some degree — react non-linearly to mechanical loading. Computational equilibrium solutions are often seen as quasi-static, parameterizing response in fictitious time, but with no inertia effects. Seeing the response as a continuous function of load level is deeply rooted in engineering, even if multi-parametric simulations could often be beneficial. A fundamental assumption is also often a conservative system.

Closely related to this view is that of stability. This concept is fundamentally dynamic in nature, but can for a loaded structure loosely be seen as a capacity to remain close to the static equilibrium situation. Stability thereby refers to one particular equilibrium load state, even if engineering views focus on a stability limit, i.e., when and how stability is lost under a parameterized loading. A sufficient condition for static stability is then defined as a local minimum for the total potential energy, being the strain energy and the potential of external loads.

The presentation will discuss the static view on structural stability, and situations where a minimum of potential energy is not necessary for stability of an equilibrium state, in particular cases when passive physical constraints restrict the kinematic possibilities.

The most commonly considered static instabilities are limit and bifurcation states. The latter, i.e., the typical structural buckling situations, are always related to a symmetry-breaking response to loading. The presentation will discuss the influence of symmetries — present or lacking in a model — on the instability conclusions.

Keywords: Stability Criteria, Multi-parametric Settings, Physical Constraints, Model Symmetry.

REFERENCES

[1] Y. Zhou, A. Nordmark and A. Eriksson. Multi-parametric stability investigation for thin spherical membranes with contacts. *Int. J. Mech. Sci.*, **131–132**, 334–344, (2017).

[2] A. Eriksson and A. Nordmark. Symmetry aspects in stability investigations for thin membranes. *Comp. Mech.*, **58**, 747–767, (2016).

30th Nordic Seminar on Computational Mechanics
NSCM-30
J. Høgsberg. N.L. Pedersen (Eds.)
2017

SIMULATION AND ANALYSIS OF WIND TURBINE WAKES

JENS N. SØRENSEN

Department of Wind Energy
Technical University of Denmark

Abstract. Modern wind turbines are often clustered in wind farms in which the turbines are fully or partially influenced by the wake of upstream located turbines. As a consequence, the wake behind the wind turbines has a lower mean wind speed and an increased turbulence level, as compared to the undisturbed flow outside the farm. Hence, wake interaction leads to a decreased total production of power, caused by lower kinetic energy in the wind, and an increase in the turbulence intensity. The turbulence created from wind turbine wakes is mainly due to the presence of the distinct tip and root vortices, which eventually break down and forms small-scale turbulent structures. If a wind turbine is located in a wake consisting of tip and root vortices, the fatigue loading is more severe than in the case where the tip vortices have already broken down by instability mechanisms. Therefore, understanding the physical nature of the vortices and their dynamics in the wake of a turbine is important for the optimal design of a wind farm.

In the past years, wakes behind wind turbine blades have been studied both experimentally and numerically, using analytical tools as well as numerical simulations based on RANS or LES methodologies combined with actuator disc or line techniques ([1]). From these studies it has been shown that helical wakes are inherent unstable and that the flow inside a wind farm to a large extent is depending on the ambient turbulence and the stability properties of the atmospheric boundary ([2], [3]).

In the present work we study the near wake behavior of a wind turbine in order to elucidate the impact of the tip- and root vortices on the turbulence characteristics and in particular on the length of the near wake. The numerical model is based on large-eddy simulations (LES) of the Navier-Stokes equations using the actuator line (ACL) method. The wake is perturbed by applying stochastic or harmonic excitations in the neighborhood of the tips of the blades. The flow field is then analyzed to obtain the stability properties of the tip vortices in the wake of the wind turbine. As a main outcome of the study it is found that the amplification of specific waves (traveling structures) along the tip vortex spirals is responsible for triggering the instability leading to wake breakdown. The analysis furthermore leads to a simple expression for determining the length of the near wake. This expression shows that the near wake length is inversely proportional to thrust and tip speed ratio and direct proportional to the logarithmic of the turbulence intensity.

REFERENCES

[1] Sørensen, J.N. (2011) ”Instability of helical tip vortices in rotor wakes”. J. Fluid Mechanics, vol. 682, pp. 1-4.

[2] Sørensen, J.N., Mikkelsen, R.F., Henningson, D.S., Ivanell, S., Sarmast, S. and Andersen, S.J. (2015) ”Simulation of wind turbine wakes using the actuator line technique”. Phil. Trans. R. Soc. A 373: 20140071. 16 pages. http://dx.doi.org/10.1098/rsta.2014.0071.

[3] Sarmast, S., Dadfar, R., Mikkelsen, R.F., Schlatter, P., Ivanell, S., Sørensen, J.N., Henningson, D. S. (2015) “Mutual inductance instability of the tip vortices behind a wind turbine”. J. Fluid Mechanics, vol. 755, DOI: 10.1017/jfm.2014.326.

30th Nordic Seminar on Computational Mechanics
NSCM-30
J. Høsberg, N.L. Pedersen (Eds.)
2017

ADAPTIVE METHODS FOR CLASSICAL FEM AND MODERN IGA

TROND KVAMSDAL†*, KJELL M. MATHISEN‡, AND KNUT M. OKSTAD*

†NTNU, Department of Mathematical Sciences
N-7491 Trondheim, Norway
e-mail: Trond.Kvamsdal@ntnu.no - Web page: http://www.ntnu.no

‡NTNU, Department of Structural Engineering
N-7491 Trondheim, Norway
e-mail: Kjell.Mathisen@ntnu.no - Web page: http://www.ntnu.no

*SINTEF Digital, Department of Mathematics and Cybernetics
N-7465 Trondheim, Norway
e-mail: Trond.Kvamsdal@sintef.no, Knut.Morten.Okstad@sintef.no,
web page: http://www.sintef.no/

Key words: Adaptive Methods, Error Estimation, Finite Element, Isogeometric Analysis

Summary. This paper gives an overview of the work by the authors regarding development of adaptive methods for classical finite element methods in the 1990's and similar for isogeometric analysis in the 2010's. Two numerical examples illustrating the achievements obtained in the two different periods are presented.

1 Introduction

A posteriori error estimates for finite elements dates back to the pioneering work by Babuška and Rheinboldt in the late 1970's[1,2]. Claes Johnson an coworkers at Chalmers University of Technology (CTH) were the pioneers behind duality based error estimates (today often called *Goal oriented adaptivity*) starting in the mid 1980's and we refer here to the paper by Johnson and Hansbo[3] and references therein. An important step for the interest in adaptive methods within the engineering research community was the work by Zienkiewicz and Zhu starting with a *simple error estimator*[4], which we herein denote as *Continuous Global* L_2 (CGL2), and in particular the *Superconvergent Patch Recovery (SPR)* method presented in 1992[5,6]. Niels-Erik Wiberg and coworkers at CTH have made a number of interesting contribution to recovery based error estimation methods and here we mention two of their early contributions: The extension of the CGL2 to elastodynamics[7] and the enhancement of the SPR-estimator to take into account weak fullfilment of equilibrium and boundary conditions[8].

We, at NTNU (back then called NTH), started to lecture about adaptive methods for (classical) finite element methods in structural mechanics during spring 1990 based on the Chapter 14 in the textbook by Zienkiewicz and Taylor[9] that were published in 1988. In 1991 there was a major failure of a Norwegian offshore structure — *The Sleipner accident*. According to[10], one of the two main causes for the accident was inaccurate calculation of the shear force at the joint of a tricell wall. In this particular case the magnitude of the shear force at the critical section was under-estimated with approximately 45%[11]. The Sleipner accident gave us increased incentives to develop error estimates and adaptive procedures for *Quantities of Interest* like setional forces and stresses in structural mechanics.

2 Postprocessing of FE results in structural mechanics

To address error control for quantities of interest in structural mechancs like stresses, surface tractions and sectional forces we performed a thorough literature review and developed what we denoted *Variational Consistent Postprocessing (VCP)*[12]. Variationally (also denoted *virtual work*) consistent recovery of stress resultants using VCP were presented at conferences in the first half of 1990's, see[13,14,15]. The concept of VCP were developed inspired by the sequence of papers by Babuška and Miller, see[16,17,18]. In their post-processing approach they used *extraction functions* that tried to mimic the underlying Green's functions, whereas our VCP approach was based on extraction functions belonging to the finite element space on patches of elements[12,19]. Furthermore, by using the technique introduced by Ladevèze and Leguillon[20] to recover self equibrilated element boundary tractions, we enable recovery of tractions and stress resultants along curves in 2D and surfaces in 3D that does not have to be aligned with inter-element edges in 2D and inter-element surfaces in 3D, respectively.

3 Adaptive methods for classical FEM

In order to do *Goal oriented adaptivity* i.e., adapt the finite element mesh for a *Quantity of interest* (e.g., stress at a point or stress resultants at a cross section) we need an a posteriori error estimator to drive the adaptive refinement procedure. Our first attempt were based on the original simple error estimator by Zienkiewicz and Zhu[4] that were extended to handle geometrically non-linear shell problems[21]. Then, inspired by the SPR procedure[5,6], the excellent analysis of the recovery methods done by Mark Ainsworth and co-workers[22,23] and the enhancements proposed by Wiberg *et al.*[8], we developed an error estimatior based on SPR using statically admissible stress fields[24,25].

Using the concept of VCP we were able to do goal oriented adaptivity for recovering variational consistent surface tractions, sectional forces as well as pointwise stresses[12,26]. Later on this was extended to be applicable to Stokes flow problems[27].

4 Adaptive methods for modern IGA

The new paradigm of Isogeometric analysis, which was introduced by Thomas J. R. Hughes *et al.*[28], demonstrates that much is to be gained with respect to efficiency, quality and accuracy in analysis by replacing traditional Finite Elements by volumetric NURBS[1] elements. However, NURBS are not flexible enough to be a common basis for future CAD and FEA due to the lack of local refinement. The LR B-splines proposed by[29] add versatility by facilitating adaptive refinement based on *a posteriori* error estimates[30]. We have developed two alternative error estimators; One based on Serendipity pairing between two different splines spaces (utilising k-refinement)[31], and one based on superconvergent gradient recovery[32]. In[32] Kumar, Kvamsdal and Johannessen investigated both CGL2 and SPR and achieved very good results. For randomly refinded meshes the use of SPR with computed *true* superconvergent points gave best results. However, for the classical benchmark cases with a posteriori error adapted meshes both CGL2 and SPR (using predefined sampling points) gave good results, i.e., effectivity indices close to one. Thus, we have pursued the use of CGL2 approach for thin plates[33].

5 Numerical examples

A 2D frame type structure, which has fixed support at the bottom of the two vertical walls, is subjected to a uniformly distributed load of intensity $t_x = 1.0$, see Figure 1a). This problem, herein denoted *Frame*, is statically undetermined with respect to the distribution of the reaction forces between the left and right supports. Furthermore, the distribution of forces within each of the horizontal parts are unknown, as well.

Here the aim was to compute the bending moment $M(t, \Gamma, x_c)$ acting at x_c on the cross section Γ located at the right end of the lower horizontal rigel. In Figure 1a), the surface Γ is displayed as a dashed line. The purpose of the numerical study was to compare the VCP approach with the traditional methods for calculation of surface moments. We used a standard four noded bilinear quadrilateral isoparametric membrane element with selective reduced integration of shear energy.

The kinematical consistent surface moment M^{fe} were obtained by integration of the kinematical consistent FE traction field found by direct derivation of the FE displacements. The moment M^{sm} is computed by means of integration of the stresses found by the SPR-SB procedure[24]. Finally, the moments M^{vw} is found by the VCP concept[12].

From the results (presented first in[19]) presented in Figure 1d) and 1e) we clearly see the increased accuracy obtained for all meshes (except the start mesh) with the VCP recovered sectional moments compared to the integrated sectional moments based on either FE or SPR-SB stress fields. For this examples the VCP approach reduces the error approximately 10 times compared to the traditional methods. Furthermore, notice that we have achieved optimal order of convergence, which for bilinear elements are $O(h^2)$.

[1]NURBS – Non-Uniform Rational B-splines, the generic representation of freeform curves and sculptured surfaces in CAD-systems.

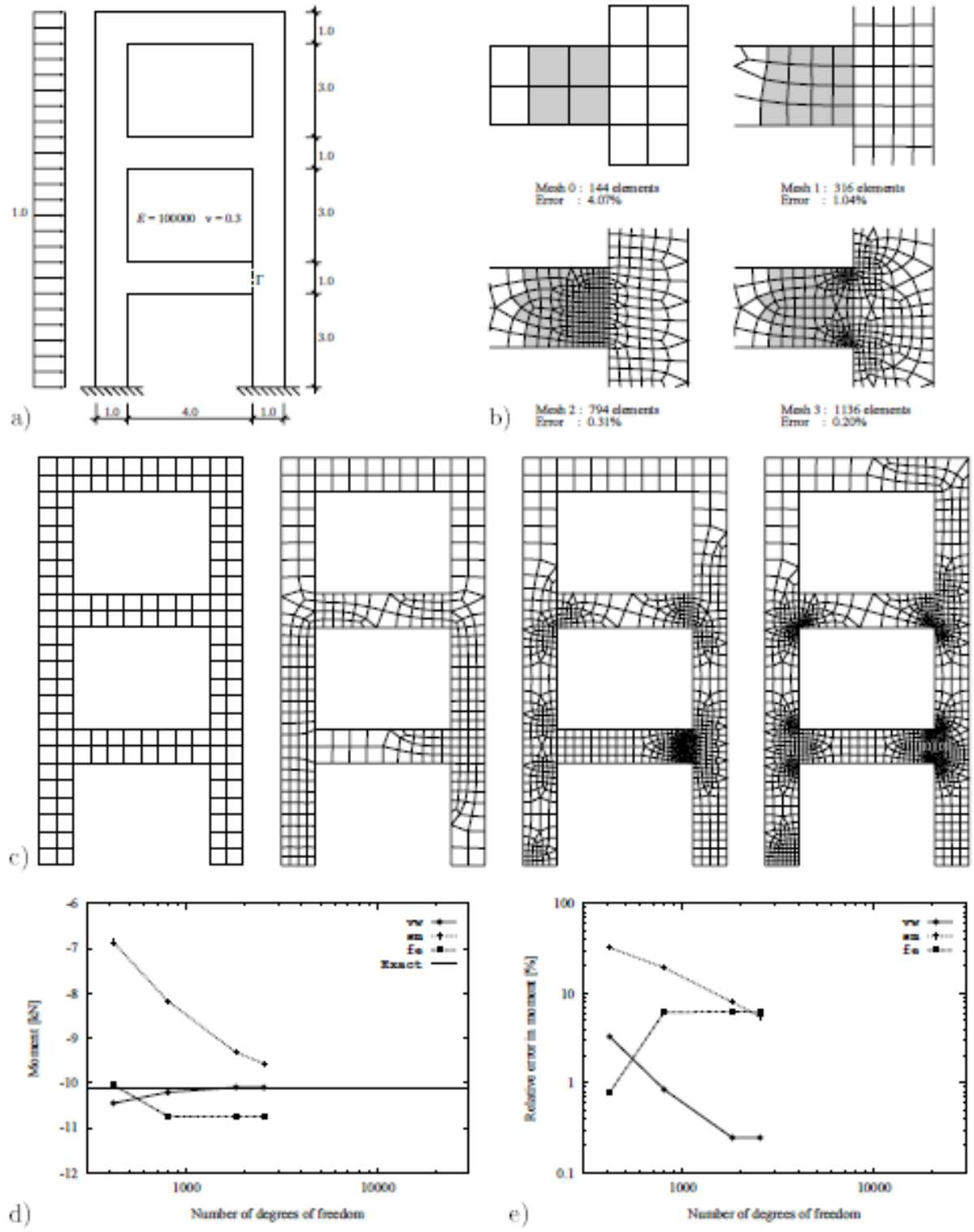

Figure 1: The Frame problem: a) Geometry and properties. b) Adapted mesh in the vicinity of the section Γ. The grey-shaded regions corrsponds to the support of the recovery function. c) Adapted mesh sequence. d) Computed moments $M^{\mathrm{vw}}, M^{\mathrm{sm}}$, and M^{fe} at Γ. e) Relative error in the moments $M^{\mathrm{vw}}, M^{\mathrm{sm}}$, and M^{fe}.

To illustrate the results obtained for adaptive IGA we report here some results related to the classical benchmark problem *Lshape*. In general we obtained very good effectivity indices, i.e., closed to one. Here we have compared the effect of use multi-patch topology to achieve cartesian grid compared to a single patch with bilinear none-affine mapping. Notice that the chosen structured mesh refinement[30] keep the elements cartesian for the multi patch case. From the results we see that affine meshes gives better accuracy.

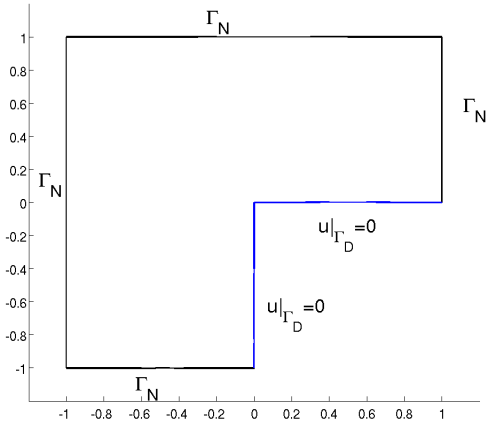

(a) Domian and boundary conditions

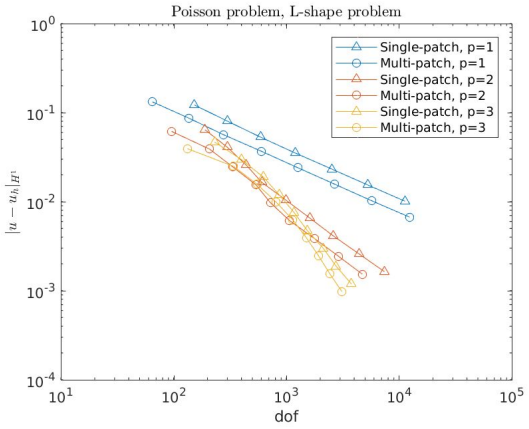

(b) Convergence rates for $p = 1, 2, 3$

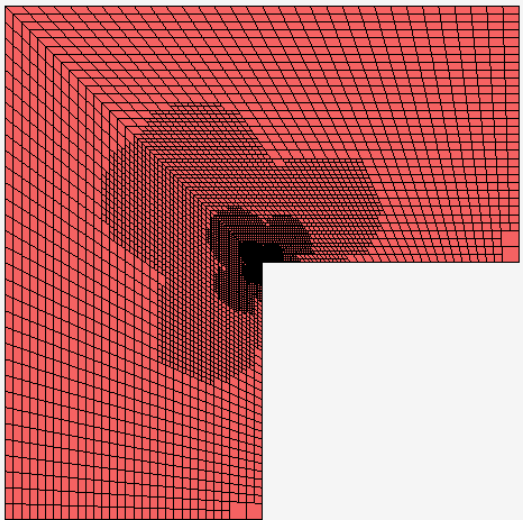

(c) Final mesh for single patch

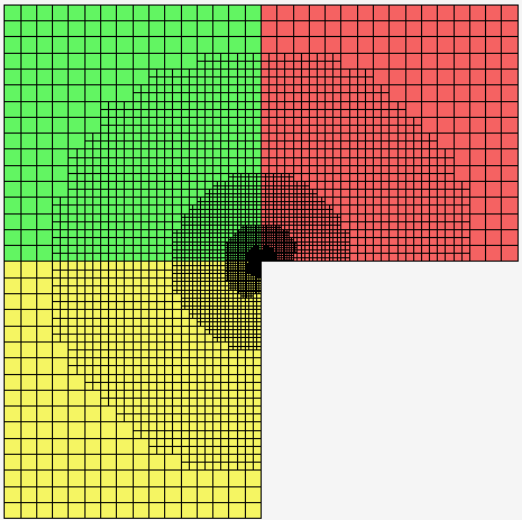

(d) Final mesh for multi patch

Figure 2: The Lshape problem: Comparing single versus multiple patch topology. The cartesian grid obtained when using multi patch topology reduces the error.

REFERENCES

[1] Babuška, I. & Rheinboldt, W. C. *A–posteriori* error estimates for the finite element method. *International Journal for Numerical Methods in Engineering* **12**, 1597–1615 (1978).

[2] Babuška, I. & Rheinboldt, W. C. Error estimates for adaptive finite element computations. *SIAM Journal on Numerical Analysis* **15**, 736–754 (1978).

[3] Johnson, C. & Hansbo, P. Adaptive finite element methods in computational mechanics. *Computer Methods in Applied Mechanics and Engineering* **101**, 143–181 (1992).

[4] Zienkiewicz, O. C. & Zhu, J. Z. A simple error estimator and adaptive procedures for practical engineering analysis. *International Journal for Numerical Methods in Engineering* **24**, 337–357 (1987).

[5] Zienkiewicz, O. C. & Zhu, J. Z. The superconvergent patch recovery and *a posteriori* error estimates. Part 1: The recovery technique. *International Journal for Numerical Methods in Engineering* **33**, 1331–1364 (1992).

[6] Zienkiewicz, O. C. & Zhu, J. Z. The superconvergent patch recovery and *a posteriori* error estimates. Part 2: Error estimates and adaptivity. *International Journal for Numerical Methods in Engineering* **33**, 1365–1382 (1992).

[7] Wiberg, N.-E., Zeng, L. & Xiangdong, L. Error estimation and adaptivity in elastodynamics. *Computer Methods in Applied Mechanics and Engineering* **101**, 369–395 (1992).

[8] Wiberg, N.-E., Abdulwahab, F. & Ziukas, S. Enhanced superconvergent patch recovery incorporating equilibrium and boundary conditions. *International Journal for Numerical Methods in Engineering* **37**, 3417–3440 (1994).

[9] Zienkiewicz, O. C. & Taylor, R. L. *The Finite Element Method, Volume 1, Basic Formulation and Linear Problems* (McGraw–Hill, London, England, 1988).

[10] Jakobsen, B. The Sleipner accident and its causes. In Robinson, J. (ed.) *FEM Today and the Future*, 102–108 (Robinson and Associates, Great Bidlake Manor, UK, 1993).

[11] Holthe, K. & Hanssen, L. SLEIPNER A GBS Loss—report 5. global structural response. Tech. Rep. STF71 F91053, SINTEF Structural Engineering, Trondheim, Norway (1991).

[12] Kvamsdal, T. Variationally consistent postprocessing (VCP). In Oñate, E. & Idelsohn, S. R. (eds.) *Computational Mechanics—New trends and Applications* (CIMNE, Barcelona, Spain, 1998).

[13] Kvamsdal, T., Mathisen, K. M., Okstad, K. M. & Aas, H. B. Techniques for reliable calculation of sectional forces. In Robinson, J. (ed.) *FEM Today and the Future*, 450–456 (Robinson and Associates, Great Bidlake Manor, UK, 1993).

[14] Kvamsdal, T. & Mathisen, K. M. Reliable recovery of stress resultants. In *Proceedings of First International Diana Conference on Computational Mechanics*, 277–286 (Delft, Netherlands, 1994).

[15] Kvamsdal, T. Virtual work consistent tractions and traction resultants. In *Proceedings of Seventh Nordic Seminar on Computational Mechanics*, 26–29 (Trondheim, Norway, 1994).

[16] Babuška, I. & Miller, A. The post–processing approach in the finite element method—Part 1: Calculation of displacements, stresses and other higher derivatives of the displacements. *International Journal for Numerical Methods in Engineering* **20**, 1085–1109 (1984).

[17] Babuška, I. & Miller, A. The post–processing approach in the finite element method—Part 2: The calculation of stress intensity factors. *International Journal for Numerical Methods in Engineering* **20**, 1111–1129 (1984).

[18] Babuška, I. & Miller, A. The post–processing approach in the finite element method—Part 3: *A posteriori* error estimates and adaptive mesh selection. *International Journal for Numerical Methods in Engineering* **20**, 2311–2324 (1984).

[19] Kvamsdal, T. Variationally consistent postprocessing for adaptive recovery of stresses. In *(ECCM'99) European Conference on Computational Mechanics*, CD–rom (CIMNE, Barcelona, Spain, Munich, Germany, 1999).

[20] Ladevèze, P. & Leguillon, D. Error estimate procedure in the finite element method and applications. *SIAM Journal on Numerical Analysis* **20**, 485–509 (1983).

[21] Okstad, K. M. & Mathisen, K. M. Towards automatic adaptive geometrically non-linear shell analysis. Part I: Implementation of an h-adaptive mesh refinement procedure. *International Journal for Numerical Methods in Engineering* **37**, 2657–2678 (1994).

[22] Ainsworth, M., Zhu, J. Z., Craig, A. W. & Zienkiewicz, O. C. Analysis of the Zienkiewicz–Zhu *a–posteriori* error estimator in the finite element method. *International Journal for Numerical Methods in Engineering* **28**, 2161–2174 (1989).

[23] Ainsworth, M. & Craig, A. A posteriori error estimators in the finite element method. *Numerische Mathematik* **60**, 429–463 (1992).

[24] Kvamsdal, T. & Okstad, K. M. Error estimation based on superconvergent patch recovery using statically admissible stress fields. *International Journal for Numerical Methods in Engineering* **42**, 443–472 (1998).

[25] Okstad, K. M., Kvamsdal, T. & Mathisen, K. M. Superconvergent patch recovery for plate problems using statically admissible stress resultant fields. *International Journal for Numerical Methods in Engineering* **44**, 697–727 (1999).

[26] Kvamsdal, T. Variationally consistent postprocessing in structural mechanics. In Wall, W. A., Bletzinger, K.-U. & Schweizerhof, K. (eds.) *Trends in Computational Structural Mechanics*, 491–498 (International Center for Numerical Methods in Engineering (CIMNE), Barcelona, Spain, 2001).

[27] Melbø, H. & Kvamsdal, T. Goal oriented error estimates for Stokes equation based on variationally consistent postprocessing. *Computer Methods in Applied Mechanics and Engineering* **192**, 613–633 (2003).

[28] Hughes, T. J. R., Cottrell, J. A. & Bazilevs, Y. Isogeometric analysis: CAD, finite elements, NURBS, exact geometry and mesh refinement. *Computer Methods in Applied Mechanics and Engineering* **194**, 4135–4195 (2005).

[29] Dokken, T., Lyche, T. & Pettersen, K. F. Polynomial splines over locally refined box-partitions. *Computer Aided Geometric Design* **30**, 331–356 (2013).

[30] Johannessen, K. A., Kvamsdal, T. & Dokken, T. Isogeometric analysis using LR B-splines. *Computer Methods in Applied Mechanics and Engineering* **269**, 471–514 (2014).

[31] Kumar, M., Kvamsdal, T. & Johannessen, K. A. A simple a posteriori error estimatior in adaptive isogeometric analysis. *Computer and Mathematics with Applications* **70**, 1555–1582 (2015).

[32] Kumar, M., Kvamsdal, T. & Johannessen, K. A. Superconvergent patch recovery and a posteriori error estimation technique in adaptive isogeometric analysis. *Computer Methods in Applied Mechanics and Engineering* **316**, 1086 – 1156 (2017).

[33] Okstad, K. M., Kvamsdal, T., Kumar, M. & Mathisen, K. M. On recovery-based error estimation in isogeometric analysis of thin plate problems. In Høsberg, J. & Pedersen, N. L. (eds.) *(NSCM 30) Nordic Seminar on Computational Mechanics*, 151–154 (Lyngby, Denmark, 2017).

30th Nordic Seminar on Computational Mechanics
NSCM-30
J. Høgsberg. N.L. Pedersen (Eds.)
2017

TOPOLOGY OPTIMIMZATION OF NON-LINEAR MATERIALS AND STRUCTURES

MATHIAS WALLIN

Division of Solid Mechanics
Lund University
e-mail: Mathias.Wallin@solid.lth.se

Abstract.

In this talk, examples of methods and algorithms for non-linear topology optimization will be discussed. In the first example, a dynamic finite strain visco-plastic model that is implemented in a gradient based topology optimization framework to design impact mitigating structures will be presented. The kinematics relies on the multiplicative split of the deformation gradient, and the constitutive model is based on isotropic hardening visco-plasticity. To solve the dynamic mechanical balance laws the implicit Newmark-beta method is used together with a total Lagrangian finite element formulation. The optimization problem is regularized using a partial differential equation filter and solved using the method of moving asymptotes (MMA). Sensitivities required to form the MMA approximation are derived using the adjoint method. To demonstrate the capability of the algorithm several protective systems are designed in which the absorbed visco-plastic energy is maximized. The numerical examples prove that inertial and viscous effects can successfully be combined with finite strain visco-plastic topology optimization. In the second part of the talk optimal design of micro-structures will be discussed. Structures that are optimized for maximal negative Poisson's ratio will be presented. It will be shown that the problem of minimizing the Poisson's ratio of a material shares many features with the problem of maximizing the tangent-stiffness of structures. In the last example, we will address the problem of designing micro-structures that are able to dissipate a large amount of energy during large deformations.

Keywords: Topology optimization, Plasticity, Finite strains, Non-linear kinematics

30th Nordic Seminar on Computational Mechanics
NSCM-30
J. Høgsberg. N.L. Pedersen (Eds.)
2017

STRATEGIES FOR SOLVING MULTIPHYSICAL PROBLEMS IN PARALLEL WITH THE FINITE ELEMENT METHOD

PETER RÅBACK

CSC – IT Center for Science
Keilaranta 14, 02110 Espoo, Finland
e-mail: peter.raback@csc.fi

Abstract.

Many problems in computational engineering require parallel computing. There are many possible bottle-necks that can arise when scaling up a serial problem into a larger parallel one. We present some strategies to overcome such bottle-necks that have been implemented in Elmer finite element software[1] and demonstrate their use in number of cases.

The eminent problem in parallel computing is the algorithmic scalability of the numerical methods. The larger the system the more important is the choice of optimal algorithm. In solving the linear systems arising from the finite element method this translates to use of multilevel strategies. Also more robust preconditioning techniques may be required to ensure convergence. Here our strategy often has been the use of block preconditioning.

Sometimes the parallel programming task may be practical bottle-neck. Then it may be desirable to circumvent the complex parallel programming and communication task by tailored partitioning techniques. For example, the communication related to rotating machines may be minimized by enforcing a partitioning where the rotating interface always recides within a subset of partitions.

There are also other issues beyond the actual solution of the finite element problem. When problems become large enough also pre- and post-processing issues may become bottle-necks. To circumvent problems with large meshes they may be finalized on the parallel level in memory. Post-processing bottle-necks are easiest overcome by computing the figures of interest in parallel without actually saving the results.

Keywords: Finite Element Method, Parallel Computing, Multiphysics, Open Source

REFERENCES

[1] *http://www.csc.fi/elmer*, CSC - IT Center for Science.

30th Nordic Seminar on Computational Mechanics
NSCM-30
J. Høgsberg. N.L. Pedersen (Eds.)
2017

CRACK TIP FLIPPING: A NEW PHENOMENON YET TO BE RESOLVED IN DUCTILE PLATE TEARING

KIM L. NIELSEN

Department of Mechanical Engineering, Solid Mechanics Section, Technical University of Denmark, DK-2800 Kongens Lyngby, Denmark
Email: kin@mek.dtu.dk - Web page: http://www.mek.dtu.dk

Key words: Plate Tearing, Flipping Mechanism, Crack Tip Condition, Micro-mechanics.

Summary. Conclusive insight to the mechanics that govern so-called "crack tip flipping" remains to be revealed, but details continue to fall into place as researcher dig deeper. The work presents an overview of the latest findings and the next steps to be made.

1 INTRODUCTION

Strong evidence exists that a number of unexplained transitions in crack surface morphology, that appears in mode I tearing of ductile plates, can be assigned to the so-called "crack tip flipping" mechanism, or element here of. But, little effort has been devoted to getting to the bottom of this intriguing plate tearing phenomenon despite numerous researchers reporting it. Crack tip flipping reveals itself when a slanted tearing crack, propagating in a ductile plate, shifts its orientation from one 45-degree angle shear band to the other. That is, the mechanics at play during crack tip flipping is strongly tied to the well-known slant crack propagation, where two equally active shear bands travel ahead of the leading tip, within a heavily strained region, such that plastic flow and damage evolution localize in one shear band and leaves the other band inactive. Figure 1 display a mode I crack that repeatedly flips back and forth in a very periodic manner and with high frequency – leaving a "shark teeth"-like surface. The flipping frequency is, however, dependent on the set-up (the constraints), the plate thickness, and plate material. For example, El-Naaman and Nielsen (2013) reports high frequencies for steel, whereas the same tests performed on aluminum shows a lower flipping frequency. In fact, a slant crack can display flipping spaced apart on the fracture surface such that the

Figure 1: Repeated crack tip flipping in large scale testing of a normal strength steel plate subject to mode I loading.

slant crack has propagated some distance before making a new flip to the other 45-degree shear band. The mechanics involved are now understood to span multiple length scales – from the micro-mechanics governing ductile damage evolution, through the plastic flow localization into shear bands and thinning ahead of the crack tip, to the competition between the near tip plasticity and the far-field elastic plate response. A status on current insight to the crack tip flipping mechanism is given.

2 INVESTIGATIONS

In a first study dedicated to the crack tip flipping mechanism, El-Naaman and Nielsen (2013) conducted an experimental investigation, where extensive crack propagation in plate metal (both steel and aluminum) was achieved. Through their effort it was cemented that; *i) the flipping mechanism develops in a very stable and controlled manner being easily traced by the naked eye on the outer free surface, ii) steel displays a higher flipping frequency compared to aluminum (the difference is roughly a factor three, when keeping the plate thickness constant), and likewise will the plate dimensions and constraints influence the flipping. Relax the constraint and the flipping frequency has been observed to drop.* The asymmetry in the mode I tearing problem, that develops once the crack slants to propagate in one 45-degree shear band, must give rise to an out-of-plane deflection and it has long been speculated to be the driving force behind the flipping mechanism. In a recent study, Nielsen and Hutchinson (2017) attempt to quantify this out-of-plane action by considering a slanted through-crack propagating in a symmetrical mode I loaded plate strip of elastic-plastic material. Here, relying on a 3D steady-state code tailored to reveal the crack tip conditions under the assumption of small strain. This is an approximation to the complex plate tearing, but the numerical framework allows extracting results without going through the long transient regime. This fundamental study brought out that; *i) a competition between the elastic far-field and the near tip elastic-plastic field unfold during slant crack propagation. Essentially, a purely elastic solution displays an out-of-plane action to one side, whereas a plate dominated by the plastic response displays an out-of-plane action to the other side, ii) a constraint on the out-of-plane bending imposes a significant influence the mixed mode behavior along the crack front (the mode III loading on the crack front increases), iii) the asymmetry in the tearing problem manifests itself in the plastic zone ahead of the crack tip and the stress distribution, in the acute angle corner where the slant crack intersects the plate outer surface, appears to be consistent with initiation of a re-orientated shear crack in the flipping direction.* Such shear cracks (also referred to as “shear-lips”) are often observed in plate tearing and they are a key ingredient in making the slanted crack flipping. Nielsen and Gundlach (2017) recently studied a slant crack tip, undergoing flipping, by use of X-ray tomography to access the plate interior (Fig. 2). While undergoing a shear band switch, such that the flipping mechanism is active, the plate tearing test was interrupted and the crack tip extracted for further investigation. Their study reveals that the failure process ahead of the flipping crack tip closely resemble that of ordinary ductile slant crack growth governed by local thinning and moderate crack tip tunneling, and that; *i) the initiation of the flipping is*

governed by the formation of shear-lips (Fig. 3c) at the both outer free surfaces simultaneously such that the flipping process poses 180-degree rotational symmetry about the growth direction (x_1-axis), ii) during flipping the crack tip consists of two leading edges – one being the edge of the primary slant crack face and one being the edge of the evolving shear-lips (Fig. 3b and d) – and upon further loading, the shear lips grow to catch up on the primary (slant) crack front such that they overtake the growth to complete the flipping and re-orient the crack face, iii) the flipping process contrasts existing tearing modes, where the orientation of the crack front remains stationary, and the near tip stress/strain field continuously chance and never settles in a steady-state. A full 3D numerical study, employing the Gurson material model and taking into account finite strain deformations, has been presented in Felter and Nielsen (2017). In their work, a slight out-of-plane action is imposed to assist the crack tip in flipping – and it really does (Fig. 3).

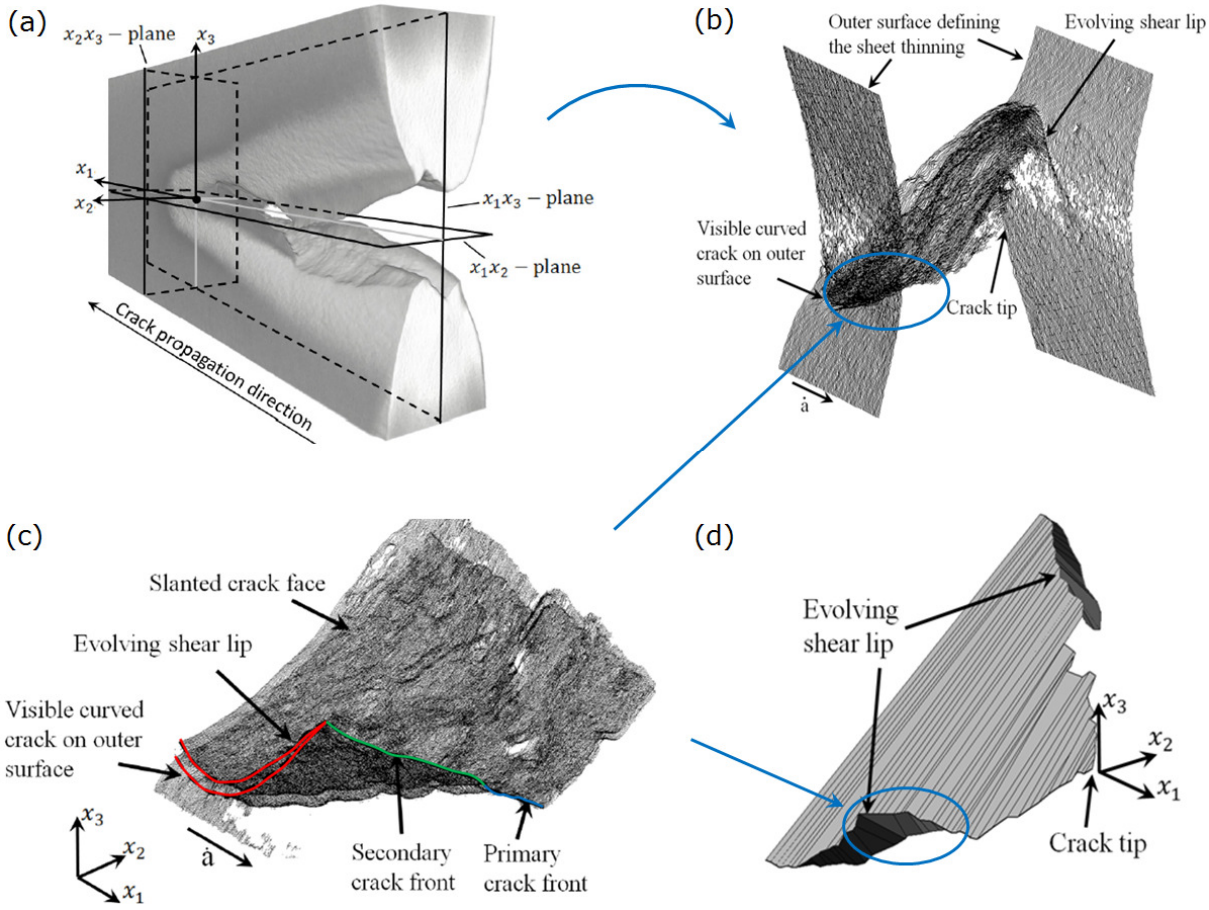

Figure 2: X-ray tomography scans of a crack tip flip underway, showing; (a) a 3D perspective of the flipping crack with growth direction along the positive x_1-axis ($\sim 100\mu$m resolution), (b) flipping crack face and outer surfaces that define the thinning region ($\sim 20\mu$m resolution), (c) details on one shear-lip close to the outer free surface within the thinning region, and (d) manual reconstruction of the flipping crack tip ($\sim 6\mu$m resolution) from the data in Fig. 2(b).

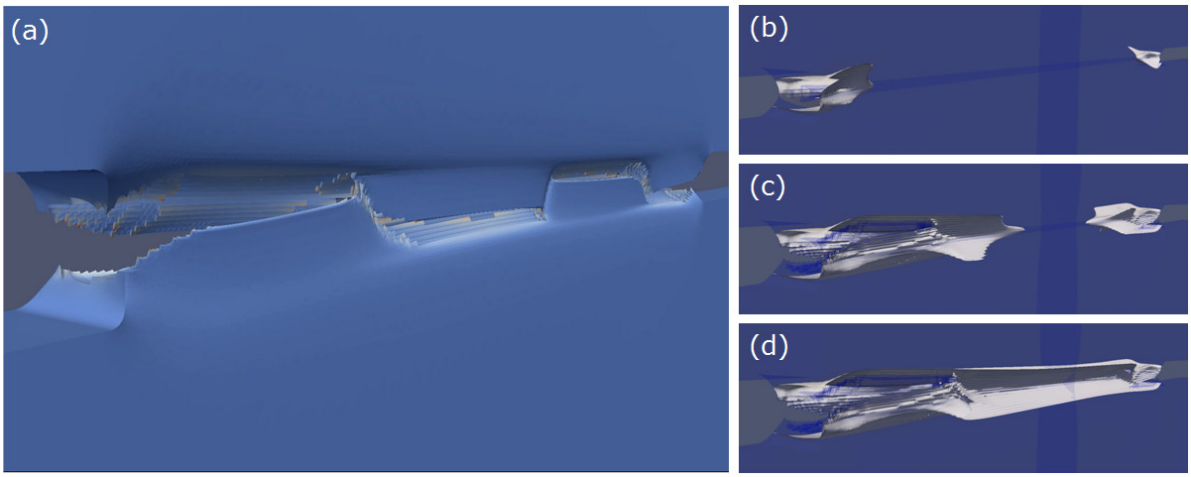

Figure 3: 3D simulation of assisted crack tip flipping using the Gurson model, showing; (a) crack surface at end of simulation, (b-d) contours of void volume fraction, with transparent geometry, at different deformation stages.

3 CONCLUSIONS

- The mechanics governing the crack tip flipping phenomenon is multi-scale as it relies on the constraint effect from the surroundings (e.g. an elastic far-field) to facilitate a favorable asymmetry in the near-tip plastic stress/strain field for damage to evolve.
- The loss of symmetry, when the crack slants, manifests itself as an out-of-plane action of the top/bottom part of the plate and drives the asymmetry in the near field.
- The crack first diverges from the slant orientation at the outer free surface as shear-lips evolve and grow to overtake and govern further advance of the crack tip.

ACKNOWLEDGEMENTS

The work is financially supported by the Villum Foundation Young Investigator Programme, grant VKR023451. Fruitful discussions with colleagues are highly appreciated.

REFERENCES

[1] K.L. Nielsen and J.W. Hutchinson, “Cohesive traction-separation laws for tearing of ductile metal plates”, *Int. J. Impact. Eng.*, **48**, 15-23 (2012).
[2] K.L. Nielsen and J.W. Hutchinson, “Steady-state, elastic-plastic growth of slanted cracks in symmetrically loaded plates”, *Int. J. Impact Eng.*, **108**, 286-294 (2017).
[3] S.A. El-Naaman and K.L. Nielsen, “Observations on mode I ductile tearing in sheet metals”, *Eur. J. Mech. A/Solids*, **42**, 54-63 (2013).
[4] C.L. Felter and K.L. Nielsen, “Assisted crack tip flipping under mode I thin sheet tearing”, *Eur. J. Mech. A/Solids*, **64**, 58-68 (2017).
[5] K.L. Nielsen and C. Gundlach, “Crack tip flipping under mode I tearing: investigated by X-ray tomography”, *Int. J. Solids Struct.*, **118**, 119-127 (2017).

30th Nordic Seminar on Computational Mechanics
NSCM-30
J. Høgsberg. N.L. Pedersen (Eds.)
2017

NANOMECHANICS OF METAL COATED POLYMER PARTICLES

JIANYING HE*

* NTNU Nanomechanical Lab
Faculty of Engineering
Norwegian University of Science and Technology (NTNU)
Richard Birkelands Vei, 7491, Trondheim, Norway
e-mail: jianying.he@ntnu.no, web page: http://www.ntnu.no/nml

Abstract. Monodisperse polymer particles have been widely used in biochemistry and pharmaceutical**Error! Reference source not found.** industry. Recently there is a growing interest in polymer particles with potential application in electronic packaging technologies, such as metal coated polymer spheres (MPS) as conductive filler in Electrical conductive adhesives (ECAs). ECAs are promising alternatives to metallic solders and compete with lead-free solders as a non-toxic alternative to traditional solder.

MPS have been applied in both isotropic conductive adhesives (ICAs) and anisotropic conductive adhesives (ACAs). Certain level of mechanical deformation of the particles is required in order to achieve electrical contact [1]. Thus it is of high interest to understand the deformation and fracture behavior of the individual particles, which will enable the development of improved particles and adhesive joining processes.

Classical molecular dynamics techniques [2] have been employed to predict the effect of internal molecular chain structure of nanoscale polyethylene (PE) particles as well as size dependent properties of both PE and Ni-coated PE particles, subjected to simulated flat-punch compression. The obtained results are compared with experimental observation and provide physical insight into the measurement. The findings from both experimental and computational tests have been tracked back to the design of micron-sized metal coated polymer particles.

Keywords: metal coated polymer particles, flat punch nanoindentation, molecular dynamics, deformation and fracture.

REFERENCES

[1] M. Bazichuk, S.R. Pettersen, H. Kristiansen, Z. Zhang and J. He, “Electromechanical characterization of individual micron-sized metal coated polymer particles”, J. Appl. Phys.119, 245102 (2016).

[2] J. Wu, S. Nagao, Z. Zhang and J. He, “Deformation and fracture of nano-sized metal-coated polymer particles: A molecular dynamics study”, Eng. Fract. Mech. 150, 209-221 (2015).

30th Nordic Seminar on Computational Mechanics
NSCM-30
J. Høgsberg. N.L. Pedersen (Eds.)
2017

IMPACT OF SUPPORT UNCERTAINTIES ON THE MODAL PROPERTIES OF FLOORING SYSTEMS

LARS V. ANDERSEN[*] AND CHRISTIAN FRIER[†]

[*] Department of Engineering
Aarhus University
Inge Lehmanns Gade 10, 8000 Aarhus C, Denmark
Email: lva@eng.au.dk

[†] Department of Civil Engineering
Aalborg University
Thomas Manns Vej 23, 9220 Aalborg Ø, Denmark
Email: cf@civil.aau.dk

Key words: Vibration, Finite Element Analysis, Floor, Uncertainty.

Summary. The paper addresses uncertainty related to boundary conditions of a rectangular concrete floor with focus on its impact on the modal properties of the flooring system. For this purpose, finite-element analysis has been performed using Mindlin theory The hypothesis is that even though a floor is intended to be simply supported along a given edge, if may to some extent be fixed, and vice versa. The influence of variation in the support conditions on the variation of eigenfrequencies of the flooring system is discussed, and the consequences for design of flooring systems is addressed.

1 INTRODUCTION

Vibration of floors has impact on human comfort in buildings. For example, vibration from external sources may cause annoyance during nighttime when inhabitants of a building are going to sleep, and vibration caused by footsteps on a floor in a large office may cause annoyance to other people working in the same room. The vibration level depends on the magnitude, duration, and frequency contents of the source. However, it also depends on the modal properties of the flooring system which in turn depend on the materials, usage, and supports of the floor. All of these are subject to uncertainty.

Pedersen et al. [1] and Frier et al. [2] studied the influence of non-structural mass (e.g. furniture) on the eigenfrequencies of a simply supported floor. Andersen and Kirkegaard [3] performed finite-element (FE) analysis of a multi-storey wooden building with varying joint stiffness between the floors and the loadbearing structure. The idea of the study was that otherwise identical floors in a building might well have different support conditions due to different positions in the building.

This paper presents a three-dimensional FE model for analysis of a concrete floor with uncertain supports conditions. Firstly, a definition of the supports in terms of relative fixity is introduced and discussed. Secondly, an example floor is analysed, and the probability density functions for eigenfrequencies are derived given a uniform distribution of the relative fixity.

2 COMPUTATIONAL MODEL AND METHOD OF ANALYSIS

A solid rectangular concrete floor with dimensions 8×9 m^2 and slab thickness 0.18 m has been considered. The material was assumed linear elastic with Young's modulus 30 GPa and Poisson's ratio 0.15. The mass density was 2400 kg/m^3. Rebar has not been modelled explicitly, but the stiffness and density are assumed representative of reinforced concrete.

The floor has been modelled using quadrilateral isoparametric shell finite elements with nine nodes and biquadratic interpolation of the displacements and cross sectional rotations. Mindlin theory has been applied to account for the thick-plate behaviour of the floor observed within higher modes of resonance. Further, selective integration has been applied to account for the full mass and stiffness in bending and membrane action while at the same time avoiding shear locking. A mesh with 12×12 elements has been found adequate in order to achieve converged results for the first five eigenmodes of the floor with fully clamped or simply supported edges. The model is illustrated in Figure 1.

Real floors are supported at the bottom of the floor. Depending on the friction and bonding between the floor and the supports, this will introduce some degree of fixity. To avoid this and allow modelling of pinned (i.e. moment free) edges, the floor is here regarded as supported along the edge at the mid-plane of the shell.

In order to model partial fixity, rotational springs are implemented uniformly and continuously along the edges of the floor. For eigenmode j, the *relative fixity* is defined as zero when the undamped eigenfrequency f_j corresponds to that of the simply supported floor, f_{js}, and it is one when the undamped eigenfrequency matches that of the clamped floor, f_{jc}. A rotational stiffness providing the eigenfrequency $f_j = (1 - a) f_{js} + a f_{jc}$ has the relative fixity a.

Figure 2 shows the rotational spring stiffnesses per unit length along the edge of the floor that are necessary in order to achieve a given relative fixity. Evidently, if the stiffness is low, such that the floor acts like a simply supported slab, the eigenfrequencies will not change significantly due to a further reduction of the stiffness. Similarly, an increase of the stiffness has no significant influence when the floor is already close to being fully clamped. Contrarily, in the transition, occurring around 10^5–10^9 Nm/m for the present floor, the eigenfrequencies, and hence also the relative fixity, are strongly influenced by the rotational stiffness.

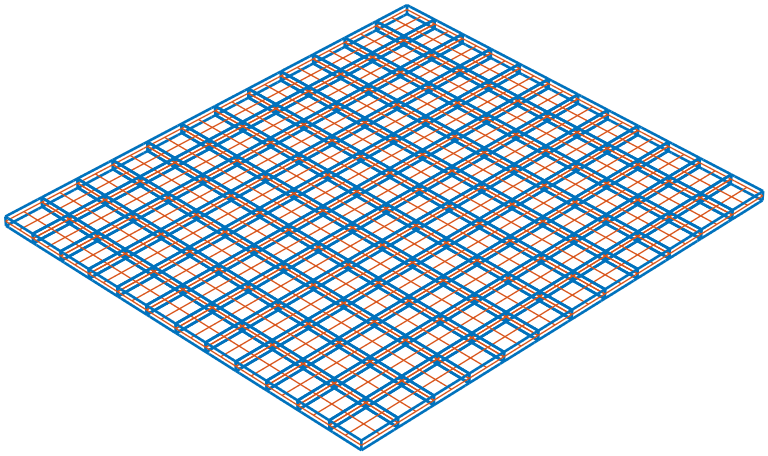

Figure 1: Finite-element model of concrete floor with uncertain fixities along the edge.

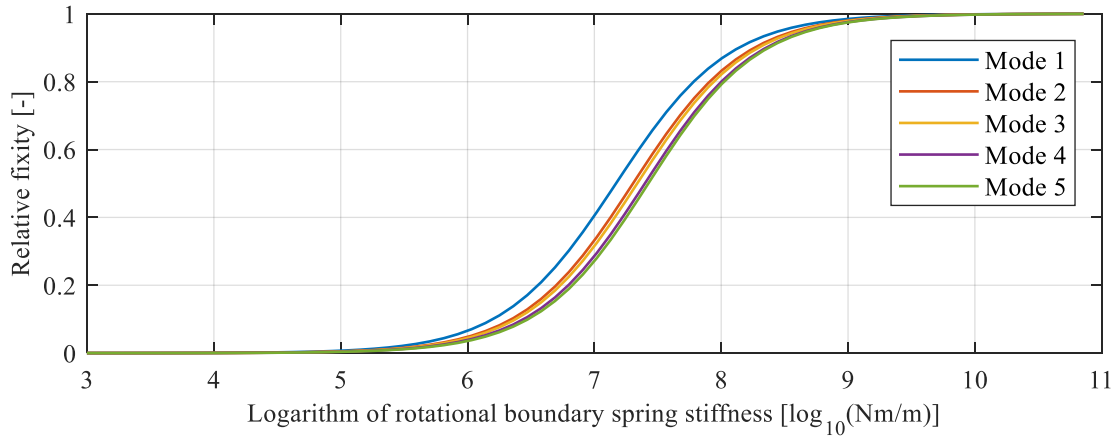

Figure 2: Calibration of rotation stiffness to provide a given relative fixity in Modes 1–5.

It can be observed in Figure 2 that the transition from pinned to clamped conditions at the boundary is not identical for the first five eigenmodes. Thus, Mode 1 requires less rotational stiffness to obtain a certain relative fixity compared to Mode 2, which in turn requires less stiffness than Mode 3, and so on.

3 RESULTS AND DISCUSSION

Figure 3 shows the results obtained by Monte Carlo simulation with 1,000,000 samples of the relative fixity, calibrated to Mode 1 and assumed uniformly distributed between the values 0 and 1. The eigenfrequencies fulfil the criterion $f_{js} \leq f_j \leq f_{jc}$, $j = 1, 2, \ldots, 5$. Further, the probability density function (PDF) for the eigenfrequency related to Mode 1 is again uniform. For the other modes, the probability distributions of the eigenfrequencies are right-skewed, i.e. not following a uniform distribution. This occurs as result of the calibration to match the relative fixity in Mode 1 and demonstrates that the relative fixity is a non-unique property.

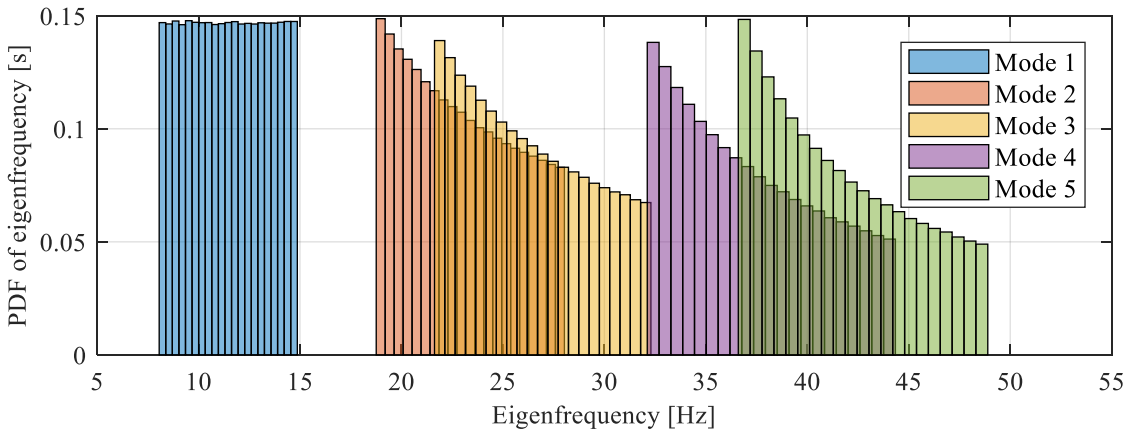

Figure 3: Probability density functions for the eigenfrequencies of Modes 1–5 based on rotation stiffness calibrated to match the target degree of fixity in Mode 1.

The boundary conditions for real floors may heterogeneous, and the uniform distribution assumed in the present analysis may oversimplify the random nature of the supports. In any case, the results presented in Figures 2 and 3 demonstrate how uncertainty related to supports of the floor edges will influence the eigenmodes of the floor. Hence, this uncertainty must be treated in the design of floors to assess the risk of noise and vibration causing annoyance to users of the floor. However, the assessment requires a proper model of the uncertainty.

4 CONCLUSIONS

- A Mindlin shell finite-element model has been utilized for modal analysis of a solid rectangular concrete floor with partial fixity along the edges.
- A relative fixity has been introduced as a means to quantify the rotational stiffness required at the edges of the floor in order to match a given eigenfrequency in the interval between pinned and fully clamped boundaries.
- It has been found that lower rotational stiffness at the boundary is required to obtain a certain relative fixity in lower modes compared to higher modes. Hence, no simple and unique relationship between constant, continuous rotational spring stiffness and relative fixity can be formulated.
- As result of this, when the relative fixity of Mode 1 is assumed uniformly distributed, the eigenfrequency of Mode 1 is uniformly distributed as well, but the probability distributions of the higher eigenfrequencies are increasingly more right-skewed.
- Future models for probabilistic assessment of the eigenfrequencies of floors with uncertain boundary conditions should focus on better estimation and modelling of the probability distributions for the rotational stiffness at the edges.

ACKNOWLEDGEMENT

The research was carried out in the framework of the project “Urban Tranquility” under the Interreg V programme. The authors of this work gratefully acknowledge the European Regional Development Fund for the financial support.

REFERENCES

[1] L. Pedersen, C. Frier, and L. Andersen, “Flooring-Systems and Their Interaction with Usage of the Floor,” in *Dynamics of Civil Structures, Volume 2 : Proceedings of the 35th IMAC, A Conference and Exposition on Structural Dynamics 2017*, 2017, pp. 205–211.

[2] C. Frier, L. Pedersen, L. V. Andersen, and P. Persson, “Flooring-systems and their interaction with furniture and humans,” in *Procedia Engineering, The X International Conference on Structural Dynamics, EURODYN 2017*, 2017.

[3] L. V. Andersen and P. H. Kirkegaard, “Vibrations in a multi-storey lightweight building structure: Influence of connections and nonstructural mass,” in *Research and Applications in Structural Engineering, Mechanics and Computation - Proceedings of the 5th International Conference on Structural Engineering, Mechanics and Computation, SEMC 2013*, 2013.

30th Nordic Seminar on Computational Mechanics
NSCM-30
J. Høgsberg, N.L. Pedersen (Eds.)
2017

STRESS INTENSITY FACTOR EVALUATION FOR ROLLING CONTACT FATIGUE CRACKS

ROBIN ANDERSSON*, FREDRIK LARSSON, ELENA KABO AND ANDERS EKBERG

*CHARMEC/Department of Industrial and Materials Science
Chalmers University of Technology
SE-412 96, Gothenburg, Sweden
e-mail: robin.andersson@chalmers.se, web page: http://www.charmec.chalmers.se/

Key words: Linear Elastic Fracture Mechanics, Rolling Contact Fatigue, Stress Intensity Factors, XFEM, Least Squares Fitting

Summary. An approach to evaluate stress intensity factors for the case of cracks exposed to compressive multiaxial loading, such as often occurs in wheel–rail contact, is proposed. It relies on the matching of displacement fields, calculated by the extended finite element method, towards a low order displacement ansatz, using the method of least squares. The functionality of the approach is demonstrated for the case of a rolling contact fatigue crack.

1 INTRODUCTION

Rolling Contact Fatigue (RCF)[1] cracks in railway applications may lead to wheel and rail failures and subsequent derailments. In order to deepen the understanding of RCF defects, and in turn optimise the rail maintenance strategies, it is worth to simulate how different crack geometries, embedded in the rail head, relate to operational scenarios and assess their severity, e.g. by Stress Intensity Factors (SIFs).

However, RCF cracks differ in several ways from cracks commonly encounter within engineering. First of all, they are mainly loaded in compression, which typically leads to crack closure. Furthermore, the loading conditions beneath a railway wheel are multiaxial, leading to mixed mode loading of the crack. In addition it is of great importance, from a practical point of view, that the crack geometry can be easily changed. These circumstances put demands on the technique chosen for SIF evaluation.

2 SIF EVALUATION

The eXtended Finite Element Method (XFEM)[2] offers a good foundation for fracture mechanics analyses since it conveniently allows for modifications of the crack geometry and is available in commercial software packages. According to linear elastic fracture mechanics theory, it is possible to describe the displacement field close to the crack front

in terms of asymptotic formulae parametrized by unknown SIFs[3]. In a post processing step, the SIFs are then obtained by fitting a developed displacement ansatz to the XFEM solution in a least squares sense[4].

In this study, it is demonstrated that even a low order displacement ansatz provides good accuracy in test cases involving pure mode I, II or III loading as well as mixed mode loading. More specifically, the proposed ansatz consists of displacement fields pertinent to the strain singularities, rigid body motion and uniform strains. The latter terms allow for high accuracy also for cracks subjected to compressive loads. The effectiveness of the method is then demonstrated in the case of an inclined surface breaking RCF crack with a curved crack front subjected to a moving Hertzian load, see Figure 1. Such cracks, in railway applications often encountered in the form of so-called squats, lead to a complex problem involving mixed mode compressive loading.

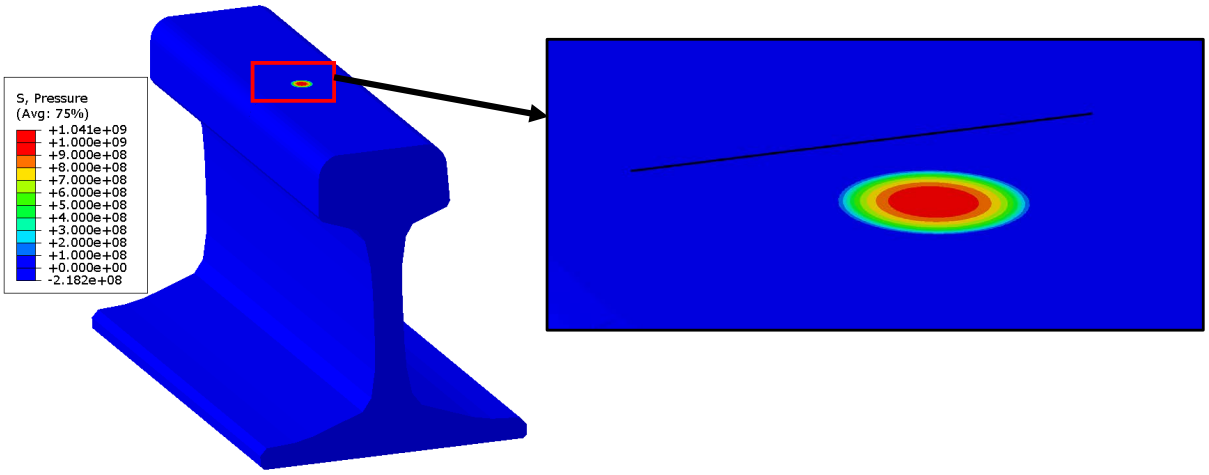

Figure 1: An inclined surface breaking RCF crack, located in the rail head, is subjected to a moving Hertzian load.

REFERENCES

[1] Ekberg, A., Åkesson, B. & Kabo, E. Wheel/rail rolling contact fatigue – probe, predict, prevent. *Wear* **314**, 2–12 (2014).

[2] Belytschko, T. & Black, T. Elastic crack growth in finite elements with minimal remeshing. *International Journal for Numerical Methods in Engineering* **45**, 601–620 (1999).

[3] Kuna, M. *Finite Elements in Fracture Mechanics: Theory - Numerics - Applications*, vol. 201 (Springer Netherlands, Dordrecht, 2013).

[4] Ju, S. H. Simulating stress intensity factors for anisotropic materials by the least-squares method. *International Journal of Fracture* **81**, 283–297 (1996).

30th Nordic Seminar on Computational Mechanics
NSCM-30
J. Høgsberg. N.L. Pedersen (Eds.))
2017

TOPOLOGY OPTIMIZATION OF ACTIVE TRANSPORT FLOWS

CASPER SCHOUSBOE ANDREASEN*

*Department of Mechanical Engineering, Section for Solid Mechanics
Technical University of Denmark
Nils Koppels Allé, Building 404
e-mail: csan@mek.dtu.dk, web page: http://www.topopt.dtu.dk

Abstract. Fluid flows with particle transport are common in many industrial processes and components. The design of components for addition or removal of particles as well as mixing or stratification is of great importance in the specific processes. This work presents a methodology to apply topology optimization to the design of multiphase flow components. The work is a natural extension of the density based topology optimization procedure applied to design of passive mixers[1] and coolers[2] where the transported matter is not influencing the properties of the governing fluid flow model. In this work the effective properties of the fluid is changing with concentration.

In this work a multiphase fluid flow model[3] is combined with a Brinkman penalization in order to introduce the design of the fluid component. Gradient based optimization is applied in order to optimize the performance of flow components. The paper present the design and optimization of a particle separator and the important interpolation for modeling both solids, fluids and particles with a monolithic problem formulation. The interplay with the physics behind the model are discussed and the influence of parameters are demonstrated.

Keywords: Topology Optimization, Multiphase flow, Particles, FEM

REFERENCES

[1] Andreasen, C. S., Gersborg, A. R. & Sigmund, O. Topology optimization of microfluidic mixers. *International Journal For Numerical Methods In Fluids* **61**, 498–513 (2009).

[2] Alexandersen, J., Aage, N., Andreasen, C. S. & Sigmund, O. Topology optimisation for natural convection problems. *International Journal for Numerical Methods in Fluids* **76**, 699–721 (2014).

[3] Manninen, V., Mikko & Taivassalo. *On the mixture model for multiphase flow* (VVT Energy, o Akademi, 1996).

30th Nordic Seminar on Computational Mechanics
NSCM-30
J. Høgsberg, N.L. Pedersen (Eds.)
2017

NUMERICAL SIMULATIONS OF BLAST-LOADED PLATES USING COMBINED FLUID AND STRUCTURE MESH ADAPTIVITY

VEGARD AUNE[1,2,*], GEORGIOS VALSAMOS[3], FOLCO CASADEI[3], MARTIN LARCHER[3], MAGNUS LANGSETH[1,2] AND TORE BØRVIK[1,2]

[1]Structural Impact Laboratory (SIMLab), Department of Structural Engineering, NTNU, Norwegian University of Science and Technology, NO-7491 Trondheim, Norway

[2]Centre for Advanced Structural Analysis (CASA), NTNU, NO-7491 Trondheim, Norway

[3]European Commission, Joint Research Centre (JRC), Directorate for Space, Security and Migration, Safety and Security of Buildings Unit, Via E. Fermi 2749, I-21027 Ispra (VA), Italy

*Corresponding author. E-mail: vegard.aune@ntnu.no

Key words: Fluid-structure Interaction, Adaptive Mesh Refinement, Ductile Failure.

Summary. This study evaluates the capabilities of adaptive mesh refinement (AMR) methods in predicting fluid-structure interaction (FSI) effects and ductile failure in blast-loaded plates. The numerical results were in good agreement with experimental observations, and able to predict the FSI effects, inelastic response and ductile failure in the plates. AMR methods were also found to significantly reduce the CPU cost and still predict the experimental observations.

1 INTRODUCTION

Simulations of blast-loaded structures can be challenging for a number of reasons and are therefore often problem dependent. One typical problem is the simulation of blast-loaded flexible plates undergoing large deformations, all the way to failure, which requires robust computational methods. Since the response of flexible blast-loaded plates is highly non-linear, both the pressure distribution and the dynamic response may be significantly influenced by FSI effects. Coupled FSI simulations may therefore be required for detailed insight in both the loading and the resulting dynamic response. A widely used design tool for this class of problems is the explicit non-linear finite element method (FEM). In the particular case of ductile failure, previous studies[1] indicate that a mesh size equal to the plate thickness may be necessary to predict realistic crack growth when using element erosion. Hence, if coupled FSI simulations are of interest, this implies that also the fluid mesh needs to be refined because the accuracy of the fluid-structure (F-S) coupling requires a sufficiently fine fluid mesh compared to that in the plate. However, the fluid

sub-domain only needs to be refined in the vicinity of the plate and the remaining part can be modelled with a coarser mesh as long as it predicts the blast wave propagation.

The objective was therefore to investigate the performance of recent developments in the FE code EUROPLEXUS (EPX)[2] using AMR methods both in the fluid and structural sub-domains. Special focus was placed on reducing the CPU cost and still retaining sufficient accuracy when predicting the response of thin metallic plates. The numerical results were compared to experimental data to ensure that the underlying physics were maintained.

2 EXPERIMENTAL WORK

Experiments were used to validate the numerical simulations and to improve the understanding of the governing phenomena. A series of tests[1,3] were therefore performed in the SIMLab Shock Tube Facility, since the shock tube produces controlled and repeatable blast loading in laboratory environments[4]. Piezoelectric pressure sensors were employed for pressure recordings, and these measurements were synchronized with two high-speed cameras in a stereoscopic setup to capture the dynamic response using three-dimensional digital image correlation. A sketch of the experimental setup is shown in Figure 1.

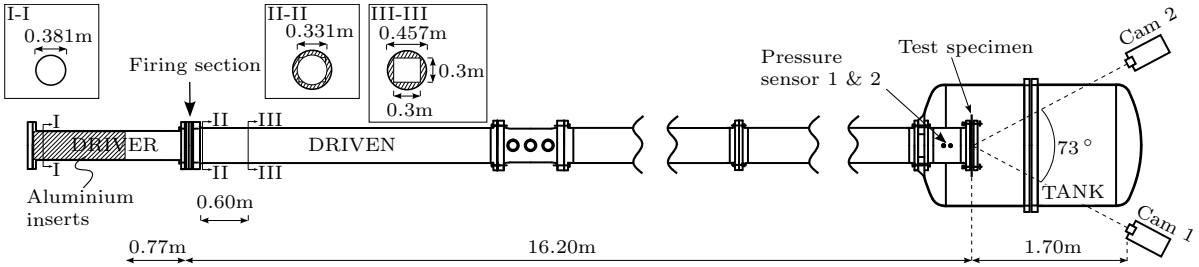

Figure 1: Sketch of the experimental setup (seen from above). Reprint from Aune et al.[1].

3 NUMERICAL SIMULATIONS

The numerical simulations were performed by the FE code EPX[2]. EPX solves the conservation of momentum (equilibrium) equations in the structural sub-domain and the conservation of mass, momentum and energy in the fluid sub-domain.

3.1 Material models

The fluid, air in this case, was considered as compressible and inviscid using the Euler equations and modelled as a perfect gas (*GAZP* material model in EPX). Initial conditions for each simulation were taken from the corresponding test in Refs.[1,3].

The structure, aluminium and steel plates in this case, was modelled using the *VPJC* material model in EPX[2]. This model allows for finite strains and rotations, high strain

rates, ductile failure and temperature softening. The plasticity was governed by the von Mises yield criterion, the associated flow rule and a modified Johnson-Cook relation for the flow stress. Ductile failure was also included in the material model by using the Cockcroft-Latham failure criterion, which is an energy-based criterion using the "plastic work" per unit volume to predict failure in the material. The material parameters were already calibrated in previous works by the authors[1,3].

3.2 Numerical model

A fully coupled FSI model using one quarter of the experimental setup was established (see Figure 2). The plate was modelled using a Lagrangian discretization with an element size of approximately 6 mm as the base mesh and 4-node Reissner-Mindlin shells (*Q4GS*) with 6 dofs per node and 20 integration points (5 through the thickness). The bolts and clamping frames were represented by 8-node brick elements (*CUB8*) with 8 integration points and elastic material behaviour using the physical constants for steel. The contact between the plate, clamping frames and the bolts was modelled by including the pre-tenisoning in the bolts and by using hierarchic pinballs based on a direct penalty method.

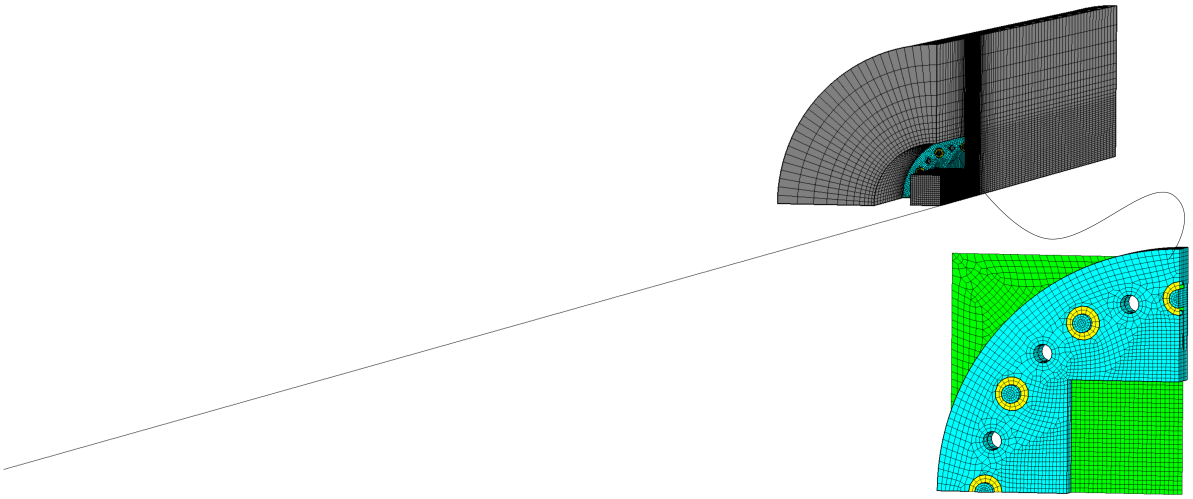

Figure 2: Computational model of the fully coupled FSI simulations. Reprint from Aune et al.[3].

The fluid sub-domain was partly discretized by 1D finite volumes (*TUVF*) and partly by 3D finite volumes (*CUVF*), where the 1D part of the air was used until 0.6 m upstream the test specimen (see Figure 2). An initial mesh size of 0.01 m was used in the entire 1D-domain and in the vicinity of the plate, whereas the cell size in the tank was increased up to 0.08 m towards the internal walls. This resulted in 1587 *TUVF*s and 105,855 *CUVF*s in the fluid sub-domain. Friction and heat exchange against the interior walls of the tube were accounted for by specifying the average roughness (0.4 micrometers) in the *PARO*

directive in EPX.

An embedded FSI technique ($FLSW$)[5] was used for the coupling at the F-S interface, i.e., the fluid and plate were discretized independently at the topological level. Recent advancements[6] in EPX allow for AMR based on user-defined criteria, which make it convenient to relate the AMR to the FSI itself and the damage evolution in the plate. This allows for a sufficiently fine mesh size to represent the near instantaneous rise in pressure over the blast wave and to predict ductile failure in the plate without too much loss of mass when using element erosion. EPX then enables automatic refinement of the fluid mesh in the vicinity of the plate which can move and undergo large deformations, while the plate mesh is refined locally based on the damage evolution during plastic deformation. FSI-driven AMR was therefore activated in the fluid sub-domain to obtain a sufficiently refined fluid mesh at the F-S interface, while damage-based AMR was used in the plate in an attempt to predict the crack propagation observed in the experiments.

4 CONCLUDING REMARKS

The numerical simulations were in very good agreement with the experiments. AMR was found to be promising in predicting FSI effects and ductile failure at a reduced CPU cost. Moreover, FSI-driven AMR improved the representation of the nearly instantaneous rise in pressure over the blast wave (due to a fine cell size). However, there are still some unsolved issues. In particular, the use of damage-based AMR needs further studies to gain more experience and to find proper thresholds.

REFERENCES

[1] Aune, V., Valsamos, G., Casadei, F., Langseth, M. & Børvik, T. On the dynamic response of blast-loaded steel plates with and without pre-formed holes. *Int. J. Impact Eng.* **108**, 27–46 (2017).

[2] EUROPLEXUS User's manual - A computer program for the finite element simulation of fluid-structure systems under transient dynamic loading. `http://europlexus.jrc.ec.europa.eu`. Accessed: 2017-09-18.

[3] Aune, V. *et al.* Use of damage-based mesh adaptivity to predict ductile failure in blast-loaded aluminium plates. *Procedia Eng.* **197**, 3–12 (2017).

[4] Aune, V., Fagerholt, E., Langseth, M. & Børvik, T. A shock tube facility to generate blast loading on structures. *Int. J. Protective Struct.* **7**, 340–366 (2016).

[5] Casadei, F., Larcher, M. & Leconte, N. Strong and weak forms of a fully non-conforming FSI algorithm in fast transient dynamics for blast loading of structures. In *Proc. COMPDYN*, 1120–1139 (2011).

[6] Casadei, F., Diez, P. & Verdugo, F. An algorithm for mesh refinement and un-refinement in fast transient dynamics. *Int. J. Comput. Methods* **10**, 1–31 (2013).

30th Nordic Seminar on Computational Mechanics
NSCM-30
J. Høgsberg. N.L. Pedersen (Eds.)
2017

EFFECTIVENESS OF OPEN TRENCHES IN REDUCING BLAST-INDUCED GROUND VIBRATIONS

NSCM-30

M. BAHREKAZEMI[*], M. SANDSTRÖM[†] AND L-O. DAHLSTRÖM[†]

[*] Golder Associates AB
P.O. Box 20127, 104 60 Stockholm, Sweden
e-mail: Mehdi_Bahrekazemi@golder.se, web page: www.golder.com

[†] Golder Associates AB
Email: Malin_Sandstrom@golder.se and Lars-Olof_Dahlstrom@golder.se

Key words: Ground Vibration, Open Trench, Mitigation

Summary. Rock blasting in urban environments could be a challenge due to the potential risk of damage to nearby buildings as well as disturbance in vibrations sensitive instrument and activities. To avoid unacceptably high vibration amplitudes in the environment the maximum amount of blast charge is usually limited. This will often results in high construction costs if the distance to the nearby buildings is too short. In order to reduce the vibrations, and thus allow higher blast charges, a barrier in the propagation path of the waves may sometimes be useful. This extended abstract presents some results from a numerical analysis using an axisymmetric 2D FE-model used to study the effectiveness of an open trench as a vibration mitigation measure. The numerical modeling shows that the open trench can reduce the vibration amplitude by about 30-70% depending on the conditions at the site.

1 INTRODUCTION

Ground-borne vibrations due to rock blasting is one of the challenges that need to be considered while planning for infrastructure projects in densely populated areas. Development needs of the cities has made it inevitable to carry out construction activities close to the existing buildings and structures. In order to avoid damage to these buildings the maximum level of ground vibrations are usually limited by national standards. In Sweden the SS 460 48 66 [1] gives guidance vibration levels caused by rock blasting. The construction methods are then adjusted so that ground vibrations are kept below the guidance levels. Usually the blast charges are adjusted so that ground vibration levels do not exceed the maximum allowable levels in the contract documents based on the guidance levels. If the distance between rock blast location and nearby building is too short the blast charges may need to be reduced so much that the rock blasting costs become too high and alternative excavation methods have to be considered. Even though other methods for rock excavation such as rock sawing are available nowadays the method is still too expensive to replace rock blasting in general. Therefore if the blast induced vibrations could be limited the rock blasting method could still be the most economical method for rock excavation even in densely populated areas.

Vibration isolation is a known method used to mitigate ground vibrations propagated from

a vibration source ([2], [3], and [4]). Here some results from a simple FE-model has been used to study the effect of such a barrier in mitigating blast induced ground vibrations.

2 METHOD

A simplified axisymmetric FE-model has been created in Plaxis 2D 2016 in order to study the mitigating effect of an open trench used to reduce ground vibrations at location behind the barrier. Ground vibrations due to a dynamic load representing rock blast were calculated using the FE- model, with and without the presence of a trench. A parameter study was carried out with respect to the location of the dynamic load (blasting front) and material properties in the model. The ratio between maximum displacements amplitude obtained with and without the trench was determined for each calculation case considered in the parameter study.

2.1 Geometry

When constructing the geometry of the model (see Figure 1) it is assumed that first the rock is uncovered by excavating the overlaying soil. The soil layer was modeled as a wedge with linearly decreasing thickness towards the model's outer edge. In order to account for the variability in soil depth around the assumed site, the analysis was also repeated with the wedge defined as rock, i.e. assuming that the bedrock appears on the ground surface.

The bottom and outer boundaries of the model were defined as absorbing boundaries. The centerline of the axisymmetric model is fixed in the x-direction and the ground surface is free in all directions. The dimensions of the model were chosen to be large enough that vibrations reflected from the outer boundaries would not affect the displacements near the trench or the buildings.

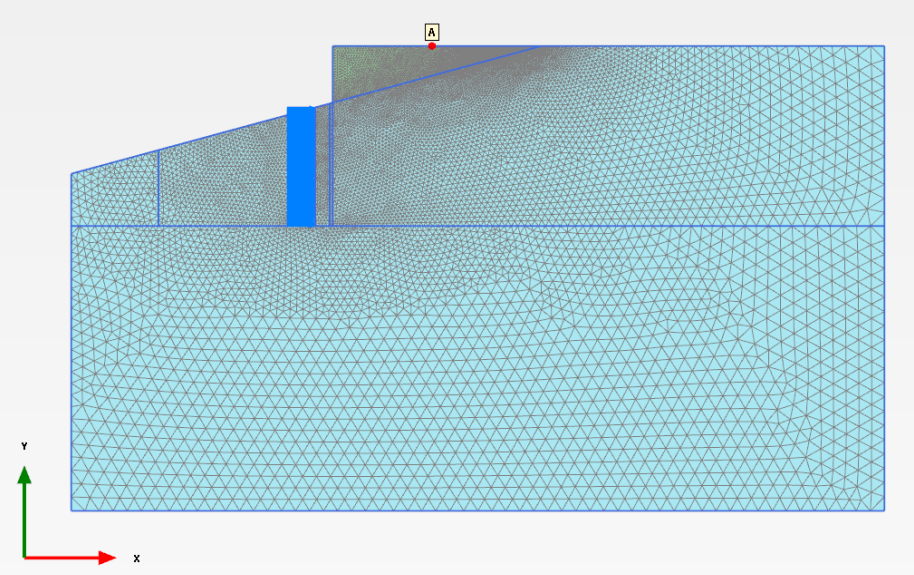

Figure 1: Model geometry created and generated mesh in Plaxis 2D. Point A on the ground surface is about 15 m behind the trench where the vibration amplitude before and after open trench is compared for this study.

2.2 Material properties

The material in the "wedge" was defined as either soil or rock depending on the calculation case, while the material in the remaining part of the model was defined as rock in all calculation cases. The rock material was defined as either soft or hard, based on the stiffness parameter, in order to cover a range of stiffness. All materials were modeled as linearly elastic for this study despite the fact that very close to the blast location the rock is expected to behave as plastic material. The chosen input parameters are presented in Table 1. The values for unit weight, Young's modulus and Poisson's ratio were selected within expected ranges for soil and rock material in Sweden while compression and shear wave velocities are calculated automatically in Plaxis from other input values.

Material	Unit weight, γ [kN/m^3]	Effective Young's modulus, E' [MPa]	Poisson's ratio, ν [-]	Compression wave velocity, c_p [m/s]	Shear wave velocity, c_s [m/s]
Soil	18	50	0,4	242	99
Soft rock	25	5000	0,25	1534	886
Hard rock	25	50 000	0,25	4852	2801

Table 1 : Material parameters used for soil, soft rock and hard rock in the model.

2.3 Loads

The load was modeled as a single pulse (half a sinus cycle), corresponding to 0.005 seconds. To account for the blasting occurring for several excavation stages, two different faces were supposed with different analysis cases as shown in Figure 2.

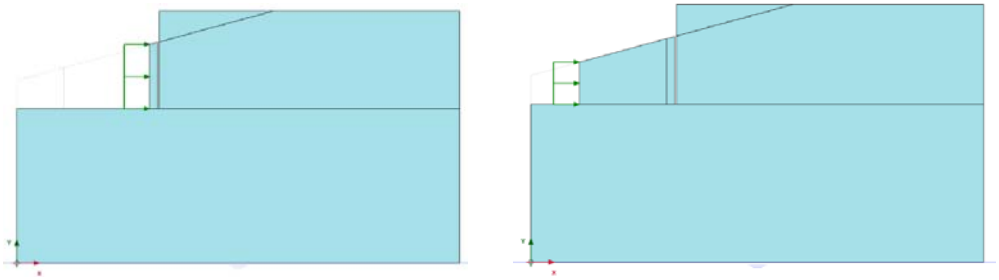

Figure 2: Loading fronts corresponding to dynamic forces due to rock blasting for two cases with respect to excavation stages.

3 RESULTS

Figure 3 shows an example of propagation of waves 0.025 seconds after the dynamic load has been applied for one analysis case. Displacements amplitude in point A (see Figure 1) due to the applied dynamic load were determined with and without the presence of the trench. The ratios were calculated to be between about 0.2 and 0.7 for different analysis cases.

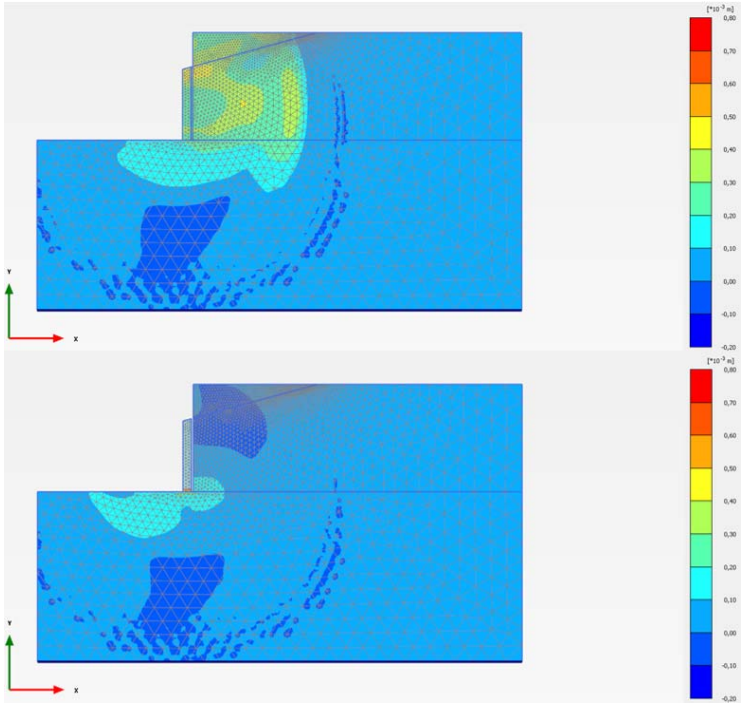

Figure 3: Example of propagation of waves 0.025 seconds after the dynamic load, top) without the open trench, bottom) with the open trench.

4 CONCLUSIONS

The results from this study indicate that vertical displacements due to blast induced vibrations at point A located about 15 m behind the open trench are reduced by approximately 30-75% compared to the case without the open trench. Horizontal displacements are reduced by approximately 65-80%. It is important to note that the results are somewhat dependent on the chosen geometry of the rock model and location of the rock wall. The exact effectiveness of the method is thus dependent on how realistic the chosen geometry is as well as location of the blasting front.

REFERENCES

[1] SIS, SS 4604866:2011, Vibration and shock-Guidance levels for blasting-induced vibration in buildings (2011).

[2] R.D. Woods, "Screening of surface waves in soil." Journal of the Soil Mechanics and Foundation Division, ASCE, 94(SM4): 951-979 (1968).

[3] S. Ahmad and T. M. Al-Hussaini,"Simplified design for vibration screening by open and in-filled trenches", ASCE Journal of Geotechnical Engineering, Vol 117, Nr. 1, 67-88 (1991).

[4] K.R. Massarsch, "Vibration Isolation using Gas-filled Cushions." Soil Dynamics Symposium to Honor Prof. Richard D. Woods (Invited Paper.). Geo-Frontiers 2005, Austin, Texas, January 24–26 (2005).

30th Nordic Seminar on Computational Mechanics
NSCM-30
J. Høgsberg. N.L. Pedersen (Eds.)
2017

LUMPED-PARAMETER MODELS FOR STRUCTURE–SOIL INTERACTION OF MULTI-SPAN RAILWAY BRIDGES

PAULIUS BUCINSKAS[*] AND LARS V. ANDERSEN[†]

[*] Department of Civil Engineering
Aalborg University
Thomas Manns Vej 23, 9220 Aalborg Ø, Denmark
e-mail: pbu@civil.aau.dk

[†] Department of Engineering
Aarhus University
Inge Lehmanns Gade 10, 8000 Aarhus C, Denmark
e-mail: lva@eng.au.dk

Key words: Structure–soil interaction, railway, dynamic, bridge, lumped-parameter model.

1 INTRODUCTION

High-speed rails are an efficient and fast way of passenger transportation. For medium-distance transportation, a well-developed high-speed railway system can rival transportation by airplane, both by travel time and cost. Due to these reasons, high-speed rails are seeing an increased surge of development across the globe. Unfortunately, increased speeds lead to higher excitations of the exposed infrastructure, which in turn requires better numerical models for proper understanding of its dynamic behaviour.

The dynamic behaviour of systems excited by passing trains is a problem that has been investigated by a large number of researchers. Various analytical solutions and computational models have been created with varying complexity, starting from the most basic analytical solutions for a simply supported beam traversed by a mass to full three-dimensional finite element solutions. However, currently existing methods are often too simplified, disregarding such phenomena as structure–soil–structure interaction, or on the other end—are extremely computationally demanding. This work aims to produce a computational model that considers the most important phenomena such as structure–soil interaction (SSI), stochastic railway track unevenness, vehicle suspension system, etc.

A multi-span bridge structure with surface footings resting on soil is considered. Similar models, modelling the railway track placed directly on the soil surface, have been used by Nielsen et al. [1] and Koroma et al. [2]. However, in this case a bridge structure is introduced. It is modelled using a finite-element (FE) approach using beam elements, with a layered deck structure. Further, the soil is modelled with a semi-analytical approach, as originally proposed by Thomson [3] and Haskell [4]. To transform the solution into time domain, consistent lumped-parameter models (LPMs) are used as described by Wolf [5] and Andersen [6]. The vehicle is modelled as a simplified two-dimensional spring and dashpot system. Further, non-linear Hertzian springs are used to account for wheel–rail interaction including random railway track unevenness.

2 COMPUTATIONAL MODEL

The computational model used is very similar as already presented in previous work [7]. Therefore, only a general description of the model is given.

The vehicle is modelled as a two dimensional system with 10 degrees-of-freedom. This way the model accounts for both primary and secondary suspension of a railway locomotive. Only a single passing vehicle is considered. The railway track and the vehicle interact only through vertical forces and the vehicle travels along the centre line of the bridge.

The bridge structure is modelled using the FE method. Three-dimensional Euler-Bernoulli beam elements with three translational and three rotational degrees of freedom per node are used to model both the bridge deck and the pylons. The railway track is modelled as a layered structure with rails modelled as a single beam discretely connected to single-degree-of-freedom sleepers and further connected to the bridge deck. The rail pads and ballast are modelled as spring/dashpot systems with appropriate stiffness and damping values.

The footings are modelled as rigid slabs resting on the ground surface, and the soil is modelled by a semi-analytical approach employing Green's function in frequency-wavenumber domain to obtain a flexibility matrix for the soil–foundation interface. The flexibility matrix is then inverted and integrated over the interface area to obtain a dynamic stiffness matrix for the foundation system. The bridge structure and the soil interact through structure–soil interaction (SSI) nodes, as shown in Figure 1. However, this approach provides only a frequency domain solution. Thus, LPMs are used as described in Subsection 2.3.

The rail track unevenness is generated from a power density spectrum by assigning random phase angles to each wavenumber. Only vertical track unevenness is considered. Describing the interaction force through a non-linear Hertzian spring requires a time-domain solution as the force needs to be determined by iteration at every time step. Therefore, the whole system needs to be solved in time domain.

To transform the obtained dynamic stiffness matrix of soil to time domain consistent LPM are used. This way, the standard stiffness, damping and mass matrices for soil are obtained, which then can be coupled to the FE bridge structure. Consistent LPMs use a polynomial-fraction approximation to recreate the system behaviour. Curve fitting is performed by changing the polynomial coefficients and polynomial order. This can be done by a least-squares minimization of the error, or in Matlab using the function *invfreqs*.

The obtained solution can then be represented by a combination of linear, first order and second order systems, for which the stiffness, mass and damping matrices are readily available. The approach does introduce some additional degrees-of-freedom in the system, especially when using high order polynomials. However, the number of additional degrees of freedom is low when compared with FE or boundary element solutions.

3 TEST CASE

To test the performance and the solution procedure of the proposed computational model, a test case was created. A bridge structure with three pylons is analysed, as shown in Figure 1. The material and cross-sectional parameters of the bridge are the same as in [7]. The distance between footings is 30 m. The footings are resting on a 5 m layer of soft soil (the primary wave

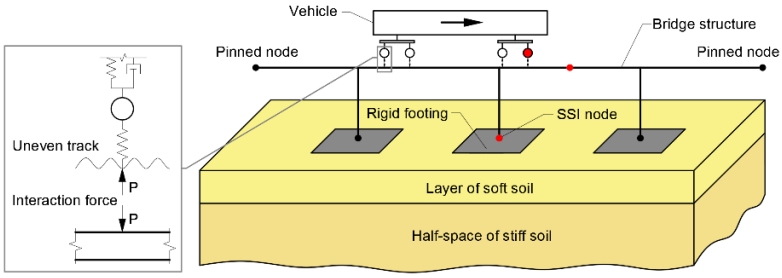

Figure 1: Analysed case: bridge structure supported by three pylons, with rigid footings resting on the soil surface. Red dots indicate positions from which results were extracted.

speed is $c_P = 116$ m/s and the secondary wave speed $c_s = 62$ m/s) with an underlying half-space of stiffer soil ($c_P = 414$ m/s and $c_s = 169$ m/s). Three different speeds of the vehicle are tested: 30 m/s, 60 m/s and 90 m/s. For each speed, 100 simulations are performed, each time generating new random rail profile. The wavelengths used for the rail-profile generation are between 0.2 m and 100 m. Three points of interest are checked: the first wheel of the vehicle, the rail in the middle between second and third pylon and the SSI node of the second footing.

4 RESULTS AND DISCUSSION

The Fourier transform of the wheel–rail interaction forces, as experienced by the first wheel of the vehicle, is shown in Figure 2. The coloured area represents the maximum and minimum values, while the darker lines show the mean values from all simulations. It can be seen that with increasing vehicle speeds, the interaction forces become higher and, furthermore, a wider frequency range is excited. Some peaks are at the same frequencies no matter the vehicle speed. This is due to excitation of eigenmodes of various parts of the vehicle and the structure. Other peaks are only observed at certain speeds and are caused by wheels passing certain parts of the structure, such as the wheel passing the discrete sleepers—at 60 Hz for vehicle speed of 30m/s, 100 Hz for 60 m/s, and 150 Hz for 90 m/s.

Further, Figure 3 shows the acceleration of the rail in the middle of a span and at the SSI node of the second footing. The same trend can be seen as for the wheel–rail interaction forces, with higher vehicle speeds leading to higher excitation. However, especially for the rail, the excited frequency range is spread out through a wider frequency range. Comparing the response at the rail and SSI node, it is evident that the response is reduced significantly closer to the soil,

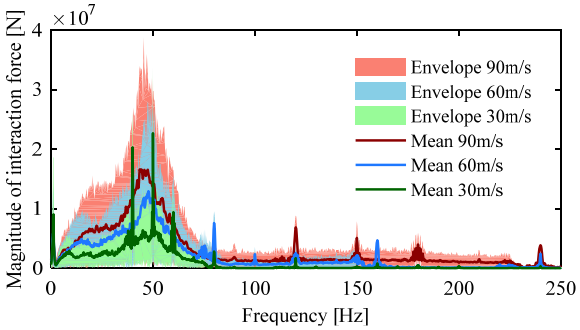

Figure 2: Fourier coefficients for wheel–rail interaction force for the first wheel of the vehicle.

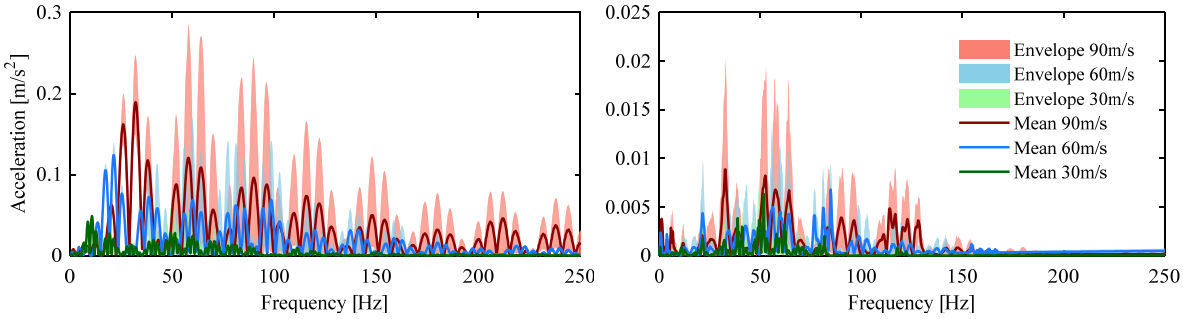

Figure 3: System excitation. On the left—rail, on the right—SSI node.

with high-frequency response (above 150 Hz) disappearing almost completely. Finally, the response at the SSI node shows that at some frequencies the excitations at 60 m/s and 90 m/s are almost equal. This can be caused by the Rayleigh wave travelling in the soft top layer of soil, when the wave speed is close to the vehicle speed.

4 CONCLUSION

- The proposed model of a railway bridge interacting with soil offers an approach that can be used in early design phases, when considering elevated railway tracks.
- Stochastic railway track unevenness, vehicle speed and structure–soil interaction all have an effect of the system behavior and must be considered when modelling such systems.

ACKNOWLEDGMENTS

The research was carried out in the framework of the project "Urban Tranquility. The authors of this work gratefully acknowledge the Interreg V European Regional Development Fund for the financial support.

REFERENCES

[1] J.C. Nielsen, G. Lombaert, S. François, "A hybrid model for prediction of ground-borne vibration due to discrete wheel/rail irregularities", *Journal of Sound and Vibration*, **345**, 103-20 (2015).

[2] S.G. Koroma, D.J. Thompson, M.F. Hussein, E. Ntotsios, "A mixed space-time and wavenumber-frequency domain procedure for modelling ground vibration from surface railway tracks", *Journal of Sound and Vibration*, **32**, 400–508 (2017).

[3] W. T. Thomson, "Transmission of elastic waves through a stratified solid medium", *Journal of applied Physics*, **21.2**, 89–93 (1950).

[4] N. A. Haskell, "The dispersion of surface waves on multilayered media", *Journal of Sound and Vibration*, **43.1**, 17–34 (1953).

[5] J. P. Wolf, "Consistent lumped-parameter models for unbounded soil: Frequency-independent stiffness, damping and mass matrices", *Earthquake Engineering & Structural Dynamics*, **20(1)**, 33–41 (1991).

[6] L. Andersen, "Assessment of lumped-parameter models for rigid footings", *Computers & structures*, **88(23)**, 1333-1347 (2010).

[7] P. Bucinskas, L. Agapii, J. Sneideris, L.V. Andersen, "Numerical modelling of the dynamic response of high-speed railway bridges considering vehicle-structure and structure-soil-structure interaction", *Computational Techniques for Civil and Structural Engineering,* 125-152 (2015).

30th Nordic Seminar on Computational Mechanics
NSCM-30
J. Høgsberg. N.L. Pedersen (Eds.)
2017

EFFECT OF DAMAGE MODELING IN STRUCTURAL HEALTH MONITORING

THOMAS BULL†, BILAL A. QADRI, MARTIN D. ULRIKSEN AND LARS DAMKILDE

Department of Civil Engineering,
Aalborg University
Niels Bohrs Vej 8, 6700 Esbjerg, Denmark
Email: tb@civil.aau.dk† - Web page: http://www.en.aau.dk/

Keywords: Structural health monitoring, steady state shift damage localization, damage modeling

1 INTRODUCTION

The interest in reliable structural health monitoring (SHM) systems has increased during the last couple of decades, as they have the potential to reduce the operational costs of structural systems. The SHM systems can provide information about the structural deterioration, which allows for efficient inspections and repairs, hence leading to reduced downtime. An example is wind turbines that are subject to regular inspections, as these inspections can be replaced by a SHM system. However, this requires for robust solutions to all four components of damage identification as proposed by Rytter[1]; detection, localization, quantification, and consequence. Detection of damages in wind turbines has been resolved with reasonable success[2], but a robust solution for the next logical step, localization, has not yet been provided.

A typical localization is performed by mapping the damage-induced change in the structural response, from an undamaged and damaged state, to a theoretical model of the structure. This paper concentrates on the effect of damage modeling in localization methods, whose premise is to postulate a damage pattern in a finite element (FE) model. These postulates are conventionally modeled by a local reduction of stiffness, which may not represent the actual physical behavior adequately for some damage types, leading to a reduced localization resolution. The present paper investigates a characteristic debonding failure, typically found in wind turbine blades, where the physical stiffness reduction is due to a separation of two surfaces. This behavior is modeled by decoupling the degrees of freedom (DOF) between two surfaces, and the localization results obtained hereby are compared to those deduced from the conventional approach of reducing the stiffness across an element. The comparison is conducted using the steady state shift damage localization[3] (S3DL) method in the context of a residential-sized wind turbine blade, for which the S3DL method has previously been tested successfully[4].

2 DAMAGE MODELLING

The conventional approach with local reduction of stiffness is popular due to the simple implementation in FE-models. The approach is, in this paper, performed by reducing the

stiffness in each of the elements, one at a time, as illustrated by the gray element in Fig. 1a. The separation approach is resolved by decoupling four DOF at a time, along the edge of the blade (depicted in Fig. 1b by the opening). It is contended that the decoupling of the two surfaces emulates the physical attributes of the debonding failure, which, in this study, is introduced by loosening three bolts along the trailing edge of the residential-sized wind turbine blade shown in Fig. 2. The red line in the Fig. 2 marks the extent and position of the damage.

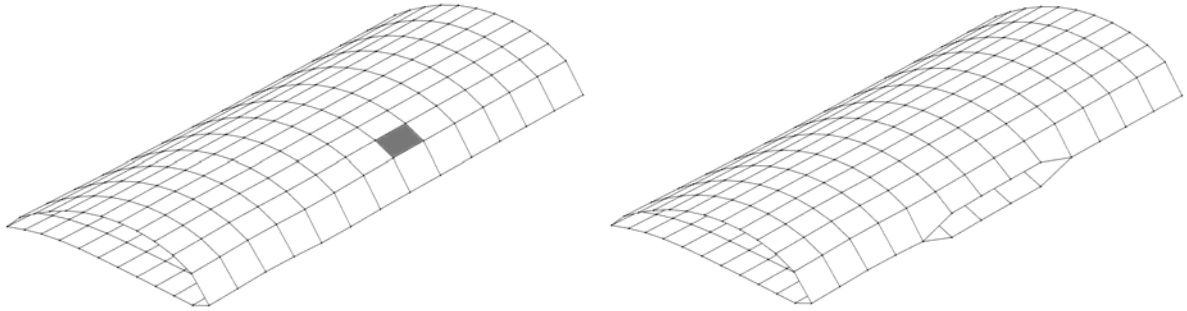

a) Local stiffness reduction in one element. b) Decoupling of four DOF along the edge.

Figure 1: Procedure behind the two investigated damage modeling approaches.

3 STEADY STATE SHIFT DAMAGE LOCALIZATION

A brief description of the S3DL method is provided for this paper to be self-contained. The method operates by measuring the deviation between a postulated damage pattern and changes in steady-state measurements from an undamaged and damaged state. The Fourier transform of the accelerations, obtained from single realizations of the undamaged state (denoted by superscript u) and damaged state (denoted by superscript d), are organized in

$$\boldsymbol{E}(i\omega) = [X_m^u(i\omega) \;\; X_m^d(i\omega)], \tag{1}$$

where the subscript m refers to the rows associated with the sensor coordinates. A linear model consisting of the mass, damping and stiffness matrices can be expressed in the frequency domain by $\boldsymbol{G}^u(i\omega) = (-\boldsymbol{M}\omega^2 + \boldsymbol{C}i\omega + \boldsymbol{K})^{-1}$. When subjected to a spatially invariant, repeatable excitation, a stiffness perturbation, $\Delta\boldsymbol{K}$, can be postulated in the model by the interrogation matrix

$$\boldsymbol{D}_{m,j}(i\omega) = \boldsymbol{G}_m^u(i\omega)\Delta\boldsymbol{K}_j, \tag{2}$$

in which the subscript $j \in [1, k]$ denotes the number of the postulated damage and k the total amount of postulates one seeks to interrogate for. The damage-induced difference between the measurements in $\boldsymbol{E}$, can be removed by the correct postulated damage in $\boldsymbol{D_m}$ with

$$\boldsymbol{R}_j(i\omega) = (\boldsymbol{I} - \boldsymbol{D}_{m,j}(i\omega)\left(\boldsymbol{D}_{m,j}^T(i\omega)\boldsymbol{D}_{m,j}(i\omega)\right)^{-1}\boldsymbol{D}_{m,j}^T(i\omega))\boldsymbol{E}(i\omega), \tag{3}$$

where $\boldsymbol{I}$ is the identity matrix. The correct damage pattern is postulated when the minimum singular value, σ_j, of $\boldsymbol{R}_j$, under ideal circumstances, is zero. The localization metric is defined

as

$$\delta_j = \frac{1}{\sigma_j}, \tag{4}$$

where a value of δ_j being significantly higher than the rest suggests that a correct damage is postulated.

4 LOCALIZATION RESULTS

The residential-sized wind turbine blade used in the study, illustrated in Fig. 2, is approximately 800 mm long and consists of two surfaces bolted together along the edges. The bolts allow for the introduction of debonding failures, and three adjacent bolts are, in this case, loosened along the trailing edge; spanning 7.5 % of the total length. The blade is subjected to a harmonic input with a frequency of 75 Hz using a shaker mounted at the tip of the blade, and the response is captured for 10 seconds in 14 uniaxial accelerometers measuring perpendicular to the blade surface.

Figure 2: The residential-sized wind turbine blade. (a) Shaker to excite the blade. (b) Stinger between shaker and blade. (c) Accelerometers. (d) Clamp to resemble a fixed support.

The FE-model, used for the interrogations, is discretized using 3450 first-order shell elements and has been calibrated based on modal parameters of the physical blade found through an operational modal analysis[4]. A damage pattern consisting of a local stiffness reduction in each of the elements yield the results depicted in Fig. 3a, where elements are colored based on the corresponding normalized δ-value with respect to δ_{max}. To investigate if the damage pattern consisting of decoupling is superior, the localization values are illustrated in Fig. 3b, together with the conventional approach, such that the decoupling represents the edge values and the conventional approach represents the remainder of the blade. This permits for a direct comparison between the two approaches by studying the differences.

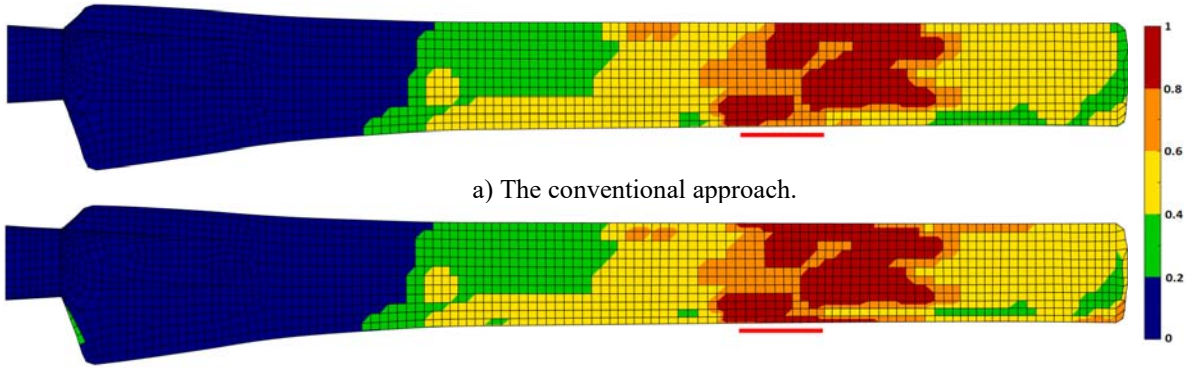

a) The conventional approach.

b) The decoupling approach.

Figure 3: Localization results for the two approaches, where the elements have been colored based on their normalized δ-value.

The localization results obtained from both modeling approaches are nearly identical and give a clear indication of the correct area of the damage. However, an advantage of the decoupling approach is the lower calculation time, as there are significantly fewer interrogations to investigate. Here, the number of interrogations is approximately 12 times lower than the original 3450, resulting in a time saving of the same order.

5 CONCLUSIONS

This paper deals with the effects of damage modeling in damage localization schemes, whose premise is to postulate damages in a theoretical model. The two approaches considered for the postulations are; the conventional one based on a local reduction of stiffness and the other based on a decoupling of DOF. The localization results are insensitive to the postulations being equal to the physically induced damage, as both approaches locate the damage at the correct area with only minor discrepancies. The conventional approach is therefore adequate for general applications. However, if knowledge is present of where damages typically are found, the calculation time can be reduced, as the number of interrogations decreases.

REFERENCES

[1] A. Rytter, “Vibrational based inspection of civil engineering structures”, *Ph.D. dissertation,* (1993).

[2] M. D. Ulriksen, D. Tcherniak and L. Damkilde, “Damage Detection in an Operating Vestas V27 Wind Turbine Blade by use of Outlier Analysis”, *IEEE Workshop on Environmental, Energy and Structural Monitoring Systems*, (2015).

[3] D. Bernal and A. Kunwar, “Steady state shift damage localization”, *Meccanica,* **51(11)**, 2861-2871 (2016).

[4] M. K. Markvart et al., “Steady State Shift Damage Localization in a Residential-sized Wind Turbine Blade”, *Proceedings of the International Conference on Structural Engineering Dynamics*, (2017)

30th Nordic Seminar on Computational Mechanics
NSCM-30
J. Høgsberg. N.L. Pedersen (Eds.)
2017

PLASTIC LENGTH SCALE EVOLUTION

CARL F.O. DAHLBERG* AND MAGNUS BOÅSEN*

*KTH Royal Institute of Technology
Department of Solid Mechanics
Teknikringen 8D, 100 44 Stockholm, Sweden

Abstract. An extension to an isotropic strain gradient plasticity theory[1,2] is presented based on a hypothesis regarding the length scale, ℓ. The length scale is often taken to be a constant phenomenological constitutive parameter but here it is hypothesized to evolve with accumulation of plastic deformation. Theoretical analysis[3] and experimental investigations[4] of the relation between the dislocation density, ρ, and a microstructural length scale, Λ, of dislocation patterning indicates that $\Lambda \propto \rho^{-1/2}$. Assuming that the constitutive length scale ℓ is proportional to the microstructural length scale Λ the relation $\ell = A/\sqrt{\rho}$ results, where A is a dimensionless constant of proportionality. From this an evolution equation can be derived as $\mathrm{d}\ell = -\ell^3/(2A^2)\mathrm{d}\rho$. Gradients of plastic strain can be treated as proxy to a density of geometrically necessary dislocations or the equivalent plastic strain can be assumed proportional to the total dislocation density leading to different evolution equations. The extended theory have been implemented in a 2D FE code. Results from beam bending are discussed to show the implications of the theory and are compared to results from 3D discrete dislocation dynamics simulations[5].

Keywords: Gradient Plasticity, Length Scale Evolution

REFERENCES

[1] Gudmundson, P. A unified treatment of strain gradient plasticity. *J. Mech. Phys. Solids* **52**, 1379–1406 (2004).

[2] Dahlberg, C. & Faleskog, J. Strain gradient plasticity analysis of the influence of grain size and distribution on the yield strength in polycrystals. *Euro. J. Mech. A* **44**, 1–16 (2014).

[3] Holt, D. Dislocation cell formation in metals. *J. App. Phys.* **41**, 3197–3201 (1970).

[4] Kysar, J., Saito, Y., Öztop, M., Lee, D. & Huh, W. Experimental lower bounds on geometrically necessary dislocation density. *Int. J. Plas.* **26**, 1097–1123 (2010).

[5] Motz, C., Weygand, D., Senger, J. & Gumbsch, P. Micro-bending tests: A comparison between three-dimensional discrete dislocation dynamics simulations and experiments. *Acta Mater.* **56**, 1942–1955 (2008).

30th Nordic Seminar on Computational Mechanics
NSCM-30
J. Høgsberg. N.L. Pedersen (Eds.)
2017

GEOMETRICAL CHARACTERISATION OF INDIVIDUAL FIBRES FROM X-RAY TOMOGRAMS

MONICA J. EMERSON [*†], VEDRANA A. DAHL[†], LARS P. MIKKELSEN[‡], ANDERS B. DAHL[†] AND KNUT CONRADSEN[†]

[†]Image Analysis and Computer Graphics
Department of Applied Mathematics and Computer Science, Technical University of Denmark
e-mail: monj@dtu.dk

[‡]Composites and Materials Mechanics
Department of Wind Energy, Technical University of Denmark

Abstract. Numerous modelling possibilities are opened up by an advanced image analysis pipeline that can accurately extract individual fibres from X-ray tomograms.

Keywords: X-ray tomography, Individual Fibres, Unidirectional Composites, Modelling.

We have developed an image analysis pipeline[1] that can extract individual fibre tracks from low contrast X-ray tomograms of unidirectional composites with high fibre volume fraction. Measuring individual fibre tracks opens up the possibility of modelling this empirical data in a statistical manner. Thus, allowing to analyse the spatial distributions of the parameters characterising the orientation and curvature of these individual fibres, which can also provide insights on the interactions amongst the individual fibres.

Finite element models (FEMs) can be built from the extracted geometry to simulate the performance of the scanned fibre structure under realistic conditions. Moreover, aspects of the fibre architecture that influence the macroscopic behaviour of the composite can be quantified. Examples are 2D FEMs to predict the transverse stiffness[2] or the quantification of fibre orientations to estimate the compression strength.[1] And last but not least, already developed analytical and numerical models to describe the composite's behaviour can be validated against the observed data.

REFERENCES

[1] Emerson, M. J., Jespersen, K. M., Dahl, A. B., Conradsen, K. & Mikkelsen, L. P. Individual fibre segmentation from 3d x-ray computed tomography for characterising the fibre orientation in unidirectional composite materials. *Composites Part A: Applied Science and Manufacturing* **97**, 83–92 (2017).

[2] Mikkelsen, L. P. *et al.* X-ray based micromechanical finite element modeling of composite materials. In *In Proceedings of 29th Nordic Seminar on Computational Mechanics* (2016).

30th Nordic Seminar on Computational Mechanics
NSCM-30
J. Høgsberg. N.L. Pedersen (Eds.)
2017

AN EXPERIMENTALLY MOTIVATED MODEL FOR GLASSY POLYMERS

JONAS ENGQVIST, MATHIAS WALLIN, MATTI RISTINMAA AND STEPHEN HALL

Division of Solid Mechanics Lund University
Box 118, 221 00 Lund, Sweden
e-mail: jonas.engqvist@solid.lth.se, web page: http://www.solid.lth.se/

Abstract. The mechanical response of glassy polymers is often described in terms of the Helmholtz free energy and a set of evolution laws. The format for the free energy and the evolution laws have historically been developed to fit simple uni-axial tests assuming a homogeneous state. This limits the ability of the models to accurately predict the response during multi-axial loading conditions[1]. In this work we make use of modern experimental techniques to gain information which enables us to develop and improve the predictive capability of polymer material models[2,3].

An enhanced form for the Helmholtz's free energy, which is based on biaxial tests in combination with full-field deformation measurements using digital image correlation (DIC), will be presented. The new material model is implemented in a finite element environment and the new material model is verified for biaxial loading situations. It will be shown that with the proposed Helmholtz's free energy, the mechanical response during biaxial loading is captured in a satisfactory manner.

Keywords: Constitutive Modelling, Experimental Mechanics.

REFERENCES

[1] Engqvist, J., Wallin, M., Ristinmaa, M. & Hall, S. A. Modelling and experiments of glassy polymers using biaxial loading and digital image correlation. *Int. J. Solids Struct.* **102**, 100–111 (2016).

[2] Engqvist, J., Wallin, M., Hall, S. A., Ristinmaa, M. & Plivelic, T. S. Measurement of multi-scale deformation of polycarbonate using x-ray scattering with in-situ loading and digital image correlation. *Polymer* **82**, 190–197 (2016).

[3] Engqvist, J., Wallin, M., Ristinmaa, M., Hall, S. A. & Plivelic, T. S. Modelling multi-scale deformation of amorphous glassy polymers with experimentally motivated evolution of the microstructure. *J. Mechan. Phys. Solids* **96**, 497–510 (2016).

30th Nordic Seminar on Computational Mechanics
NSCM-30
J. Høgsberg. N.L. Pedersen (Eds.)
2017

NUMERICAL CALIBRATION OF COHESIVE ZONE ENERGY FOR PLATE TEARING

C.L. FELTER*, R.G. RASMUSSEN* AND K.L. NIELSEN*

*Technical University of Denmark (DTU)
Anker Engelunds Vej 1
Bygning 404
2800 Kgs. Lyngby
e-mail: dtu@dtu.dk, web page: http://www.dtu.dk/

Abstract. In a cohesive zone model, neighboring elements are connected by nonlinear springs (instead of directly sharing a node) which are designed to i) absorb the fracture energy, ii) release the connection between elements in the fracture zone. Unfortunately, it is often necessary to conduct lab tests combined with curve fitting in order to define the potential energy and the peak traction of the nonlinear springs.

The present work extends earlier 2D work[1] by applying a full 3D numerical model to the plate tearing problem. A through thickness discretization of 64 elements, and a total of approximately 500,000 solid finite elements, are used together with the Gurson-Tvergaard-Neddleman model for simulation of growth and collapse of micro-voids in the material. Sub-domains of material between planes perpendicular to the crack growth direction are identified and for each sub-domain the elastic energy, plastic energy, and the force-displacement curve are extracted. These values allow to directly define the cohesive zone parameters without the need to apply a fitting technique on the global traction-separation curve of the crack mouth.

The method is used to subsequently define cohesive zone models of different discretizations and the performance, and validity, of the procedure is demonstrated and discussed in relation to results from the literature[2].

Keywords: Gurson model, Cohesive Zone, Plate Tearing.

REFERENCES

[1] Nielsen, K. & Hutchinson, J. Cohesive traction-separation laws for tearing of ductile metal plates. *International Journal of Impact Engineering* **48**, 15–23 (2012).

[2] Woelke, P., Schields, M. & Hutchinson, J. Cohesive zone modeling and calibration for mode i tearing of large ductile plates. *Engineering Fracture Mechanics* **147**, 293–305 (2015).

30th Nordic Seminar on Computational Mechanics
NSCM-30
J. Høgsberg. N.L. Pedersen (Eds.)
2017

EVALUATION OF MIXED MODE CRACK GROWTH CRITERIA

DIMOSTHENIS FLOROS*, FREDRIK LARSSON, ANDERS EKBERG AND KENNETH RUNESSON

*Chalmers University of Technology
Department of Industrial and Materials Science
412 96 Gothenburg, Sweden
e-mail: florosd@chalmers.se

Key words: Mixed mode loading, Crack growth criteria, Numerical simulations.

Summary. A framework for the evaluation of mixed mode crack growth criteria is proposed. The evaluation is based on numerical simulations of crack growth experiments from the literature. The aim of the evaluation is to investigate the abilities of different criteria to capture effects of varying operational conditions, crack face contact and friction.

1 INTRODUCTION

It is natural to assume that the evaluation of mixed mode crack growth criteria in the literature is strongly related to the way numerical modelling of the fracture problem is performed. In cases of primarily opening mode of fracture and elastic bulk material response, (traditional) linear elastic fracture mechanics (LEFM) criteria perform well. In more convoluted crack situations with complicated specimen geometries, pronounced inelastic material response and crack closure (they may all be present in e.g. rolling contact fatigue), more sophisticated criteria need to be employed. These criteria are based on quantities (crack driving forces) computed by the solution of the relevant fracture problem, which eventually needs to be accurate. For this purpose, a multitude of techniques exists in the literature: explicit crack models with high mesh resolution in the near-tip region and/or special crack tip elements, mesh-less methods (such as eXtended Finite Element Method[1]). With the computed crack driving forces at hand, stationary or propagating crack strategies may be employed; both strategies come with known advantages and limitations.

In this work, we propose a framework for the evaluation of mixed mode crack growth criteria through numerical simulations of experiments from the literature. The proposed framework requires only one FE-mesh to be used for modelling the known crack paths from the experiments at different instances of the fatigue life. This comprises a major advantage compared to e.g. propagating crack models, in which the computed fields need to be mapped to the new mesh upon remeshing.

2 FRAMEWORK FOR THE EVALUATION OF MIXED MODE CRACK GROWTH CRITERIA

For validation purposes, finite element simulations of crack growth experiments are carried out, for the measured crack path. The final crack configuration of each experiment is embedded in an FE-mesh and tie-constraints are enforced between the nodes along the crack faces. The crack growth directions predicted by different criteria are compared to the known crack path from the experiment at selected instances of the fatigue life. In order to model the crack length at each instance of the fatigue life, the appropriate tie-constrained nodes are released. This requires the use of only one FE-mesh for the simulation of all the history of crack extension.

As regards candidate criteria for evaluation, they are distinguished here according to the bulk material response they are related to. In case of elastic response, widely used LEFM criteria from the literature are employed. These are maximum tangential stress (MTS[2]), maximum shear stress (MSS[2]) and minimum strain energy density (MSE[3]) criteria. All the aforementioned criteria rely on *a priori* determined stress intensity factors.

3 SIMULATION OF FOUR-POINT BENDING EXPERIMENT

The evaluation of criteria based on the framework described in Section 2 is demonstrated on an asymmetric four-point bending experiment[4], see Fig. 1a. The experimental setting is described in Table 1. The material used in the experiment is SAE 1045 hot rolled and normalized steel. The precrack and final crack configurations after execution of the experiment are illustrated in Fig. 1b.

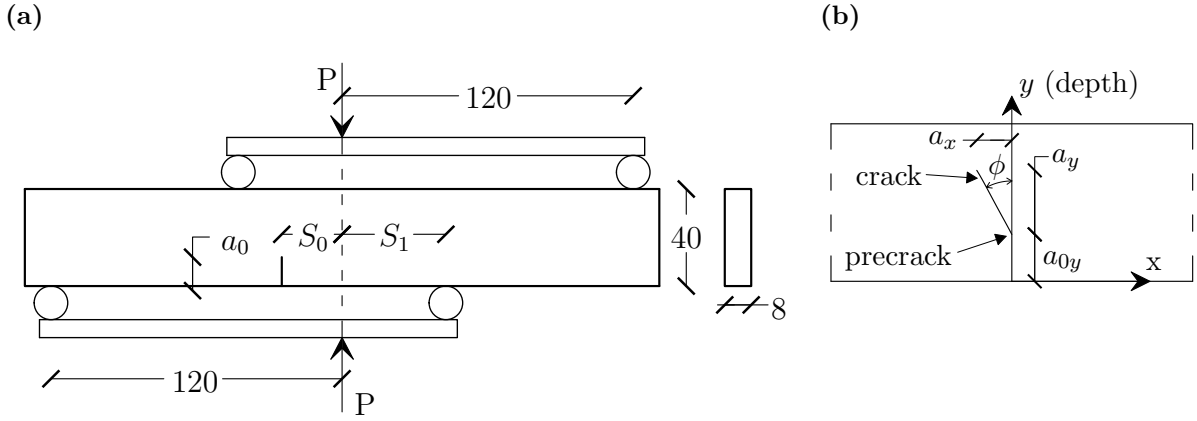

Figure 1: (a) Setting of asymmetric four-point bending experiment[4]. (b) Precrack and final crack configurations.

Simulation of the experiment was run for linear elastic material response, with Young's modulus and Poisson's ratio of SAE 1045 steel, $E = 202\,\text{GPa}$ and $\nu = 0.29$, respectively. The direction of growth, as predicted by MTS, MSE and MSS criteria at four instances

Initial $K_{\mathrm{II}}/K_{\mathrm{I}}$	**Precrack length** a_{0y} mm	S_0 mm	S_1 mm	$P_{\max}$ kN	$P_{\min}$ kN	**Final crack length** a_x mm	a_y mm	Cycles to failure
0.262	11.91	21	40	14.3	0.89	7.39	13.48	208,900

Table 1: Test conditions of asymmetric four-point bending experiment[4].

of the fatigue life, is compared to the direction of the embedded crack path from the experiment in Fig. 2. As expected, for moderate ratio $K_{\mathrm{II}}/K_{\mathrm{I}} = 0.262$, all but MSS, LEFM criteria can capture crack growth direction satisfactorily.

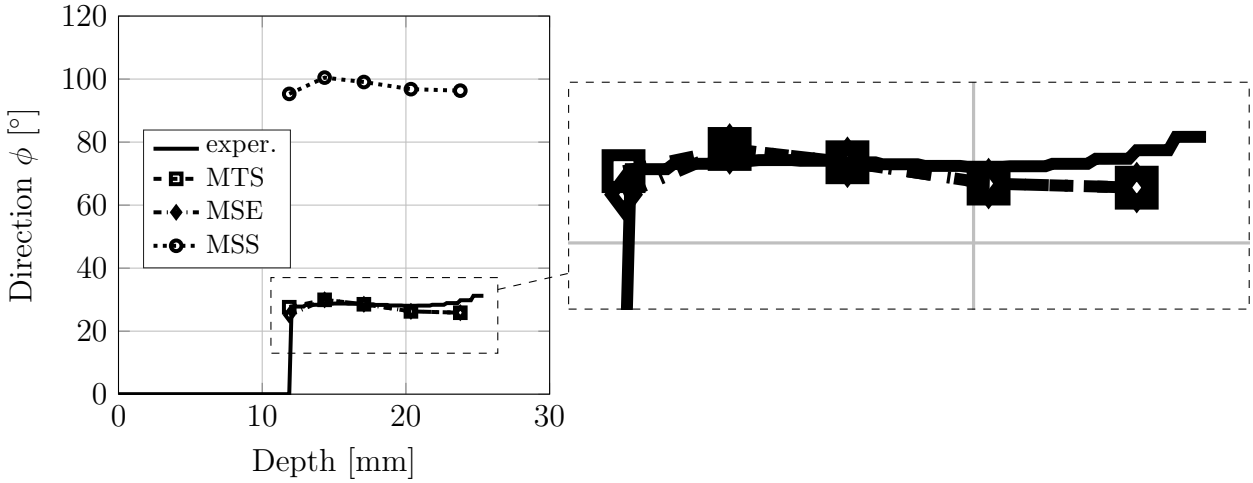

Figure 2: Experimentally observed and predicted crack path directions.

4 CONCLUSIONS AND OUTLOOK

A framework for the evaluation of mixed mode crack growth criteria has been proposed, based on simulation of crack growth experiments from the literature. The crack paths from the experiments are compared to predictions from the criteria at different instances of the fatigue life. Criteria that are not bound to elastic material response can also be evaluated. More specifically, elastic-plastic fracture mechanics criteria will be evaluated in future work, such as crack tip displacement[5] and criteria based on configurational forces[6,7].

REFERENCES

[1] Xu, Y. & Yuan, H. Computational modeling of mixed-mode fatigue crack growth using extended finite element methods. *International Journal of Fracture* **159**, 151–

165 (2009).

[2] Erdogan, F. & Sih, G. On the crack extension in plates under plane loading and transverse shear. *Journal of basic engineering* **85**, 519–525 (1963).

[3] Sih, G. C. Strain-energy-density factor applied to mixed mode crack problems. *International Journal of Fracture* **10**, 305–321 (1974).

[4] Qian, J. & Fatemi, A. Fatigue crack growth under mixed-mode I and II loading. *Fatigue and Fracture of Engineering Materials and Structures* **19** (1996).

[5] Li, C. Vector CTD criterion applied to mixed mode fatigue crack growth. *Fatigue & Fracture of Engineering Materials & Structures* **12**, 59–65 (1989).

[6] Hellen, T. & Blackburn, W. The calculation of stress intensity factors for combined tensile and shear loading. *International Journal of Fracture* **11**, 605–617 (1975).

[7] Floros, D., Larsson, F. & Runesson, K. On configurational forces for gradient-enhanced inelasticity. *Computational Mechanics* (Article in press, 2017).

30th Nordic Seminar on Computational Mechanics
NSCM-30
J. Høgsberg. N.L. Pedersen (Eds.)
2017

OPTIMIZATION OF TOPOLOGICAL COMPLEXITY FOR 1D ARTERIAL BLOOD FLOW MODELS

FREDRIK E. FOSSAN*, JORGE MARISCAL-HARANA†, JORDI ALASTRUEY† AND LEIF R. HELLEVIK*

*Division of Biomechanics
Norwegian University of Science and Technology (NTNU)
NO-7491 Trondheim, Norway
e-mail: fredrik.e.fossan@ntnu.no, web page:
http://ec2-52-26-116-174.us-west-2.compute.amazonaws.com:5006/app96Simple

†Division of Imaging Sciences and Biomedical Engineering
St. Thomas' Hospital, King's College London (KCL)
London, SE1 7EH, UK
e-mail: jorge.mariscal_harana@kcl.ac.u

Abstract. As computational models of the cardiovascular system are applied in modern personalized medicine, maximizing certainty of model input becomes crucial. Increasing the number of arterial segments in a model result in a more realistic description of the system, but also introduces more uncertain parameters. We present a framework that aims at minimizing the number of arteries in distributed one-dimensional models, preserving key features of flow and pressure waveforms. A previously proposed method and a new method for lumping 1D segments into equivalent 0D windkessel models is incorporated in the framework. The framework is tested with different criteria for maximum deviation with the original 96-artery model. By employing our methods for network reduction we created approximately 30 000 simpler models (in terms of number of 1D segments), meant to represent the same physical problem. Our novel framework makes it possible to find the optimal number of arterial segments required to capture the main features of pressure and flow waveforms at a given arterial location and up to a prescribed error threshold. We present the optimal arterial networks that produce Aortic, Carotid, internal Carotid, Brachial and Femoral waveforms for a range of threshold relative errors. An interactive web illustration of the framework can be found at http://ec2-52-26-116-174.us-west-2.compute.amazonaws.com:5006/app96Simple.
In order to perform patient specific simulations we want the simplest model able to capture the physical problem, but not simpler. With this framework we are one step closer to finding the most appropriate model for a given clinical application.

Keywords: 1D blood flow, 0D models, model reduction.

30th Nordic Seminar on Computational Mechanics
NSCM-30
J. Høgsberg. N.L. Pedersen (Eds.)
2017

VALIDATION OF AN IN VIVO PARAMETER IDENTIFICATION METHOD FOR THE HUMAN ABDOMINAL AORTA

JAN-LUCAS GADE*, CARL-JOHAN THORE* AND JONAS STÅLHAND*

*Solid Mechanics, Department of Management and Engineering, Linköping University
581 83 Linköping, Sweden
e-mail: jan-lucas.gade@liu.se, web page: http://www.solidmechanics.iei.liu.se/

Key words: Model, Validation, Parameter Identification, Artery.

1 INTRODUCTION

The leading cause of death in Europe are cardiovascular diseases (CVD)[1]. The development of CVD is closely related to changes in the mechanical properties of the arterial tissue. Disease diagnostization could, therefore, benefit from a non-invasive method that can estimate arterial mechanical parameters in situ (in place). This requires a meaningful mechanical description of the artery and a robust parameter identification (PI) method. Towards this end, our group has proposed a method[2] that utilizes a Holzapfel-Gasser-Ogden (HGO) material model[3] and approximates the artery as a pressurized tube. Supplied with pressure-radius data, this method is capable of determining parameters describing the mechanical properties of the tissue[4]. The method has not been validated for robustness, however. Inspired by a recent study[5], we address this shortcoming by using in silico generated pressure-radius data. This data is obtained from finite element (FE) simulations on abdominal aorta (AA) like geometries for pre-defined sets of material parameters. Since the material models in both the PI method[2] and the FE model are identical, it is possible to directly compare identified and pre-defined parameters to validate the method.

2 GENERATION OF IN SILICO PRESSURE-RADIUS DATA

To generate in silico pressure-radius data, relevant geometrical and HGO material data are taken from the literature[6,7]. The geometrical and material data include inner radius R_i, wall thickness H, a parameter c associated to elastin and parameters k_1, k_2 and β associated with the collagen fibers.

The AA is modelled as a cylindrical membrane with a mean radius $R_\mathrm{m} = R_\mathrm{i} + 0.5H$, wall thickness H and length L, see Figure 1. For each FE model symmetry in the geometry and the loading is utilized and only one quarter of the AA is modelled. The mesh consists

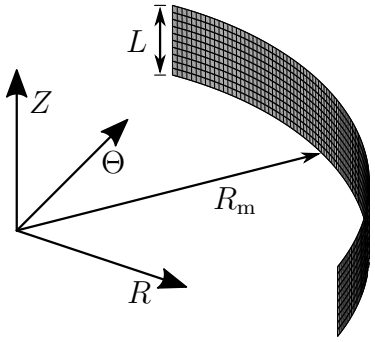

Figure 1: Finite element mesh of one arterial model.

of 4-node, reduced-integration shell elements, 100 in the circumferential direction and 10 in the axial direction, see Figure 1.

The simulation is divided into two steps. First the AA is prestretched. The magnitude of the axial prestretch λ_z is chosen such that the reduced axial force is approximately constant throughout the pulse cycle, in line with experimental observations[8]. Afterwards the artery is pressurized using a pressure range from 9.3 kPa (70 mmHg) for diastole to 16 kPa (120 mmHg) for systole, following Smoljkić et al.[5].

The FE solver Abaqus (Standard version 6.12-3) and the HGO material model are used for all simulations. From the FE simulation the inner radius of the artery and the pressure are extracted to serve as a pressure-radius data set. In total eight in silico pressure-radius data sets are generated.

3 PARAMETER IDENTIFICATION METHOD

The fundamental idea of the PI method[2] is to calculate two sets of stresses and determine the model parameters by a non-linear least squares (LS) fitting of the stresses. The first set is an equilibrium stress σ^{Lp} computed by using the Laplace laws while the second set is a constitutively determined stress σ^{mod} based on the HGO model. Both stresses are determined by a pressure-radius data set and information about the wall thickness for one arbitrary pressure. The non-linear LS fitting is implemented in Matlab R2015a (The MathWorks Inc., Natick, MA, USA) and the six unknown model parameters R_{i}, λ_z, c, k_1, k_2 and β are determined.

4 RESULTS

All eight generated pressure-radius data sets are used in the PI method to identify the mechanical properties of the simulated tissue. Since both the FE simulation and the PI method use the HGO material model it is possible to directly compare the identified

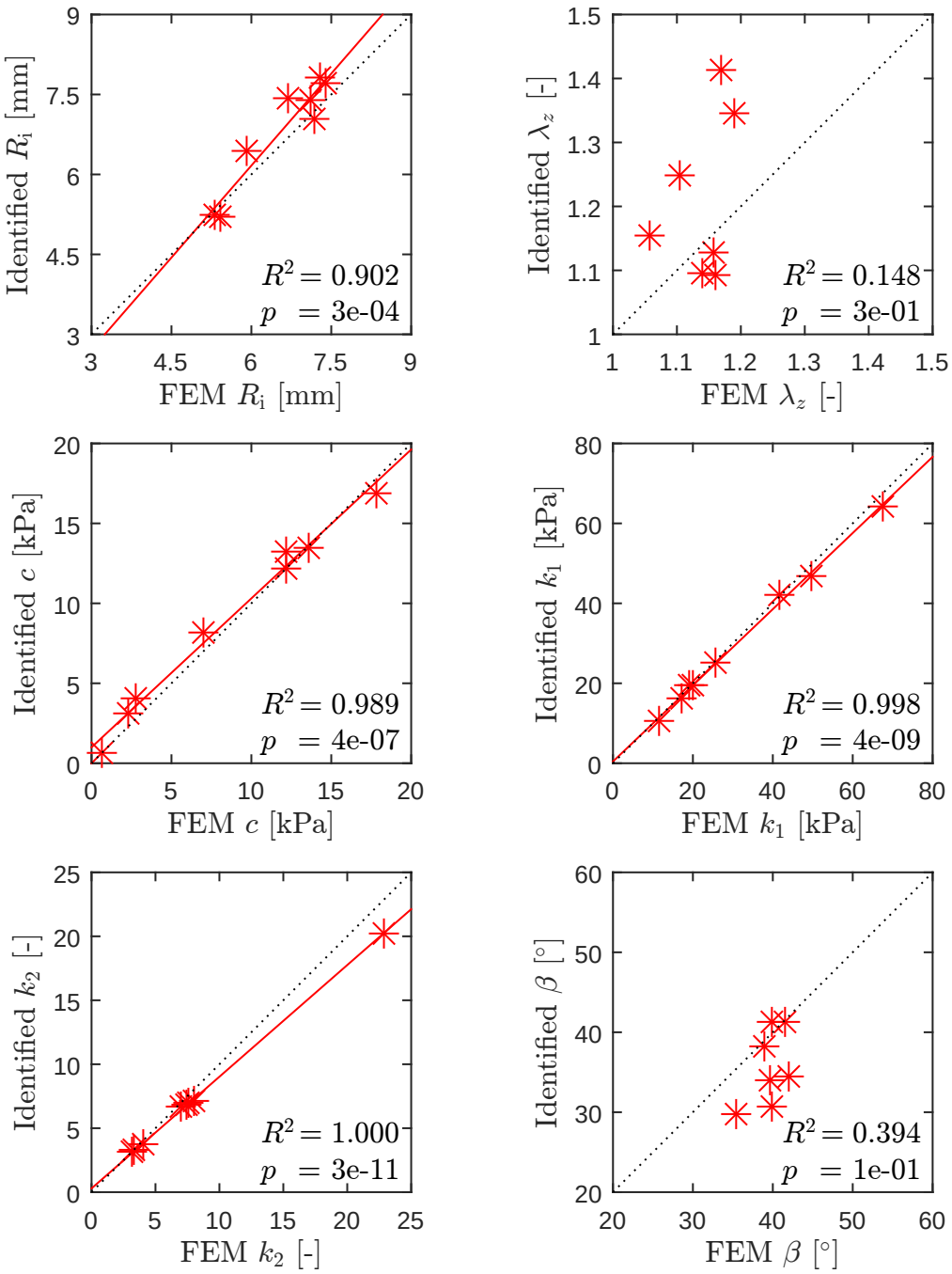

Figure 2: Correlation of identified parameters with the ones used in the FE simulations. In case of significant correlation ($p < 0.05$) the linear regression line is presented in solid red. The dotted black line represents perfect agreement.

parameters with the ones used for the FE simulation.

Figure 2 shows the correlation for all six parameters, the coefficient of determination R^2 and the associated P-value. As can be seen in the plots the identified values and the values from the FE simulations are highly correlated for the parameters R_i, c, k_1 and k_2. For the parameters λ_z and β notable differences occur. These differences are explained by the lack of information about the axial deformation in the in vivo measurable data and the accompanied estimation of the reduced axial force in the PI method.

REFERENCES

[1] Wilkins, E. *et al.* European Cardiovascular Disease Statistics 2017 edition. *European Heart Network, Brussels* 192 (2017).

[2] Stålhand, J. Determination of human arterial wall parameters from clinical data. *Biomechanics and Modeling in Mechanobiology* **8**, 141–148 (2009).

[3] Holzapfel, G. A., Gasser, T. C. & Ogden, R. W. A new constitutive framework for arterial wall mechanics and a comperative study of material models. *J. Elasticity* **61**, 1–48 (2000).

[4] Åstrand, H. *et al.* In vivo estimation of the contribution of elastin and collagen to the mechanical properties in the human abdominal aorta: effect of age and sex. *Journal of Applied Physiology* **110**, 176–187 (2011).

[5] Smoljkić, M., Vander Sloten, J., Segers, P. & Famaey, N. Non-invasive, energy-based assessment of patient-specific material properties of arterial tissue. *Biomechanics and Modeling in Mechanobiology* **14**, 1045–1056 (2015).

[6] Labrosse, M. R., Gerson, E. R., Veinot, J. P. & Beller, C. J. Mechanical characterization of human aortas from pressurization testing and a paradigm shift for circumferential residual stress. *Journal of the Mechanical Behavior of Biomedical Materials* **17**, 44–55 (2012).

[7] Horný, L., Netušil, M. & Daniel, M. Limiting extensibility constitutive model with distributed fibre orientations and ageing of abdominal aorta. *Journal of the Mechanical Behavior of Biomedical Materials* **38**, 39–51 (2014).

[8] Weizsäcker, H. W., Lambert, H. & Pascale, K. Analysis of the passive mechanical properties of rat carotid arteries. *Journal of Biomechanics* **16**, 703–15 (1983).

30th Nordic Seminar on Computational Mechanics
NSCM-30
J. Høgsberg. N.L. Pedersen (Eds.)
2017

ADJOINT OPTIMISATION OF (THE TURBULENT FLOW IN/THROUGH) AN ANNULAR DIFFUSER

ERIK GOTFREDSEN*, CHRISTIAN AGULAR KNUDSEN*, JENS DAHL KUNOY‡, KNUD ERIK MEYER* AND JENS HONORE WALTHER*†

*Department of Mechanical Engineering, Technical University of Denmark, Building 403, DK-2800 Kgs. Lyngby, Denmark

†Computational Science and Engineering Laboratory, ETH Zürich, Clausiusstrasse 33, CH-8092 Zürich, Switzerland

‡ MAN Diesel & Turbo, Teglholmsgade 41, DK-2450 Copenhagen SV, Denmark

Key words: Fluid Mechanics, Optimisation, Sudden Expansion, Adjoint Solver, CFD.

Summary. In the present study, a numerical optimisation of guide vanes in an annular diffuser, is performed. The optimisation is preformed for the purpose of improving the following two parameters simultaneously; the first parameter is the uniformity perpendicular to the flow direction, a 1/3 diameter downstream of the expansion. The second parameter is the pressure loss introduced by these guide vanes. The optimisation yields an improvement of the uniformity of 1.5% and a 28% reduction in the over all pressure loss.

1 INTRODUCTION

The flow in an axisymmetric expansion (circular diffusor) is used in many different engineering applications, such as heat exchangers, catalytic converters and filters. These applications require a relatively uniform flow just after the expansion. To minimise the pressure loss in the expansion, an ideal solution would be to use a quite long expansion, but this is often not possible due to space restrictions. Therefore, a short expansion combined with e.g. guide vanes is often used potentially leading to an inhomogeneous flow distribution. The present study will use a Selective Catalytic Reduction (SCR) system for large marine diesel engines as a test case. The catalyst is designed for a specific flow rate at the inlet. A non-uniform inflow to the catalyst will severely reduce the efficiency of the process. The SCR system is placed on the high-pressure side of the turbocharger and in order to maintain the efficiency of the engine, the pressure losses has to be minimised. The present study analyses the flow using the commercial computational fluid dynamics (CFD) software STAR-CCM+[1] and the geometry with guide vanes in the inlet pipe[2] is optimised using the adjoint capabilities of the software.

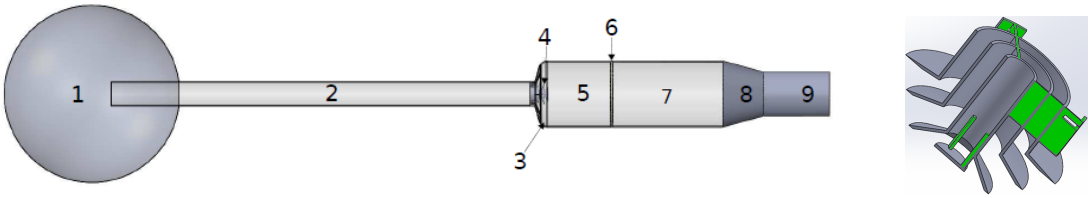

Figure 1: Left: Geometry of the model[4], where the numbers refer to: 1) inlet surface 2) straight pipe 3) expansion 4) guide vanes 5) upstream reactor 6) catalytic element 7) downstream reactor 8) diffuser 9) outlet straight. Right: A cross section of the experimental guide vanes where the connection plates is highlighted in green.

The uniformity is based on the velocity spatial flow variation in sub parts of the area weighted with the total area and mean velocity.

2 MODEL

A three-dimensional CFD model is created and shown in figure 1. The geometrical model corresponds to the experimental model described in the technical report[3]. An hemisphere is added to the inlet pipe to represent the laboratory facilities regrading the inflow. The catalytic element is modelled as a porous element. The physics in the CFD model consisted of a flow solver where the turbulence is modelled with Reynolds-Average Naiver-Stokes (RANS) equations with a realizable $k-\varepsilon$ turbulent model with two layer all y^+ wall treatment. The no-slip condition is imposed at solid walls and the flow is imposed by applying a mass flow inlet and pressure outlet. The models are chosen such that the adjoint method can be applied on the guide vanes.

3 MODEL VALIDATION

The CFD models are validated with experimental results obtained from a downscaled experimental model[3] of the catalytic converter. The Reynolds number is 10^5 upstream the expansion. The experiments are performed at laboratory conditions, with lower pressure, temperature and velocity than the full-scale catalytic converter. The results consist of different velocity planes obtained with Particle Image Velocimetry (PIV) and velocity along different lines obtained with Laser Doppler Anemometry (LDA). A measured and simulated out-of-plane velocity field upstream the catalytic element are shown in figure 2. The tendencies from the numerical results of the flow show high velocities near the reactor wall, while a triangular shaped backwards flow appears in the center. This is in good agreement with the experimental results A difference can be seen radially outwards from the connection plates for the guide vanes. From the simulation, it is seen that vortices are created at the connection plates. The impact of these vortices could be decreased but not removed by refining the mesh around the connection plates[4].

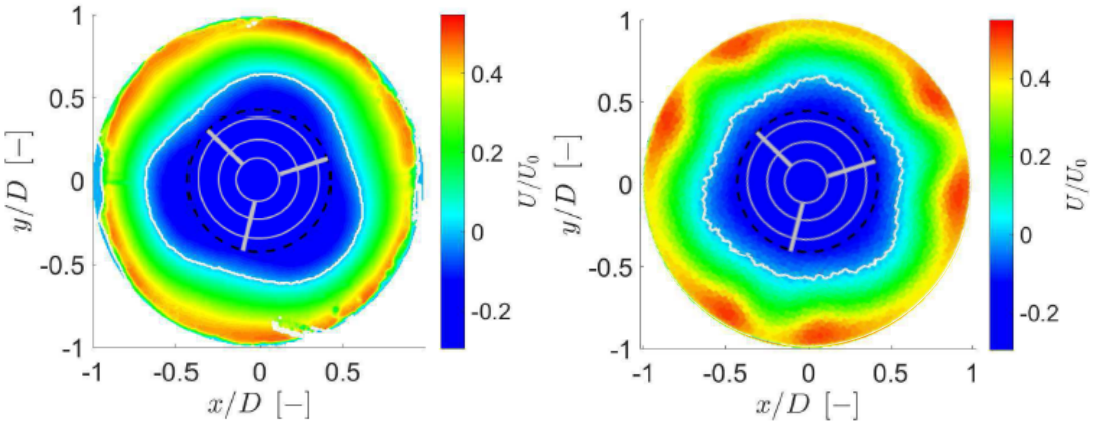

Figure 2: Visual comparison of the experimental and numerical results[4]. Left: experimental, right: simulated. The white line indicated 0. A cross section of the guide vanes is projected down on the measuring plane and showed as gray.

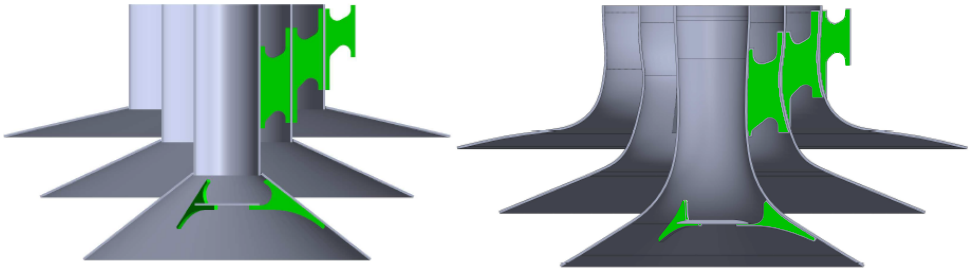

Figure 3: The guide vanes[4]. Left original, right optimised, connection plates are highlighted in green.

4 OPTIMISATION OF guide vanes

The validated numerical model is applied on an updated geometry, where the catalytic element is moved closer to the expansion. Furthermore is the guide vanes changed to the orginal design[2]. This geometrical update is done to achieve a more realistic down-scale model of the SCR-system. The calculation time is reduced by removing the inlet hemisphere. The connection plates are highlighted in green and shown in figure 1 and 3. The connection plates are not optimised an remain unchanged. The experimental guide vanes is thicker and larger than the two, shown in figure 3. The adjoint method is used to see tendencies for the optimisation and then manually applied the changes to the design, in order obtain a geometry that can be produced without excessive costs. The result in figure 3 indicates that the pressure loss and uniformity are improved by changing the cross sectional area and smoothing out the sharp bends. A velocity field for both cases are showed in figure 4. This indicate a small change in the uniformity, but as stated a pressure drop is observe. The reduction in pressure loss is 28%.

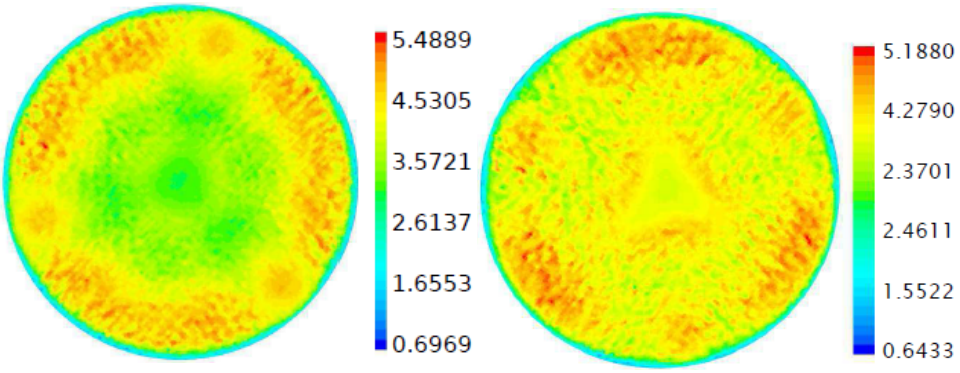

Figure 4: Colours indicate axial velocity field before the catalyc element. Left: the original guide vanes with a pressure drop of 316 Pa. Right the optimised guide vanes with a pressure loss of 226 Pa[4].

5 CONCLUSION

The present study shows that it is possible to achieve a uniform velocity distribution of $\gamma > 0.95$, just 1/3 large diameter downstream of the sudden expansion. It shows also that the initial design of guide vanes could be improved, such as the pressure loss reduces by 28% for the entire system.

REFERENCES

[1] *STAR-CCM+ Documentation,* (CD-Adapco, 2015).

[2] Kunoy, J. D. SCR WP-05: Guide vanes in SCR reactor inlet. Confidential internal MAN Turbo and Diesel report.

[3] Gotfredsen, E. & Meyer, K. E. Measurements in a model of an SCR system for large ships. Tech. Rep., Technical University of Denmark (2017).

[4] Knudsen, C. A. *Optimization of an Annular Diffuser.* Master's thesis, Tecnical University of Danmark (2017).

30th Nordic Seminar on Computational Mechanics
NSCM-30
J. Høgsberg. N.L. Pedersen (Eds.)
2017

Homogenization-based topology optimization for high-resolution continuum, frame and truss structures

JEROEN GROEN[*] AND OLE SIGMUND[*]

[*] Department of Mechanical Engineering, Solid Mechanics
Technical University of Denmark
Nils Koppels Allé, Building 404, 2800 Kgs. Lynbgy, Denmark
e-mail: jergro@mek.dtu.dk

The objective of this work is to present a projection method to obtain high-resolution manufacturable structures from efficient and coarse-scale, homogenization-based topology optimization results[1]. The focus of this work is on compliance minimization of linear-elasticity problems, for which it is known that the optimal solution is in the space of layered materials, the so-called rank-n laminates[2]. Here rank-2 laminates are optimal for plane problems subject to a single load case, and rank-3 laminates are optimal for plane problems subject to multiple load cases.

In a very appealing approach Pantz and Trabelsi introduced a method to project the microstructures from homogenization-based topology optimization to obtain a solid-void design with finite length-scale[3]. The local structure is oriented along the directions of lamination such that a well-connected design is achieved. This work shall be seen as a simplification and improvement of the approach introduced by Pantz and Trabelsi[3]. We simplify the projection approach and introduce procedures for controlling the size and shape of the projected design, such that high-resolution (e.g. 1 million elements in 2D), near-optimal and manufacturable lattice designs can be achieved within a few minutes in a single processor Matlab code on a standard PC.

Furthermore, a novel method is presented to obtain a near-optimal frame structure[4]. In an extension of the previous approach, we can obtain a frame structures based on a homogenization-based topology optimization model that is equivalent to Michell's problem of least-weight trusses. We introduce a simple frame optimization approach to optimize the extracted structures in a few minutes, such that the final designs perform close to analytical optima.

Keywords: Topology Optimization, Homogenization, Compliance Minimization, Michell Theory.

REFERENCES

[1] J.P. Groen and O. Sigmund. Homogenization-based topology optimization for high-resolution manufacturable micro-structures. *International Journal of Numerical Methods in Engineering* , 2017;: 1–18, doi: 10.1002/nme.5575

[2] Avellaneda M. Optimal bounds and microgeometries for elastic two-phase composites. *SIAM Journal on Applied Mathematics* 1987; 47(6):1216–1228, doi:10.1137/0147082.

[3] Pantz O, Trabelsi K. A post-treatment of the homogenization method for shape optimization. *SIAM Journal on Control and Optimization* 2008; 4s7(3):1380–1398, doi:10.1137/070688900\

[4] S.D. Larsen, O. Sigmund and J.P. Groen. Optimal truss and frame design from projected homogenization-based topology optimization. *Structural and Multidisciplinary Optimization (Submitted)*, 2017;: 1–15

30th Nordic Seminar on Computational Mechanics
NSCM-30
J. Høgsberg. N.L. Pedersen (Eds.)
2017

PREDICTION OF CRACK PARAMETERS IN NANO-BEAMS USING MACHINE LEARNING METHODS

H. HEIN*, L. JAANUSKA†

*†Institute of Compute Science
University of Tartu
Liivi 2, 50409 Tartu, Estonia
e-mail: helle.hein@ut.ee, ljubov.jaanuska@ut.ee

Key words: Nano-Beam, Crack, Non-Local Elasticity, Machine Learning Methods**.**

Summary. This article addresses a crack identification problem in vibrating nano-beams. The nonlocal elasticity theory of Euler-Bernoulli nano-beams was applied. The cracks were modeled as massless rotational springs connected to the adjacent segments of the nano-beam. The machine learning methods were applied to predict the crack positions or crack flexibility constants. The integrity and computational efficiency of the methods have been demonstrated through a couple of case studies.

1 INTRODUCTION

The study of simplified models as nano-beams has received an increasing attention in recent decades. Nonlocal elasticity has been proposed by Eringen[1] and has been widely applied in the vibration problems of nano-beams. Reddy[2] has developed analytical solutions for bending, vibration and buckling for various beam theories like Euler-Bernoulli, Timoshenko, Reddy and Levinson.

In the present paper, a nonlocal elasticity type approach has been developed for the investigation of nano-beams with cracks. The cracks have been modeled as rotational springs located at the crack section.

There are many studies on the identification of cracks in beams using analytical, numerical or experimental methods. The methods based on changes in natural frequencies or mode shapes have several advantage such as simplicity and quick applicability in practical engineering[3,4]. In the present paper the first natural frequencies and mode shapes have been used in predicting the crack parameters in vibrating nano-beams. The characteristic parameters of nano-beams with cracks have been predicted using machine learning methods[5].

2 GOVERNING EQUATIONS

2.1 Free vibrations of intact nano-beam

The constitutive equation of non-local elasticity can be written as follows

$$(1-\mu^2 L^2\nabla^2)\sigma_{ij} = \sigma_{ij}^c \quad , \tag{1}$$

where σ_{ij} is the stress tensor of non-local elasticity, σ_{ij}^c is the classical stress tensor and the

operator ∇^2 is the Laplace operator and $\mu = (e_0 a)/L$. The parameter e_0 is a physical constant, a stands for the characteristic internal length and L is the beam length. In the generalized stresses, (1) has the form:

$$M - \mu^2 L^2 \frac{\partial^2 M}{\partial x^2} = M_c, \tag{2}$$

where M is the bending moment of non-local elasticity and M_c is the classical bending moment. According to the Euler-Bernoulli bending theory, M_c takes the form:

$$M_c = -EI \frac{\partial^2 W}{\partial x^2}, \tag{3}$$

where E is the Young's modulus and I stands for the moment of inertia of the beam cross-section. The quantity W denotes the transverse deflection. The equilibrium conditions for a beam element can be presented as:

$$\frac{\partial M}{\partial x} - Q = 0, \tag{4}$$

$$\frac{\partial Q}{\partial x} + N \frac{\partial^2 W}{\partial x^2} - \rho A \frac{\partial^2 W}{\partial t^2} = 0. \tag{5}$$

In (4) and (5), $Q, N, \rho A$ are the resultant shear force, the external axial force and the mass per unit, respectively. Assuming that N and EI are constants, substituting (4) into (5) and taking into account (3), the equation (2) takes the form:

$$M = \mu^2 L^2 \left(- N \frac{\partial^2 W}{\partial x^2} + \rho A \frac{\partial^2 W}{\partial t^2} \right) - EI \frac{\partial^2 W}{\partial x^2}. \tag{6}$$

Substitution (6) into (4) and (5) leads to the equation

$$EI \frac{\partial^4 W}{\partial x^4} + \mu^2 L^2 \left(N \frac{\partial^4 W}{\partial x^4} - \rho A \frac{\partial^4 W}{\partial x^2 \partial t^2} \right) - N \frac{\partial^2 W}{\partial x^2} + \rho A \frac{\partial^2 W}{\partial t^2} = 0. \tag{7}$$

For the free vibration, the transverse displacement is assumed to take the form:

$$W(x,t) = w(x)\cos(\omega t), \tag{8}$$

where ω is the frequency and $w(x)$ presents the mode shape. Substitution (8) into (7) leads to: the equation:

$$w^{IV} - \frac{N w''}{EI + \mu^2 L^2 N} + \frac{\rho A \omega^2}{EI + \mu^2 L^2 N} (\mu^2 L^2 w'' - w) = 0. \tag{9}$$

The solution of (9) can be presented as

$$w = C_1 ch\beta_r x + C_2 sh\beta_r x + C_3 \cos\beta_c x + C_4 \sin\beta_c x, \tag{10}$$

where β_r and β_c can be found from the corresponding characteristic equation of (9). In (10), $C_1 - C_4$ stand for the arbitrary constants and are determined from the boundary conditions.

2.2 Free vibrations of cracked nano-beam

It is assumed that a crack is located at $x = x_1$. The open crack is represented as a rotational spring connecting two segments at the cracked section. The equation (9) should be solved separately in regions $x \in [0, x_1]$ and $x \in [x_1, L]$. The solutions w_1 and w_2 contain eight unknown constants which must be determined from boundary conditions and the compatibility conditions at the cracked section. The compatibility conditions can be presented as[6, 7]:

$$\begin{aligned} & w_1(x_1) = w_2(x_1), \\ & w_2'(x_1) - w_1'(x_1) = KM_1(x_1), \\ & M_1(x_1) = M_2(x_1), \\ & Q_1(x_1) = Q_2(x_1), \end{aligned} \tag{11}$$

where K stands for the flexibility of the rotational spring, M_i, Q_i are the bending moments and shear force in the corresponding region.

3 PREDICTION OF PARAMETERS

The parameter determination includes the following steps: determination of neural networks (NN) or random forests (RF) structure, selection of the parameters, collection and normalization of the training examples. In the following examples, a three-layered feed-forward back propagation NN has been trained using Bayesian regularization and elliot sigmoid activation function. The random forest has had 64 trees with two examples at each terminal node and six predictors at each node. The input of the models was composed using the Haar transform of normalized mode shapes[8, 9]. Eighty five percent of the data were applied to train the models and fifteen percent of data were used to test the models.

In the first example, the location of the crack in the clamped nano-beam was predicted. In Table 1, average mean square errors of 50 runs are shown.

	ANN (16:4:1)	RF
MSE (training)	0.9508	0.9671
MSE (test)	0.9390	0.9209

Table 1: Prediction of the crack location in a clamped nano-beam (μ=0.6; K/L=0.35).

In the second example, the flexibility of a rotational spring representing a crack was predicted. The crack was located in the middle of the clamped nano-beam. In Table 2, average mean square errors of 50 runs are shown.

	ANN (16:4:1)	RF
MSE (training)	0.9863	0.9786
MSE (test)	0.9898	0.9468

Table 2: Prediction of the spring flexibility representing a crack at $x_1/L=0.5$ and μ=0.6.

4 CONCLUSION

The major aim of this study was to show that Haar wavelet transform and machine learning methods (neural networks and random forest) can be successfully applied to the crack parameter identification in nano-beams with different boundry conditions. The hypotheses was evaluated on the test set (not shown to the models in advance) calculating the mean square error between the output and target values.

5 ACKNOWLEDGEMENT

Financial support from the Estonian Research Council under Grant IUT34-16 is gratefully acknowledged.

REFERENCES

[1] A.C. Eringen, "On differential equations of nonlocal elasticity and solutions of screw dislocation and surface waves", *J. Appl. Phys*, **54**, 4703-4710 (1983).

[2] J. Reddy, "Nonlocal theories for bending, buckling and vibration of beams", *Int. J. Eng.Sci*, **45**, 288-307 (2007).

[3] M.B. Rosales, C.P. Filipich, F.S. Buezas, "Crack detection in beam-like structures", *Eng. Struct.*, **31,** 2257-2264 (2009).

[4] A.C. Altunısık, F.Y. Okur, V. Kahya, "Modal parameter identification and vibration based damage detection of a multiple cracked cantilever beam", *Eng. Fail. Anal*, **70**, 154-170 (2017).

[5] S. Shalev-Shwartz and S. Ben-David, *Understanding machine learning: from theory to algorithms*, Cambridge University Press, (2014).

[6] J. Loya, J. Lopez-Puente, R. Zaera, J. Fernandez-Saeza, "Free transverse vibrations of cracked nanobeams using a nonlocal elasticity model", *J. Appl. Phys*, **105**, 443-449, (2009).

[7] H. Roostai, M. Haghpanahi, "Vibration of nanobeams of different boundary conditions with multiple cracks based on nonlocal elasticity theory", *Appl. Math. Modelling.* **38**, 1159-1169 (2014).

[8] Ü. Lepik and H. Hein, *Haar wavelets: with applications*, Springer, (2014).

[9] H. Hein, L.Feklistova, "Computationally efficient delamination detection in composite beams using Haar wavelets", *Mech. Syst. Sign. Proc*, **25**, 2257-2270 (2011).

30th Nordic Seminar on Computational Mechanics
NSCM-30
J. Høgsberg, N.L. Pedersen (Eds.)
2017

ON THE IMPLEMENTATION OF ISOGEOMETRIC ANALYSIS FOR THIN SHELLS

PURIA SAFARI HESARI[*], SARA ALMSTEDT[†], FREDRIK LARSSON[‡], MATS ANDER[‡], VEDAD ALIC[♯] AND RASTI BARTEK[†]

[*]BuroHappold Engineering, 17 Newman St, London W1T 1PD, United Kingdom
e-mail: puria.hesari@burohappold.com

[†]Cundall, One Carter Ln, London EC4V 5ER, United Kingdom

[‡]Department of Industrial and Materials Science, Chalmers University of Technology
SE-412 96 Gothenburg, Sweden

[♯]Division of Structural Mechanics, Lund University
Box 118, SE-221 00 Lund, Sweden

Key words: Isogeometric Analysis, Thin shell analysis, Kirchhoff-Love shell theory, Integrated design and analysis.

Summary. This paper concerns the implementation of Isogeometric Analysis (IGA) for analysis of free-form shells using Kirchhoff-Love theory. The objective is the study of accuracy and convergence rate obtained with IGA compared to classic FEA on a per-degree-of-freedom basis. Findings suggest that the IGA model is more accurate for the considered problems, due to an accurate geometric description. By utilization of high continuity over element boundaries, IGA also exhibits superior rates of convergence compared to classic FEA. These advantages are discussed in relation to the application of the implemented model to analyse a real shell structure.

1 INTRODUCTION

Reports from several industries state that 80% or more of analysis time is spent on converting Computer Aided Design (CAD) data to analysis suitable models. The high percentage is due to continuously increasing geometrical complexity. A technique that stands out in its ability to integrate analysis with CAD is Isogeometric Analysis (IGA). The technique omits change of geometry between models as it shares the Non-Uniform Rational B-Splines (NURBS) basis, i.e. the mathematical representations of geometries that are standard in CAD software[1]. Using a NURBS basis instead of the traditional Lagrange polynomial basis to describe the geometry also allows for utilization of high regularity over element boundaries. This property simplifies the implementation of Kirchhoff-Love

shell theory[2]. It is of interest to investigate whether these properties make IGA more advantageous for shell analysis compared to classic FEA.

2 THIN SHELLS

2.1 Analysis model and problem description

The IGA model is set up in Matlab® and developed based on the work by Hughes et al.[1]. It is built from scratch with some routines from the IGA analysis toolbox by Alic[3]. It is also inspired by the open source IGA library "igafem" by Nguyen et al.[4]. With Kirchhoff-Love shell theory as basis, the model serves to study accuracy and convergence rate for shell analysis. In the model, advantage is taken of the increased continuity over element boundaries that is enabled by IGA. The commercial FEA software programs used for comparison include COMSOL Multiphysics® and Abaqus™. The model is initially used to analyse the "Pinched hemisphere", a classic benchmark problem described by Belytschko et al.[5]

2.2 Results

A convergence analysis is carried out with uniform enrichment of the discretization grid. The error in strain energy vs. number of degrees of freedom is studied. The finite element analysis software COMSOL Multiphysics® is used for the comparison.

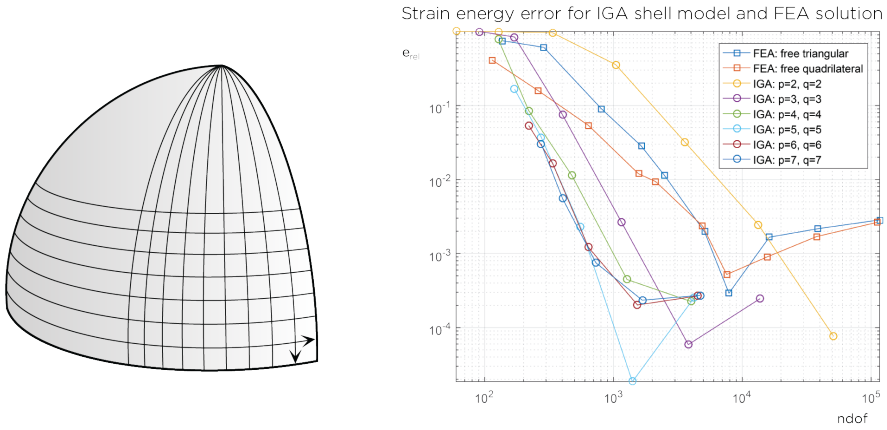

Figure 1: A quarter of the "pinched hemisphere" benchmark problem is modelled, here with the local directions illustrated on the surface (left). The approximation error is shown for FEA (squares) and IGA (circles) vs. number of degrees of freedom (ndof) for mesh refinement using different element orders (right).

Two FE solutions are computed, one with the program's free triangular mesh and one with its' free quadrilateral mesh. The IGA solutions are computed for degrees ranging from $p = q = 2$ to $p = q = 7$. The degree is one of the four parts that defines a NURBS curve. A NURBS surface can have different degrees along the NURBS curves that defines

it. The degree is always an integer and a positive number, for example, NURBS polylines typically have degree 1 and a NURBS circle degree 2. The degree can be raised without altering the geometry.

The results which are presented in Fig. 1 show similar accuracy for both IGA and FEA. The locking problems in the isogeometric model with $p = q = 2$ are seen (yellow line). The finite element solution with the free quadrilateral mesh performs well, however, the convergence is not quite as smooth as with the IGA shell model. The most accurate analysis setup with the highest convergence rate is given by IGA with $p = q = 7$. In general it can be seen that the IGA solutions with $p, q > 3$ show faster convergence rates than what is given by the finite element analyses.

3 CASE STUDY

3.1 The Crest analysis model

The purpose of the case study is to explore what it is like to work with IGA in a real project scenario. The shell chosen for analysis is a thin aluminium shell designed by BuroHappold Engineering and Zaha Hadid Architects and installed at the V&A museum in London the summer of 2014. The structure was freestanding and depended only on self-weight and friction to counteract critical loads. The geometry input is defined by a single patch NURBS surface delivered as a Rhinoceros® model. This reflects one of the most common processes in the industry where a design is delivered in a NURBS based environment. The isogeometric analysis process then starts with the NURBS data being structured and exported using the Grasshopper® component that was written for this project. The remaining data required to complete the model can be found in the thesis report by Safari Hesari and Almstedt[6]. The FEA results for comparison are obtained with the software Abaqus™. The input is the NURBS surface exported from Rhinoceros® in SAT-format.

3.2 Results

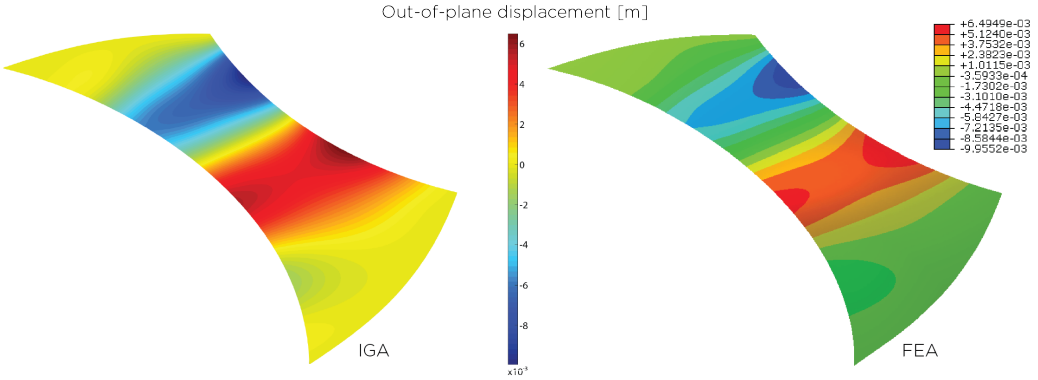

Figure 2: Comparison of deformation of the "Crest" shell analysed by IGA (left) and FEA (right).

The analysis output consists of deformations and in-plane membrane and bending stresses. In Fig. 2, the out-of-plane displacement results are shown. Abaqus™ and the implemented IGA model use different colour maps, but it can still be seen that the IGA solution corresponds well with the FE results in terms of displacement values and patterns on the surface. The FEA model requires approximately 450 000 degrees of freedom to reach about the same results that are obtained with 14 000 degrees of freedom in the IGA shell model.

4 DISCUSSION

It is well-known in the industry, and also noted during the case study, that geometry transfer and meshing for FEA compatibility is tedious. Since it is necessary to return to the CAD interface to generate a finer mesh one ends up with a time-consuming iterative procedure. However, in IGA, meshes reflecting the exact geometry are automatically generated. The geometry and the mesh are inherently connected by sharing the same underlying description. In industry reports it is stated that about 20% of analysis time consists of meshing[1], and potential for time-savings can thus be seen here.

In conclusion, there are strong upsides to working with IGA such as potential for more accurate results for fewer degrees of freedom and time-savings in the design process. However, it is also noted that developments, for example in terms of computational efficiency, are necessary before IGA can be a practical tool for engineers.

REFERENCES

[1] Cottrell, J. A., Hughes, T. J. & Bazilevs, Y. *Isogeometric Analysis: Toward Integration of CAD and FEA* (Wiley, 2009).

[2] Hughes, T. J. Isogeometric analysis: Where we are and where we are going (2014). URL `https://www.youtube.com/watch?v=Vwl69Ds69y0`.

[3] Alic, V. Isogeometric analysis toolbox for calfem (2017). URL `https://github.com/CALFEM/calfem-matlab-iga`.

[4] Nguyen, V. P., Anitescu, C., Bordas, S. P. & Rabczuk, T. Isogeometric analysis: an overview and computer implementation aspects **117**, 89–116 (2015).

[5] Belytschko, T., Stolarski, H., Liu, W. K., Carpenter, N. & Ong, J. S. Stress projection for membrane and shear locking in shell finite elements **51**, 221–258 (1985).

[6] Hesari, P. S. & Almstedt, S. Isogeometric analysis of curved beams and thin shells (2017).

30th Nordic Seminar on Computational Mechanics
NSCM-30
J. Høgsberg. N.L. Pedersen (Eds.)
2017

FATIGUE FAILURE PREDICTIONS IN THICKNESS TAPERED AREAS OF A GLASS/POLYESTER FIBER COMPOSITE

S.AYDIN RAEIS HOSSEINY* AND JOHNNY JAKOBSEN†

*,†Department of Materials and Production
Aalborg University
Fibigerstræde 16, 9220 Aalborg east, Denmark
*e-mail: aydin@mp.aau.dk, †e-mail: joj@mp.aau.dk
Web page: http://www.aau.dk

Key words: Wind Turbines, Damage Mechanics, Computational Methods

Summary. Optimization process may consider thousands of thickness transition areas in a single blade design. These areas may act as crack initiators that cause delamination and further catastrophic failure of an entire blade. The haphazardness of fatigue process makes each fatigue failure incident a unique case to be verified experimentally. A numerical approach is developed in this study to predict the occurrence of fatigue failure and reduce the number of required experiments.

1 INTRODUCTION

Thickness transitions in composite materials are also known as "ply-drops". They are commonly known to be structural weak points and failure often initiates and propagates from these locations. Ply-drops are unavoidable in the manufacturing of large wind turbine blades and therefore it is a necessity to have reliable models that can predict the event of material failure in their vicinity. Numerical studies utilizing a finite element scheme of a ply-drop under even simple fatigue loading show that each element in the ply-drop region may experience highly different fatigue stress ratios. Accurate predictions of the fatigue stress ratios are important if reliable fatigue failure have to be estimated. Adopting the progressive fatigue failure method proposed by Shokrieh et al.[1] and utilizing it on more complex stress states as in a ply-drop is the scope of this paper.
It is expected that the out-of-plane shear behavior of the material have a significant role in the failure initiation within a ply-drop region. Chang et al.[2] found that shear non-linearities are responsible for nonlinearly elastic behaviour of the ply-drop models. These nonlinearities are accounted for by following the approach taken by He et al.[3].
This study compares the numerical based predictions of both static and fatigue failure with experimentally obtained results for a ply-drop definition under similar loading conditions.

2 METHODS

The process of fatigue failure is defined as monotonic degradation of material properties depending on 9 different fatigue failure criteria. Each criterion formulates one of the fatigue failure modes by considering the effect of residual strength and stiffness, remaining life of the material, and shear nonlinearities that contribute to the process of failure. Numerical solutions to a chosen ply-drop configuration loaded in fatigue is developed using user subroutines in ABAQUS finite element package[4]. The subroutine reduces the material properties, updates stiffness matrices, and redistribute stresses in all integration points, as the fatigue proceeds. Failure happens in one or some of the criteria, when residual material properties under fatigue loading reduce to a level that is lower than the applied stress. The material properties, corresponding to the failed mode, are then set to zero to account for the failure. Subsequently, other failure criteria which may be influenced by the failing element are disturbed in the following increment. The process continues until catastrophic failure of the material is reached and all material strength and stiffness values get removed from simulation. Figure (1) shows the effect of high and low stress levels on final fatigue life of the composite.

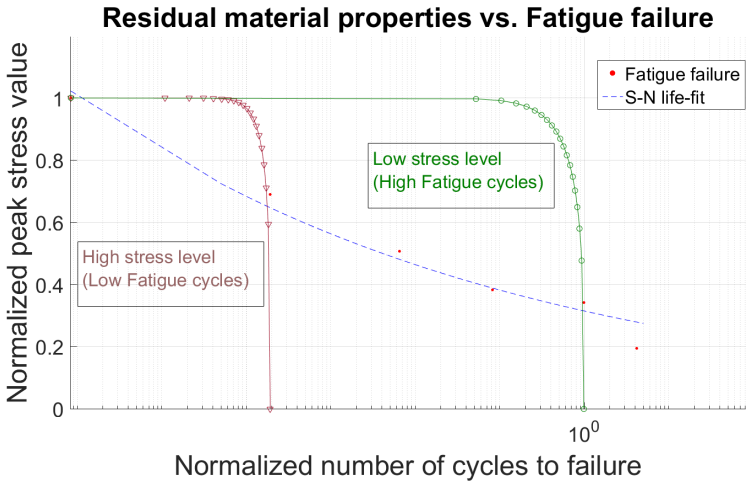

Figure 1: Strength degradation under different stress levels versus fatigue life by number of cycles.

The residual material properties are formulated based on the remaining fatigue life of the material. Even in a simple case of ply-drop under constant fatigue loading, each element may experience different fatigue ratios and stress levels. Consequently, the remaining life of each point with its specific stress state may be different than others. This mandates the availability of fatigue failure results for different fatigue ratios of all stress components, which is almost impossible. A method of normalizing the results of constant life diagram and predicting the final fatigue life for other mean and amplitude stress combinations by Gathercole at al.[5] is employed and shown in figure (2). By knowing the

mean and amplitude stresses at each material point, the remaining fatigue life can be calculated and used in calculating the residual material properties.

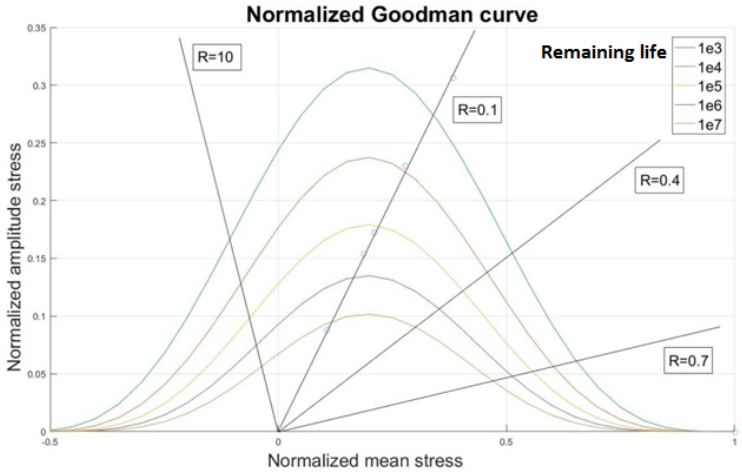

Figure 2: Normalized life prediction of material under different fatigue ratios.

3 RESULTS

A ply-drop specimen with normalized layup of [8-2-6], tapered normal to the longitudinal direction is simulated under loading with fatigue ratio of 0.1. Experiments show that the failure initiates at the tip of the resin pocket in all stress levels. However, evolution of damage depend on fatigue stress levels. Final failure and separation of the specimens under mean stress levels lower than 0.21 times the ultimate strength, happen near thick side of the resin pocket and develop through its faces, while under higher mean stress levels, specimens break in the vicinity of fixture area away from the ply-drop. The numerical model results fairly represent the test data in predicting the initiation and evolution of the fatigue damage. The simulated S-N curve results are compared with experimental data, as shown on figure (3). The predicted fatigue life is in a good agreement with experiment for high stress levels, but the accuracy reduces for lower stress levels, until the simulated fatigue life results are about 15% lower than the experiment for mean stresses equal to 0.18 times the ultimate strength value.

4 CONCLUSIONS

The numerical method shows a good capability of following the actual wőhler curve and predicting the damage mechanism. However, the accuracy level reduces in predicting the fatigue life of the test specimen under low stress levels.

1. The main reason for this drawback may be the fewer experimental data from residual material properties and final failure results for high cycle fatigue tests,

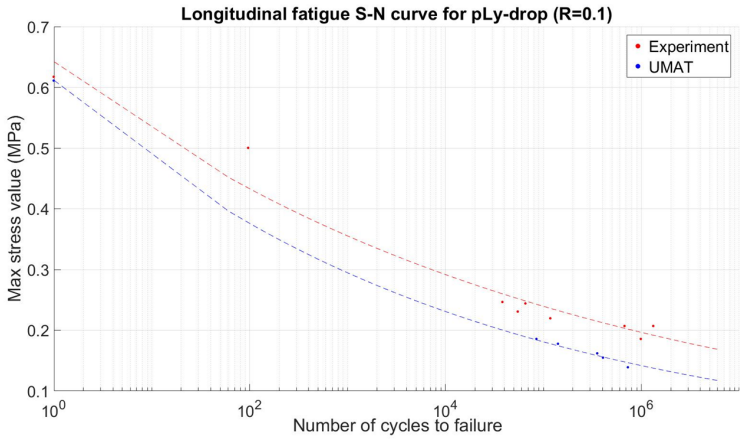

Figure 3: Comparison of the actual and numerical test over ply-drop specimen under 0.1 fatigue ratio.

2. Reducing the number of cycle jump can also provide a better resolution in result of such problems.

However, to the authors' knowledge, the other methods that use fracture mechanics approach by measuring the damage based on energy release rate, calculations result in similar levels of accuracy. They then improve their results by performing reliability analyses and/or calibrating the results with experimental data. However, this study aimed to assess the level of uncertainty for the current approach and uses untouched results for comparison. Unlike other approaches that use cohesive elements and need to be analyzed with explicit solvers, the current method is highly stable with implicit formulations until final failure stage. The reason is that the mesh dependency is only to the level of calculating acceptable stresses and the technique determines damage state by failure criteria within the subroutine.

REFERENCES

[1] Shokrieh, M. M. & Lessard, L. B. Progressive fatigue damage modeling of composite materials, part i: Modeling. *Journal of Composite Materials* **34**, 1056–1080 (2000).

[2] Chang, F.-K. & Chang, K.-Y. A progressive damage model for laminated composites containing stress concentrations. *Journal of composite materials* **21**, 834–855 (1987).

[3] He, Y., Makeev, A. & Shonkwiler, B. Characterization of nonlinear shear properties for composite materials. *Composites Science and Technology* **73**, 64–71 (2012).

[4] ABAQUS, V. 6.14 documentation. *Dassault Systemes Simulia Corporation* (2014).

[5] Gathercole, N., Reiter, H., Adam, T. & Harris, B. Life prediction for fatigue of t800/5245 carbon-fibre composites: I. constant-amplitude loading. *International Journal of Fatigue* **16**, 523–532 (1994).

30th Nordic Seminar on Computational Mechanics
NSCM-30
J. Høgsberg. N.L. Pedersen (Eds.)
2017

TOPOLOGY OPTIMIZATION METHODS FOR ACOUSTIC-MECHANICAL COUPLING PROBLEMS

JAKOB S. JENSEN, CETIN B. DILGEN, SÜMER B. DILGEN AND NIELS AAGE

Centre for Acoustic-Mechanical Micro Systems (CAMM)
Technical University of Denmark
2800 Kgs. Lyngby, Denmark
e-mail: json@elektro.dtu.dk

Abstract. A comparative overview of methods for topology optimization of acoustic-mechanical coupling problems is provided. The goal is to pave the road for developing efficient optimization schemes for the design of complex acoustic devices such as hearing aids.

Topology optimization methods have gained tremendous popularity in the last decades and are now used routinely e.g. in aviation and automotive industries. Applications have spread from pure mechanics to various physics such as heat transfer, fluid mechanics, optics and acoustics. However, a major challenge exists when considering problems that involve coupling of physics through boundaries including acoustic-mechanical coupling where structural vibrations and acoustic pressure interact at the boundary. Analysis methods that require boundary tracking is difficult to combine with a traditional density-based parametrization (pixel- or voxel-based design description) and a varying topology. This calls for alternative analysis and/or design parametrization schemes to be developed.

A mixed finite element approach was proposed earlier[1], in which the pressure was introduced as an auxiliary variable. This allowed the element physics to be interpolated between acoustics and structural vibrations with use of standard design parametrization. Another approach was proposed using a level-set design parametrization[2]. Here, a level-set function explicitly separates the physical domains and facilitates the boundary coupling formulation.

In this work we compare variants of two mentioned formulations as well as a newly proposed scheme[3] based on acoustic and mechanical computations on fictitious domains and globally assembled coupling without explicit boundary tracking.

Keywords: Topology Optimization, Acoustic-Structure Interaction.

REFERENCES

[1] G.H. Yoon, J.S. Jensen and O. Sigmund, “Topology optimization of acoustic–structure interaction problems using a mixed finite element formulation”, *Int. J. Num. Meth. Engng*, **70**, 1049-1075 (2007).

[2] L. Shu, M. Wang and Z. Ma, “Level set based topology optimization of vibrating structures for coupled acoustic–structural dynamics”, *Comp. Struct.*, **132**, 34-42 (2014).

[3] J.S. Jensen, “Topology optimization of acoustic-structure interaction problems using fictitious domains and global interpolated coupling matrices”, *in preparation* (2017).

30th Nordic Seminar on Computational Mechanics
NSCM-30
J. Høgsberg. N.L. Pedersen (Eds.)
2017

3D FINITE ELEMENT MODELLING OF NON-CRIMP FABRIC BASED FIBRE COMPOSITE BASED ON X-RAY CT DATA

KRISTINE M. JESPERSEN[*], LEIF ASP[†] AND LARS P. MIKKELSEN[*]

[*] Department of Wind Energy
Technical University of Denmark
Risø Campus, Fredriksborgvej 399, 4000 Roskilde, Denmark
e-mail: kmun@dtu.dk, lapm@dtu.dk, web page: http://www.vindenergi.dtu.dk/

[†] Department of Industrial and Materials Science
Chalmers University of Technology
Hörsalsvägen 7A, 412 58 Göteborg, Sweden
Email: leif.asp@chalmers.se - Web page: http://www.chalmers.se

Abstract. Due to the high number of fatigue load cycles during the life of a wind turbine blade, fatigue is one of the main design concerns. However, it is still not possible to realistically predict the fatigue life of the non-crimp fabric based fibre composites commonly used for the main load carrying parts of wind turbine blades. Existing modelling attempts generally consider the fibre bundle structure as a perfect pattern, however recent experimental X-ray CT studies [1,2] have shown that the local variations in the fibre bundle structure have a large influence on the observed fatigue damage initiation and progression in the material. In the current study, the real bundle structure inside a non-crimp fabric based fibre composite is extracted from 3D X-ray CT images and imported into ABAQUS for numerical modelling. The local stress concentrations when loaded in tension caused by the fibre bundle structure are examined and compared to experimental observations of the fatigue damage. In the current study the bundle structure is manually segmented, however the possibility of automatic segmentation in the future is also discussed. The study shows the potential of X-ray CT based modelling for increased understanding of the fatigue damage mechanisms, but also sets the stage for modelling across scales including the variations caused by manufacturing process.

Keywords: Non-crimp fabric based composite, X-ray CT based modelling, Finite element modelling, Fatigue damage.

REFERENCES

[1] Zangenberg, J., Brondsted, P., & Gillespie, J. W., "Fatigue damage propagation in unidirectional glass fibre reinforced composites made of a non-crimp fabric", *Journal of Composite Materials*, ***48***(22), 2711–2727 (2014).

[2] Jespersen, K. M., Zangenberg, J., Lowe, T., Withers, P. J., & Mikkelsen, L. P., "Fatigue damage assessment of uni-directional non-crimp fabric reinforced polyester composite using X-ray computed tomography", *Composites Science and Technology*, ***136***, 94–103 (2016).

30th Nordic Seminar on Computational Mechanics
NSCM-30
J. Høgsberg. N.L. Pedersen (Eds.)
2017

A NOVEL APPROACH FOR SIMULATING PRESSURE TUBE SENSORS IN PEDESTRIAN CRASH SIMULATIONS

JESPER KARLSSON *

* DYNAmore Nordic AB
Bror Nilssons gata 16, 417 55 Gothenburg, Sweden
E-mail: jesper@dynamore.se - Web page: http://www.dynamore.se

Key words: Computational Methods, Automotive Safety, Pedestrian Crash, LS-DYNA.

Summary. This talk presents a novel method to efficiently simulate a new crash detection system for pedestrian impact.

1 INTRODUCTION

Automotive crash simulation is paramount to the safety of today's cars. With increasing computational resources, cars are becoming safer every year, and today less than half of the road fatalities are car occupants1. However, as cars are becoming safer for occupants, pedestrian fatalities are an increasing share of all road fatalities. Pedestrian safety is thus a future key area in automotive safety, presenting new challenges for automotive crash simulation.

This talk presents a novel method to efficiently simulate a new crash detection system for pedestrian impact, see Figure 1. In this system, a thin air-filled tube is embedded in the front bumper and fitted with pressure sensors at the ends. On impact, the tube is compressed and a pressure wave travels to the sensors, enabling localization and extent of the impact. In recent years, such systems have gained popularity in the automotive industry, posing a challenging task in efficient and accurate simulations.

The method presented here is implemented as a standard keyword in the finite element software LS-DYNA[2]. The tube is simulated with beam elements, and pressure propagation is governed by a 1D model based on the compressible Euler equations, resulting in a very efficient method compared to 3D CFD or particle methods. The talk aims to give an overview of the theory, as well as to show comparisons with experiments and existing methods in LS-DYNA.

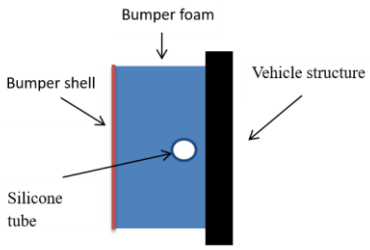

Figure 1: Schematics of bumper cross section with embedded tube

2 THE TUBE MODEL

Pressure propagation is governed by a 1D acoustic approximation of the compressible Euler equations, resulting in a very efficient method compared to 3D CFD or particle methods. We assume that the tube cross section is circular but with varying area, $A = A(x,t)$, in time and along the tube length. The *quasi*-1D Euler equations[3] for a compressible inviscid fluid (in thermal equilibrium) are then given by

$$\begin{aligned} (A\rho)_t + (A\rho u)_x &= 0, \\ (A\rho u)_t + (A\rho u^2 + Ap)_x &= pA_x, \\ (AE)_t + \big(Au(E+p)\big)_x &= 0. \end{aligned} \tag{1}$$

where the independent variables are: fluid density ρ, velocity u, energy per unit volume E, and pressure p. Since this system is underdetermined, we close it with the ideal gas law for a polytropic gas

$$E = \frac{p}{(\gamma - 1)} + \frac{\rho}{2}u^2, \tag{3}$$

where $\gamma = c_p/c_v$ is the adiabatic index, $c_p$is the specific heat at constant pressure, and c_v is the specific heat at constant volume.

After a series of simplifications, where we first assume a smooth flow (e.g. acoustic waves) where the entropy is constant along a particle path, and then a constant temperature, we arrive at the *isothermal* (and *isentropic*) Euler equations

$$\begin{aligned} (A\rho)_t + (A\rho u)_x &= 0, \\ (A\rho u)_t + (A\rho u^2 + Ac^2\rho)_x &= pA_x. \end{aligned} \tag{4}$$

The pressure is here proportional to the density through

$$p = c^2\rho,$$

and the sound speed, c, is constant.

Finally, a linearization around $(\rho_0, p_0, u_0 = 0)$ gives the acoustic approximation

$$\begin{aligned} (A\rho)_t + \rho_0(Au)_x &= 0, \\ \rho_0(Au)_t + c^2(A\rho)_x &= pA_x. \end{aligned} \tag{5}$$

or

$$\begin{aligned} p_t + \frac{A_t}{A}p + \frac{p_0}{A}(Au)_{x_x} &= 0, \\ (Au)_t + \frac{Ac^2}{p_0}p_x &= 0. \end{aligned} \tag{6}$$

Note that treating Au as an independent variable gives a hyperbolic system with A_t/A as a source term.

3 IMPLEMENTATION

The above tube model is implemented as a new keyword (*DEFINE_PRESSURE_TUBE) in LS-DYNA, where the tube is modeled by beam elements. At initilization, the beam elements give the initial tube dimensions as input to the pressure solver. The pressure and velocity is then updated on each beam node using a standard continuous Galerkin method, and the cross section area is given by contact penetration from surrounding structures. Apart from contact penetration, the pressure solver is fully independent of the beam element deformation.

3 VALIDATION

As test example, a mass is dropped onto a 1.7 m long silicone tube with inner diameter 4 mm and outer diameter 8 mm (Figure 2, left). Three methods were tested; the Corpuscular Particle Method (Figure 3), the pressure tube embedded in a shell tube, and the pressure tube by itself (Figure 2, right). Experimental data were provided by Volvo Car Corporation.

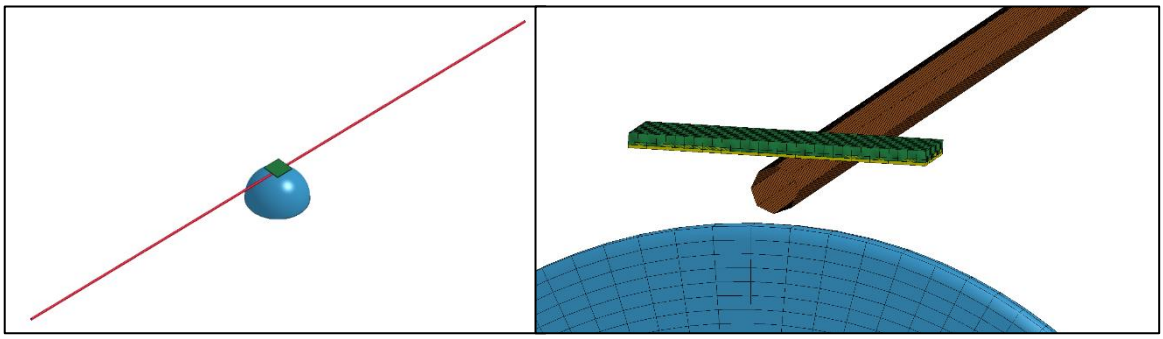

Figure 2: Test setup with beam elements

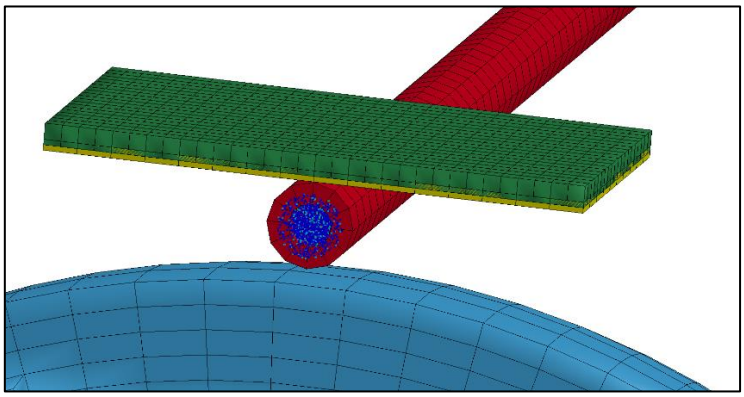

Figure 3: CPM setup where a shell tube filled with particles.

Approximate run times for the different methods were 170 hours for CPM, 4 hours for the embedded pressure tube, and 10 minutes for the pressure tube by itself. The results gave reasonable pressures compared to experimental data, see Figure 4. CPM is the most expensive method due to the number of particles required, two million in this case, but is in some sense the most physically accurate. On the other hand, the pressure tube by itself relies solely on

contact stiffness to model the radial stiffness, with may negatively influence tube compression. Note that in all three examples no damping was used to model pressure loss, and contact stiffness was adjusted to give roughly the same tube compression at impact. The tube compression for the experimental setup was unknown.

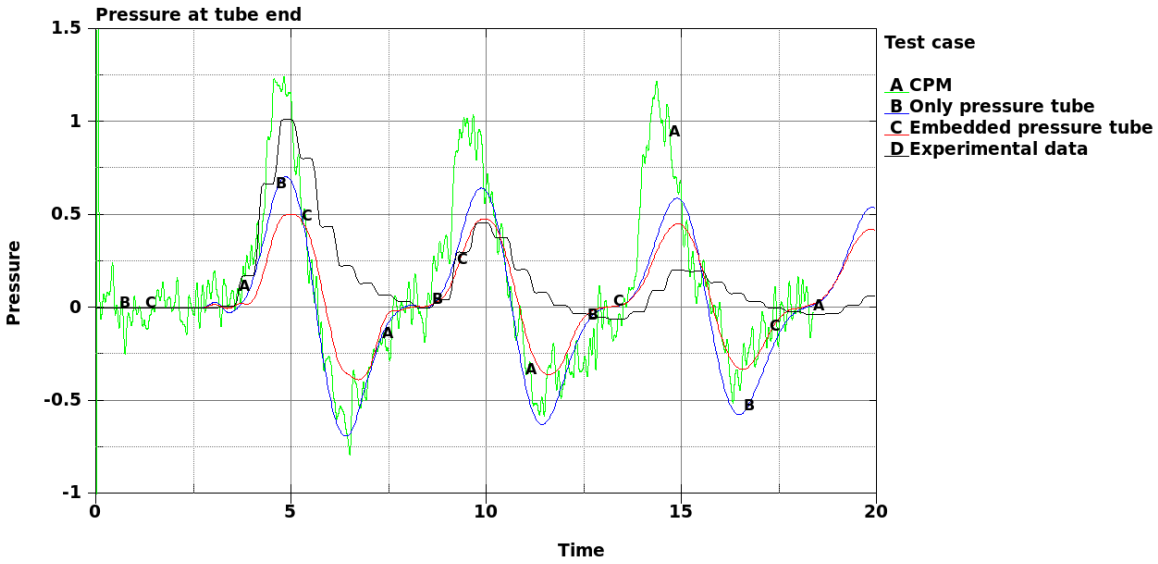

Figure 4: Pressure at tube end

REFERENCES

[1] World Health Organization. *Global Status Report on Road Safety 2015*. World Health Organization (2015).

[2] J.O. Hallquist, *LS-DYNA Keyword Manual, Vol I*, Livermore Software Technology Corporation (2017).

[3] T. H. Pulliam, *The Euler Equations*, NASA Ames Research Center (1994).

30th Nordic Seminar on Computational Mechanics
NSCM-30
J. Høgsberg. N.L. Pedersen (Eds.)
2017

AN ANALYSIS OF GLASS FRACTURE STATISTICS

DAVID T. KINSELLA* AND KENT PERSSON†

*Div. of Structural Mechanics
Faculty of Engineering LTH
Lund University
P.O. Box 118
SE-221 00 Lund, Sweden
e-mail: david.kinsella@construction.lth.se, web page: http://www.byggmek.lth.se/

†Div. of Structural Mechanics
Faculty of Engineering LTH
Lund University
P.O. Box 118
SE-221 00 Lund, Sweden
e-mail: kent.persson@construction.lth.se, web page: http://www.byggmek.lth.se/

Key words: Glass, Fracture, Stochastic methods

Summary. Glass fracture statistics are analyzed using a numerical modelling tool based on the weakest-link principle and Griffith flaws with stochastic crack size, crack plane orientation and location on the surface. The effect of adopting various fracture criteria is investigated as well as the effect of varying the distribution of the crack plane angles and comparisons are made based on simulations of a double ring bending test.

1 INTRODUCTION

Glass as a building material is gaining in popularity and load-bearing units are being installed into structures at an increasing rate. Strength predictions are in practice based either on some standard distribution or on tables and diagrams obtained using a modelling tool such as the Glass Failure Prediction Model[1]. However, there is disagreement among researchers as to which prediction model is the correct one to use[2,3]. There is a need for further development of a strength prediction model.

2 BACKGROUND

Most often, the strength is explained assuming the existence of Griffith flaws while adopting the weakest-link principle. According to the weakest-link principle the strength of a chain is governed by its weakest link[4]. Griffith[5] modelled crack growth as a reversible thermodynamical process. Griffith flaws in glass are usually represented as plane edge cracks. Consider a crack subjected to a biaxial stress field with the crack plane inclined at some angle in the coordinate system of the principal stresses. It is usually assumed that

only mode I displacement plays into the onset of fracture in glass[2]. Fracture is governed by the following criterion

$$K_{\mathrm{I}} \leq K_{\mathrm{I}c} \tag{1}$$

where K_{I} denotes the mode I Stress Intensity Factor (SIF) and $K_{\mathrm{I}c}$ denotes the fracture toughness[6]. It is sometimes assumed that all crack planes are oriented in the worst possible way, i.e. perpendicular to the Maximum Principal Tensile Stress (MPTS)[2]. However, this assumption may be overly conservative. It has also been hypothesized that the strength is decreased when glass has to withstand shear stress[7]. Current design methods do not account for the potential effect on the strength due to the presence of shear stress. A mixed mode fracture criterion based on the maximum non-coplanar energy release rate[8] is given by the following inequality

$$\sqrt[4]{K_{\mathrm{I}}^4 + 6K_{\mathrm{I}}^2 K_{\mathrm{II}}^2 + K_{\mathrm{II}}^4} \leq K_{\mathrm{I}c} \tag{2}$$

where the left-hand side of inequality (2) is a mode I-equivalent SIF[9].

3 NUMERICAL MODELLING TOOL

Using a new numerical method, the strength and fracture locations of glass plates subjected to bending are simulated and the results are analyzed and compared with experimental data. The method which is similar to the Monte Carlo simulations carried out by Yankelevsky[10] is based on the assumption of the existence of Griffith flaws as well as the adoption of the weakest-link principle. The method is also dependent on a representation of the surface flaws condition in glass. Using this numerical method it is possible to estimate the effect on the strength while adopting various fracture criteria including mixed mode criteria and while making different assumptions about the crack plane angles in the coordinate system of the principal stresses.

4 RESULTS

Small glass plates subjected to double ring bending were analyzed using the numerical method. The mode I fracture criterion produced only a minor difference in the strength data sample compared with the mixed mode criterion when it was assumed that the stochastic crack plane angles are distributed uniformly between $[0, \pi)$. In this case, however, the proportion of failures originating from outside the loading ring increased significantly when taking mode II shearing displacement into consideration. On the other hand, when it was assumed that the crack planes are always oriented in the worst possible way, i.e. perpendicular to the MPTS, then the mode I fracture criterion yielded a significantly lower mean strength value. It also produced the largest proportion of failures originating from outside the loading ring. The results are illustrated in Fig. 1.

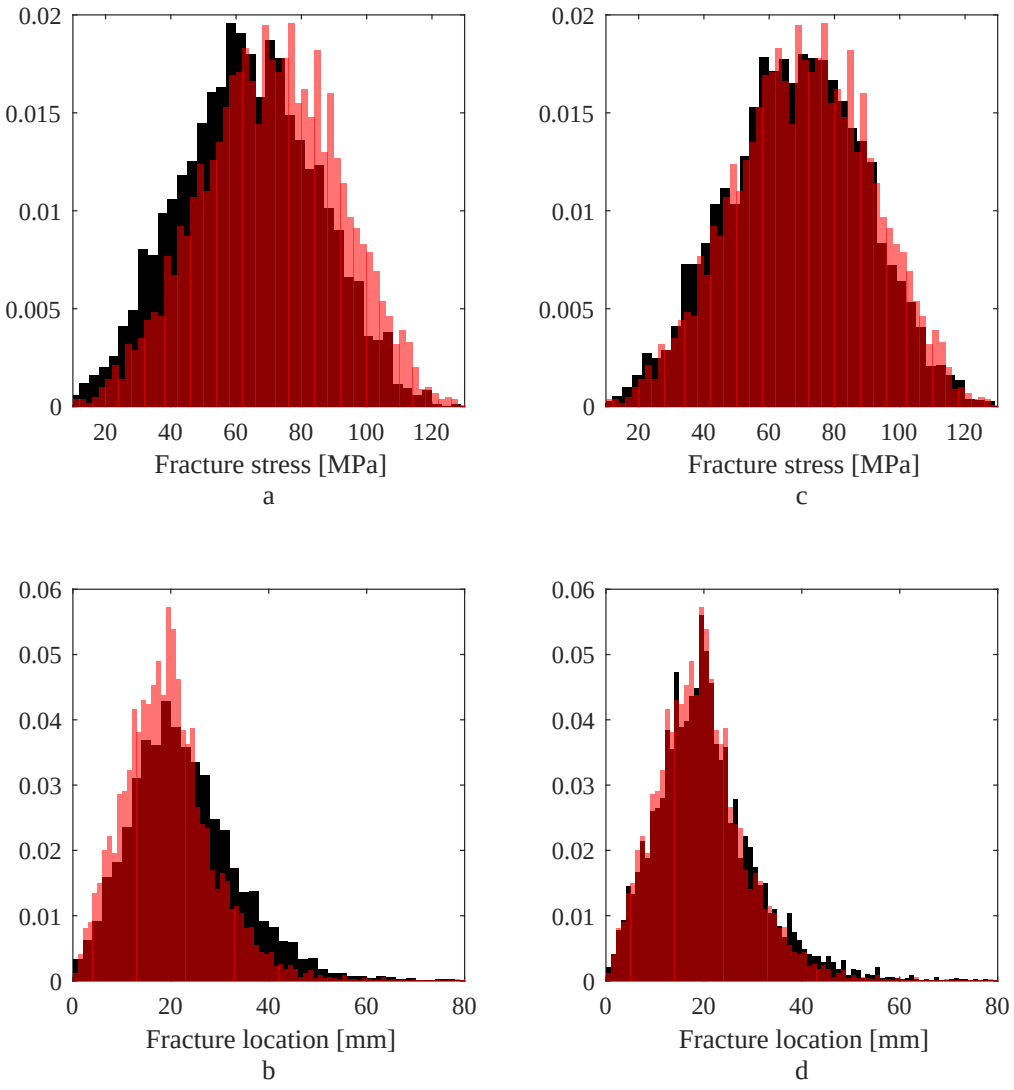

Figure 1: Left: Uniformly distributed crack plane angles vs crack planes oriented perpendicular to the MPTS with mode I fracture criterion. Right: Uniformly distributed crack plane angles with mode I fracture criterion vs mixed mode fracture criterion. Semi-transparent (red) bars indicate the uniformly distributed crack plane angle mode I data. Overlapping histograms are dark red.

REFERENCES

[1] Beason, W. & Morgan, J. Glass failure prediction model. *J Struct Eng* **110**, 197–212 (1984).

[2] Haldimann, M. *Fracture strength of structural glass elements - analytical and numerical modelling, testing and design.* PhD thesis, Ecole Polytechnique Fédérale de Lausanne EPFL (2006).

[3] Veer, F., Louter, C. & Bos, F. The strength of annealed, heat-strengthened and fully tempered float glass. *Fatigue Fract Eng M* **32**, 18–25 (2009).

[4] Peirce, F. *J. of Textile Inst. Trans.* **17**, 355 (1926).

[5] Griffith, A. The phenomena of rupture and flow in solids. *Phil. Trans. R. Soc.* **A221**, 163 (1920).

[6] Irwin, G. Analysis of stresses and strains near the end of a crack traversing a plate. *J. Appl. Mech.* **24**, 361 (1957).

[7] Reid, S. Effects of spatial variability of glass strength in ring-on-ring tests. *Civ Eng Environ Syst* **24**, 139–148 (2007).

[8] Hellen, T. & Blackburn, W. The calculation of stress intensity factors for combined tensile and shear loading. *Int J Fract* **11**, 605 (1975).

[9] Thiemeier, T., Brückner-Foit, A. & Kölker, H. Influence of the fracture criterion on the failure prediction of ceramics loaded in biaxial flexure. *J. Am. Ceram. Soc.* **74**, 48–52 (1991).

[10] Yankelevsky, D. Strength prediction of annealed glass plates - a new model. *Eng Struct* **79**, 244 – 255 (2014).

30th Nordic Seminar on Computational Mechanics
NSCM-30
J. Høgsberg. N.L. Pedersen (Eds.)
2017

AN ORTHOTROPIC MULTIAXIAL HIGH-CYCLE FATIGUE MODEL

SAMI HOLOPAINEN[1], REIJO KOUHIA[1], NIELS-SAABYE OTTOSEN[2], MATTI RISTINMAA[2] AND TIMO SAKSALA[1]

[1]Tampere University of Technology, Structural Mechanics
P.O. Box 600, FI-33101 Tampere, Finland
e-mail: sami.holopainen@tut.fi, reijo.kouhia@tut.fi, timo.saksala@tut.fi, web page: http://www.tut.fi

[2]Lund University, Solid Mechanics
SE-22100 Lund, Sweden
e-mail: niels_saabye.ottosen@solid.lth.se, matti.ristinmaa@solid.lth.se - Web page: http://www.lunduniversity.lu.se

Abstract. A continuum approach is proposed for modelling multiaxial high-cycle fatigue of solids which exhibit orthotropic fatigue properties. The model is an extension of the original isotropic model proposed by Ottosen et al.[1], which is based on the concept of a moving endurance surface in the stress space and an evolving damage variable. Movement of the endurance surface is modelled with a deviatoric stress tensor which defines the center of the endurance surface in a similar way than the back-stress tensor in plasticity, thus memorizing the load history. Damage evolution is activated whenever the stress state is outside the endurance domain defined by the endurance surface, and the time rate of the endurance surface is positive. In this model uniaxial and multiaxial stress states are treated in a unified manner for arbitrary loading histories, thus avoiding cycle-counting techniques.

The proposed model is formulated using the integrity basis for orthotropic symmetry group. Also reduction to the transversely isotropic case is given and the derived model is compared to the previously proposed transversely isotropic model[2].

Keywords: High Cycle Fatigue, Anisotropy, Endurance Surface, Evolution Equations, Fatigue Damage.

REFERENCES

[1] N.S. Ottosen, R. Stenström, and M. Ristinmaa. Continuum approach to high-cycle fatigue modeling. *International Journal of Fatigue*, 30(6):996–1006, June 2008. URL http://dx.doi.org/10.1016/j.ijfatigue.2007.08.009.

[2] S. Holopainen, R. Kouhia, T. Saksala. Continuum approach for modelling transversely isotropic high-cycle fatigue. *European Journal of Mechanics A/Solids*, 60: 183–195, 2016. URL https://doi.org/10.1016/j.euromechsol/2016.06.007.

30th Nordic Seminar on Computational Mechanics
NSCM-30
J. Høgsberg. N.L. Pedersen (Eds.)
2017

MODELLING OF STRUCTURAL LOADS IN DRAG AUGMENTED SPACE DEBRIS REMOVAL CONCEPTS

ANDERS S. KRISTENSEN[*], JAN A. NIKOLAJSEN[†] AND PETER R. LAURIDSEN[†]

[*] Department of Civil Engineering, Division of Structural and Offshore Engineering
Aalborg University Esbjerg
Niels Bohrs Vej 8, 6700 Esbjerg, Denmark
e-mail: ask@civil.aau.dk,

[†] Department of Civil Engineering, Division of Structural and Offshore Engineering
Aalborg University Esbjerg
Niels Bohrs Vej 8, 6700 Esbjerg, Denmark
e-mail: jan@civil.aau.dk e-mail: prl@civil.aau.dk

Abstract. A Self-deployable Deorbiting Space Structure (SDSS) is used for drag augmented space debris removal. A highly flexible frame allows for a folding of the structure by bifurcation. This research models the structural loads during the deployment and unfolding of the drag sail in Low Earth Orbit (LEO). The Spacecraft travels with 7.8 km/s at deployment. As the drag sail unfolds instantaneously the structure must withstand the loads from the unfolding and the drag. Thermal loads are included in the FEA as the temperature varies from -80°C to +80°C during deorbit. The results are used to verify the structural integrity, reliability and prepare for approval tests prior to launch.

Keywords: Foldable structures, Spacecraft, CubeSat, Dynamic loads, Thermal loads, Applications, Computational Methods, PEEK, Austenitic stainless steel, Aluminum.

1 INTRODUCTION

This paper outlines the mission analysis undertaken in support of the TeSeR (Technology for Self-Removal) project. The TeSeR project is a European Commission funded project (Grant Agreement 687295 – H2020) to provide a standardized PMD (post mission disposal) module for spacecraft. Removal of space debris is becoming a critical issue for continued activities in space as stated by UN mitigation guidelines of Active Debris removal[1,5]. The so-called Kessler effect or syndrome predicts an exponential increase of human made space debris. Thus space debris mitigation will be an important aspect of future spacecraft development. However, the cost factor is of outmost importance for operators of commercial satellites for communication, surveillance, meteorological monitoring, GPS etc. The technology assessed to be the most feasible, for LEO up to 700km, uses drag membranes or drag sails[5], i.e. also called drag augmented debris removal. A design using a highly flexible frame to deploy the drag sail is devised, i.e. a Self-deployable Deorbiting Space Structure (SDSS)[2]. This design, using self-deployable structures for debris removal, is unique and requires multidisciplinary research areas such as non-linear structural analysis, electronic systems, mechanical

engineering, material technology, spacecraft dynamics and satellite mission analysis etc. For example a satellite experiences a wide spectrum of loads occurring during transport, launch, deployment, orbit or mission lifetime and re-entry[7]. For the SDSS principle the de-orbiting is initiated by unfolding a drag sail, i.e. the unfolding sequence is seen in figure 1[3,4].

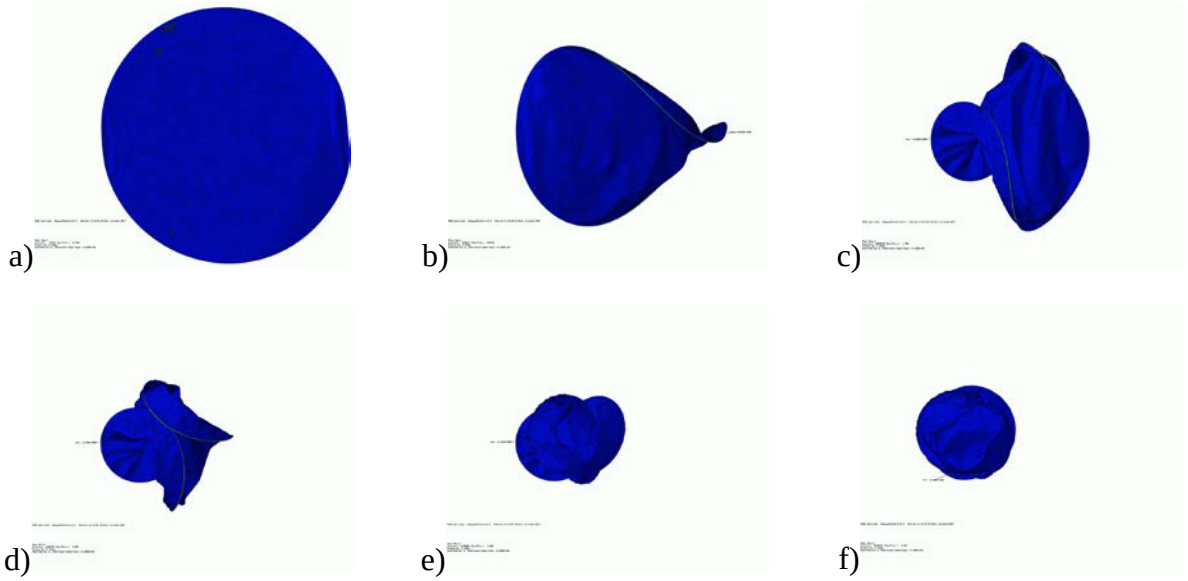

Figure 1: a) - f) folding of the drag sail 3 times. The highly non-linear folding is achieved by activating bifurcations in the flexible frame[3,4]. The flexible frame has a rectangular cross-section.

In the present work structural loads from temperature and the drag pressure is considered in the SDSS deployment phase.

2 THERMAL LOADS

A SDSS module is required to be mounted on CubeSat satellites orbiting in LEO up to 700 km. In these orbits the satellites travels with speeds of about 7.8 km/s. The heat on the exterior surfaces of the spacecraft primarily arises from direct solar radiation. In most cases a CubeSat is orbiting in an angle relatively to the sun, i.e. the solar flux affect maximum 3 faces on the CubeSat the remaining faces being in the shadow absorbing the earths albedo. The worst case scenario is when one side of the CubeSat faces directly the sun. The steady-state analyses conducted are divided into a hot (facing the sun) and cold (during eclipse) load-case, i.e. a temperature ranging from [-80; +80] °C[6]. The generated heat for different subsystems is disregarded in the SDSS deployment phase as deorbit is initiated, i.e. the spacecraft should be passivated. At a 700 km mission altitude a CubeSat orbit about 65 minutes in the sun, and about 35 minutes in the eclipse region for each orbital period.

3 THE SDSS CONFIGURATIONS

Two design configurations are evaluated, i.e. an In-line and a Side-mounted. In figure 2 two SDSS modules are mounted In-line in a CubeSat frame with a sliding release tray[2]. As the In-line SDSS configuration rely on a mechanical guided system and hinged apertures even small distortions can affect the functionality of the deployment mechanism. The main components are designed in Al-6060-T6, PEEK and austenitic stainless steel.

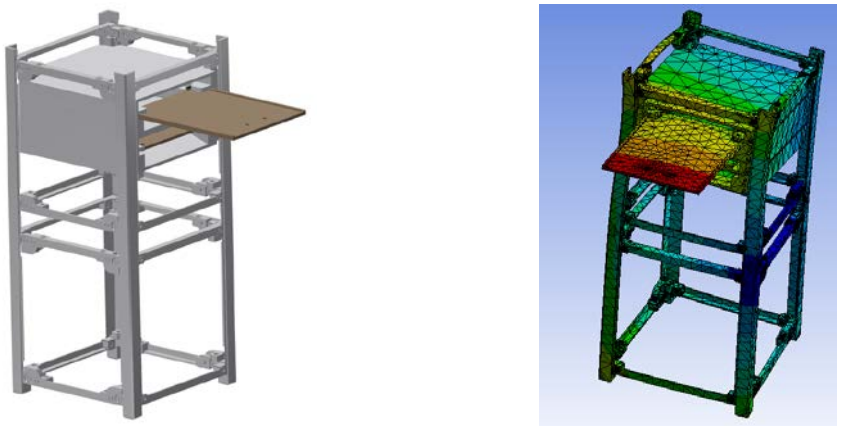

Figure 2: Left – Two SDSS modules placed In-line in the AL-6060-T6 frame. Right – The SDSS model used for thermal analysis.

In order to withstand loads during launch the SDSS module is mounted using pre-tensioned bolts in the Al frame. A thermal FEA is conducted to inspect the resulting distortion of the SDSS module as seen figure 2 (right). The maximum deformations found in mechanical guide are up to 0.3 mm. Although, this load-case is a maximum steady-state thermal load-case this highlight some concerns with the In-line approach. Due to these concerns the Side-mounted SDSS configuration as shown in figure 3 has been preferred in the H2020 TeSeR project[5]. This concept offers increased scalability for larger spacecrafts.

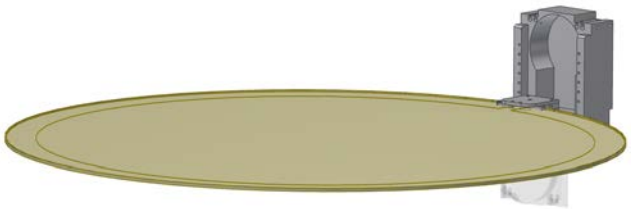

Figure 3: A Side-mounted SDSS module with a deployed sail. The drag sail is stowed in the compartment during mission lifetime and at deployment a protecting cover is removed to allow the release spring to push out the drag sail a initiate the automatic unfolding[3,4].

In the Side-mounted configuration the SDSS modules mechanical functionality is less

sensitive to thermal distortions, i.e. the drag sail is hinged. However, when the SDSS deploys in this configuration, the rotation caused by the torsional release spring in the hinge causes a dynamic response in the clamp and hinge bearing. As the clamp and structure holding the drag sail is designed in PEEK this load-case is inspected. The drag pressure is 0.1 Pa and the drag sail area obtained for one SDSS module adapted for CubeSats is 0.27 m^2. From a FEA analysis with 5523477 dof's a maximum stress level of 15 MPa (using a dynamic amplification factor of 10) is found for the clamp, designed in PEEK, holding the drag sail.

4 CONCLUSION

Two SDSS configurations have been investigated for two basic load-cases, i.e. thermal and drag forces. Either of the load-cases result in critical stress levels, however a basis for establishing continued analysis have been achieved. Having modelled the folding process the next step is to include the thermal loads and drag forces in a transient dynamic simulation however damping may be an issue due to highly non-linear deformations.

REFERENCES

[1] A. S. Kristensen, L. Damkilde, and L. Alminde, "Self-Deployable Deorbiting Space Structure (SDSS)", Proceedings of the 6th European Conference on Space Debris: Darmstadt, Germany, 22–25 April 2013, European Space Agency, ESA, 2013.

[2] Anders S. Kristensen, Martin D. Ulriksen, Lars Damkilde, "Self-Deployable Deorbiting Space Structure for Active Debris Removal", Journal of Spacecraft And Rockets, DOI: 10.2514/1.A33321, 2017.

[3] J. A. Nikolajsen, P. R. Lauridsen, and A. S. Kristensen, "Modelling and analysis of the folding principle used in self-deployable deorbiting space structures", Proceedings of the 7th European Conference on Space Debris: Darmstadt, Germany, 18–21 April 2017, European Space Agency, ESA, 2017.

[4] P. R. Lauridsen, J. A. Nikolajsen, and A. S. Kristensen, "Analysis of pretension and stress stiffening in a self-deployable deorbiting space structure", Proceedings of the 7th European Conference on Space Debris: Darmstadt, Germany, 18–21 April 2017, European Space Agency, ESA, 2017.

[5] "TeSeR – Technology for Self-Removal" Available: http://teserproject.eu/.

[6] M. Gadalla, "Prediction of temperature variation in a rotating spacecraft in space environment." Applied Thermal Engineering, Vol. 25, No. 14-15, 17 Feb. 2005, pp. 2379-2397, 2005.

[7] P. Fortescue, G. Swinerd, and J. Stark, "Spacecraft Systems Engineering", 4th. Chichester, West Sussex: John Wiley & Sons, Ltd, 2011.

30th Nordic Seminar on Computational Mechanics
NSCM-30
J. Høgsberg. N.L. Pedersen (Eds.)
2017

MODELING OF ROBOT DRAPING SEQUENCES WITH PREPREG PLIES

CHRISTIAN KROGH* **AND JOHNNY JAKOBSEN†**

Department of Materials and Production, Aalborg University
Fibigerstraede 16, 9220 Aalborg, Denmark
e-mail: *ck@mp.aau.dk, †joj@mp.aau.dk

Key words: Carbon Fiber Prepreg, Nonlinear Finite Element, Process Simulation.

Summary. The draping of woven prepreg fabric onto a double curved mold is currently done manually but a robot system under development will enable to automate the process. This automation relies on modeling of the fabric during manipulation such that satisfactory layups can be achieved. The present study presents a Virtual Draping Environment (VDE) that can aid in the generation of robot sequences as well as simulate the process off-line as a verification. Amongst other things, the VDE consists of a nonlinear transient Finite Element (FE) model based upon experimental data obtained at different strain rates. The numerical results illustrate that the model can predict the final configuration with the fabric on the mold, but that the robot sequences should be chosen carefully in order to avoid defects such as wrinkles.

1 INTRODUCTION

Woven carbon fiber plies which are pre-impregnated with resin, so-called prepregs, find considerable application in the aerospace industry due to the favorable mechanical properties. In the production process of carbon fiber parts, a substantial number of plies are draped onto a double curved mold prior to curing. This process is manual which not only is costly but also prone to variations in the final product quality. An automatic robot draping system which can handle entire prepreg plies is therefore under development as part of the research project FlexDraper. It features a specially designed tool with an array of actuated grippers for manipulation of the ply. Current automatic solutions are restricted to unidirectional plies[1].

The ideal draped configuration implies that the ply follows the mold surface within tight tolerances and that the fiber angles match prescribed angles. While the ideal end configuration is straightforward to calculate, it is not trivial how to reach it with the robot. That is, the grippers can move in infinitely many ways but some draping sequences will result in wrinkles and air pockets. Such flaws will deteriorate the mechanical properties of the final part and cannot be tolerated. One of the major tasks associated with development of the robot system is thus to generate feasible draping sequences. To this end,

off-line simulation is very convenient during the development process.

The modeling of fabric dates back to 1956 with the kinematic pin-jointed net model proposed by Mack and Taylor[2]. More recently the Finite Element (FE) method has yielded more accurate modeling of reinforcement fabric e.g. for simulating preforming as part of the Resin Transfer Molding (RTM) process. In the work by Peng et al.[3] a hyperelastic material model with test data input was presented. Hamila et al.[4] developed a special purpose finite element for the simulation of woven fabric. Common for all models is, that they must account for the changing fiber angles, i.e. shearing or trellising, which is a result of the transformation from a flat to a double curved mold surface. Experimental characterization is also a well visited field, see e.g. Cao et al.[5].

This study will combine a kinematic mapping algorithm and a nonlinear FE model to investigate robot draping sequences with emphasis on the path taken to the draped configuration.

2 THE VIRTUAL DRAPING ENVIRONMENT

The system under consideration consists of the mold, the ply and the grid of actuated grippers. During draping, the grippers will move the ply down to the mold. In order to generate and assess draping sequences a Virtual Draping Environment (VDE) has been developed, see Fig. 1. It consists of a module that can predict the ideal draped configuration on the mold and generate draping sequences by means of various interpolation schemes. The second module it a nonlinear transient Finite Element (FE) model used to assess the draping sequence by including the physics of the prepreg material. In the following, the mapping algorithm and the transient FE model is elaborated.

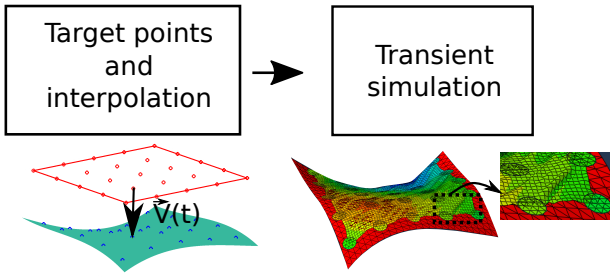

Figure 1: The virtual draping environment.

2.1 Kinematic Mapping Algorithm and Interpolation

The kinematic mapping algorithm[6] assumes that the fibers do not extend while the ply is allowed to shear infinitely. The mapping of the ply from the flat configuration in $\mathbf{R^2}$ onto the mold in $\mathbf{R^3}$ is then uniquely determined by a starting point with known fiber angles. From the mapped ply it is possible to extract target points for the actuated grippers. That is, the points that the grippers should move to in the final configuration.

Next, an interpolation from the gripper points in the initial configuration to the gripper points in the final configuration is carried out. Here, a linear interpolation in time is employed.

2.2 Nonlinear Transient Finite Element Model

The nonlinear transient Finite Element (FE) model is built using Abaqus Explicit and linear shell elements. The mold and the grippers are modeled as rigid with the latter represented by the lower contact surface. The ply is modeled as nonlinear rate-dependent, which is accomplished by the intrinsic phenomenological material model *fabric* which is indeed suitable for fabric material with two initially orthogonal structural directions. While the fibers are stiff in tension, relative fiber motion within the yarns results in a low bending stiffness. In order to capture this phenomenon with shell elements based on lamination theory, the compressive stiffness is lowered effectively causing the Young's modulus to be asymmetric. The material model uses test data as input, i.e. nominal stress and strain for fiber direction 1, direction 2 and for shear. These data are obtained by material characterization at different strain rates, i.e. tensile tests, bias-extension tests and cantilever bending tests. The latter is used to determine the compressive stiffness of the fibers. The grippers are fixed to the ply, such that no slipping is possible. The contact formulation between the mold and the ply uses a Coulomb friction model in the tangential direction with an experimentally determined coefficient of friction equal to 1.5.

3 NUMERICAL RESULTS

The ply is mapped onto the mold and the linear interpolation is done for all 25 grippers. The draping sequence is then simulated using the FE model and the results are depicted in Fig. 2. As is evident from the figure the draped configuration has large diagonal wrinkles

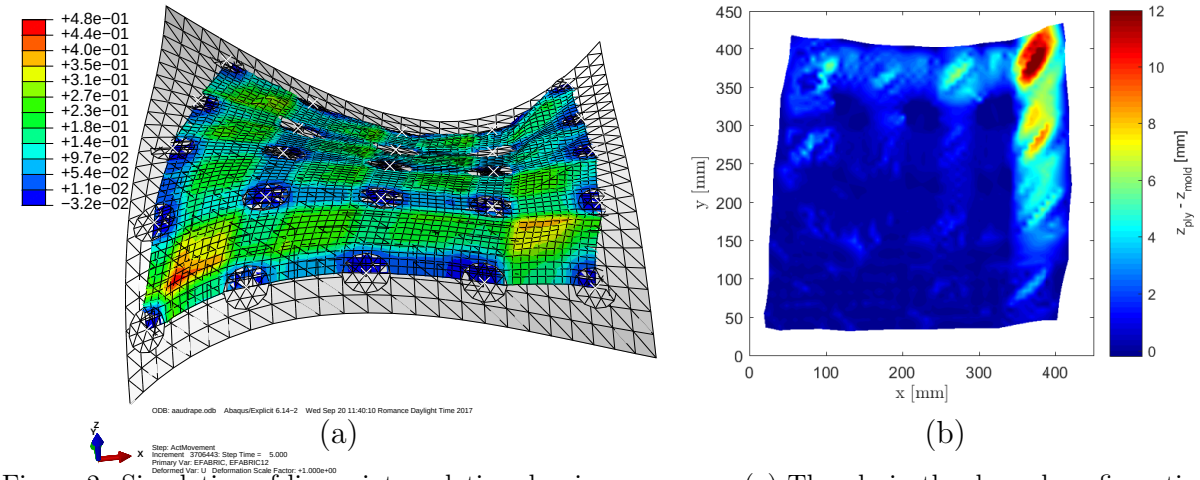

Figure 2: Simulation of linear interpolation draping sequence. (a) The ply in the draped configuration on the mold. Contours: shear strain. (b) The height (z) difference between the ply and the mold.

or shear buckles, mostly in the concave areas. They can in part be attributed to the no-slip condition between the grippers and the ply which over-constrains the material but more importantly to the simple draping sequence employed. So while the model is capable of simulating the process, more work should be put into developing feasible draping sequences.

4 CONCLUSIONS

This study has presented a Virtual Draping Environment (VDE) and demonstrated its applicability in the development of automatic robot draping sequences. The kinematic mapping algorithm can easily predict the ideal draped configuration, but it doesn't include information about how it is reached. This is the reason why the transient Finite Element (FE) model is employed. The simulation with the simple linear interpolation draping sequence predicted wrinkles in the draped configuration. Thus, the conclusion is that feasible draping sequences are path dependent and non-trivial to generate. The problem will be addressed in a future study.

Acknowledgement. This research is part of the project FlexDraper - An Intelligent Robot-Vision System for Draping Fiber Plies sponsored by the Innovation Fund Denmark, Grant no. 5163-00003B. This funding is gratefully acknowledged.

REFERENCES

[1] Lukaszewicz, D., Ward, C. & Potter, K. D. The engineering aspects of automated prepreg layup: History, present and future. *Composites Part B: Engineering* **43**, 997–1009 (2012).

[2] Mack, C. & Taylor, H. M. The Fitting of Woven Cloth to Surfaces. *Journal of the Textile Institute Transactions* **47**, T477–T488 (1956).

[3] Peng, X., Guo, Z., Du, T. & Yu, W. A simple anisotropic hyperelastic constitutive model for textile fabrics with application to forming simulation. *Composites Part B: Engineering* **52**, 275–281 (2013).

[4] Hamila, N., Boisse, P. & Chatel, S. Semi-discrete shell finite elements for textile composite forming simulation. *International Journal of Material Forming* **2**, 169–172 (2009). `1010.1724`.

[5] Cao, J. *et al.* Characterization of mechanical behavior of woven fabrics: Experimental methods and benchmark results. *Composites Part A: Applied Science and Manufacturing* **39**, 1037–1053 (2008).

[6] Van Der Weeën, F. Algorithms for draping fabrics on doubly-curved surfaces. *International Journal for Numerical Methods in Engineering* **31**, 1415–1426 (1991).

30th Nordic Seminar on Computational Mechanics
NSCM-30
J. Høgsberg. N.L. Pedersen (Eds.)
2017

MODELING OF DAMAGE AND CRACK GROWTH IN SEMI-CRYSTALLINE POLYMERS

MARTIN KROON[*] AND ESKIL ANDREASSON[†]

[*] Department of Mechanical engineering
Linnaeus University
Växjö, Sweden
E-mail: martin.kroon@lnu.se

[†] Tetra Pak
Lund, Sweden
Email: Eskil.Andreasson@tetrapak.com

Abstract. Crack growth in semi-crystalline polymers, represented by polyethylene, is considered. The material considered comes in plates that had been created through an injection-molding process. Hence, the material was taken to be orthotropic. Material directions were identified as MD: molding direction, CD: transverse direction, TD: thickness direction. Uniaxial tensile testing was performed in order to establish the direction-specific elastic-plastic behaviour of the polymer. In addition, the fracture mechanics properties of the material was determined by performing fracture mechanics testing on plates with side cracks of different lengths. The fracture mechanics tests were filmed using a video camera. Based on this information, the force vs. load-line displacement could be established for the fracture mechanics tests, in which also the current length of the crack was indicated, since crack growth took place. In parallel to the experimental testing, an anisotropic plasticity model for finite strains was developed, which accounts for orthotropic elasticity and orthotropic plastic yielding and hardening. That plasticity model was implemented as a user subroutine in Abaqus. The crack growth experiments were then simulated using Abaqus, using the implemented plasticity model in combination with a damage model. Different types of crack initiation and growth criteria were explored, and the force-displacement-crack length data from the experiments could be well reproduced. Furthermore, the direction-specific work of fracture had been established from the experiments and these energies could be compared to the values of the J-integral from the simulations for the different crack lengths.

Keywords: constitutive modelling, damage, polymers, crack growth.

30th Nordic Seminar on Computational Mechanics
NSCM-30
J. Høgsberg. N.L. Pedersen (Eds.)
2017

VALIDATION AND MODEL UPDATING OF WELD IN FINITE ELEMENT MODEL OF K-NODE STRUCTURE USING EXPERIMENTAL DATA FOR FATIGUE ANALYSIS

NSCM-30

MIKKEL L. LARSEN[*], VIKAS ARORA[*], MARIE LÜTZEN[*] AND RONNIE R. PEDERSEN[†]

[*] Department of Technology and Innovation (ITI)
University of Southern Denmark
Campusvej 55, 5230 Odense, Denmark
E-mail: milar11@student.sdu.dk, web page: http://www.sdu.dk

[†] Ramboll Offshore Wind
Bavnehøjvej 5, 6700 Esbjerg, Denmark
E-mail: rrp@ramboll.com, web page: http://www.ramboll.com/energy

Key words: Finite element analysis, finite element validation, model updating, tubular joint, K-node.

1 INTRODUCTION

Offshore jacket structures are in risk of fatigue damage due to cyclic loading of e.g. wind and waves. The welded joints between the braces and chords are especially prone to fatigue damage. This is due to the weld geometry itself, giving rise to stress concentrations at the weld toes but also as any possible weld defects likewise will lead to stress concentrations[1].

As the stresses and strains around tubular joints are complex and difficult to estimate, it has become more and more convenient to use finite element analysis when analysing such tubular joints[2]. Depending on the stress estimation method used and geometry of the problem, the welds can be included or excluded in the FE models[3]. Difficulty, however, arises when the welds should be included in the FE models. Many different weld modelling techniques for FE modelling have been proposed, including welds modelled with shell elements and solid elements, depending on mesh element type, local bending, loading, gap size, etc[2,3,4]., thus no unique method to model the welded joint are present.

In this paper, a finite element model of a K-node have been developed based on a full-scale K-node, manufactured for fatigue testing as part of an EUDP supported project by Siemens Wind Power, FORCE Technology and Bladt Industries. As difficulty often arises when modelling the weld, this paper proposes a simple modelling technique using a simple fillet blend between the chord and brace surfaces in the FE model. The experimental strain gauge

results from the fatigue testing of the K-node are compared to the FE model to study the accuracy of the weld model. Furthermore, the weld model using a simple blend is compared to the weld model proposed in the DNV-GL-C203[4].

Another difficulty when using finite element analysis to predict the stresses and strains in any construction is that the predictions often are not consistent with actual tests[5]. The difference between test results and the FE analysis can be due to incorrect modelling of e.g. boundary conditions, joints, material properties and geometry. To reduce these errors in the analytical FE model, model updating techniques can be used. As the welds in the finite element model, is difficult to model using a simple fillet blend function so that it resembles the actual weld geometry, parameter based finite element model updating of the fillet blend parameters are performed.

The results showed that the simple fillet weld geometry were less accurate than the weld model suggested by DNV-GL-C203. A model update of the simple weld were made to increase the accuracy of the results, which resulted in the simple weld geometry being as accurate as the more complex weld geometry from the DNV.

2 METHODOLOGY

To test the simple weld modelling technique two finite element models of the tested K-node were developed, using the commercial FE software *ANSYS Workbench*. The FE models were modelled linear. In one model the proposed simple weld geometry using a fillet blend with variable radius at the heel and toe locations at the brace-chord joint was used, and in the other model the weld modelling technique proposed in the DNV-GL-C203 was used. Both modelled welds, were modelled with solid elements and are shown in Figure 1.

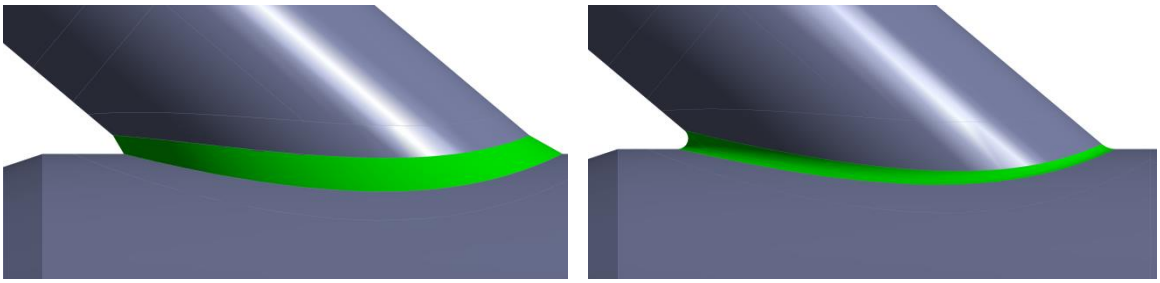

Figure 1: Welds used in FE models

The manufactured K-node was loaded axially and with in-plane bending at the braces, in order to test the fatigue performance of the weld at the heel and toe points around the brace-chord joint. To record the strains multiple strain gauges were attached, mainly at the targeted points. These gauges were fitted based on the recommendations for capturing hot-spot strains,

from the IIW (International Institute of Welding)[3]. Global strain gauges were likewise fitted, to capture the strains far from the weld at the braces. All loads were in sync, thus the maximum and minimum loading occurred simultaneously.

The FE model was loaded similar to the actual tested K-node and the strain predictions from the analysis were extracted at the locations corresponding to the strain gauges on the real K-node. The results were hereafter compared in order to test the accuracy of the weld modelling techniques.

3 RESULTS

The experimental results from the fatigue testing have been compared to the two FE models using the simplified weld geometry and the weld geometry proposed by the DNV-GL-C203, respectively. The strains, captured by strain gauges in the experiments, have been compared to the strains at the same locations from the finite element models. The normalised experimental strains are plotted together with the normalised finite element strains from both weld models in Figure 2, corresponding to the strains recorded at the maximum load from one fatigue load cycle. Discrepancies were observed between the results from the FE model using the simplified fillet blend weld and the actual test results. In order to improve the results a parameter based model update were performed on the input parameters of the simple weld. The updated results are also shown in Figure 2.

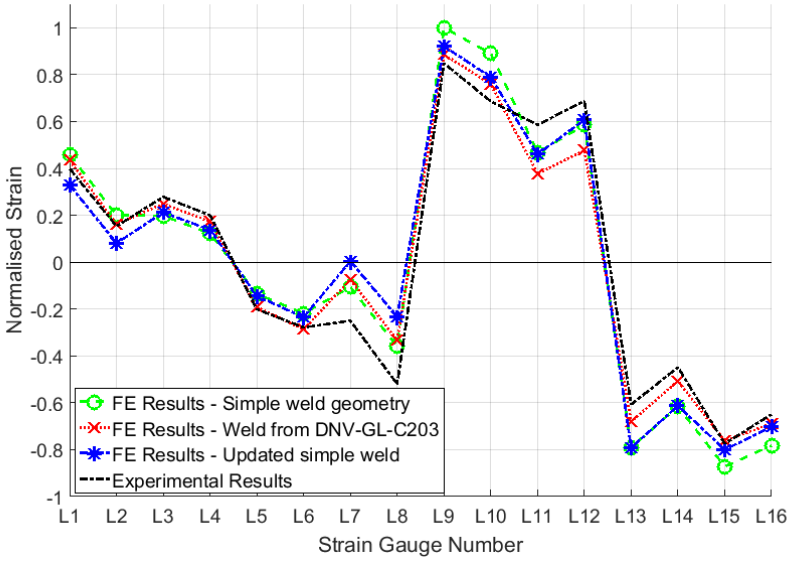

Figure 2: Comparison of strains between experiment results and finite element predictions

In order to better compare the results the average errors have been calculated as the root-mean-square-error and are given in Table 1.

Model	Weld from DNV-GL-C203	Updated Simple Weld Geometry
RMSE	0.10	0.13

Table 1: RMS-error between finite element predictions and experimental strain gauge results

It can be observed from Figure 2, that the updated finite element model is able to predict the strains at the maximum load. It can also be observed from Figure 2 and Table 1, that the updated weld model is comparable to the complex DNV-GL-C203.

3 CONCLUSIONS

In this paper, fatigue experiments have been performed on a full-scale K-node to obtain experimental strain results. A finite element model has been developed based on the full-scale K-node in order to validate a simple weld modelling technique. Some discrepancies have been observed between the experimental strain results and the finite element predications. To decrease these discrepancies a parametric finite element model updating method has been applied. The updated finite element model, using a simplified weld geometry have been compared to the more complex weld geometry from the DNV-GL-C203. The results shows that the simple fillet blend weld is as accurate as the complex weld from the DNV.

In the future, the updated K-node finite element model will be used for fatigue analysis, with the purpose of estimating the fatigue life of the welded K-node.

REFERENCES

[1] P.H. Wirshing. “Fatigue reliability for offshore structures”, *J. Struct. Eng.*, **110(10)**, 2340-56 (1984).

[2] M.K. Lee. “Strenght, stress and fracture analysus of offshore tubular joints using finite elements”,*JCSR*, **51(3)**, 265-86 (1999).

[3] A.F. Hobbacher. “Recommendations for fatigue design of welded joints and components”, *Springer* (2016).

[4] DNV GL. *“DNV-GL-C203: Fatigue design of offshore steel structures”*, (2016).

[5] M.K. Lee. “Strength, stress and fracture analysis of offshore tubular joints using finite elements”, *JCSR*, **51(3)**, 265-86 (1999).

[5] V. Arora. “Comparative study of finite element model updating methods”,*J. Viv. Contro.*, **17(13)**, 2023-39 (2011).

30th Nordic Seminar on Computational Mechanics
NSCM-30
J. Høgsberg. N.L. Pedersen (Eds.)
2017

MOLECULAR DYNAMIC AND CONTINUUM MODELINGS OF NANOPORE GROWTH IN COPPER AT HIGH-RATE TENSION

F.T. LATYPOV, V.S. KRASNIKOV AND A.E. MAYER,

Chelyabinsk State University (CSU)
Bratiev Kashirinykh Street 129, 454001 Chelyabinsk, Russia
email: latypovfanil@gmail.com, web page: http://www.csu.ru

Abstract. Destruction of metals occurs by two mechanisms: the ductile fracture realized by means of the nucleation, growth and coalescence of voids and the brittle fracture realized by means of the formation and growth of cracks as a dominant process[1]. Attention to the plastic deformation near the voids and cracks is due to the assumption of the dislocation stimulated growth of them[2]. A two-level model of the dislocation-stimulated growth of nanopores in aluminum was proposed earlier[3] in order to predict the critical pressure of fracture and to use the obtained void growth equation within the fracture models. The growth of nanopores was connected with the plastic deformation in the region close to the pore leading to the atoms rearrangement on the pore surface. Molecular dynamic simulations were used to verify the proposed continuum model and to fit their parameters. Here we continue this work and apply the proposed model[3] to the case of copper. In the presentation, the results of molecular dynamic simulations in comparison with the continuum model are presented. This research work is supported by the Ministry of Education and Science of the Russian Federation (Project 3.2510.2017/PP).

Keywords: Dislocation, Fracture, Nanovoids, High-rate deformation.

REFERENCES

[1] B. Dodd and Y. Bai, “Ductile fracture and ductility”, *Academic Press, New York,* (1987).

[2] F. Fischer and T. Antretter, ” Deformation, stress state and thermodynamic force for a growing void in an elastic–plastic material”, *International Journal of Plasticity,* **25**, 1819–1832, (2009).

[3] V.S. Krasnikov and A.E. Mayer, “Plasticity driven growth of nanovoids and strength of aluminum at high rate tension: Molecular dynamics simulations and continuum modeling”, *International Journal of Plasticity*, **17**, 75–91, (2015).

30th Nordic Seminar on Computational Mechanics
NSCM-30
J. Høgsberg. N.L. Pedersen (Eds.)
2017

NON-LINEAR STRUCTURAL ANALYSIS OF THE FOLDING PROCESS IN A DEPLOYABLE SYSTEM FOR SATELLITES

PETER R. LAURIDSEN, JAN A. NIKOLAJSEN AND ANDERS S. KRISTENSEN

Aalborg University
Department of Civil Engineering
Niels Bohrs Vej 8, Esbjerg, Denmark
e-mail: prl@civil.aau.dk, web page: http://www.esbjerg.aau.dk

Keywords: Space Debris, Deployable Systems, Non-Linear Geometric Effects, FEA, Slenderness, Structural Analysis.

1 INTRODUCTION

Structural analysis of a sail solution[1] to deorbit satellites is presented in this paper. The deployable drag sail consists of a circular highly flexible frame, sail and housing. The folding process of the highly flexible frame is complex and is only possible to describe analytical[2] without a sail attached to the highly flexible frame. FEA has shown a significant difference in the structural behavior with a sail attached to the highly flexible frame and this paper will present these results. Stresses, moment reactions and kinematics are compared in two system (e.g. with and without a drag sail attached to the highly flexible frame). Simulation of folding a drag sail can be challenging due to the instability and slenderness of the structure.

2 METHOD

A circular highly flexible frame is discretized with shell elements[3] and a rectangular cross section is used. The highly flexible frame is made of austenitic stainless steel due to the hostile space environment (e.g. ultra violet radiation)[4]. In one of the two models are beam elements used to constraint the highly flexible frame in the positive x-direction. The cross sectional area of the beam elements are 1 mm^2 . The beam elements represent the effect of a sail attached to the highly flexible frame and the two models are shown in Figure 1A and 1B. A ratio of $b/h \leq 1.52$ results in only one buckling load[2] in the simulation. However is the simulation still displacement driven due to this challenge of the buckling load. Dimensions and material properties are shown in Table 1.

Diameter	4,000 mm
Width of cross section	10 mm
Height of cross section	3 mm
Young's modulus	2e5 MPa

Table 1: Dimensions and material properties of the highly flexible frame.

In the FEA is energy stabilization used due to instability and slenderness of the structure. When the highly flexible frame is twisted is the diameter reduced 9 times and the area reduced 81 times compared to the original size of the structure. In Figure 1B it is easily seen that the highly flexible frame is constrained in the positive x-direction.

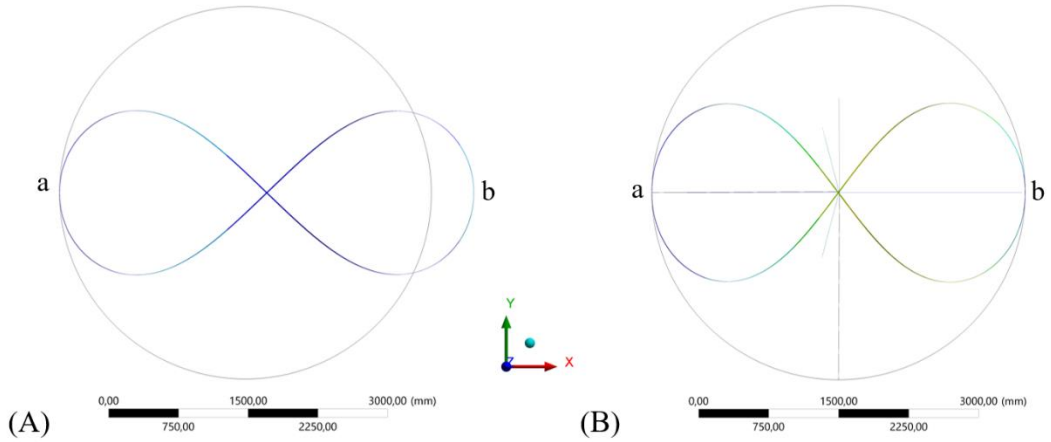

Figure 1: A. Illustrates the deformation of the highly flexible frame without a sail attached. B. Shows the highly flexible frame with a sail attached (beam elements). (ROTX = π, the undeformed shape is also shown in the figures).

In Table 2 is it described how the highly flexible frame is constraint. During the folding process is point b applied from 0 to 2π rotation around the x-axis. In point a and point b are all rotations constrained and the reason is to ensure convergence in the structural analysis.

DOF	Point a	Point b
UX	0	free
UY	0	0
UZ	0	0
ROTX	0	$0 \rightarrow 2\pi$
ROTY	0	0
ROTZ	0	0

Table 2: Shows how the highly flexible frame is constrained in point a and b.

3 RESULTS

In both simulations are the force reactions $\approx 0\ N$ and the reason is the symmetry and that only rotation is applied the highly flexible frame. There is a difference in the structural behavior when the moment reactions are compared in the two analyses. In Figure 2 is it shown how the moment reaction varies during the folding process and there is a slightly difference. Comparing peak values in Figure 2 shows that the moment reaction is 6 % higher in the simulation with a sail attached to the highly elastic frame. The maximum moment reaction peaks with 9.3 Nm in the highly flexible frame with sail attached. However the moment reaction is almost similar in last part of the folding process where the sail is loose. The moment of inertia in the beam elements are inconsiderable and these will easily buckle in the structural analyses.

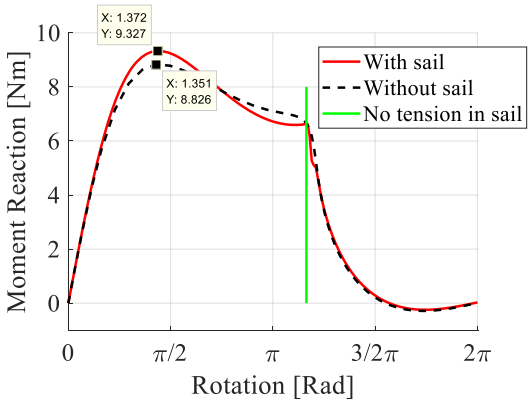

Figure 2: Illustrates how the moment reaction varies during the folding process of the SDSS with and without a sail attached to the highly flexible frame.

In the folding process is the highly elastic frame exposed to high stress levels and these stresses will be evaluated. In Figure 3 are the maximum principal stresses compared in the two analyses and there is a difference during the folding process. In Figure 3 is it easily seen that the maximum principal stresses are almost similar when the rotation is between 0 and $\pi/4$. When the rotation is between $\pi/4$ and $5\pi/4$ is there a significant difference in the maximum principal stresses and the stresses are lowest in the highly flexible frame with a sail attached. In the last part of the rotation where the highly flexible frame rotates between $5\pi/4$ and 2π are the maximum principal stresses again comparable. In this part of the rotation are the stresses also peaking and stresses are decreasing when the rotation is conducted. The location of the maximum principal stress is varying during the folding process.

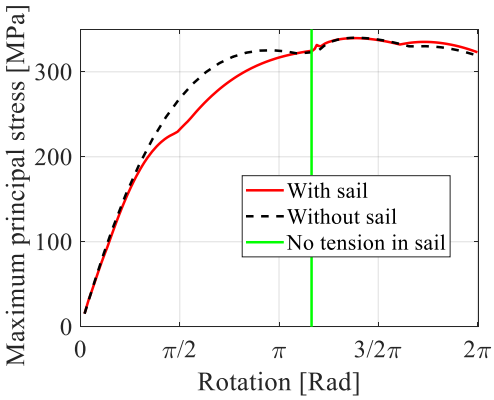

Figure 3: Illustrates how the maximum principal stresses varies during the folding process of the highly flexible frame with and without a sail attached.

Twisting a highly flexible frame with this method results in pure shear stresses in some parts of the folding process. When then highly flexible frame is folded is it exposed to pure bending stresses. This is not a problem when material is isotropic, however this must be taken into consideration if an orthotropic material is used.

4 CONCLUSIONS

The results shows that a sail attached to the highly flexible has an influence on the structural behavior when folding the structure. From the peaks in moment reactions, it can be concluded that the higher reaction moment in the highly elastic frame has no influence on a higher stress level. The kinematics are influenced when a sail is attached to the highly elastic frame however has it minor influence on the stress level during the folding.
The maximum principal stresses are almost similar in the two simulations and attaching a sail to the highly flexible frame is actually an advantage due to the lower or equivalent stress level in the folding process. Peak values are similar in the two systems and this is useful knowledge to have when the drag solution is developed.

REFERENCES

[1] A. S. Kristensen, L. Damkilde, and L. Alminde, “SELF-DEPLOYABLE DEORBITING SPACE STRUCTURE (SDSS),” WO/2012/092933, 2014.
[2] P. F. Pai, *Highly Flexible Structures: Modeling, Computation, and Experimentation*. Reston ,VA: American Institute of Aeronautics and Astronautics, 2007.
[3] ANSYS, *ANSYS, Inc. Theory Reference, Release 9.0*, no. November. ANSYS, 2004.
[4] J. I. Kleiman and R. C. Tennyson, Eds., *Protection of Space Materials from the Space Environment*, vol. 4. Dordrecht: Springer Netherlands, 2001.

30th Nordic Seminar on Computational Mechanics
NSCM-30
J. Høgsberg. N.L. Pedersen (Eds.)
2017

SIMULATION OF CYLINDRICAL SHELL COLLAPSE WITH CONSIDERING PLASTICITY AND FRACTURE OF METALS

M. V. LEKANOV, A. E. MAYER

Chelyabinsk State University (CSU),
Bratiev Kashirinykh Street 129, 454001 Chelyabinsk, Russia
email: lemih1989@gmail.com, web page: http://www.csu.ru

Abstract. Experiments on collapse of cylindrical metal shells[1] are used for researching the deformation behavior of metals in the conditions of energy accumulation in the converging shock waves. Important experimental data has been accumulated currently including the results of metallographic researches[1]. The simulation of this process is basically carried out in the hydrodynamic approximation or with using the simplest models of the plastic behavior of metals. More realistic models include a specification of the dynamics of dislocations and twins, and voids formation process in the material. In the present work, we perform modeling of the collapse of the cylindrical aluminum shells. Equations of continuum mechanics are solved numerically in the one-dimensional cylindrical formulation with using the numerical method[2]; behavior of material is described by using the of dislocation plasticity model[3] and fracture model[4,5]. This research work is supported by the Ministry of Education and Science of the Russian Federation (Project 3.2510.2017/PP).

Keywords: High-rate deformation, Plasticity, Fracture, Dislocations, Voids

REFERENCES

[1] V.I. Zel'dovich and N.Y. Frolova and A.E. Kheifets and S.M. Dolgikh and K.V. Gaan and E.V. Shorokhov, "Deformation and Temperature Related Processes that Occur upon the Collapse of a Thick Cylindrical Shell Made of Steel", *Physics of Metals and Metallography*, **116**, 285–292, (2005).

[2] M.L. Wilkins, "Calculation of elastic-plastic flow", *Methods in Computational Physics*, **3**, 211–263, (1964).

[3] V.S. Krasnikov and A.E. Mayer and A.P. Yalovets, "Dislocation based high-rate plasticity model and its application to plate-impact and ultra short electron irradiation simulations", *International Journal of Plasticity*, **27**, 1294–1307, (2011).

[4] V.S. Krasnikov and A.E. Mayer, "Plasticity driven growth of nanovoids and strength of aluminum at high rate tension: Molecular dynamics simulations and continuum modeling", *International Journal of Plasticity*, **74**, 75–91, (2015).

[5] A.E. Mayer, "Continuum model of tensile fracture of pure aluminum and D16 alloy and its application to the shock wave problems", *Journal of Physics: Conference Series*, **774**, 012061, (2016).

30th Nordic Seminar on Computational Mechanics
NSCM-30
J. Høgsberg. N.L. Pedersen (Eds.)
2017

TRAIN-INDUCED GROUND VIBRATIONS: ANALYSIS IN A MOVING FRAME OF REFERENCE

J. MALMBORG[*], K. PERSSON[*], P. PERSSON[*]

[*] Department of Construction Sciences
Lund University
221 00, Lund, Sweden
e-mail: jens.malmborg@construction.lth.se, web page: http://www.byggvetenskaper.lth.se/english/

Key words: Ground vibrations, Railway, Train, Moving frame.

1 INTRODUCTION

Many cities experience urban densification due to an increasing population. In these cities, previously undeveloped land close to railways are being used for new residential and office buildings. The infrastructural demand will also increase, resulting in heavily trafficked roads and railways close to where people work and live. Annoyance from traffic-induced vibrations and noise is expected to be a growing issue. To predict the level of ground-borne vibration and noise in buildings caused by railway traffic, models are needed to estimate the load from the vibration source, the vibration transmission through the ground and finally the response of the building structure.

A problem that arises in modeling and analysis of moving loads in a fixed frame of reference, is that the computational domain must be very large, for the moving load to stay within the computational domain during the time of the analysis. To avoid this problem, models can be established in a frame of reference following the moving load. Here, two such models are implemented to study the interaction forces between the rail and the wheels, and the ground-borne vibrations, respectively. The first model is a three-layer railway track model on an elastic foundation, the other model being a three-dimensional (3D) solid finite element model.

2 TRAIN-TRACK MODEL

To analyze the effect of a train passage on the ground vibrations, one of the difficulties is that of describing the load. The excitation caused by a moving train is often divided into a quasi-static and a dynamic part. The quasi-static part is simply the static deflection due to the weight of the train. The dynamic part is much more complex and involves several different phenomena that are either periodic or random in nature, such as wheel flats, wheel/rail roughness and varying sleeper/subgrade stiffness[1]. For low speeds, track unevenness is generally considered the main contributing factor to the dynamic excitation of the ground. In the sub-section below, a method to estimate the dynamic interaction forces between the rail and the wheels due to track unevenness, is described.

2.1 Three-layer track model in a moving frame of reference

Train-track analyses are often performed in using two-dimensional models. A train cart is commonly modeled with masses, springs, dashpots and rigid connections, such as the 10 degree of freedom model shown in Figure 1. The element coefficients can be adjusted to fit many different train types[2]. The track and subsoil is then modeled with varying level of detail, the simplest representation being a Winkler beam, i.e. a beam representing the rail, continuously supported along its length by springs.

Lei et al[3] presented a three-layer beam model of a slab track formulated in a moving frame of reference. The three layers (beams) represent the rail, the concrete slab, and the hydraulically bonded layer, which are continuously connected through springs and dashpots representing railpads, cement-asphalt (CA) mortar and subgrade, respectively, see Figure 1. The derivation of such a three-layer finite element is shown in detail in reference[3].

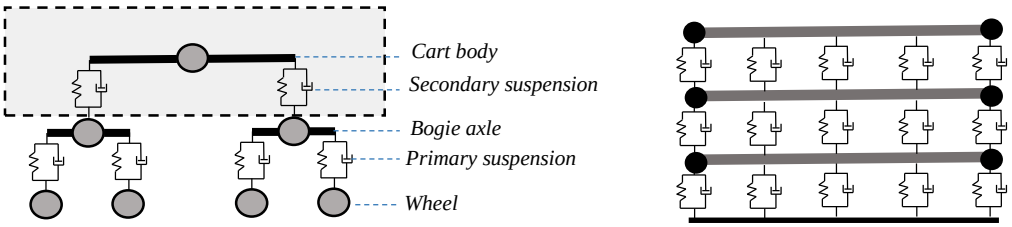

Figure 1: Left: Simple representation of train cart. Right: Three-layer track element

In the present study, the three-layer track element has been implemented in MATLAB to estimate the wheel-rail interaction forces due to track irregularities. Track irregularities are regularly measured using special measuring carts. The measured unevenness is then characterized in a statistical sense by decomposing the irregularities into power (variance) at different wavenumbers by means of a power-spectral-density (PSD). A synthetic unevenness curve that has the same statistical properties as the original measured curve, can be generated from the PSD and used in a spatial/time domain analysis. However, using the track model formulated in a moving frame, the interaction forces can be established efficiently in the frequency domain as described below.

The train model is connected to the track elements by means of constraints. A steady-state analysis is performed for a range of frequencies, where each wheel is separately subjected to a unit harmonic irregularity. The constraint forces between the rail and all four wheels are determined, i.e. a frequency response function matrix $\mathbf{H}(f)$ is obtained. From the PSD describing the rail irregularity $R_{\tilde{x}}(k)$, where k is the wave-number, a PSD of the time-dependent rail profile can be obtained[4] for a specific speed v as $R_x(f) = v^{-1}R_{\tilde{x}}(f/v)$. The PSD function of the response, i.e. constraint forces between the rail and the wheels due to the rail irregularities, is then computed according to theory of random response for multiple input/output systems[5] as $\mathbf{S}_{\mathrm{r}}(f) = \mathbf{H}^*(f)\mathbf{S}_{\mathrm{e}}(f)\mathbf{H}^T(f)$, where $\mathbf{H}^*(f)$ denotes the complex conjugate of $\mathbf{H}(f)$. $\mathbf{S}_{\mathrm{e}}(f)$ is an excitation spectral matrix containing the PSD of the time-dependent rail profile, $R_x(f)$, on the main diagonal since all wheels are subjected to the same

irregularities. The off-diagonal terms are cross spectral density functions obtained by again observing that all wheels are subjected to the same irregularities, but with different time delays.

3 THREE-DIMENSIONAL SOLID MODEL

The 2D model described in the previous section can be used to efficiently estimate the effect of different train and track parameters on the interaction forces. To determine the vibration levels on the ground surface due to these interaction forces, a model that includes both the track and the surrounding soil is needed. Such a model can be established by means of 3D solid finite elements in a moving frame of reference.

The starting point for the finite element formulation of a 3D continuum is the Navier equations (1). Assuming that the load moves at a constant velocity v_i a Galilean transformation from a fixed Cartesian coordinate system x_i to a co-directional coordinate system $\tilde{x}_i$ following the load, is given by (2), which leads to the convective Navier equations (3).

$$(\lambda+\mu)\frac{\partial^2 u_j}{\partial x_i \partial x_j}+\mu\frac{\partial^2 u_i}{\partial x_j \partial x_j}=\rho\frac{\partial^2 u_i}{\partial t^2} \tag{1}$$

$$\tilde{x}_i = x_i - v_i(t-\tau) \tag{2}$$

$$(\lambda+\mu)\frac{\partial^2 \tilde{u}_j}{\partial \tilde{x}_i \partial \tilde{x}_j}+\mu\frac{\partial^2 \tilde{u}_i}{\partial \tilde{x}_j \partial \tilde{x}_j}+\rho\tilde{b}_i=\rho\left(\frac{\partial^2}{\partial t^2}-2v_j\frac{\partial^2}{\partial \tilde{x}_j \partial t}+v_j v_k\frac{\partial^2}{\partial \tilde{x}_j \partial \tilde{x}_k}\right)\tilde{u}_i \tag{3}$$

Multiplication by an arbitrary weight function and integration over a volume, leads to the weak formulation. Adopting Galerkins method, i.e. choosing the element shape functions $\mathbf{N}(\tilde{\mathbf{x}})$ as weight functions, the finite element matrices are obtained.

In the present study a quadratic isoparametric brick element with 20 nodes is implemented based on equations (1)-(3). In dynamic problems involving infinite domains such as soil, special care has to be taken at the boundaries of the finite element model to avoid reflection of waves back into the computational domain. In this study so called impedance boundary conditions are implemented. Impedance boundary conditions generate a traction at the boundary, proportional to the nodal velocities at the boundary. The idea is to, for each point at the boundary, mimic the stress state in an infinite domain due to planar P- and S-waves coming from a distant source. Impedance boundary conditions are completely silent for P- and S-waves impinging on the boundary in a specific pre-defined direction, but for other angles of incidence and other wave types such as the Rayleigh surface waves, partial reflection occurs. However, with fairly high damping in the soil and with the boundaries located sufficiently far away from the region of interest, the reflected energy is generally small.

For a non-moving source, both the P- and the S-wave will arrive at the boundary with the same angle of incidence. However, this is not the case for moving sources, due to the different phase velocities of P- and S-waves. Andersen et al[6] derived impedance boundary conditions for a moving frame of reference, which are implemented in the present study. Again, the idea is to describe the stress state in an infinite media due to planar P- and S-waves, as a function of the particle velocities, but now the P- and the S-waves impinge with different angles.

Figure 2 shows a symmetry model of a railway embankment and the surrounding soil,

established in a frame of reference moving with a speed of 30 m/s, subjected to a harmonic load at 20 Hz acting on top of the embankment. The Doppler effect is clearly visible, as the wavelengths are shorter in front (to the left) of the load than behind the load.

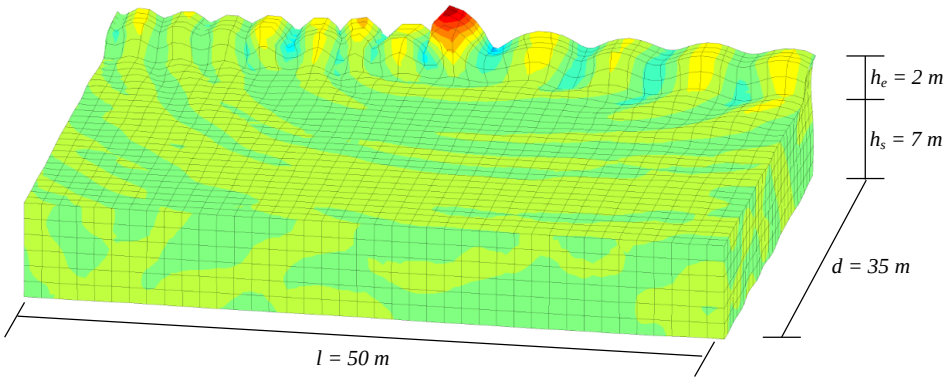

Figure 2: Displacements of a railway embankment and surrounding soil in a frame of reference moving at a speed of 30 m/s subjected to a harmonic load at 20 Hz.

4 ONGOING WORK

The ongoing work involves implementing shell elements in a moving frame of reference that can be placed together with beam elements on top of the embankment of the 3D model in Figure 2, to represent the slab track. Following the methodology described in Section 2.1, PSD of the free-field vibrations may then be obtained.

The research was carried out in the framework of the project “Urban Tranquility” under the Interreg V programme. The authors of this work gratefully acknowledge the European Regional Development Fund for the financial support.

REFERENCES

[1] G. Lombaert, G. Degrande, S. François, D.J. Thompson, “Ground-Borne Vibration due to Railway Traffic: A Review of Excitation Mechanisms, Prediction Methods and Mitigation Measures”, *Proceedings of the 11th International Workshop on Railway Noise, Uddevalla, Sweden* (2013).

[2] D. Cantero, T. Arvidsson, E. Obrien, R. Karoumi, “Train–track–bridge modelling and review of parameters*”, Structure and Infrastructure Engineering*, 12:(9), 1051-1064, (2016).

[3] X. Lei, J. Wang, “Dynamic analysis of the train and slab track coupling system with finite elements in a moving frame of reference”, *Journal of Vibration and Control*, Vol. 20(9), 1301-1317, (2014).

[4] G. Lindgren, H. Rootzén, M. Sandsten, *Stationary stochastic processes for scientists and engineers*, CRC Press, (2014).

[5] K. Shin, J.K. Hammond, *Fundamentals of signal processing for sound and vibration engineeers*, Wiley, (2008).

[6] L. Andersen, S.R.K. Nielsen, S. Krenk, “Numerical methods for analysis of structure and ground vibration from moving loads”, *Computers and Structures* 85(1–2), (2007).

30th Nordic Seminar on Computational Mechanics
NSCM-30
J. Høgsberg. N.L. Pedersen (Eds.)
2017

LINKING SCALES IN PLASTIC DEFORMATION AND FRACTURE

EMILIO MARTÍNEZ-PAÑEDA*, CHRISTIAN F. NIORDSON*, VIKRAM S. DESHPANDE† AND NORMAN A. FLECK†

*Department of Mechanical Engineering
Technical University of Denmark
2800 Kgs. Lyngby, Denmark
e-mail: mail@empaneda.com - Web page: http://www.empaneda.com

†Department of Engineering
Cambridge University
Trumpington St., Cambridge CB2 1PZ, UK

Abstract. We investigate crack growth initiation and subsequent resistance in metallic materials by means of an implicit multi-scale approach. Strain gradient plasticity is employed to model the mechanical response of the solid so as to incorporate the role of geometrically necessary dislocations (GNDs) and accurately capture plasticity at the small scales involved in crack tip deformation. The response ahead of the crack is described by means of a traction-separation law, which is characterized by the cohesive strength and the fracture energy. Results reveal that large gradients of plastic strain accumulate in the vicinity of the crack, elevating the dislocation density and the local stress[1]. This stress elevation enhances crack propagation and significantly lowers the steady state fracture toughness with respect to conventional plasticity[2]. Important insight is gained into fracture phenomena that cannot be explained on the grounds of classic continuum theories. Namely, we show that strain gradient plasticity provides a rational basis for cleavage fracture in the presence of significant plastic flow, with the lattice cohesive strength being attained with meaningful values of the fracture energy and the length scale parameter. In addition, the investigation of short cracks in hydrogen-embrittled steels accounting for the GND-effect shows that failure takes place at low ductility levels, in agreement with experimental observations.

Keywords: Fracture, Cohesive zone model, Strain gradient plasticity, Cleavage.

REFERENCES

[1] E. Martínez-Pañeda and C.F. Niordson. On fracture in finite strain gradient plasticity. *Int. J. Plast.*, **80**, 154–167, (2016).

[2] E. Martínez-Pañeda, V.S. Deshpande, C.F. Niordson, and N.A. Fleck. Crack growth resistance in metals (submitted)

30th Nordic Seminar on Computational Mechanics
NSCM-30
J. Høgsberg. N.L. Pedersen (Eds.)
2017

TWO-LEVEL INVESTIGATION OF DYNAMIC PLASTICITY AND FRACTURE OF MAGNESIUM

ALEXANDER E. MAYER*, VICTOR V. POGORELKO AND VASILIY S. KRASNIKOV

* Department of Physics
Chelyabinsk State University (CSU)
Bratiev Kashirinykh 129, 454001, Chelyabinsk, Russia
e-mail: mayer@csu.ru, web page: http://www.csu.ru

Abstract. Magnesium and magnesium alloys attract increasing attention as lightweight structural materials with high specific strength. Appropriate models of plasticity and fracture of such materials are necessary tools for prediction of their behavior in mechanical computations. Among others, structural models considering evolution of structural defects (dislocations, voids) have obvious advantages in possibility to take into account the initial microstructure and to be valid in a substantially wide range of loading parameters including dynamical regimes with high strain rates. The disadvantage of these models consisting in higher number of parameters can be partially compensated by application of atomistic simulation for their determination as these parameters typically have clear physical meaning.

Earlier we developed structural models of plasticity and fracture of several metals using two-level approach. Here we present their modification for the case of magnesium single crystals. The plasticity model is developed to take into account the crystal anisotropy and the finite deformations. Thermodynamic consistency of the model is discussed. On the atomic level, the molecular dynamic (MD) simulations are used to determine the dislocation motion equation and corresponding parameters, as well as the temperature and pressure dependences of the elastic modules. The obtained data are used on the continuum level to close the plasticity model. The fracture model is developed to take into account the anisotropy of magnesium single crystal; it is also based on MD simulations. The models are verified by comparison with the literature experimental data for the high velocity plate impact.

This work is supported by the grant from the President of the Russian Federation (Project No. MD-7481.2016.1) and by the grant from the Ministry of Education and Science of the Russian Federation (Project 3.2510.2017/PP).

Keywords: Dynamic Plasticity, Dynamic Fracture, Continuum Models, Molecular Dynamics, Magnesium.

30th Nordic Seminar on Computational Mechanics
NSCM-30
J. Høgsberg. N.L. Pedersen (Eds.)
2017

PLASTIC DEFORMATION OF NANOPOROUS ALUMINUM AT COMPRESSION AND TENSION

POLINA N. MAYER AND ALEXANDER E. MAYER

Department of Physics
Chelyabinsk State University (CSU)
Bratiev Kashirinykh 129, 454001, Chelyabinsk, Russia
e-mail: polina.nik@mail.ru, web page: http://www.csu.ru

Key words: Porous Aluminum, High Strain Rates, Molecular Dynamics, Continuum Model.

Summary. Plastic deformation of nanoporous aluminum at both compression and tension is investigated. Molecular dynamic simulation of the deformation process is performed in comparison with the results of the continuum model of the plasticity-driven variation of the pore size with accounting of the dislocation activity in the pore vicinity.

1 INTRODUCTION

Porous materials have attractive mechanical properties, such as low density together with high specific stiffness. Nanopores can be more suitable in comparison with micropores due to the larger pressure required for their compression and more uniform properties of material on the macroscale. Various methods are developed for production of nanoporous metals, including nanoparticle sintering, gas bubbles introduction in melt and others. Plastic deformation regularities of the nanoporous structure are of significant interest for possible applications. Models of plastic behavior of nanoporous materials are necessary for mechanical computations.

In present work, we investigate the plastic deformation of nanoporous aluminum at both compression and tension. We use molecular dynamic (MD) simulations in comparison with the continuum modeling based on the model[1] of the plasticity-driven growth of pores. This model takes into account the dislocation activity in the pore vicinity; here it is applied to the case of pore compaction as well. Influence of size, volume fraction and form of pores on the stress-strain curves is numerically investigated.

2 MOLECULAR DYNAMIC SIMULATIONS

We use LAMMPS[2] for MD simulations and OVITO[3] for visualization and analysis of the obtained data. The "Construct surface mesh" algorithm[4] is used for calculation of the pore volume and size. The EAM-type potential[5] is used for description of the interaction of Al atoms. The MD system is a cube with the face length of 20 nm, it initially contains 0.5 million atoms. A single spherical or cubic pore is cut out in the center of the system. In the case of spherical shape, the pore diameter varies in the range 8.3–16.4 nm, and the volume fraction of pores varies in the range 0.036–0.27. In the case of cubic shape, the pore face length varies in the range 6.5–19.4 nm, and the volume fraction of pores varies in the range 0.039–0.94. Periodic conditions are set for all the boundaries. The system is thermalized, and then

compressed or stretched at a constant temperature from the range 100–900 K; the uniform deformation is applied by rescaling of atom coordinates with the strain rates 1, 3 and 0.3 ns^{-1}.

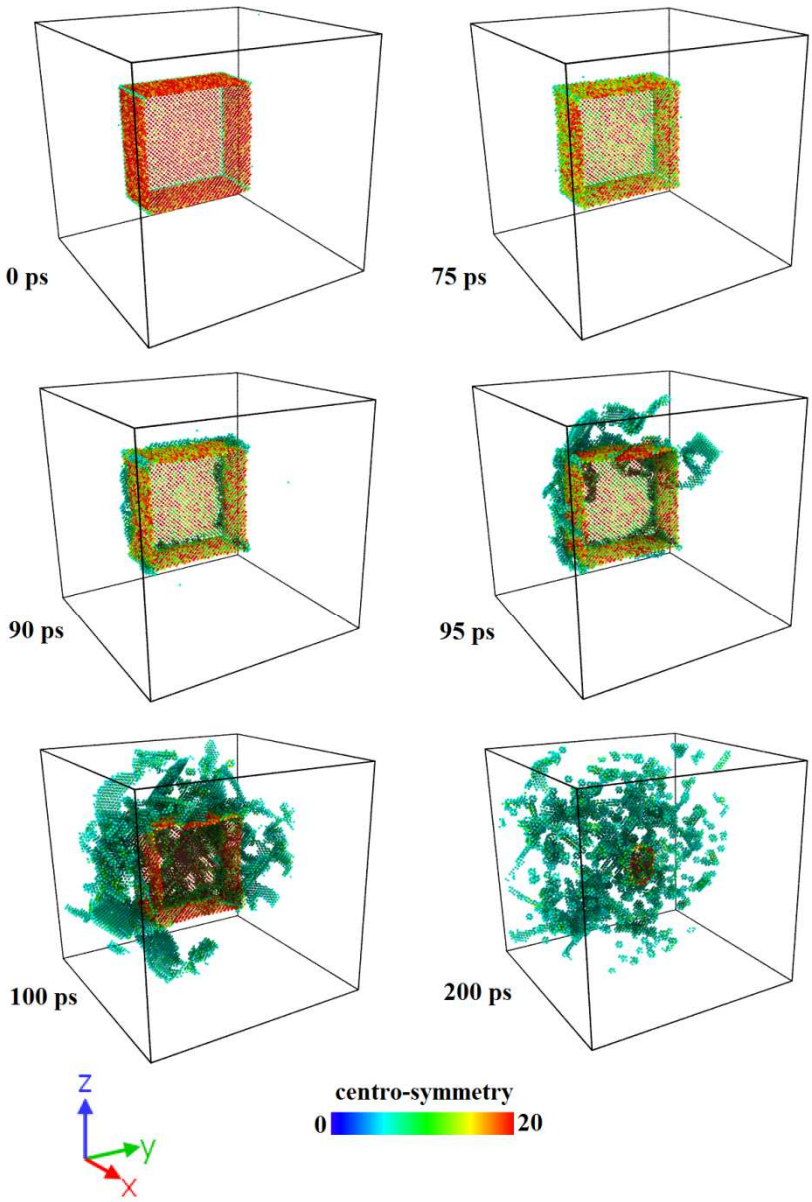

Figure 1: Compression of cubic pore in Al : MD simulations. The strain rate is 1 ns^{-1} ; the temperature is 300 K ; the initial pore size is 9.7 nm ; the system size is 20 nm (about half a million atoms). The color scale shows the centro-symmetry parameter indicating the degree of defectness : red color (about 20) corresponds to the pore surface ; green color (5–10) corresponds to the lattice defects (dislocations and stacking faults) ; atoms of perfect lattice are not shown, only atoms along the defects in the far half of the MD system are shown.

An example of the system behavior is shown in Figure 1. The initial elastic deformation of

the sample with retaining of the crystalline lattice around the pore is replaced by the emission of dislocations from the pore surface and following plastic collapse or growth of the pore. The transition to plastic flow is sharp, especially in the case of cubic pores (Figure 1). The length of dislocations quickly increases till some saturation value, and then oscillates around a constant level. The plastic deformation at the expansion starts earlier than at the compression. It is revealed that the smaller pores require the higher pressure for initiation of the plastic stage of compaction. Initiation of plasticity for cubic pores occurs later and goes sharper than for spherical ones; after the plasticity initiation, behavior is similar for both shapes of pores. Increase in temperature leads to earlier plastic flow at lesser absolute values of pressure.

3 CONTINUUM MODEL

Here we refine the continuum model[1] and apply it to both compression and tension, see Figure 3 as an example. The stabilized radius R_p differs from the current one R by the elastic deformation. Variation of R_p is determined by the plastic strain rate $\dot{w}_{rr}$ in the pore vicinity

$$\dot{R}_p = (R/2)\dot{w}_{rr}, \tag{1}$$

$$\dot{w}_{rr} = bV_D\rho_D/2, \tag{2}$$

where ρ_D is the scalar density of dislocations, V_D is the velocity of dislocations

$$V_D = (b/B)[\sigma - Y/2][1 - (V_D/c_t)]^{3/2}, \tag{3}$$

where b is the modulus of Burgers vector; B is the drag coefficient; c_t is the transverse sound speed; σ is the shear stress in the pore vicinity; $Y = Y_0 + 0.5Gb\sqrt{\rho_D}$ is the static yield strength with accounting of the deformation hardening.

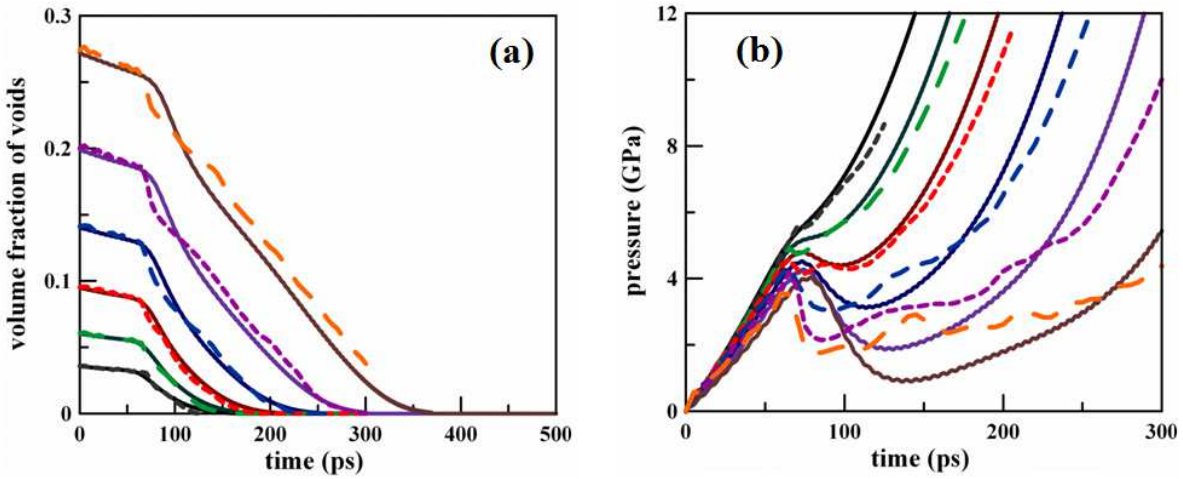

Figure 2: Comparison of continuum model (solid lines) with MD (dashed lines) for spherical pores with initial diameters of 8.3, 10, 11.5, 13.1, 14.7 and 16.4 nm : time dependences of the pore volume fraction (a) and average pressute in the MD system (b). The strain rate of compression is 1 ns^{-1} ; the temperature is 300 K.

The kinetics of dislocations is described by the following equation

$$\dot{\rho}_D = \frac{\pi c_t}{2d^3}\left(\frac{4\pi R^2 b}{a_c^3}\right)\exp\left(-\frac{\pi\varepsilon_s}{2k_BT}\right) + \frac{0.01}{\varepsilon_D}(b\sigma V_D)\rho_D - 10b\rho_D^2 V_D, \quad (4)$$

and takes into account the nucleation on the pore surface (the first summand), the multiplication (the second summand) and annihilation (the third summand). Here $a_c = \varepsilon_s/(b\sigma)$ is the critical radius of a nucleating semi-loop; ε_s is the energy per unit length of dislocation formation from the pore surface; ε_D is the energy of dislocation multiplication.

The shear stress can be calculated from the stabilized and current radii

$$\sigma = 3G\left[1 + P/(3K) - R_p/R\right], \quad (5)$$

where G and K is the shear modulus and the bulk modulus, respectively; P is the pressure applied to the material. The current radius can be calculated as follows

$$R = \frac{R_p - \gamma/(2G)}{1 + P[1/(4G) + 1/(3K)]}, \quad (6)$$

this expression reflects the balance of forces on the pore surface; γ is the surface tension.

4 CONCLUSIONS

- Compression and tension of aluminium with nanopores are investigated by means of MD simulations.
- Elastic variation of pore size continues till nucleation of dislocations from pore surface and then is replaced by plastic compaction or growth of pores.
- For the case of spherical pores, the continuum model of plasticity-driven growth is employed for description of both compression and tension of nanoporous aluminum. The behavior close to MD is observed.
- For the case of cubic pores, the continuum model requires modification.

This work is supported by the grant from the President of the Russian Federation (Project No. MK-9111.2016.8) and by the grant from the Ministry of Education and Science of the Russian Federation (Project 3.2510.2017/PP).

REFERENCES

[1] V.S. Krasnikov and A.E. Mayer, “Plasticity driven growth of nanovoids and strength of aluminum at high rate tension: Molecular dynamics simulations and continuum modeling”, *Int. J. Plast.*, **74**, 75-91 (2015).

[2] S. Plimpton, “Fast parallel algorithms for short-range molecular dynamics”, *J. Comp. Phys.* **117**, 1-19 (1995).

[3] A. Stukowski, “Visualization and analysis of atomistic simulation data with OVITO–the Open Visualization Tool”, *Modell. Simul. Mater. Sci. Eng.* **18**, 015012 (2010).

[4] A. Stukowski, “Computational analysis methods in atomistic modeling of crystals”, *JOM* **66**, 399-407 (2014).

[5] R. R. Zope and Y. Mishin, “Interatomic potentials for atomistic simulations of the Ti-Al system”, *Phys. Rev. B.* **68**, 024102 (2003).

30th Nordic Seminar on Computational Mechanics
NSCM-30
J. Høgsberg. N.L. Pedersen (Eds.)
2017

QUASI-STATIC CONDENSATION OF AEROELASTIC SUSPENSION BRIDGE MODEL

RANDI N. MØLLER*†, STEEN KRENK* AND MARTIN N. SVENDSEN†

*Department of Mechanical Engineering, Technical University of Denmark
DK-2800 Lyngby, Denmark
e-mail: randinm@mek.dtu.dk,sk@mek.dtu.dk, web page: http://www.mek.dtu.dk

†Rambøll, Hannemanns Allé, DK-2300 Copenhagen, Denmark
e-mail: mnns@ramboll.dk, web page: http://www.ramboll.dk

Key words: Structural Dynamics, Quasi-static Condensation, Aerodynamic Stability, Long Span Bridges.

1 INTRODUCTION

For long span bridges the wind-induced dynamic response is a design driving factor and therefore continuously a subject for detailed analysis. Traditionally both buffeting and stability calculations have been considered in the frequency domain. However, this yields a limitation in accounting for turbulence when considering the stability limit and further it is not possible to account for non-linear effects. These limitations suggest to do simulations of the aeroelastic response of long span bridges in the time domain. For this it is of interest to have an efficient model while still maintaining sufficient accuracy.

This contribution is on quasi-static reduction of an aeroelastic finite element model of a 3000m suspension bridge proposed for crossing Sulafjorden in Norway[1]. The model is intended for stability limit calculation where the representation of higher modes is of less importance. The present contribution demonstrates the application of quasi-static condensation to long suspension bridges as well as introduces an extension of the method to include the full aeroelastic system. This includes considerations on reduction of external wind loading as well as motion-induced forces.

2 AEROELASTIC BRIDGE MODEL

The suspension bridge is depicted in Figure 1(a). The bridge is implemented as a finite element model in Matlab using 3D beam elements for the towers and Green strain truss elements for the cables. The deck to hanger connections are modelled with rigid links and the bridge deck elements are aeroelastic beam elements including aerodynamic properties through additional degrees of freedom in the system.

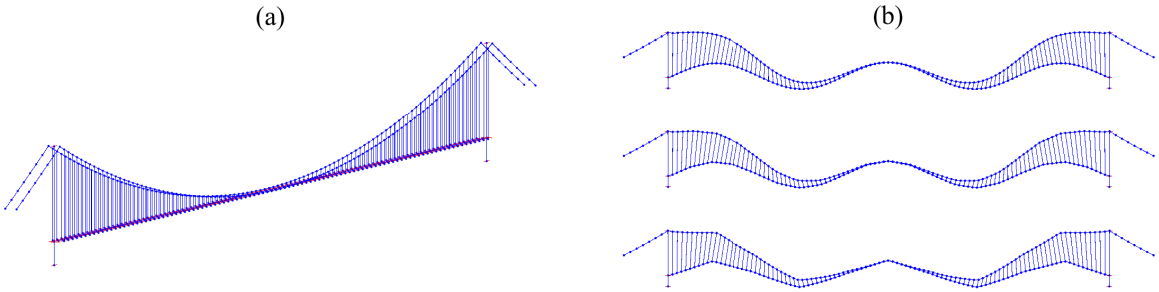

Figure 1: (a) Bridge model (b) Mode shapes: Full model, 1:5 and 1:10 reduction.

The equation of motion for the system including motion-induced forces can be written as

$$\mathbf{M}\ddot{\mathbf{q}}(t) + \mathbf{C}\dot{\mathbf{q}}(t) + \mathbf{K}\mathbf{q}(t) = \mathbf{f}_m(t) + \mathbf{f}_{ext}(t) \tag{1}$$

where $\mathbf{q}$ is the displacement vector. The coefficient matrices $\mathbf{M} = \mathbf{M}_s + \mathbf{M}_a$, $\mathbf{C} = \mathbf{C}_s + \mathbf{C}_a$ and $\mathbf{K} = \mathbf{K}_s + \mathbf{K}_a$ are the mass, damping and stiffness matrices. Here index s and a refers to structural and aerodynamic property matrices respectively. On the right hand side there is a contribution from the external forces $\mathbf{f}_{ext}$ and from the memory part of the motion-induced forces $\mathbf{f}_m$. To enable the memory part of the motion-induced forces to appear as additional degrees of freedom in the system, a number of j first order differential equations on the form

$$\dot{\mathbf{f}}_{m,j}(t) + \mathbf{D}_j\mathbf{f}_{m,j}(t) = \mathbf{A}_j\mathbf{q}(t) \tag{2}$$

are introduced[2,3]. Here the matrix $\mathbf{A}_j$ and the diagonal matrix $\mathbf{D}_j$ are shape specific property matrices. The aerodynamic properties are implemented as a single term approximation to the Theodorsen flat plate theory.

3 QUASI-STATIC CONDENSATION

The method of quasi-static condensation builds on the master-slave constraint principle, but instead of introducing rigid links between master and slave nodes a stiffness relation is used to describe the master-slave relation:

$$\mathbf{q} = \begin{bmatrix}\mathbf{q}_d \\ \mathbf{q}_s\end{bmatrix} = \begin{bmatrix}\mathbf{I} \\ \mathbf{S}\end{bmatrix}\mathbf{q}_d\,, \quad \mathbf{S} = -\mathbf{K}_{ss}^{-1}\mathbf{K}_{sd} \tag{3}$$

Here $\mathbf{q}_d$ and $\mathbf{q}_s$ are the displacement vectors of the master and the slave degrees of freedom respectively. The first and second index on the stiffness matrix $\mathbf{K}$ refer to master or slave rows and columns respectively. Extending the method to include motion-induced forces suggest to treat the state proportional aeroelastic terms as the structural mass, damping and stiffness while the memory part of the motion-induced forces are reduced by considering the rate of work. Hereby the reduced form of the equation of motion including motion-induced forces is

$$\bar{\mathbf{M}}\ddot{\mathbf{q}}_d(t) + \bar{\mathbf{C}}\dot{\mathbf{q}}_d(t) + \bar{\mathbf{K}}\mathbf{q}_d(t) = \bar{\mathbf{f}}_m(t) + \bar{\mathbf{f}}_{ext}(t) \tag{4}$$

and the differential equation describing the relation between the system displacements and the memory part of the motion-induced forces is found as:

$$\dot{\bar{\mathbf{f}}}_{m,j}(t) + \gamma_j \bar{\mathbf{f}}_{m,j}(t) = \bar{\mathbf{A}}_j \mathbf{q}_d(t) \tag{5}$$

The differential equation has maintained the form beneficial for implementation assuming that $\mathbf{D}_j = \gamma_j \mathbf{I}$. In equation (4) and (5) the reduced coefficient matrices, external forces and memory forces are found on the general form:

$$\bar{\mathbf{X}} = \mathbf{X}_{dd} + \mathbf{S}^T \mathbf{X}_{sd} + \mathbf{X}_{ds}\mathbf{S} + \mathbf{S}^T \mathbf{X}_{ss}\mathbf{S}\,, \quad \bar{\mathbf{x}} = \mathbf{x}_d + \mathbf{S}^T \mathbf{x}_s \tag{6}$$

where $\mathbf{X} \in \{\mathbf{M}, \mathbf{C}, \mathbf{K}, \mathbf{A}_j\}$ and $\mathbf{x} \in \{\mathbf{f}_{ext}, \mathbf{f}_m, \dot{\mathbf{f}}_m\}$.

4 ACCURACY OF REDUCED SYSTEM

The quasi-static system condensation has been applied to the bridge model and reduced model results are in this section compared to results obtained for the full system. Figure 1(b) shows mode shapes of the 14th still-air mode obtained with the full model, a model reduced to one fifth and to one tenth of the full model size respectively. It is seen that the mode shape obtained with the 1:5 model reduction is very similar to the mode shape obtained with the full model while the 1:10 reduction is resulting in a less smooth mode shape. This implies that the 1:10 reduction is too coarse and is no longer capturing the behaviour of the full model.

Figure 2 shows the natural frequencies for the full model (∘), the 1:5 reduction (∗) and the 1:10 reduction (◇). The left plot shows the natural frequencies for the still-air system and the right plot shows the natural frequencies for the aeroelastic system with wind speed $U = U_{cr}$. Both plots indicate that the 1:5 reduction gives a good representation of modes up to around mode number 15 while the 1:10 reduction shows divergence at mode 9 and up.

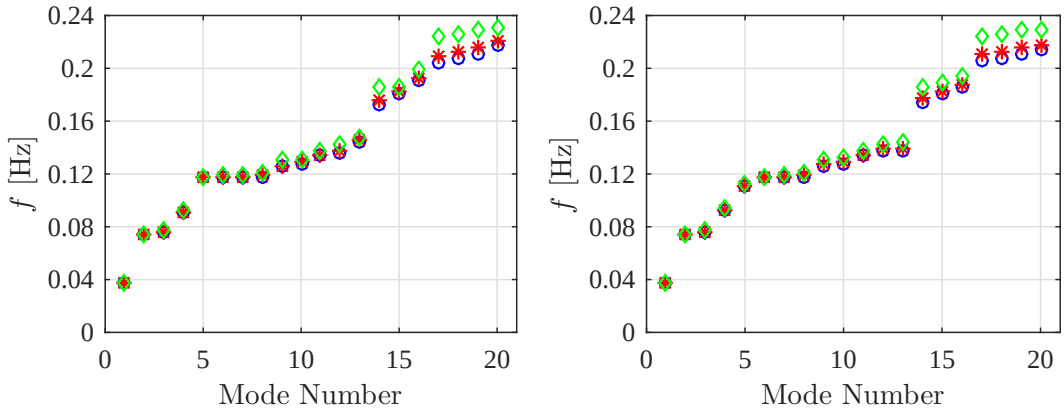

Figure 2: Modal frequencies: (left) still air (right) critical wind speed.

The time domain responses of the full bridge model and the 1:5 reduction are now considered when excited by turbulent wind loading. The mean wind loading influencing the aeroelastic terms is set to $U = 0.6U_{cr}$, the turbulence intensity is $I_u = 0.134$ and the integral length scale is $\lambda = 200$m. Figure 3 shows the drag q_y, the heave q_z and the torsional r_x response for a five minute time interval. It is seen that the response obtained by the reduced model is corresponding well with the response found by the full model. The calculation time for the five minute time history is significantly reduced from 59.3s to 0.7s making use of the reduced model instead of the full model.

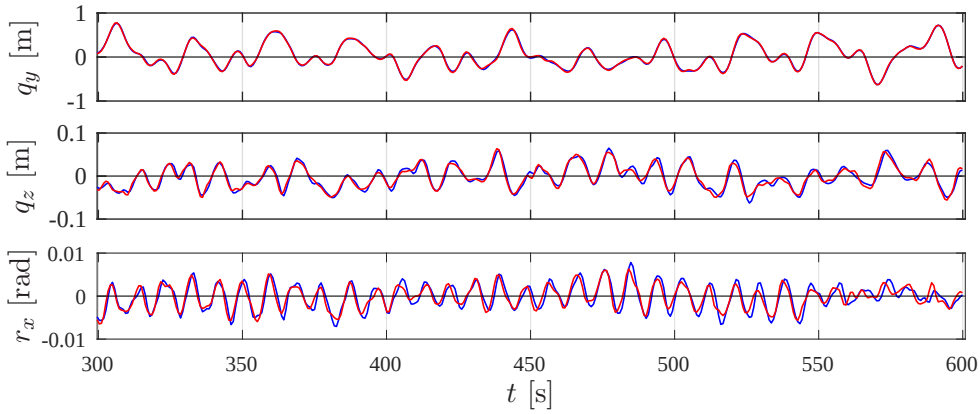

Figure 3: Time response at quarter span: Full model (−), 1:5 reduction (−).

5 CONCLUSIONS

It has been demonstrated that flutter analysis of a typical long suspension bridge can be performed using a model reduced by quasi-static condensation. A reduced model with a number of around 20 master nodes along the bridge deck and corresponding master nodes in the suspension cables has been shown to represent the behaviour of the bridge with sufficient accuracy. A further reduction of the model did not capture the essentials of relevant modes due to the coarseness.

REFERENCES

[1] Ramboll, for the Norwegian Public Roads Administration, Konseptrapport Hengebru i Korridor 1, November 2015.

[2] JR. Høgsberg, J. Krabbenhøft and S. Krenk, State space representation of bridge deck aeroelasticity, 13th Nordic Seminar on Computational Mechanics (NSCM-13), Oslo University, 109-112, (2000).

[3] O. Øiseth, A. Rönnquist and R. Sigbjörnsson, Finite element formulation of the self-excited forces for time-domain assessment of wind-induced dynamic response and flutter stability limit of cable-supported bridges. *Finite Elements in Analysis and Design*, **50**, 173-183, (2012)

30th Nordic Seminar on Computational Mechanics
NSCM-30
J. Høgsberg. N.L. Pedersen (Eds.)
2017

PID-CONTROLLED FLOW-THROUGH BIOREACTOR

ANATOLIJ NEČIPORENKO*, FELIKSAS IVANAUSKAS*, VALDAS LAURINAVIČIUS†, MIFODIJUS SAPAGOVAS‡

*Vilnius University Dept. Mathematics and Informatics, Lithuania
email: feliksas.ivanauskas@mif.vu.lt, anatolij.neciporenko@mif.vu.lt

†Vilnius University Institute of Biochemistry, Lithuania
email: valdas.laurinavicius@bchi.vu.lt

‡Vilnius University Institute of Mathematics and Informatics, Lithuania
email: mifodijus.sapagovas@mii.vu.lt

Key words: nonlocal boundary condition, reaction–diffusion, bioreactor, PID controller

Summary. The system of two parabolic nonlinear reaction–diffusion equations with nonlocal boundary condition is used to model the PID-controlled flow-through bioreactor. Integral-type nonlocal boundary condition links the solution on the system boundary to the integral of the solution within the system inner range.

The given bioreactor can be represented as an active transdermal patch which can be applied to the patient's skin. Equipped with two electrodes which measure the electrochemical characteristics of the specific drug it controls the concentration of the drug in the inner range of the transdermal patch.[1]

1 INTRODUCTION

Present mathematical model belongs to an intensely studied class of problems, namely differential equations subject to nonlocal boundary conditions. Nonlocal boundary conditions are commonly referred to as the boundary (or initial) conditions describing the relationship between the desired solution values on multiple points. Unlike classical boundary conditions, nonlocal conditions do not describe the values of the solution or its derivative in a particular range of the single boundary point. The expressions describing the nonlocal boundary conditions may contain integral expressions of the desired solution, as is the case with our model. This is commonly called a problem with nonlocal integral conditions.

Main peculiarity of the present work is a sufficiently detailed explanation of the physical principles that were the basis of the nonlocal boundary condition, which reflects the control (regulation) principle. The solution at boundary points is calculated using the integral combined with the proportional-integral-derivative (PID) controller algorithm. We monitor the drug delivery on the bioreactors output edge attached to the body.

We study a system of two parabolic nonlinear reaction–diffusion equations subject to a nonlocal boundary condition. This system of nonlinear equations is used for mathematical modeling of biosensors and bioreactors[2]. We provide a mathematical model suitable for the monitoring of the product molar flow into the body. To this end, a control system is used to monitor the outflow of a bioreactor through manipulation of its input parameters.

This model not only provides a set of diffusion–reaction equations, but also describes the underlying physical process together with its possible applications.

Today about 5–10% of newly introduced drugs are prodrugs, as they are more stable and sometimes possess special parameters necessary for the treatment. We model the controlled immobilized enzyme-containing flow-through reactor for the conversion of prodrug into an active form.

However, this approach has some limitations. There is a limited number of suitable enzymatic systems in the body and/or too low enzymatic activity. Also, there is a problem with side products of the enzymatic conversion of the prodrug into an active form. Sometimes, side products are toxic or causing undesirable effects in the body.

In some cases, before delivering the drug into the body, a prodrug outside the body should be activated. Immobilized enzyme-containing flow-through reactors can be used in this case, the prodrug on the inlet of the reactor and an active form on the outlet.[1]

2 MATHEMATICAL MODEL

We analyze a system of two differential equations widely used in mathematical modeling[2]. The key feature of this model is the nonlocal boundary condition that combines two different components of the solution.

We consider the boundary value problem for the system of two nonlinear diffusion–reaction equations

$$\begin{aligned} \frac{\partial S}{\partial t} &= \mathcal{D}_S \frac{\partial^2 S}{\partial x^2} - \frac{V_{max} S}{K_M + S}, \\ \frac{\partial P}{\partial t} &= \mathcal{D}_P \frac{\partial^2 P}{\partial x^2} + \frac{V_{max} S}{K_M + S}, \end{aligned} \qquad (x,t) \in D = \{0 < x < d, 0 < t \le T\}, \tag{1}$$

with initial conditions

$$S(x,0) = \begin{cases} 0, & 0 \le x < d, \\ S_0, & x = d, \end{cases} \qquad P(x,0) = 0, \quad 0 \le x \le d, \tag{2}$$

and boundary conditions

$$P(0,t) = 0, \quad 0 < t \le T; \qquad \left.\frac{\partial P}{\partial x}\right|_{x=d} = 0, \quad 0 < t \le T; \qquad \left.\frac{\partial S}{\partial x}\right|_{x=0} = 0, \quad 0 < t \le T. \tag{3}$$

The last nonlocal boundary condition is

$$S(d,t) = \mathcal{K}_p e(t) + \mathcal{K}_i \int_0^t e(\tau)d\tau + \mathcal{K}_d \frac{de(t)}{dt}, \quad 0 < t \le T. \tag{4}$$

Here

$$e(t) = Q(t) - \frac{2\mathcal{D}_p}{m^2 - n^2} \int_n^m P(x,t)dx, \quad 0 < m, n < d, \tag{5}$$

$Q(t)$ is a given function (set-point), and K_p, K_i, and K_d are nonnegative coefficients for the proportional, integral, and derivative terms.

The error function $e(t)$ defines the difference between the required product molar flow $Q(t)$ and the measured flow

$$\frac{2\mathcal{D}_p}{m^2 - n^2} \int_n^m P(x,t)dx.$$

The nonlocal boundary condition (4) links the value of substrate concentration $S(x,t)$ on the boundary (input edge) where $x = d$ to the integral value of product concentration $P(x,t)$ in the inner range $[n,m]$. The main peculiarity of the boundary condition (4) is its nonlocality due to the integration not only in the space domain $[n,m]$, but also in the time domain $[0,t]$. The PID controller continuously evaluates the error value $e(t)$ and attempts to minimize the error over time by adjusting the control variable $S(d,t)$ to a new value determined by (4).

We examine the problem of maintaining the molar outflow of a drug (product), which may vary over time. It is worth noting that the properties of the physical process prohibit direct measurements at the boundary of the bioreactor; therefore, the viable options are to regulate either the concentration or the flow of the substrate (or both). In the present work, the substrate concentration is regulated.[1]

3 PHYSICAL MODEL

Suppose that an enzyme is immobilized in a drug delivery system named as a bioreactor (Fig. 1). The enzyme is uniformly distributed in the bioreactor. Inside the bioreactor, an electrode wire net (electrode) is deposited in order to perform the electrochemical monitoring of the enzymatic reaction. On the outer surface of the bioreactor, a reservoir with variable concentration of substrate is deposited. Let us consider that the concentration of the substrate S can be monitored depending on the response of the electrochemical electrode.

The given bioreactor can be represented as an active transdermal patch. The transdermal patch is applied to the patient's skin; one side of the transdermal patch delivers the drug (product) to the patient, whereas the other side is equipped with a controlled substrate (prodrug) supply system, which is designed to alter the substrate concentration or its flow. The transdermal patch is equipped with two electrodes that measure the electrochemical characteristics of the specific drug. In this way, it controls the concentration of the drug in the inner range of the transdermal patch.

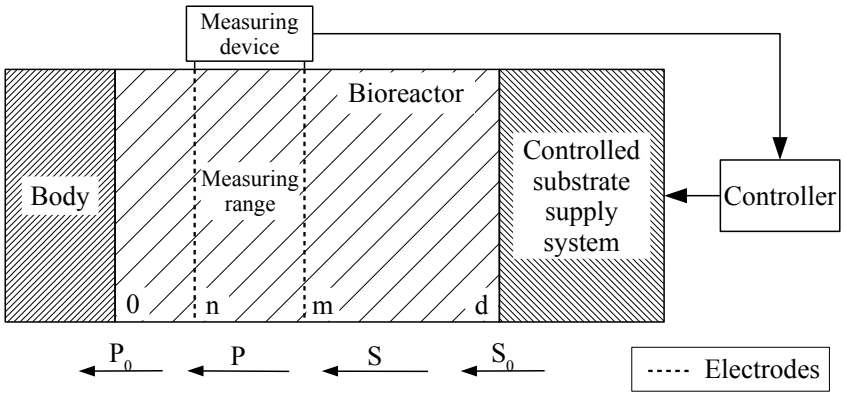

Figure 1: Principal structure of bioreactor

The treatment process requires the drug to be transferred to a patient in accordance with the therapeutic protocol. This can be either a constant flow or a function of the time, eg., in the early treatment stage the drug flow must start at a high value and then gradually decline as the treatment progresses, or the drug dose must continually rise until reaching a prescribed value.[1]

4 CONCLUSIONS

We propose a new type of nonlocal boundary condition for the parabolic reaction–diffusion equation system applied to the bioreactor modeling. The condition is nonlocal w.r.t. the time and space domains. The double integral of this type in the nonlocal condition poses new challenges for numerical experiments related to this mathematical model.

The mathematical model was applied for the modeling operation and control of drug delivery systems when the prodrug is converted into an active form in the enzyme-containing bioreactor before being delivered into the body.

The linear, exponential, and stepwise protocols of drug delivery were investigated, and the corresponding mathematical models for the prodrug delivery were created.[1]

REFERENCES

[1] Ivanauskas, F., Laurinavičius, V., Sapagovas, M. & Nečiporenko, A. Reaction–diffusion equation with nonlocal boundary condition subject to PID-controlled bioreactor. *Nonlinear Analysis: Modelling and Control* **22**, 261–272 (2017).

[2] Baronas, R., Ivanauskas, F. & Kulys, J. *Mathematical Modeling of Biosensors: An Introduction for Chemists and Mathematicians*. Springer Series on Chemical Sensors and Biosensors (Springer, 2009).

30th Nordic Seminar on Computational Mechanics
NSCM-30
J. Høgsberg. N.L. Pedersen (Eds.)
2017

MESHLESS METHODS FOR POTENTIAL FLOW PAST A CIRCULAR CYLINDER

MORTEN E. NIELSEN* AND LARS DAMKILDE†

Department of Civil Engineering
Aalborg University
Niels Bohrs Vej 8, 6700 Esbjerg, Denmark
*e-mail: men@civil.aau.dk, †e-mail: lda@civil.aau.dk

Key words: Computational methods, Meshless, Radial basis functions, RBF-FD, Potential flow.

1 INTRODUCTION

Floating substructures receive great interest within the offshore wind and wave energy sector. In the design stage of these substructures, computational methods are often used to analyze and optimize the structural response. Many of the present computational methods solve the linearized fluid-structure interaction problem, but more insight may be gained by analyzing the fully non-linear problem. Regardless of the fluid model, the non-linear problem requires a computational method which is able to handle the moving fluid-structure interface. Traditional numerical methods, such as those based on finite difference, finite volume and finite element, are capable of handling the fluid-structure interface either directly or indirectly by an immersed boundary method. However, these methods all have drawbacks due to grid/mesh requirements. Finite difference is in general not well-suited for irregular boundaries and finite volume/element may require significant effort in volume/element generation when used for three-dimensional applications. Different meshless methods have been proposed in order to circumvent these drawbacks[1,2]. Two such methods are briefly introduced in section 2 and applied to solve a benchmark problem stated in section 3. Numerical results are shown in section 4 and the final conclusion is drawn in section 5.

2 METHODOLOGY

In this section, two meshless methods are briefly introduced. The first, Kansa's method[1], is one of the initially proposed methods for solving partial differential equations by means of radial basis functions. Next, the radial basis function-generated finite difference[2] (RBF-FD), which recently have gained great interest, is introduced. In general, we may formulate a boundary value problem as

$$Lu(\mathbf{x}) = f(\mathbf{x}), \qquad \text{for } \mathbf{x} \in \Omega, \tag{1}$$
$$Bu(\mathbf{x}) = g(\mathbf{x}), \qquad \text{for } \mathbf{x} \in \partial\Omega, \tag{2}$$

where L is a linear operator for the interior domain, B is a linear operator for the boundary, $u(\mathbf{x})$ is the unknown function, $f(\mathbf{x})$ is the source term and $g(\mathbf{x})$ is the boundary condition.

2.1 Kansa's method

In Kansa's method[1] the solution is approximated by a linear combination of a radial basis function, which is collocated at N points, such that

$$u(\mathbf{x}) \approx \sum_{k=1}^{N} c_k \phi(\|\mathbf{x} - \mathbf{x}_k\|) = \begin{bmatrix} \phi(\|\mathbf{x}_1 - \mathbf{x}_1\|) & \cdots & \phi(\|\mathbf{x}_1 - \mathbf{x}_N\|) \\ \vdots & \ddots & \vdots \\ \phi(\|\mathbf{x}_N - \mathbf{x}_1\|) & \cdots & \phi(\|\mathbf{x}_N - \mathbf{x}_N\|) \end{bmatrix} \begin{bmatrix} c_1 \\ \vdots \\ c_N \end{bmatrix}, \tag{3}$$

where $\mathbf{x}_k$ is the kth cartesian coordinate vector, $\|\cdot\|$ is the Euclidean norm, c_k are expansion coefficients, N is the total number of collocation points and ϕ is a chosen radial basis function. Now, the governing equation is collocated at n_L nodes in Ω and the boundary conditions are collocated at n_B nodes on $\partial\Omega$, which leads to the system of equations

$$\begin{bmatrix} L\phi(\|\mathbf{x}_1 - \mathbf{x}_1\|) & \cdots & L\phi(\|\mathbf{x}_1 - \mathbf{x}_N\|) \\ \vdots & \ddots & \vdots \\ L\phi(\|\mathbf{x}_{n_L} - \mathbf{x}_1\|) & \cdots & L\phi(\|\mathbf{x}_{n_L} - \mathbf{x}_N\|) \\ B\phi(\|\mathbf{x}_{n_L+1} - \mathbf{x}_1\|) & \cdots & B\phi(\|\mathbf{x}_{n_L+1} - \mathbf{x}_N\|) \\ \vdots & \ddots & \vdots \\ B\phi(\|\mathbf{x}_N - \mathbf{x}_1\|) & \cdots & B\phi(\|\mathbf{x}_N - \mathbf{x}_N\|) \end{bmatrix} \begin{bmatrix} c_1 \\ \vdots \\ c_{n_L} \\ c_{n_L+1} \\ \vdots \\ c_N \end{bmatrix} = \begin{bmatrix} f(\mathbf{x}_1) \\ \vdots \\ f(\mathbf{x}_{n_L}) \\ g(\mathbf{x}_{n_L+1}) \\ \vdots \\ g(\mathbf{x}_N) \end{bmatrix}, \tag{4}$$

where the total number of nodes $N = n_L + n_B$ and finally the solution can be obtained from scattered data interpolation by means of equation (3).

2.2 Radial basis function-generated finite difference

In radial basis function-generated finite difference[2] (RBF-FD), the methodology is similar to the traditional FD method. The finite difference weights are determined by solving the following equation:

$$\sum_{k=1}^{n} w_k u_k \approx Lu(\mathbf{x})|_{\mathbf{x}=\mathbf{x}_e}, \tag{5}$$

where w_k corresponds to finite difference weights of the differential operator L evaluated at $\mathbf{x} = \mathbf{x}_e$. In this paper, the RBF is augmented by polynomials, due to several advantages[2]. If augmented up to linear polynomial terms, the weights are found by solving

$$\begin{bmatrix} & & & 1 & x_1 & y_1 \\ & \mathbf{A} & & \vdots & \vdots & \vdots \\ & & & 1 & x_n & y_n \\ 1 & \dots & 1 & & & \\ x_1 & \dots & x_n & & \mathbf{0} & \\ y_1 & \dots & y_n & & & \end{bmatrix} \begin{bmatrix} w_1 \\ \vdots \\ w_n \\ \gamma_1 \\ \vdots \\ \gamma_n \end{bmatrix} = \begin{bmatrix} L\phi(\|\mathbf{x}_e - \mathbf{x}_1\|)|_{\mathbf{x}=\mathbf{x}_e} \\ \vdots \\ L\phi(\|\mathbf{x} - \mathbf{x}_n\|)|_{\mathbf{x}=\mathbf{x}_e} \\ L1|_{\mathbf{x}=\mathbf{x}_e} \\ Lx|_{\mathbf{x}=\mathbf{x}_e} \\ Ly|_{\mathbf{x}=\mathbf{x}_e} \end{bmatrix}, \tag{6}$$

where $\mathbf{A}$ is the RBF collocation matrix, for example, from equation (3), $\mathbf{0}$ is a $m \times m$ zero matrix and $m = \binom{p+d}{p}$ is the number of polynomial terms for a pth order polynomial in d dimensions. After the differentiation weights w_k are established, the governing equations are solved in a similar manner as in the FD method. Further details about RBF-FD and polynomial augmentation have been provided by, for example, Bayona et al.[2].

3 POTENTIAL FLOW PAST A CIRCULAR CYLINDER

Assuming inviscid, irrotational and incompressible flow allows one to model the flow around an object by means of potential flow theory. In this study, a circular cylinder is used as benchmark and the mathematical problem is stated as

$$\nabla^2 \Phi = 0, \qquad \text{for } \mathbf{x} \in \Omega = [-1, 1]^2, \tag{7}$$

$$\frac{\partial \Phi}{\partial n} = 0, \qquad \text{for } \mathbf{x} \in \partial\Gamma, \tag{8}$$

$$\Phi = g(\mathbf{x}), \qquad \text{for } \mathbf{x} \in \partial\Omega, \tag{9}$$

where Φ is the velocity potential, $g(\mathbf{x})$ is the analytical solution, Ω specifies the fluid domain, while $\partial\Omega$ and $\partial\Gamma$ specify the outer boundaries of the fluid and cylinder domain, respectively.

4 RESULTS

Both meshless methods are tested with the radial basis function $\phi(r) = r^5$, also known as a 5th order polyharmonic spline (PHS). The RBF-FD method is augmented by 4th order bivariate polynomials and a stencil size of 38 nodes is used. In figure 1, the different node layouts are illustrated, along with relative errors based on the ℓ^2-norm. Relative errors from a finite element method (FEM) solution is also plotted, where CST-elements have been used. Expectedly, the RBF-FD shows a higher convergence rate compared to Kansa's method, which may be attributed the polynomial terms. It is also noticed that even Kansa's method provides relative stable behavior for the triangular node layouts, whereas the quasi-random node layout seems rather unstable for both methods. Finally, the RBF-FD method achieves the highest accuracy, while Kansa's method achieves less accurate solutions, but at the same order as the FEM solution.

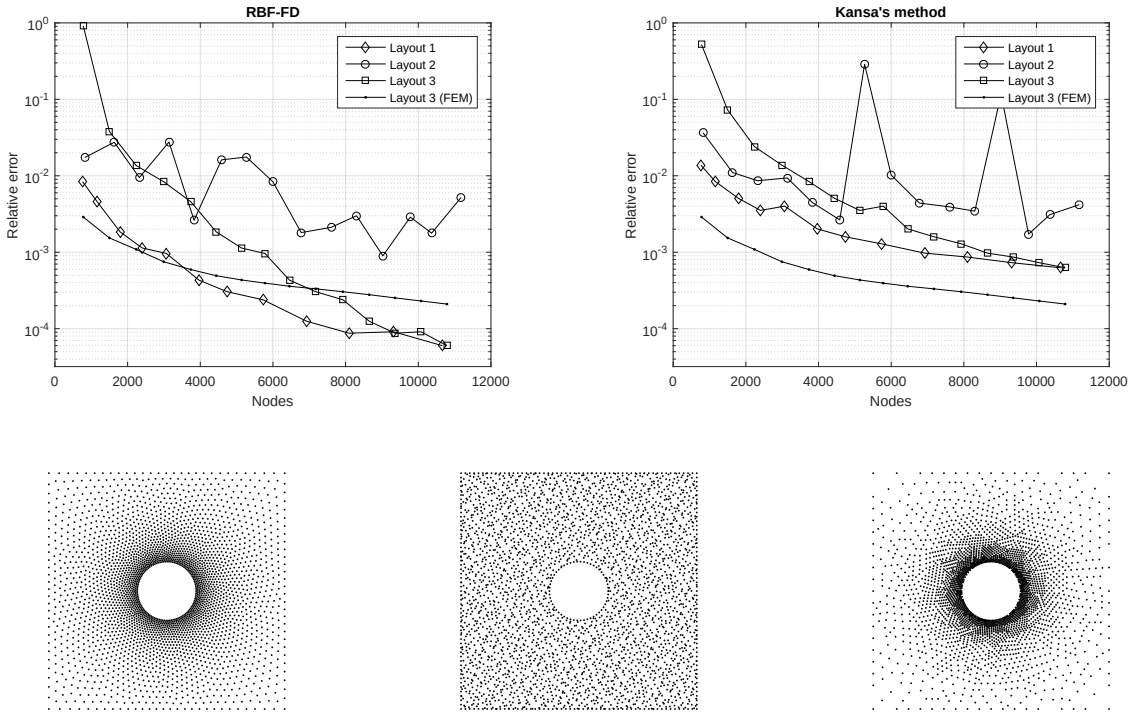

Figure 1: Relative errors for the benchmark problem and the different node layouts used.

5 CONCLUSION

Two meshless methods were introduced, namely Kansa's method and radial basis function-generated finite difference. A benchmark problem was solved and relative errors were compared to those from a finite element solution. The comparison shows that meshless methods are interesting alternatives to other numerical methods for solving potential flow past solid objects.

REFERENCES

[1] E.J. Kansa. Multiquadrics – A scattered data approximation scheme with applications to computational fluid dynamics – II: Solutions to parabolic, hyperbolic and elliptic partial differential equations. *Computers & Mathematics with Applications*, **19**, 147–161, (1990).

[2] V. Bayona, N. Flyer, B. Fornberg and G. A. Barnett. On the role of polynomials in RBF-FD approximations: II. Numerical solution of elliptic PDEs. *Journal of Computational Physics*, **332**, 257–273, (2017).

30th Nordic Seminar on Computational Mechanics
NSCM-30
J. Høgsberg. N.L. Pedersen (Eds.)
2017

COMPARISON OF SERVECIABILITY CRITERIA FOR PEDESTRIAN BRIDGES

ANTTI H. NIEMI*, JANI KOSKELA† AND FILIP FEDORIK*

*Research Unit of Structures and Construction Technology
University of Oulu
P.O. Box 4200 (Linnanmaa), FI-90014 University of Oulu
e-mail: antti.niemi@oulu.fi, web page: http://www.oulu.fi

†Pöyry Finland Oy
Elektroniikkatie 13, 90590 Oulu
e-mail: jani.koskela@poyry.fi - Web page: http://www.poyry.fi

Key words: Structural Design, Vibrations, Structural Dynamics, Footbridges, Computational Methods.

Summary. Current design trends of footbridges lead towards light and slender structures susceptible to vibrations induced by walking or running pedestrians. In this work, the dynamic response of a composite (steel & concrete) bridge is analyzed. The bridge is designed so that the fundamental frequency of the structure is close to the load excitation frequencies of pedestrians. Different load models are studied in the context of a simplified structural model and the results can then be compared to those of more advanced models. Also the sensitivity of the results to the values of the main design parameters can be evaluated.

1 INTRODUCTION

A simplified model for a single-spand footbridge can be based on the Euler-Bernoulli beam theory where the governing differential equation can be written in terms of the beam deflection w as

$$EI\frac{\partial^4 w}{\partial x^4}(x,t) + c\frac{\partial w}{\partial t}(x,t) + \rho A\frac{\partial^2 w}{\partial t^2}(x,t) = f(x,t), \quad 0 < x < L,\ t > 0, \tag{1}$$

where E is Young's modulus of the material and I and A are the moment of inertia and area of the beam cross section, respectively. The parameter c is the viscous damping parameter and ρ stands for the mass density of the material. All parameters are assumed to be constant over the interval $(0, L)$, where L is the length of the bridge and the external load is represented by the function $f(x,t)$.

The equation of motion can be decoupled in space and time and transformed to an ordinary differential equation for the deflection amplitude $z(t)$:

$$\tilde{k}z(t) + \tilde{c}z'(t) + \tilde{m}z''(t) = \tilde{f}(t). \tag{2}$$

For simply supported or hinged ends, the first bending mode is $\phi(x) = \sin(\pi x/L)$ and the corresponding generalized stiffness, mass and damping coefficients are

$$\tilde{k} = \int_0^L EI[\phi''(x)]^2 \,\mathrm{d}x = EI\frac{\pi^4}{2L^3},$$
$$\tilde{c} = \int_0^L c[\phi(x)]^2 \,\mathrm{d}x = \frac{cL}{2},$$
$$\tilde{m} = \int_0^L \rho A[\phi(x)]^2 \,\mathrm{d}x = \frac{M}{2},$$

where $M = \rho AL$ is the total mass of the bridge and the generalized load is defined as

$$\tilde{f}(t) = \int_0^L f(x,t)\phi(x) \,\mathrm{d}x. \tag{3}$$

Division of Eq. (2) by the modal mass $\tilde{m}$ yields the customary form of a damped harmonic oscillator

$$z''(t) + 2\zeta\omega z'(t) + \omega^2 z(t) = \frac{\tilde{f}(t)}{\tilde{m}}, \tag{4}$$

where

$$\omega = \sqrt{\frac{\tilde{k}}{\tilde{m}}} = \pi^2\sqrt{\frac{EI}{ML^3}}$$

is the natural frequency of the bridge and

$$\zeta = \frac{\tilde{c}}{2\sqrt{\tilde{m}\tilde{k}}}$$

is the dimensionless damping ratio.

2 LOAD MODELS

Referring to the above model, three conventional harmonic loads of the form

$$f_i(x,t) = p_i(x,t)\sin(\omega t), \quad i = 1,2,3$$

can be specified. The first model is associated to the so called pedestrian stream model, where the random load due to a stream of random pedestrians is replaced by an equivalent uniformly distributed load p_1 over the bridge surface area. The second load consists of a pedestrian group of weight P_2 moving with a constant velocity v across the bridge. Finally, in the third case the load P_3 is assumed to act at the center of the bridge at $x = L/2$, where the maximum amplitude of the first bending mode occurs. This kind of models have been advocated in[2] and in the references therein.

Referring to the assumed structural model, the load functions for the above load cases are

$$f_1(x,t) = p_1 \sin(\omega t),$$
$$f_2(x,t) = P_2 \delta(x - vt) \sin(\omega t),$$
$$f_3(x,t) = P_3 \delta(x - L/2) \sin(\omega t),$$

where $\delta(\cdot)$ stands for the Dirac delta function. The corresponding generalized loads according to Eq. (3) are then

$$\tilde{f}_1(t) = \frac{2}{\pi} L \cdot p_1 \sin(\omega t),$$
$$\tilde{f}_2(t) = P_2 \sin\left(\frac{\pi t}{T}\right) \sin(\omega t),$$
$$\tilde{f}_3(t) = P_3 \sin(\omega t),$$

where $T = L/v$ is the time it takes for the group to cross the bridge in the second load case.

3 NUMERICAL RESULTS

We consider now a steel-concrete composite single-span bridge model which has been verified in the ultimate limit state. The bridge properties are as follows:

- Length and width: $L = 28\,\mathrm{m}$ & $H = 3\,\mathrm{m}$
- Total mass: $M = 77\,158\,\mathrm{kg}$
- Bending rigidity: $EI = 2\,891\,201\,\mathrm{kN \cdot m^2}$
- Natural frequency: $f = \dfrac{\omega}{2\pi} = 2.052\,\mathrm{Hz}$
- Assumed damping ratio: $\zeta = 0.3\%$

In the first loading case, we assume a pedestrian density of $d = 0.5\,\mathrm{m^{-2}}$. According to the pedestrian stream model, see[2], the corresponding equivalent number of pedestrians uniformly distributed on the loaded surface is

$$n' = 10.8 \frac{\sqrt{\zeta d LH}}{LH} = 0.046\,\mathrm{m^{-2}}.$$

In this model, the vertical load is assumed as $P_\mathrm{w} = 280\,\mathrm{N}$ and the reduction factor $\psi_1 = 1$ corresponding to the natural frequency is determined based on Table 4-8 of[2]. The distributed load over the beam length becomes $p_1 = P_\mathrm{w} \cdot \psi_1 \cdot n' \cdot H = 38.336\,\mathrm{N/m}$.

In the second loading case with a moving load, we assume a group of four pedestrians ($n = 4$) moving with a constant velocity.

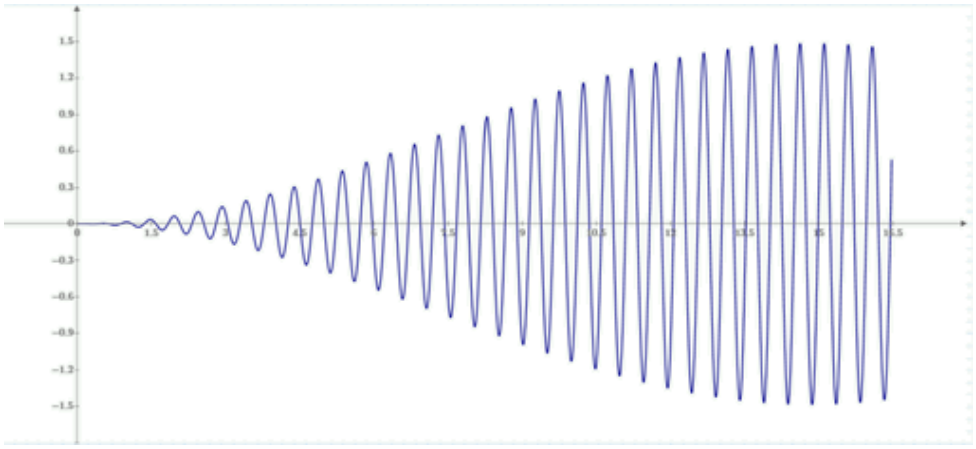

Figure 1: Acceleration response of the model bridge for a moving load.

In the third loading case with a stationary load at the center, we reduce the number of pedestrians as $n' = \sqrt{n}$ so that $P_3 = n' \cdot P_\mathrm{w} \cdot \psi_2 = 560\,\mathrm{N}$.

The maximum acceleration in the first and third cases can be calculated as based on the analytic solution of the damped harmonic oscillator (4):

$$a_{\max,1} = \frac{2}{\pi}\frac{p_1 L}{\zeta M} = 2.952\,\frac{\mathrm{m}}{\mathrm{s}^2} \quad \& \quad a_{\max,3} = \frac{P_3}{\zeta M} = 2.419\,\frac{\mathrm{m}}{\mathrm{s}^2}$$

In the second case, the acceleration response was evaluated numerically and is shown in Fig. 1. The corresponding maximum acceleration is estimated to be around

$$a_{\max,2} = 1.5\,\frac{\mathrm{m}}{\mathrm{s}^2}.$$

REFERENCES

[1] EN 1991-2. *Eurocode 1: Actions on structures - Part 2: Traffic loads on bridges.* 2003.

[2] C. Heinemeyer et al. Design of Lightweight Footbridges for Human Induced Vibrations *JRC Scientific and Technical Reports*, 2009.

[3] K. Van Nimmen, G. Lombaert, G. De Roeck, and P. Van den Broeck. Vibration serviceability of footbridges: Evaluation of the current codes of practice. *Engineering Structures*, 59:448–461, 2014.

30th Nordic Seminar on Computational Mechanics
NSCM-30
J. Høgsberg. N.L. Pedersen (Eds.)
2017

CONTACT ISSUES ON A HIGHLY FLEXIBLE FRAME FOR A SATELLITE DRAG SAIL

NSCM-30

JAN A. NIKOLAJSEN[*], PETER R. LAURIDSEN [†] ANDERS S. KRISTENSEN [†]

[*] Department of Civil Engineering, Division Structural and Offshore Engineering
Aalborg University Esbjerg
Niels Bohrs Vej 8, 6700 Esbjerg, Denmark
e-mail: jan@civil.aau.dk,
[†]e-mail: prl@civil.aau.dk e-mail: ask@civil.aau.dk

Key words: Highly flexible structure, Computational Methods, Nonlinear FEA, Contact problems, Penalty Methods.

Summary. This processes the highly flexible frame for a drag sail in FEA with contacts and compared with experiments to get a better understanding of how well ANSYS can describe highly non-linear systems.

1 INTRODUCTION

Space Debris is a growing concern because the need for more satellites in Low Earth Orbit is imminent for many companies. With drag augmented solutions as Self-deployable Space Structures (SDSS)[1] that rely on drag sails, new satellites can be deorbited after the end of their operation. The SDSS drag sail is deployed with a highly flexible frame[2]. For the system to deploy from its complex folding position, the elastic energy in the frame is used. The highly flexible frames are made of stainless steel with a yield strength of 1600 MPa. From related research[3],[4] stress levels during the folding process have been determined. The folding of the highly flexible frame is done by holding one point and twisting at another point by 360 degrees[3]. To get an insight into the influence from self-contact in the highly flexible frame while folding a transient FEA with pure penalty contact elements has been performed in order to understand the complex stress state and frictional condition in the folding process. Pure penalty based contact gives the fastest and easiest convergence to model the full folding process. This transient FEA is then compared to experimentally determined forces and torsional moments and validate the ANSYS solution[5].

2 THE HIGHLY FLEXIBLE FRAME

The drag sail is developed for a CubeSat system as this is currently the smallest system on the market for satellites. By understanding the complexity and limitations this Spacecraft size impose, it is relatively easy to scale up of the drag sail for larger satellites. The setup for the numerical analysis and the experiment is done by holding point A in Figure **1** of the highly flexible frame and rotating the point B of the frame 360 degrees. The cross-section is

rectangular with the frames inner diameter D=245 mm as illustrated in Figure 1and the selected material is an austenitic stainless steel with an Elastic modulus of E = 200,000 MPa. This research considers an SDSS without the drag sail, i.e. only self-contact of the flexible frame is considered.

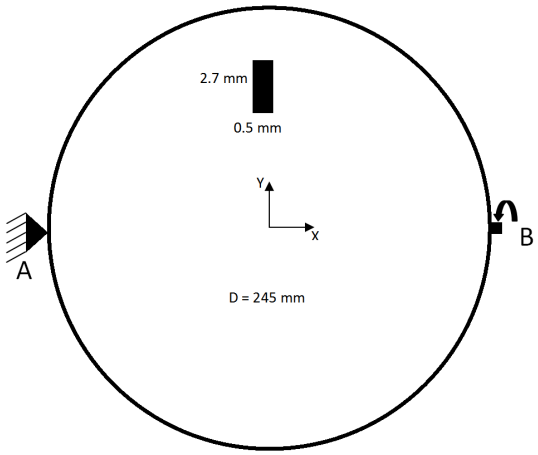

Figure 1: Boundary condition for the highly flexible frame and the cross-section. D is the inner diameter of flexible frame. The material used is an austenitic stainless Steel with an Elastic modulus of E = 200,000 MPa

By using a rectangular cross-section, the instability from its weak axis is utilized for an easier folding (bifurcation) and lower stresses as seen in earlier research[3]. The ratio between height and wide of the cross-section needs to be 3 or higher to assure a smooth folding process. The setup for the experiment is done in a holding test rig to control the movement (rotation and linear translation of point B in figure 1) and holds the HBM multiaxial measurement tool, so the 3 forces and 3 moments are measured as seen in Figure 2.

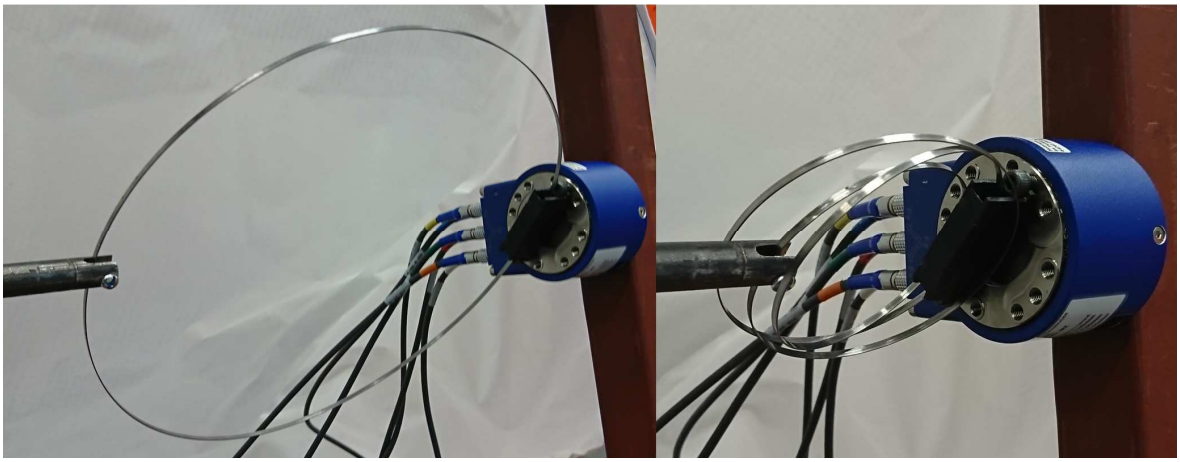

Figure 2: Configuration of the test setup unfolded(left) and folded frame(right) Left - The HBM multiaxial measurement tool (blue) in the unloaded condition. Right - The folded frame where the self-contact can be observed.

In the FEA point B in figure 1 translates frictionless whereas in the experiment point B is supported in a mechanical guide. In the FEA the contact elements are configured as a pure penalty to achieve convergence in the simulations. Pure penalty contacts use the normal force P as seen in equation 1. This is a factor between the penetration u of elements and a normal stiffness K and where the normal stiffness K is a factor of Young's modulus E standard set to 0.1 times the Young's modulus.

$$P = \begin{Bmatrix} 0, \ if \ u_n > 0 \\ K \, u_n, \ if \ u_n \leq 0 \end{Bmatrix} \begin{matrix} u_n \ disten \ of \ penatreation \\ K \ contact \ normal \ stiffness \end{matrix} \tag{1}$$

The friction coefficient μ of the material gives frictional stresses $\tau_{y,z}$ as seen in equation 2.

$$\tau_y = \begin{Bmatrix} K_s u_y, & if \ \tau = \sqrt{\tau_y^2 + \tau_z^2} - \mu P < 0 \ (sticking) \\ \mu K_n u_y, & if \ \tau = \sqrt{\tau_y^2 + \tau_z^2} - \mu P = 0 \ (sliding) \end{Bmatrix} \tag{2}$$

These parameters are then adjusted to give a comparable solution to the experiment the allowable penetration factor u_n, normal stiffness k and friction μ:

- Penetration factor u_n 0.5 mm - 2.5 mm
- Normal stiffness factor K 0.1
- Friction factor μ 0.2

The FEA is a solid model with low order elements, and all the surfaces are selected to be contact and target to describe the self-contact issues in the folding process. Gravity is neglected under these circumstances as the forces are so small compared to the torsional moment needed to fold the frame.

3 RESULTS

Comparing the results from FEA and the experiment gives a good correlation up to 210 degrees here the experiment moment do not drop as far down as the FEA as seen in Figure **3**. At a rotation angle of 210 degrees, the torsional moment found in the FEA is lower than found in the measurements. This is due to that at this point the terminal bifurcation of the folding has occurred, and the friction in the guide is dominating the response. The FEA continues to go down and ends up in a self-locking position so that the frame will not unfold by itself when released.

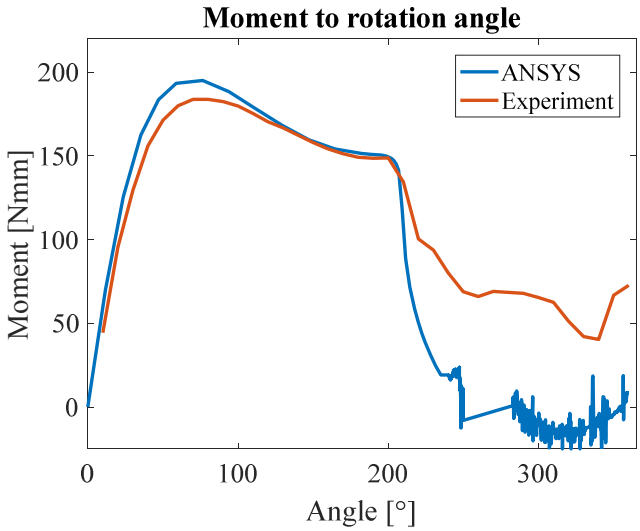

Figure 3: Comparing the torsional moment between FEA (blue curve) and experiment (red curve). There is a good comparison between FEA and measurements until a rotation angle of 210 degrees. Only up to a rotation angle of 340 degrees are the measurements valid due to boundary conditions in the test rig

4 CONCLUSIONS

A test rig to study internal forces and frictional forces during folding of highly flexible frames has been devised. The initial test indicates good agreement with numerical models. By comparing the moment under the folding process between the FEA and the experiments, it is seen that op to a rotation angle of 210 degrees is incoherence. By changing the penetration factor u_n in the contact elements gives no noticeable difference only fluctuation with the moment. The test rig will be used in further work to determine the forces and moments in unfolding which is non-linear dynamic and the highly flexible frame with and without drag sail.

REFERENCES

[1] A. S. Kristensen, L. Damkilde, and L. Alminde, “Self-Deployable Deorbiting Space Structure (Sdss),” vol. 2013, no. April 2013, pp. 2–4, 2014.

[2] P. Frank Pai and C. W. LaPierre, *Highly Flexible Structures Modeling Computation and Experimentation*. American Institute of Aeronautics and Astronuutics, 2007.

[3] J. A. Nikolajsen, P. R. Lauridsen, and A. S. Kristensen, “Modelling and analysis of the folding principle used in self-deployable deorbiting space structures,” in *7th European Conference on Space Debris*, 2017, no. April, pp. 18–21.

[4] P. R. Lauridsen, J. A. Nikolajsen, and A. S. Kristensen, “Analysis of pretension and stress stiffening in a self-deployable deorbiting space structure,” in *7th European Conference on Space Debris*, 2017, no. April, pp. 18–21.

[5] Ansys, “ANSYS, Inc. Theory Reference,” *User Ref. Man. Version 9.0*, no. November, p. 1067, 2004.

30th Nordic Seminar on Computational Mechanics
NSCM-30
J. Høgsberg. N.L. Pedersen (Eds.)
2017

FINITE-LIFE FATIGUE CONSTRAINTS IN 2D TOPOLOGY OPTIMIZATION OF CONTINUA

JACOB OEST* AND ERIK LUND†

Materials and Production, Aalborg University
Fibigerstraede 16, 9220 Aalborg East, Denmark
e-mail: *oest@mp.aau.dk, †el@mp.aau.dk

Key words: Topology Optimization, Fatigue Constraints, Adjoint Method.

Summary. Topology optimization of 2D continua with the objective of minimizing the mass while considering finite-life fatigue constraint is considered. The structure is subjected to proportional variable-amplitude loading. The topology optimization problem is solved using the density approach. The fractions of fatigue damage are estimated using the stress-based Sines fatigue criterion and $S-N$ curves, while the accumulated damage is estimated using Palmgren-Miner's rule. The method is a natural extension of classical density-based topology optimization with static stress constraints, and thus utilizes many of the same methods. A benchmark example is presented.

1 INTRODUCTION

Since the seminal work by Bendsøe and Kikuchi[1], the topology method has been applied to the optimal material distribution problem in a variety of fields. Most work has been done on minimizing compliance subject to an overall volume constraint, but the method has also been extended to e.g. stress-constrained optimization, fluid-structure interaction problems, and many complicated multi-physics problems. Limited research on fatigue-constrained topology optimization has been published. However, fatigue failure is one of the most common failure modes of structures subjected to repeated loading. A few works on fatigue-constrained topology optimization have been published, where most work either design for infinite life, e.g. Collet et al.[2], or reformulate the fatigue problem into a static stress-constrained problem, see e.g. Holmberg, Torstenfeldt, and Klarbring[3].

In the recently published work by Oest and Lund[4] a method is proposed where the entire fatigue analysis is included directly in the optimization problem, including the entire load-history. By utilizing an effective adjoint formulation of the design sensitivities, the computational cost of the finite-life fatigue-constrained problem is comparable to static stress-constrained topology optimization. The method is currently limited to linear quasi-static finite element analysis, linear elastic material behavior, and proportional loading. The method can sometimes experience gray-scale issues, which in the current work is addressed using the heaviside density filter.

2 PHYSICS

A reference load vector $\hat{\boldsymbol{P}}$ is applied to a structure, and a reference displacement $\hat{\boldsymbol{u}}$ is obtained by solving the static equilibrium state equation:

$$\boldsymbol{K}(\tilde{\boldsymbol{x}}(\boldsymbol{x}))\hat{\boldsymbol{u}} = \hat{\boldsymbol{P}} \tag{1}$$

$\boldsymbol{K}$ is the interpolated global stiffness matrix, $\tilde{\boldsymbol{x}}$ is the vector containing the filtered (physical) variables, and $\boldsymbol{x}$ is the design variables. The response for any other magnitude of the reference load can then be determined efficiently by linear superposition of the reference displacement vector. The global stiffness matrix is interpolated using the well-known modified SIMP with a penalization factor $p = 3$. Consequently, the effective Young's modulus E_e in each element e is given by:

$$E_e(\tilde{x}_e(\boldsymbol{x})) = E_{min} + \tilde{x}_e(\boldsymbol{x})^p(E_0 - E_{min}), \qquad \boldsymbol{x} \in [0;1] \tag{2}$$

Here $E_{min} << E_0$ is a lower bound on the effective modulus representing the stiffness of a void region. The element reference stresses $\hat{\sigma}_e$ are obtained using the reference displacement and relaxed using the *qp*-stress relaxation method[5,6]:

$$\hat{\sigma}_e = \tilde{x}_e(\boldsymbol{x})^q \boldsymbol{E}\boldsymbol{B}\hat{\boldsymbol{u}}_e \tag{3}$$

Here $0 \leq q < 1$ is the stress interpolation exponent, $\boldsymbol{E}$ is the constitutive matrix, $\boldsymbol{B}$ is the strain-displacement matrix, and $\boldsymbol{u}_e$ is the vector of element displacements.

To estimate each fraction of damage caused by each load cycle, the stress-based Sines criterion is applied. The Sines criterion includes all stress components and accounts for amplitude and mean stresses, which are determined using traditional rainflow-counting. A beneficial property of the Sines criterion is that it reduces the stress state to an equivalent uniaxial stress, $\tilde{\sigma}_{e_i}$, for each stress cycle i. This allows for the use of $S - N$ curves and Palmgren-Miner's rule. In the present work, a linear $S - N$ curve has been applied. Expressed in stress reversals, the $S - N$ relation is:

$$\tilde{\sigma}_{e_i} = \sigma_f^{'}(2N_{e_i})^b \tag{4}$$

$\sigma_f^{'}$ and b are material parameters, and N_{e_i} is the expected amount of cycles to failure in each element e for stress cycle i. The fractions of damage are accumulated using Palmgren-Miner's rule by:

$$D_e = c_D \sum_{i=1}^{n_i} \frac{n_i}{N_{e_i}} \leq \eta \tag{5}$$

$c_D \geq 1$ is a scaling factor to make the data representative of a lifetime, n_i is the amount of cycles for a stress cycle, and η is the allowable damage. The above equation constitutes a fatigue constraint in every element. To reduce the computational costs, the P-norm method is applied to reduce the large amount of constraints to a single global constraint.

Due to the cumulative nature of Palmgren-Miner's rule, it is possible to solve just one adjoint equation per load case[4]. Thus, for large load series, the computational costs are only increased slightly, as the amount of adjoint equations is independent of the size of the load cases.

In the original work, it was shown that grayscale issues may occur. To address this the regularization scheme has in this work been changed from the consistent density filter to the heaviside density filter[7]. The heaviside filter is given by:

$$\tilde{x}_e = 1 - e^{-\beta \bar{x}_e} + \bar{x}_e e^{-\beta} \tag{6}$$

$\bar{x}_e$ is the density as obtained using the classical density filter, and β is a filter parameter. For a β value of zero, the physical variables $\tilde{\boldsymbol{x}}$ are similar to those obtained using the classical density filter. When β goes to infinity the design variables are all $0-1$. Note that the implementation is using the standard element density, and not the mapped nodal design variables which reportedly improves the problem numerically.

3 EXAMPLES

An optimized cantilever beam with two holes added to introduce stress concentrations is shown in Figure 1. The asymmetric design is a direct consequence of the mean stress contributions caused by the loading condition. The example is obtained using careful optimizer settings, a very slowly increasing β parameter, and with a P-norm factor of $P = 8$. For comparison, the same problem is solved using the original formulation, i.e. with a density filter and a P-norm factor of $P = 12$. However, as compared with the original publication, more iterations are allowed in this framework in both examples. The

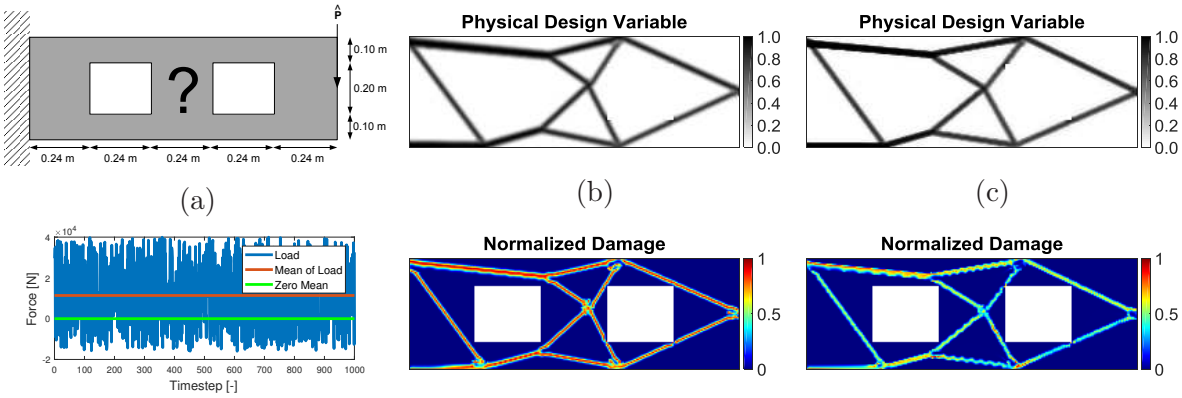

Figure 1: Minimization of mass problem with fatigue constraints demonstrated on a cantilever beam, sketched in (a). The time-varying load is shown in (d). The original formulation from Oest and Lund[4] is shown in (b) and (e), and the results obtained using Heaviside filtering is shown in (c) and (f).

design obtained using the heaviside is with $\beta = 20$, presents a slightly more $0 - 1$ design. However, the formulation adds an additional tuning parameter and is more difficult to solve. Thus, a lower P-norm factor had to be applied, which resulted in a less well-distributed damage as compared with the original formulation.

3.1 CONCLUSION

A minimization of mass topology optimization problem constrained by finite-life fatigue is demonstrated using the heaviside filter. However, the added non-linearity makes the already very non-linear problem even more difficult to solve. Thus, the example shown here is solved with a P-norm parameter lower than in the original work. It is not necessarily worth the extra effort to use the heaviside filter for this specific purpose as compared with the density filter. However, if the optimization can be made more stable by other means, the heaviside filter may prove a good regularization approach for fatigue constrained topology optimization using the density method.

Acknowledgements This research is part of the ABYSS project, sponsored by the Danish Council for Strategic Research, Grant no. 1305-00020B. The support is acknowledged.

REFERENCES

[1] Bendsøe, M. P. & Kikuchi, N. Generating optimal topologies in structural design using a homogenization method. *Computer Methods in Applied Mechanics and Engineering* **71**, 197–224 (1988).

[2] Collet, M., Bruggi, M. & Duysinx, P. Topology optimization for minimum weight with compliance and simplified nominal stress constraints for fatigue resistance. *Structural and Multidisciplinary Optimization* **55**, 839–855 (2017).

[3] Holmberg, E., Torstenfelt, B. & Klarbring, A. Fatigue constrained topology optimization. *Structural and Multidisciplinary Optimization* **50**, 207–219 (2014).

[4] Oest, J. & Lund, E. Topology optimization with finite-life fatigue constraints. *Structural and Multidisciplinary Optimization* 1–15 (2017).

[5] Bruggi, M. On an alternative approach to stress constraints relaxation in topology optimization. *Structural and Multidisciplinary Optimization* **36**, 125–141 (2008).

[6] Le, C., Norato, J., Bruns, T., Ha, C. & Tortorelli, D. Stress-based topology optimization for continua. *Structural and Multidisciplinary Optimization* **41**, 605–620 (2010).

[7] Guest, J. K., Prévost, J. H. & Belytschko, T. Achieving minimum length scale in topology optimization using nodal design variables and projection functions. *International Journal for Numerical Methods in Engineering* **61**, 238–254 (2004).

30th Nordic Seminar on Computational Mechanics
NSCM-30
J. Høgsberg. N.L. Pedersen (Eds.)
2017

ON RECOVERY-BASED ERROR ESTIMATION IN ISOGEOMETRIC ANALYSIS OF THIN PLATE PROBLEMS

KNUT M. OKSTAD*, TROND KVAMSDAL*†, MUKESH KUMAR‡ AND KJELL M. MATHISEN♯

*SINTEF Digital, Department of Mathematics and Cybernetics
N-7465 Trondheim, Norway
e-mail: Knut.Morten.Okstad@sintef.no, Trond.Kvamsdal@sintef.no,
web page: http://www.sintef.no/

†NTNU, Department of Mathematical Sciences
N-7491 Trondheim, Norway
e-mail: Trond.Kvamsdal@ntnu.no - Web page: http://www.ntnu.no

‡College of Charleston, South Carolina, USA
e-mail: kumarm@cofc.edu

♯NTNU, Department of Structural Engineering
N-7491 Trondheim, Norway
e-mail: Kjell.Mathisen@ntnu.no - Web page: http://www.ntnu.no

Key words: Error Estimation, Isogeometric Analysis, Thin Plate Problems.

Summary. Recovery-based error estimation for thin plate problems (the bi-harmonic equation) is revisited in the context of Isogeometric analysis. The energy-norm error between the recovered and finite element solutions is appended by the residual error in the recovered solution, to obtain an upper bound estimate.

1 Introduction

Through the isogeometric finite element analysis concept[1] using splines as basis functions instead of traditional Lagrange polynomials, the Kirchhoff-Love thin plate equations can efficiently be solved numerically without the introduction of rotational degrees of freedom, since the inter-element continuity is of order $p-1$ for elements of order p. Using the more recently proposed Locally Refined B-splines[2], we may also perform adaptive analyses of such problems based on a posteriori error estimates.

In the current study, the recovery techniques studied by the authors earlier[3,4] are revisited and enhanced by including residual-based estimates as proposed by Kumar *et al.*[5,6]. Due to the increased inter-element continuity resulting from the use of the splines discretization, the inclusion of such estimates is rather simple and can be added without significant computational cost.

2 The thin plate problem

The partial differential equation based on Kirchhoff-Love plate theory for a thin plate with a constant stiffness $D = \frac{Et^3}{12(1-\nu^2)}$, where E is the Young's modulus, ν the Poisson's ratio, and t the plate thickness, can be written

$$
\begin{aligned}
w_{,\alpha\alpha\beta\beta} &= \frac{p}{D} && \forall\, x_\alpha \in \overline{\Omega} && (1)\\
m_{\alpha\beta} n_\beta &= \bar{M}_\alpha && \forall\, x_\alpha \in \partial\Omega_m && (2)\\
D\, w_{,\alpha\alpha\beta} n_\beta &= -\bar{Q} && \forall\, x_\alpha \in \partial\Omega_q && (3)\\
w &= \bar{w} && \forall\, x_\alpha \in \partial\Omega_w && (4)\\
w_{,\alpha} n_\alpha &= \bar{\theta} && \forall\, x_\alpha \in \partial\Omega_\theta && (5)
\end{aligned}
$$

where Einsteins summation convention over repetitive indices is assumed and α and β are running indices over coordinate directions, i.e., $w_{,\alpha\alpha\beta\beta} := w_{,xxxx} + 2w_{,xxyy} + w_{,yyyy}$. The bending moments, $m_{\alpha\beta}$, are related to the unknown transverse displacement field w, through $m_{xx} = -D(w_{,xx} + \nu w_{,yy})$, $m_{yy} = -D(w_{,yy} + \nu w_{,xx})$ and $m_{xy} = -D(1-\nu)w_{,xy}$. Furthermore, n_α is the outward-directed normal vector on the boundary $\partial\Omega$, $\bar{M}_\alpha$ denote some applies edge torque and moment in the local axes directions of $\partial\Omega_m = \partial\Omega \setminus \partial\omega_\theta$, and $\bar{Q}$ denotes the applied transverse shear force on $\partial\Omega_q = \partial\Omega \setminus \partial\omega_w$. Finally, $p = p(x_\alpha)$ is the distributed transverse load, whereas $\bar{w}$ and $\bar{\theta}$ denote the prescribed transverse displacement and normal rotation at the boundaries $\partial\Omega_q$ and $\partial\Omega_\theta$, respectively.

The weak form is obtained by multiplying Equation (1) by a test function $v(x_\alpha) \in \mathcal{V}(x_\alpha)$ and then integrating over the domain Ω. The, after applying Green's identity twice and other manipulations, we arrive at the following. Find $w \in \mathcal{W}(x_{,\alpha})$ such that

$$
a(w, v) \;=\; l(v) \quad \forall\, v \in \mathcal{V}(x_\alpha) \tag{6}
$$

where we introduce the bilinear form $a(w, v)$ and the linear functional $l(v)$ as follows

$$
\begin{aligned}
a(w, v) &:= D \int_\Omega w_{,\alpha\beta}\, v_{,\alpha\beta}\, \mathrm{d}A && (7)\\
l(v) &:= \int_\Omega p\, v\, \mathrm{d}A + \int_{\partial\Omega_q} \bar{Q}\, v\, \mathrm{d}S + \int_{\partial\Omega_m} \bar{M}_\alpha\, v_{,\alpha}\, \mathrm{d}S && (8)
\end{aligned}
$$

Proper function spaces for the trial- and test displacements w and v are, respectively

$$
\begin{aligned}
\mathcal{W} &= \left\{ w \in H^2(\Omega) \mid w = \bar{w} \text{ on } \partial\Omega_w \text{ and } v_{,\alpha} n_\alpha = \bar{\theta} \text{ on } \partial\Omega_\theta \right\} && (9)\\
\mathcal{V} &= \left\{ v \in H^2(\Omega) \mid v = 0 \text{ on } \partial\Omega_w \text{ and } v_{,\alpha} n_\alpha = 0 \text{ on } \partial\Omega_\theta \right\} && (10)
\end{aligned}
$$

and we then introduce finite dimensional sub-spaces of $\mathcal{W}^h \subset \mathcal{W}$ and $\mathcal{V}^h \subset \mathcal{V}$ to obtain our finite element (FE) formulation. In the current study, we use quadratic tensor-product splines in our discretization.

3 Error estimates

An estimate of the discretization error in the FE solution is obtained by projecting the discontinuous secondary solution, $w^h_{,\alpha\beta}$ onto the basis used for the the primary solution w^h, resulting in the recovered solution, $w^*_{,\alpha\beta}$. Herein, we use global L_2-projection to obtain this recovered continuous solution. An error indicator based on the energy norm is then

$$\eta^* = \|w^* - w^h\|_E \tag{11}$$

where $\|w\|_E := \sqrt{a(w,w)}$. The error estimate given by Equation (11) will underestimate the true error, defined as $\|w - w^h\|_E$, which is bounded by

$$\|w - w^h\|_E \leq \|w^* - w^h\|_E + \|w - w^*\|_E \tag{12}$$

An upper bound estimate of the second term of Equation (12) can be obtained by a residual-based estimate $\|w - w^*\|_E \leq \mathrm{Res}(w^*)_E$, with

$$\mathrm{Res}(w^*)_E := \sqrt{\sum_{k=1}^{n_{\mathrm{el}}} \left\{ h_k^4 \|R^*\|^2_{L_2(\Omega_k)} + h_k \|J^*_m\|^2_{L_2(\partial\Omega_{m\,k})} + h_k^3 \|J^*_q\|^2_{L_2(\partial\Omega_{q\,k})} \right\}} \tag{13}$$

where h_k denotes some characteristic size of element k (typically the length of the longest diagonal). R^*, J^*_m, J^*_q are, respectively, the interior residual of the recovered solution $w^*_{,\alpha\beta}$, and the jump (boundary residual) between the recovered solution and the prescribed edge moment $\bar{M}_\alpha$ and shear force $\bar{Q}$.

4 Numerical example

We consider the bi-harmonic equation solved on the bi-unit domain:

$$\nabla^4 w = w_{,xxxx} + 2w_{,xxyy} + w_{,yyyy} = f(x,y) \quad \forall\, (x,y) \in [-1,1] \times [-1,1] \tag{14}$$

subjected to the homogeneous Dirichlet boundary conditions

$$\begin{aligned} w &= 0 \quad \forall\, (x,y) \in (\{-1,1\} \times [-1,1]) \cup ([-1,1] \times \{-1,1\}) \\ w_{,x} &= 0 \quad \forall\, (x,y) \in \{-1,1\} \times [-1,1] \\ w_{,y} &= 0 \quad \forall\, (x,y) \in [-1,1] \times \{-1,1\} \end{aligned} \tag{15}$$

With the loading function equal to

$$f(x,y) = 24(5x-1)(y^2-1)^2 + 32(x-1)(5x^2+2x-1)(3y^2-1) + 24(x-1)(x^2-1)^2 \tag{16}$$

the solution that satisfies Equations (14) and (15) becomes

$$w(x,y) = (x-1)(x^2-1)^2(y^2-1)^2 \tag{17}$$

which is 5^{th} order in x-direction and 4^{th} order in y-direction.

We then conduct a FE analysis on a series of uniformly refined meshes, using a bi-quadratic spline basis. Since the analytical solution is available, we can compare the following error quantities and their associated effectivity indices

- $\eta^* = \|w^* - w^h\|_E$ $\quad \theta^* = \eta^*/\|w - w^h\|_E$
- $\eta^{EX} = \|w^* - w^h\|_E + \|w - w^*\|_E$ $\quad \theta^{EX} = \eta^{EX}/\|w - w^h\|_E$
- $\eta^{RES} = \|w^* - w^h\|_E + \mathrm{Res}(w^*)_E$ $\quad \theta^{RES} = \eta^{RES}/\|w - w^h\|_E$

The results are shown in Figure 1. We see that the residual estimate $\mathrm{Res}(w^*)_E$ has the same rate of convergence as the corresponding true error $\|w-w^*\|_E$ and give a conservative estimate, but its convergence rate is higher than that of η^* such that the corresponding effectivity index approach unity as the mesh is refined.

REFERENCES

[1] Hughes, T. J. R., Cottrell, J. A. & Bazilevs, Y. Isogeometric Analysis: CAD, Finite Elements, NURBS, Exact Geometry and Mesh Refinement. *Computer Methods in Applied Mechanics and Engineering* **194**, 4135–4195 (2005).

[2] Johannessen, K. A., Kvamsdal, T. & Dokken, T. Isogeometric Analysis using LR B-splines. *Computer Methods in Applied Mechanics and Engineering* **269**, 471–514 (2014).

[3] Kvamsdal, T. & Okstad, K. M. Error Estimation based on Superconvergent Patch Recovery using Statically Admissible Stress Fields. *International Journal for Numerical Methods in Engineering* **42**, 443–472 (1998).

[4] Okstad, K. M., Kvamsdal, T. & Mathisen, K. M. Superconvergent Patch Recovery for Plate Problems using Statically Admissible Stress Resultant Fields. *International Journal for Numerical Methods in Engineering* **44**, 697–727 (1999).

[5] Kumar, M., Kvamsdal, T. & Johannessen, K. A. Simple a Posteriori Error Estimators in Adaptive Isogeometric Analysis. *Computers and Mathematics with Applications* **70**, 1555–1582 (2015).

[6] Kumar, M., Kvamsdal, T. & Johannessen, K. A. Superconvergent Patch Recovery and a Posteriori Error Estimation Technique in Adaptive Isogeometric Analysis. *Computer Methods in Applied Mechanics and Engineering* **316**, 1086–1156 (2017).

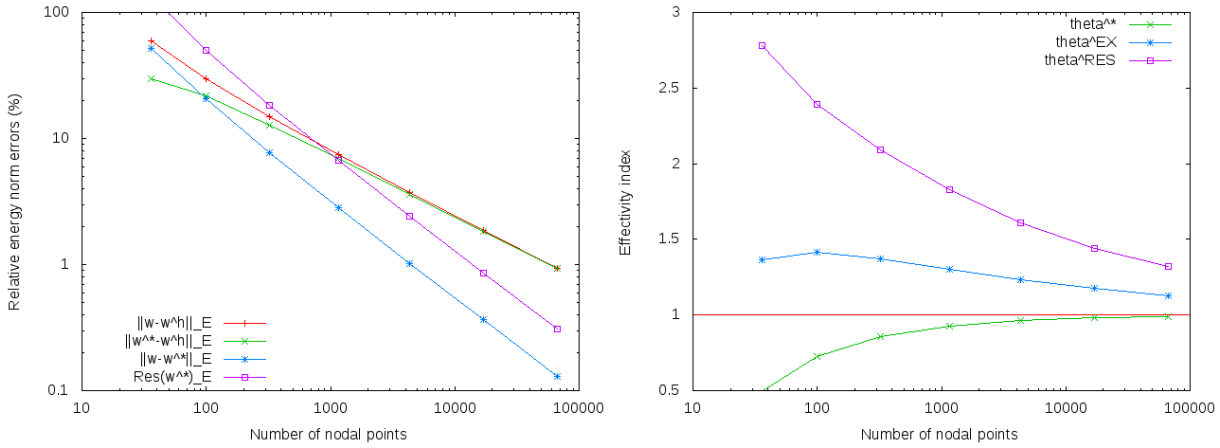

Figure 1: Convergence results for the bi-harmonic problem using quadratic splines discretization.

30th Nordic Seminar on Computational Mechanics
NSCM-30
J. Høgsberg. N.L. Pedersen (Eds.)
2017

MULTIAXIAL FATIGUE ANALYSIS SOFTWARE - FATLAB

M.M. PEDERSEN

Department of Engineering
Mechanical Engineering Section
Aarhus University, Denmark
e-mail: mmp@eng.au.dk, web page: www.fatiguetoolbox.org

Key words: Fatigue, FE post processing, multiaxial fatigue, critical plane analysis.

Summary. This paper presents a novel fatigue analysis software, called Fatlab, for post processing FE models. The program is open-source and intended for teaching and research as well as practical engineering. It handles both non-linear FE models and multiaxial loading using the critical plane approach.

1 INTRODUCTION

Fatigue analysis can be a very cumbersome and time-consuming process especially in case of non-simple geometry and/or loading, e.g. multiaxial loading. A number of FE post-processing softwares have therefore been developed, e.g. MSC.Fatigue[1], nCode DesignLife[2], FEMFAT[3], winLIFE[4], etc.

The drawback of using such commercial software, except from the generally high price[5], is the closed nature of the code. The user cannot see *exactly* how the calculations are performed. It is also difficult to adapt the software to industry-specific requirements, e.g. special load simulators, special assessment criteria or the like. Additionally, the implementation and testing of newly proposed scientific methods is difficult or impossible.

To remedy these shortcomings many companies develop their own in-house fatigue software. Recently, some research groups have also developed such software, e.g. P-FAT[6] and PragTic[5]. Neither are open-source, but PragTic is available as freeware.

This paper serves as short introduction to Fatlab, a novel post processing software for fatigue analysis developed by the author. Whereas the calculation procedures applied in Fatlab are probably more or less identical to the other programs, Fatlab is different on the following key aspects; 1) It is free and open-source, 2) It is developed in Matlab, enabling easy modification by engineers and students with limited programming experience. 3) It has an intuitive, visual user interface designed for learning and de-mystifying advanced concepts in fatigue analysis.

2 FATLAB WORKFLOW

Figure 1 shows the workflow of the program. The process is repeated for each node in the model or for a selected subset.

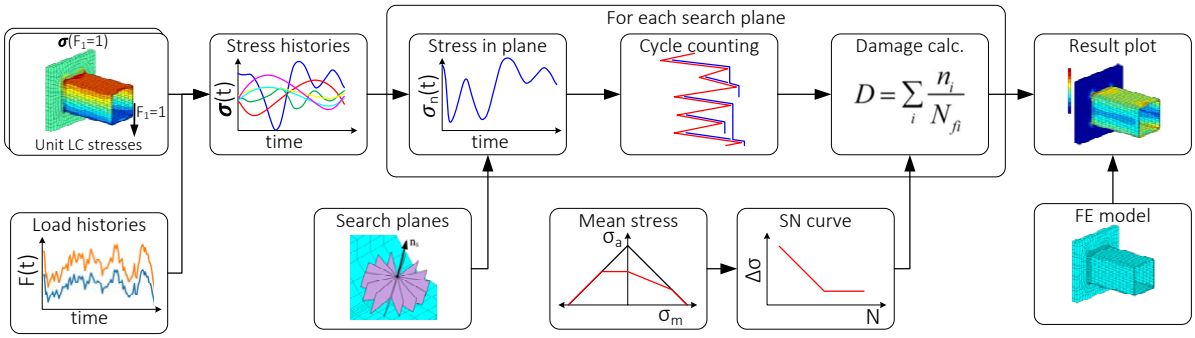

Figure 1: Fatigue analysis flow.

Firstly, the time-dependent stress tensor (the stress-time history) is established as a starting point for the analysis.

$$\boldsymbol{\sigma}(t) = \begin{bmatrix} \sigma_{xx}(t) & \tau_{xy}(t) & \tau_{xz}(t) \\ \tau_{xy}(t) & \sigma_{yy}(t) & \tau_{yz}(t) \\ \tau_{xz}(t) & \tau_{yz}(t) & \sigma_{zz}(t) \end{bmatrix} \tag{1}$$

This can be achieved in several ways using scaling/interpolation and superposition of stresses from unit load cases (LCs). Non-linear behavior in the FE model (e.g. contact, large displacement, varying load directions, etc.) is also supported by allowing two or more separate unit LC stresses for each load component and using interpolation.

In the most elementary case, unit LC stresses $\boldsymbol{\sigma}_{F_i=1}$ are scaled linearly with the associated load-time history $F_i(t)$ and superimposed.

$$\boldsymbol{\sigma}(t) = \sum_{i=1}^{n} \boldsymbol{\sigma}_{F_i=1} \cdot F_i(t) \tag{2}$$

Various measures of fatigue relevant stresses can then be resolved from this, e.g. principal stresses. In case of multiaxial loading however, the direction of the principal stresses may change over time and therefore they constitute a poor choice. Multiaxial fatigue is usually analyzed using the critical plane approach.

3 CRITICAL PLANE ANALYSIS

The idea behind the critical plane approach is to find the plane in which cracking will initiate, i.e. *the critical plane*. To do so, a number of search planes intersecting the surface orthogonally and at some inclination are searched for the maximum value of a damage parameter. The plane that maximizes the damage parameter is then called the critical

plane. Each search plane is defined by its unit normal vector $\mathbf{n}$, which is again defined by the angle to the local x-axis θ and the inclination angle ϕ, as shown in Figure 2a.

The tip of the stress vector $\boldsymbol{S}_n$ describes some curve in stress space, as illustrated in Figure 2b. It can then be divided in a component normal to the plane, i.e. the normal stress

$$\sigma_n(t) = \mathbf{n}^T \boldsymbol{\sigma}(t) \mathbf{n} \tag{3}$$

and parallel to the plane, i.e. the shear stress

$$\boldsymbol{\tau}(t) = \boldsymbol{\sigma}(t)\mathbf{n} - \mathbf{n}\mathbf{n}^T \boldsymbol{\sigma}(t)\mathbf{n} \tag{4}$$

The range of normal stress is easily resolved, also for variable amplitude loading, whereas the range of shear stress is much more difficult to find.

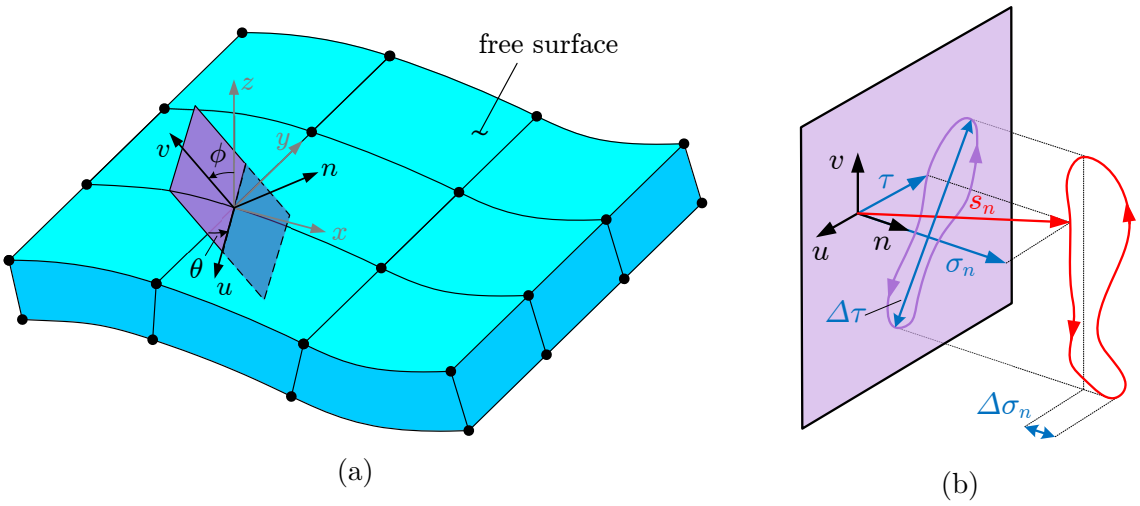

Figure 2: Search plane definition and extraction of stress ranges[7].

A damage parameter must then be calculated for each search plane in order to determine which is the critical one. Many proposals have been made as to which particular combination of normal- and shear stress ranges should be the relevant for fatigue.

The simplest is the so-called normal stress criterion, typically applied in the Danish wind industry for fatigue assessment of ductile cast iron components. Here, we search for the plane that experience the maximum damage calculated from normal stress alone.

The criterion can be expressed as

$$\max_{0 \le \theta \le \pi} \Delta\sigma_{n,eq}(\theta) \le \Delta\sigma_R \tag{5}$$

where $\Delta\sigma_{n,eq}$ is the damage equivalent stress range calculated using Rainflow counting and Palmgren-Miner damage accumulation and $\Delta\sigma_R$ is the fatigue resistance.

4 RESULTS

Figure 3 shows example results for a wind turbine hub; utilization ratio as contour plot over the model. The lower right part shows an assessment of multiaxiality in a selected node, i.e. the magnitude of the largest principal stress as a function of its direction.

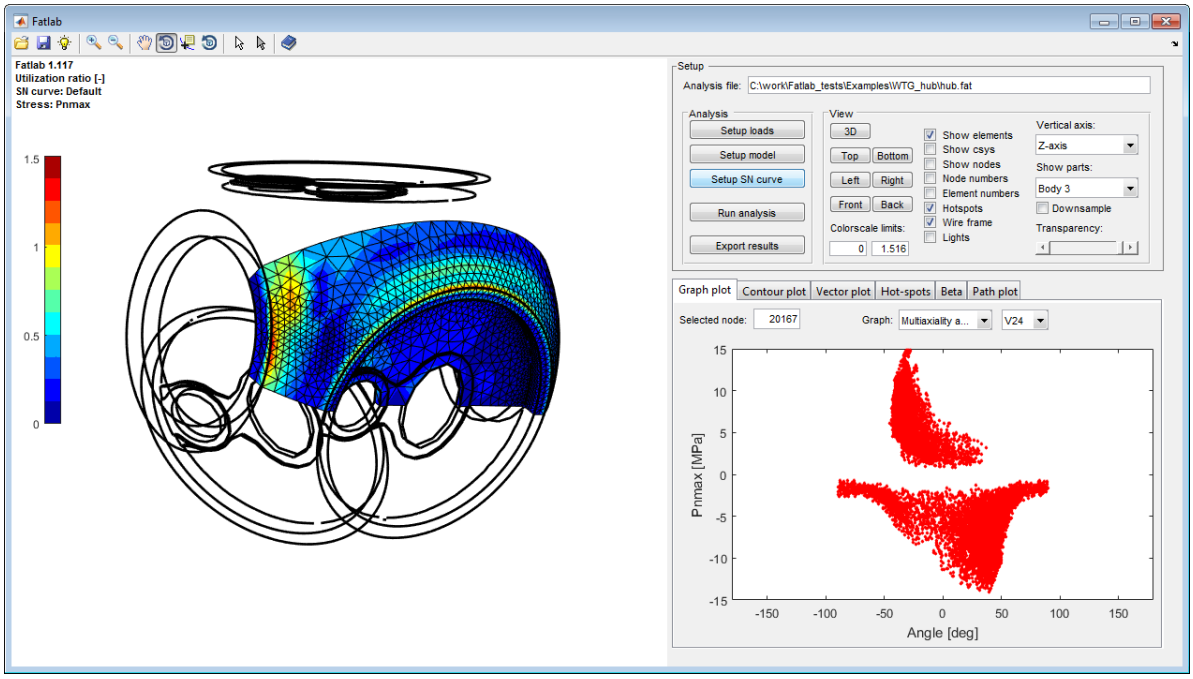

Figure 3: Example results: wind turbine hub section.

REFERENCES

[1] MSC Software. MSC.Fatigue. www.mscsoftware.com.

[2] HBM. nCode software. www.ncode.com.

[3] MAGNA. FEMFAT software. www.femfat.com.

[4] STZ Verkehr GmbH. winLIFE. www.stz-verkehr.de.

[5] Papuga, J. *Mapping of Fatigue Damages Program Shell of FE-Calculation*. Ph.D. thesis, CTU, Prague (2005).

[6] SINTEF. P-FAT, FEM post-processor for fatigue analysis. www.sintef.no/en/sintef-materials-and-chemistry/softvare/fem-post-processor-for-fatigue-analysis/.

[7] Pedersen, M. M. Multiaxial fatigue assessment of welded joints using the notch stress approach. *Int. Journal of Fatigue* (2016).

30th Nordic Seminar on Computational Mechanics
NSCM-30
J. Høgsberg. N.L. Pedersen (Eds.)
2017

ON SHAFT FILLET STRESS CONCENTRATION

N. L. PEDERSEN

Dept. of Mechanical Engineering, Solid Mechanics
Technical University of Denmark
Nils Koppels Allé, Building 404, DK-2800 Kgs. Lyngby, Denmark
e-mail: nlp@mek.dtu.dk

Abstract. A shaft is typically loaded by three different load types; torsional, bending and normal load separately or more generally in combinations. In most cases the size of the shaft is controlled by the constraints on the maximum allowable deflection and/or rotation at e.g. the position of bearings or gears. But if care is not taken to limit the stress concentrations these will control the durability of the shaft. With the use of fillets we have stress concentration described by the stress concentration factor K_t (theoretic stress concentration factor).

The stress concentration factor is typically found in charts in textbooks or papers. The charts are given for circular fillets and for the three different loading situations separately. Many of the charts are based on experimental results from photo elasticity. The typical procedure for the case of a combination of the loading situation is to find the maximum stress resulting from each of the loadings and from these maximum values calculate a reference stress although the maximum stress is not found in the same point for the different load cases. With this procedure we end with a conservative estimate on the strength. Although structural optimization is a mature science and optimization have been performed on shafts this has had limited impact on the practical design of shafts, these are still mainly based on the circular fillet design.

The minimization of maximum stress and thereby increasing the strength of components can be found in many papers. The majority of papers deals with flat or circular bars in tension. Despite the large number of publication no optimization have been reported for the combined loading case to the knowledge of the author.

Typically relatively large improvements of the strength can be found for simple design modifications. Central for these design modifications is that revised design can still operate with the design specified by the standards. The evaluation of the stress concentration is performed using the FE method. For a successful application of shape optimization a couple of point are important. The main point is that the parameterization of the shape with the high stress is done separately from the FE meshing of the design domain, i.e. the position of the nodes in the FE mesh should not be used as design variables

Keywords: Machine elements, Optimization, Bending, Torsion, Normal force, Harmonic FE.

30th Nordic Seminar on Computational Mechanics
NSCM-30
J. Høgsberg. N.L. Pedersen (Eds.)
2017

ANALYSIS OF THE EFFECT OF STRUCTURAL MODIFICATIONS ON TRAFFIC-INDUCED BUILDING VIBRATIONS

P. PERSSON*

* Department of Construction Sciences
Lund University
221 00, Lund, Sweden
e-mail: peter.persson@construction.lth.se, web page: http://www.byggvetenskaper.lth.se/english/

Keywords: Numerical simulations, Ground vibrations, Traffic-induced vibrations, Structural modifications, Building vibrations.

1 INTRODUCTION

The densification that occurs today in the urban development of cities increases the risk of having disturbing building vibrations. An example of an increasingly disturbing source is faster trains, and an example of a more sensitive receiver is the more advanced equipment housed in hospitals and research facilities. The distance between source and receiver is nowadays shortened due to densification of cities, e.g. having railways closer to buildings. Moreover, due to economic and environmental reasons, the building industry tends to build with lighter structural elements and thus use less material, for example, using wooden structures and long-span hollow-core concrete slabs. Analysis of traffic-induced ground vibration is complicated since the problem involves a vast amount of unknown factors, the problem can, in general, roughly be divided into different parts as illustrated in Figure 1: the source; the region of propagation; and the receiver. The parameters and properties of each region affect the vibration levels occurring in a building. In case of predicting or measuring too high vibration levels in a building, vibration-reduction measures can be applied, see for example: soil stabilization[1,4], wave barriers[1,3,4]. For extensive reading see, for example, [5].

The aim of the investigation presented here is to study, by using an efficient computational methodology (see Section 2), to which extent the building structure itself can be used for reducing traffic-induced building vibrations. The objective is to investigate the effect of various geometrical and material parameters of the structural building elements on the vibrational response on slabs.

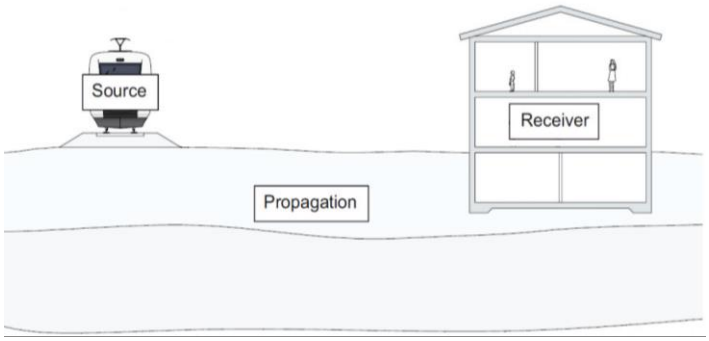

Figure 1: Simplified illustration of the vibration propagation problem.

The work presented in this paper has been performed in collaboration with the master's dissertation students Rickard Torndahl and Tobias Svensson[6], as well as with Professor Kent Persson at the Department of Construction Sciences at Lund University.

2 COMPUTATIONAL MODEL

The computational methodology described in here essentially consists of two parts: model reduction of a finite element (FE) model of the ground; and parametric studies using the reduced ground model assembled with an FE building model. In the first part, a large three-dimensional (3D) FE model of the ground using solid elements is reduced by eliminating degrees-of-freedom (DOFs) by a four step approach: (i) create a full 3D FE model; (ii) set up load cases where the retained DOFs are loaded, one at the time; (iii) using Abaqus for steady-state load case analysis, the displacement results are saved for the retained DOFs; (iv) the results are imported to Matlab where the dynamic compliance matrix is established—its being inverted to obtain a reduced dynamic stiffness matrix for each of the frequencies considered. The DOFs used for loading and evaluation are chosen as retained DOFs. In the second part of the methodology, an FE model of the building structure is established in Abaqus using structural finite elements. Thereafter the system matrices are exported to Matlab and the dynamic stiffness matrix for each frequency is calculated. The dynamic stiffness matrices of the building structure are then assembled, by sharing DOFs, with the reduced dynamic stiffness matrices of the ground model. Now the complex displacement amplitudes can be obtained by using Matlab to solve the steady-state problem.

For the example case used in this study (see Section 3), the computational time for one frequency step in a steady-state analysis took 2.8 s when using the reduced soil model, as aforementioned described, to be solved on two Intel Xeon E5-2650v3 of 2.3 GHz ten-core processors with 62 GB of RAM available. On the same set-up it took 965 s with the non-reduced ground model, hence, the computational time was reduced by 99.7%. Moreover, by using the developed methodology, the parametric studies are now possible to be solved on a regular desktop computer, e.g. Intel Core i5 3.4 GHz processor with 4 GB available RAM—the computational time being in the order of seconds per frequency.

3 PARAMETRIC STUDY

The ground in the example case employed here consists of a rather stiff soil layer resting on top of bedrock. The mass density (ρ), the Young's modulus (E), Poisson's ratio (ν) and the loss factor (η) for the ground materials, as well as the geometry of the reference building are shown in Figure 2. Seven different parameters were varied, one at the time while the others were kept constant. The parameters considered in the analyses being: slab span-length; slab thickness; cross-section of structural building elements; angle of the impinging wave front; and comparison of light-weight (wooden) versus heavy-weight (concrete) building structure. The buildings in the study are subjected to ground vibrations stemming from a vertical harmonic unit point load applied 20 m from the long-side of the building. The frequency range used in the paper is set to 5–50 Hz, applied in steps of 1 Hz. The complex magnitude of the velocities was used as a measure of the vibrational response.

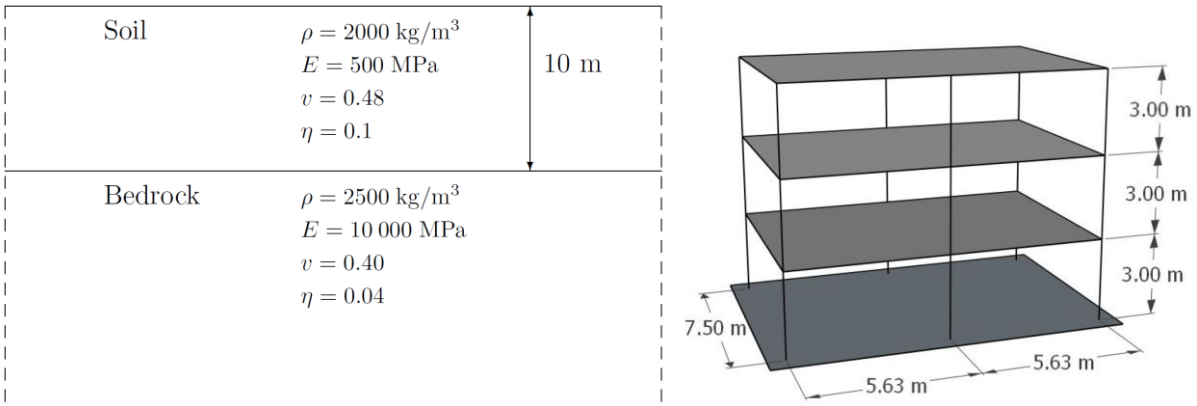

Figure 2: (left) Parameters of the ground. (right) Dimensions of the reference building.

Two examples of results are given in this paragraph. As seen in Figure 3 the response is higher in the heavier concrete building than in the lighter wooden building. This might be explained by two reasons: (1) the excited modes of the wooden building were of higher order than those excited in the concrete building—thus they may require more energy to oscillate; (2) higher damping was applied to the wooden structure than to the concrete structure. The effect of various concrete slab thicknesses on the vibration response at two different floor levels can be seen in Figure 4. As shown, the influence of varying the thickness of the slabs is modest at both slabs. Actually, the response was only decreased by 10–15% by increasing the thickness from 200 to 400 mm. In this case, it is simply not a realistic vibration-reduction measure to increase the slab thickness.

4 CONCLUDING REMARKS

The paper presents a numerical study using an efficient methodology for investigating the effects of structural modifications to a building structure exposed to traffic-induced ground vibrations. The methodology was proved efficient by reducing the computational time by up to 99.7% and making it possible to run the numerical simulations on a regular desktop computer. In this way, several reduced models of different types of soils may be computed on a high-performance computer cluster and be stored in a library. They would then be available for steady-state analysis on a regular desktop computer.

Seven different parameters were varied in order to investigate differences in the vibrational response of the slabs in the building structure. It was found, for example, that varying the slab thickness was of low importance in affecting the vibrational response. However, the order of the modes that were excited was of considerable importance for the slab response. It was also shown that a light-weight wooden building may experience lower slab response than a heavier concrete building, given external soil surface excitation.

The research was carried out in the framework of the project “Urban Tranquility” under the Interreg V program. The author gratefully acknowledge the European Regional Development Fund for the financial support.

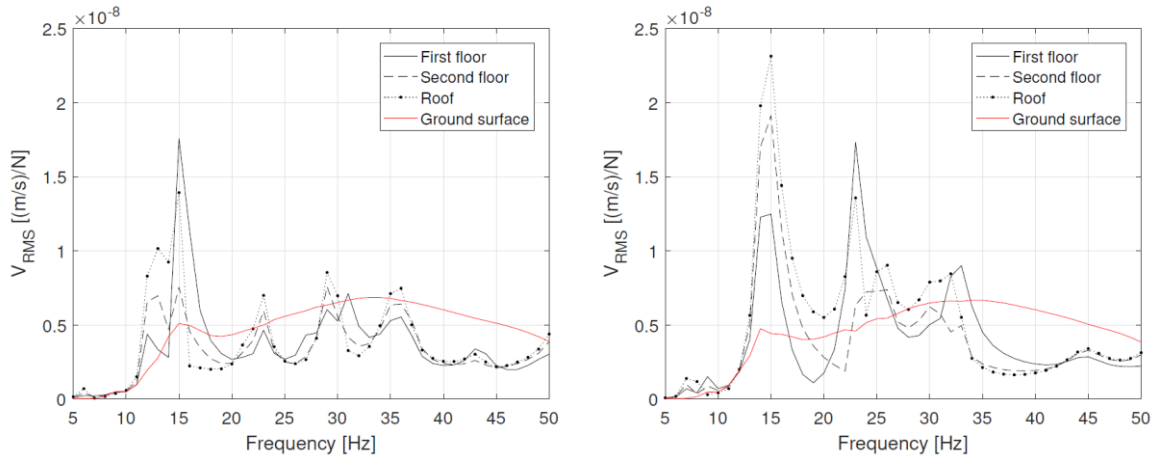

Figure 3: The vertical velocity evaluated for different locations.
(left) Light-weight wooden structure. (right) Heavy-weight concrete structure.

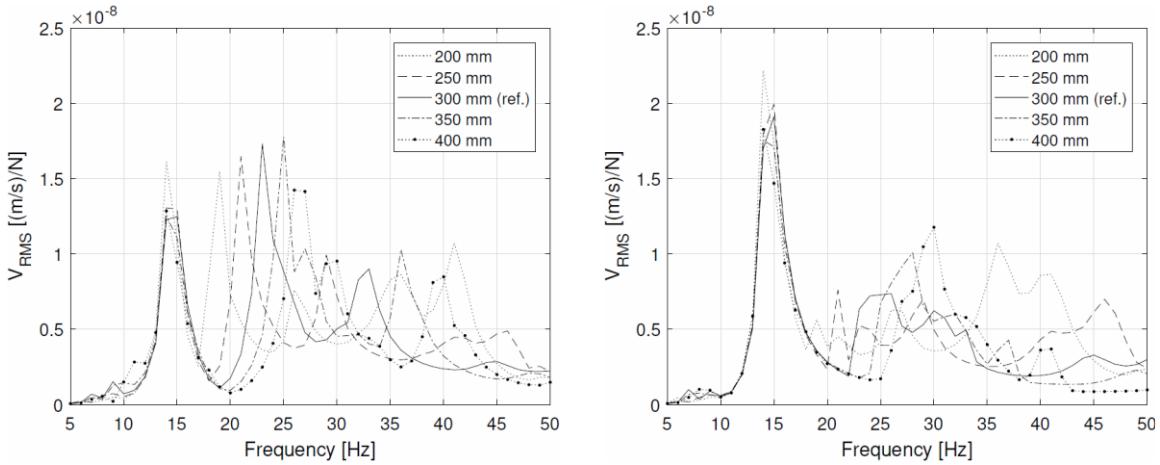

Figure 4: The vertical velocity evaluated for the heavy concrete structure with different slab thicknesses.
(left) First floor. (right) Second floor.

REFERENCES

[1] L.V. Andersen, S.R.K. Nielsen, "Reduction of ground vibration by means of barriers or soil improvement along a railway track". *Soil Dynamics and Earthquake Engineering* 25(7) (2005) 701–16.

[2] P. Persson, K. Persson, G. Sandberg, "Numerical study on reducing building vibrations by foundation improvement", *Engineering Structures* 124 (2016) 361–375.

[3] P. Persson, K. Persson, G. Sandberg, "Reduction in ground vibrations by using shaped landscapes", *Soil Dynamics and Earthquake Engineering* 60 (2014) 31–43.

[4] P. Persson, K. Persson, G. Sandberg, "Numerical study of reduction in ground vibrations by using barriers", *Engineering Structures* 115 (2016) 18–27.

[5] T. Svensson, R. Torndahl "Methodology for analysis of traffic-induced building vibrations", Master's Dissertation, Report TVSM-5224, Department of Construction Sciences, Lund University, 2017.

[6] D. Thompson, Railway noise and vibration: mechanisms, modelling, and means of control. Elsevier, 2009.

30th Nordic Seminar on Computational Mechanics
NSCM-30
J. Høgsberg. N.L. Pedersen (Eds.)
2017

FE-MODELING OF STARVED HYDRODYNAMIC LUBRICATION WITH FREE SURFACE EFFECTS

KONSTANTINOS POULIOS[1*], ANDERS VØLUND[2] AND PEDER KLIT[1]

[1] Department of Mechanical Engineering, Technical University of Denmark
Nils Koppels Allé, Building 404, 2800 Kgs. Lyngby, Denmark

[2] MAN Diesel & Turbo, Teglholmsgade 41, 2450 Copenhagen SV, Denmark.

[*]e-mail: kopo@mek.dtu.dk

Abstract. This work concerns a new finite-element formulation for solving hydrodynamic lubrication problems that include partially flooded regions, where the lubricant film behavior is governed by free surface flow.

Two rigid solids separated by a lubricant film are considered with the film assumed to remain attached to the lower of the solids. Depending on the amount of available lubricant the film may touch the upper solid or not, resulting in two distinct versions of the thin film flow equation with different boundary conditions at the top surface of the lubricant film. In fully flooded regions, the upper boundary of the film and its velocity are prescribed by the geometry and motion of the upper solid, while in partially flooded regions, a condition of prescribed pressure is employed with a capillary term superimposed to a given environmental pressure. These two distinct regimes are formulated as a complementarity problem with both a pressure field and a film thickness field as unknowns.

Due to the specific structure of the resulting equations, a C^1 continuous approximation of the film thickness field is required. In this work, both unknown fields are actually approximated with quadratic B-spline functions and the finite-element discretization of the governing PDEs is based on the Galerkin procedure. A new stabilization method is proposed to avoid oscillatory solutions around nearly discontinuous transitions of the film thickness field, which is is a consistent one, in the sense that it vanishes as the mesh is refined sufficiently.

The behavior of the developed model is illustrated by means of numerical examples and a parametric study with respect to different model parameters is presented in addition to mesh convergence studies.

Keywords: Hydrodynamic Lubrication, Thin Film Flow, Free Surface Flow, Finite-Element, Stabilization.

30th Nordic Seminar on Computational Mechanics
NSCM-30
J. Høgsberg. N.L. Pedersen (Eds.)
2017

FINITE ELEMENT MODELLING OF SWELLING KINETICS OF HYDROGELS: APPLICATION TO ACRYLAMIDE-BASED HYDROGELS

V. PROT*, A. ILSENG*, B. SKALLERUD* AND B. T. STOKKE†

*Biomechanics division, Department of Structural Engineering
The Norwegian University of Science and Technology
Norway
e-mail: victorien.prot@ntnu.no

†Department of Physics
The Norwegian University of Science and Technology
Norway

Key words: Finite element, hydrogels, swelling kinetics

Summary. Material and diffusion properties of acrylamide-based hydrogels with cationic monomers are determined by means of an inverse finite element method.

1 INTRODUCTION

Hydrogels are polymer networks swollen in an aqueous solution. In this study, we investigate the swelling kinetics of acrylamide-based hydrogels with different fractions of cationic monomers (DMAPAA)[1] with a finite element model. The constitutive material model of the gel is adapted for cationic gels from the model reported by Marcombe et al.[2] and implemented in the ABAQUS user-subroutine UMAT. In order to capture the hydrogel swelling kinetics, we used the formulation presented by Toh et al.[3]. In this work, swelling experimental data are used in two steps: first to determine the elastic material properties and second to estimate the diffusion parameter of the hydrogel, by means of an inverse finite element technique[4]. In addition, we emphasize the importance of the gel geometry for swelling behaviour.

2 Methods

2.1 Experimental data

In this study, the experimental data presented by Tierney et al.[1] for swelling of acrylamide-based hydrogels with different fractions of cationic monomers (DMAPAA) are used. These hydrogels are sensitive to pH and salt concentration in the external solution. In their experiments, hemi-ellipsoidal hydrogels (radius about 50-60 μm) were attached to the end of an optical fiber and subjected to variations in the ionic strength of

the surrounding solution. A high resolution interferometric technique was employed for monitoring the optical length changes of the hydrogels.

2.2 Constitutive model and swelling kinetics formulation

To describe the mechanical behaviour of the cationic gel used in this study, we use the following free-energy function U:

$$\begin{aligned} U &= \frac{1}{2}Nk_BT\left(I_1-3-2\ln(J)\right)+\frac{k_BT}{v_s}\left((J-1)\ln\left(1-\frac{1}{\mathrm{J}}\right)+\chi\left(1-\frac{1}{\mathrm{J}}\right)\right) \\ &\quad +k_BT\left(\sum_{\alpha\neq s}C_\alpha\left(ln\frac{C_\alpha}{Jc_\alpha^{ref}}-1\right)\right) \\ &\quad +k_BT\left(C_{AH^+}\ln\left(\frac{C_{AH^+}}{C_{AH^+}+C_A}\right)+C_A\ln\left(\frac{C_A}{C_{AH^+}+C_A}\right)\right)+\gamma C_{AH^+} \end{aligned} \tag{1}$$

where N is the network crosslink density, v_S the volume per solvent molecule, k_B is the Boltzmann constant, χ the Flory-Huggins parameter and γ the molar heat of association. C_α and c_α^{ref} are the nominal and reference concentrations, respectively, of the different mobile species (protons H^+, positive ions +, negative ions−). C_{AH^+} and C_A are the nominal concentrations of the associated group AH^+ and dissociated group A, respectively. J is the Jacobian of the deformation and I_1 is the first principal invariant of the right Cauchy-Green deformation tensor $\mathbf{C}$. This free-energy function for cationic gel[5] is adapted from the model reported by Marcombe et al.[2] for anionic gels and implemented via the ABAQUS user subroutine UMAT.

To simulate the transient process of hydrogel swelling, the migration of solvent molecules into the hydrogel network needs to be accounted for. In this work, we assume that the diffusion coefficient of the solvent molecules D is isotropic and is independent of the deformation gradient $\mathbf{F}$ and the nominal concentration of the solvent molecules C_S[6]. The flux vector $\mathbf{j}(\mathbf{X},t)$ is the number of molecules per unit time crossing per unit area of the current state of the gel and is expressed as[7]

$$j_k=-\frac{c_SD}{k_BT}\frac{\partial\mu_S}{\partial x_k},\quad \text{with } c_S=\frac{C_S}{J}, \tag{2}$$

where μ_S is the chemical potential of the solvent molecules. The methodology described by Toh et al.[3] was implemented via the ABAQUS user subroutines HETVAL ans USDFLD.

2.3 Inverse finite element procedure

A finite element model is used to simulate the ionic strength induced swelling of the cationic hydrogel (see Figure 1). The network crosslink density N, the Flory-Huggins parameter χ and the diffusion coefficient D are identified by fitting the computed length L (Figure 1) to the corresponding experimental length.

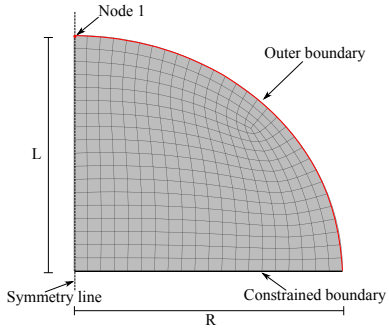

Figure 1: Illustration of axisymmetric finite element model of the hemi-ellipsoidal hydrogel of radius R and height L

2.4 Material and kinetic parameters

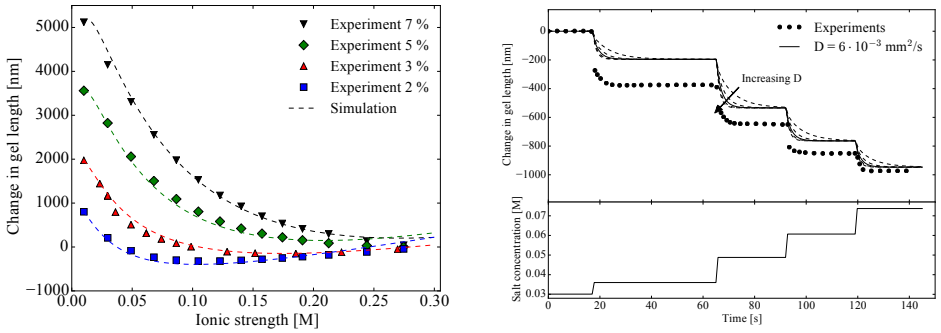

Figure 2: (left) swelling equilibium response for different levels of DMAPAA, (right) transient swelling response of the gel with 3 mol% DMAPAA

Figure 2 (left) shows that the material parameters determined by means of our inverse finite element technique gives a good agreement with the equilibrium swelling experiments. However, for transient swelling (Figure 2 (right)) , the model is unable to capture the correct level of equilibrium swelling for each step change of ionic strength but the total change in gel length agrees well with the experiment. As can be seen from Figure 2 (left) for the gel with 3 mol% DMAPAA, the response of the FE model is too stiff in the ionic strength range (0.03-0.074 M) where the transient swelling experiments are performed. This explains the discrepancies between our simulations and the experimental results for transient swelling. However, a diffusion coefficient $D = 6 \cdot 10^{-3}$ mm^2/s gives a good representation of the experimental kinetics.

2.5 Influence of geometry on free swelling response

We conduct several FE simulation of free transient swelling of spherical gels ($R = L$) and ellipsoidal gels ($R \neq L$) with different values of L. As predicted by Tanaka and

Fillmore[8], the normalized swelling behaviour is independent of the initial size and diffusion parameter for spherical gels. For ellipsoidal gels on the other hand, the normalized swelling response depends on the reference gel length L. This illustrates the importance of the initial geometry on the global response.

3 Concluding remarks

We developed a method to characterize material cationic gels. In addition, a framework for modelling kinetic properties of the gels using an analogy between heat transfer and solvent diffusion is presented. Initial conditions such as geometry and initial equilibrium are crucial to determine these properties. Additional tests to describe the transient swelling behaviour of hydrogels due to change in pH or/and ionic strength will be performed. More experimental data on transient swelling are needed to obtain more accurate diffusion parameters. This framework gives the ability to study various aspects of hydrogel swelling, one example being swelling induced buckling phenomena.

REFERENCES

[1] Tierney, S., Hjelme, D. R. & Stokke, B. T. Determination of Swelling of Responsive Gels with Nanometer Resolution. Fiber-Optic Based Platform for Hydrogels as Signal Transducers. *Analytical Chemistry* **80**, 5086–5093 (2008).

[2] Marcombe, R. *et al.* A theory of constrained swelling of a pH-sensitive hydrogel. *Soft Matter* **6**, 784–793 (2010).

[3] Toh, W., Liu, Z., Ng, T. Y. & Hong, W. Inhomogeneous Large Deformation Kinetics of Polymeric Gels. *International Journal of Applied Mechanics* **05**, 1350001 (2013).

[4] Prot, V. *et al.* Swelling of a hemi-ellipsoidal ionic hydrogel for determination of material properties of deposited thin polymer films: an inverse finite element approach. *Soft Matter* **9**, 5815–5827 (2013).

[5] Ilseng, A., Prot, V., Skallerud, B. H. & Stokke, T., Bjørn. Finite element simulations of the swelling of cationic hydrogels. *Mek'IT 17 proceeding- 9th National Conference on Computational Mechanics* in press (2017).

[6] Hong, W., Zhao, X., Zhou, J. & Suo, Z. A theory of coupled diffusion and large deformation in polymeric gels. *Journal of the Mechanics and Physics of Solids* **56**, 1779–1793 (2008).

[7] Feynman, R. P., Leighton, R. B. & Sands, M. L. *The Feynman lectures on physics* (Addison-Wesley Pub. Co., Reading, Mass., 1963).

[8] Tanaka, T. & Fillmore, D. J. Kinetics of swelling of gels. *The Journal of Chemical Physics* **70**, 1214–1218 (1979).

30th Nordic Seminar on Computational
Mechanics NSCM-30
J. Høgsberg. N.L. Pedersen (Eds.)
2017

DAMAGE LOCALIZATION IN A RESIDENTIAL-SIZED WIND TURBINE BLADE USING SUBSPACE EXCLUSION ZONES

BILAL A. QADRI†, THOMAS BULL, MARTIN D. ULRIKSEN AND LARS DAMKILDE

Department of Civil Engineering,
Aalborg University
Niels Bohrs Vej 8, 6700 Esbjerg, Denmark
†Email: baq@civil.aau.dk

Keywords: Structural health monitoring, damage localization, subspace exclusion zones, system identification-free localization.

1 INTRODUCTION

Wind turbines are repeatedly exposed to natural loads, which, in general, have a significant influence on the structural lifetime. Therefore, maintenance and manual inspection are of great importance in the attempt to reduce catastrophic failures; both in onshore and offshore scenarios. Vibration-based structural health monitoring (SHM) has the potential to provide information about potential structural deterioration, hence allowing for efficient inspection and, as such, a reduction in operational costs. However, this requires a robust method for each step of the damage identification process, which consists of four subcategories proposed by A. Rytter [1]; namely, detection, localization, assessment and consequence. The process is performed stepwise, hence leading to that detection must be completed before locating the damage. Detecting damages in wind turbines has been solved with reasonable success [2], but a robust solution to the next step in the damage identification process, finding its location, has not been provided. A contribution to the second step is the newly developed method subspace exclusion zone (SEZ), proposed by Bernal and Ulriksen [3]. The SEZ method is a model-based damage localization approach, which facilitates a user-defined localization resolution. The method operates by mapping the damage-induced difference in the kinematic response, from an undamaged and damaged state, to a theoretical model of the structure. The SEZ method has shown promising results in the context of numerical simulations and laboratory experiments with a simple beam structure [4]. Therefore, the focus of this paper is to test the SEZ method on a more complex geometry, here, the residential-sized wind turbine blade in a laboratory environment.

2 SUBSPACE EXCLUSION ZONE

The SEZ method is a model-based damage localization scheme, which seeks for differences in two domains, a physical and a theoretical one. With reference to figure 1, consider now the physical and theoretical domains where Ω_u and Ω_d are, respectively, the undamaged subdomain and damaged one. The dashed boundary, Γ, represents the boundary of an EZ of

user-defined size. The principles of locating damages are to obtain an experimental feature, for instance, accelerations or displacements, from an undamaged and damaged state of the structure in question. Subsequently, one postulates an EZ in a theoretical model, for instance a finite element (FE) model, of a user defined size and removes the DOF within the interior of the EZ. If the damage is within the postulated area, the experimental feature can, under ideal circumstances, be reproduced by applying a stress field across the boundary of the EZ.

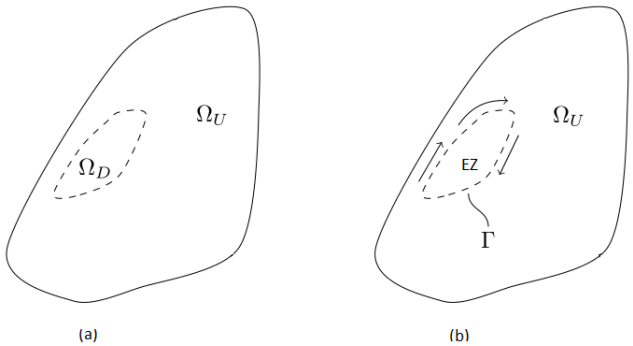

Figure 1: (a) Physical model presented with a damaged area. (b) Theoretical model with a postulated EZ subjected to a stress field.

Suppose now a linear transformation

$$\alpha A x = b, \tag{1}$$

where $A \in \mathbb{R}^{mxp}$ is the interrogation matrix, populated with m observations for each of the p DOF on the boundary of the exclusion zone. Matrix A is generated by applying the stress field across the boundary of the EZ. The damage-induced difference, $b = \eta_u - \eta_d$, is here denoted as the experimental feature, and α is an arbitrary scaling factor that corrects the discrepancy between the input loading magnitude in the undamaged and damaged state. By rearranging equation 1, one gets

$$x = bA^{\dagger}\frac{1}{\alpha} \rightarrow \alpha A\frac{1}{\alpha}A^{\dagger}b = b \rightarrow \epsilon = (I - AA^{\dagger})b, \tag{2}$$

with † denoting the Moore-Penrose pseudo-inverse based on the assumption, $m > p$, indicating that SEZ operates with more rows than columns. Subsequently a residual, ϵ, value being significantly close to zero, indicates that the damage is within the postulated EZ. The formulation for the interrogation matrix, A, can be expressed by modal parameters

$$A_k(s) = \sum_{j=1}^{n} \frac{\phi_j \phi_j^{\mathrm{T}}}{s^2 + 2\zeta_j \omega_j s + \omega_j^2} F_k(s), \tag{3}$$

in which, equation (3) represents a sum of stresses accumulated in the matrix, A, for the

respective EZ, where ω_j, ζ_j and ϕ_j are the natural frequency, damping ratio and mass normalized eigenmodes, respectively, for the j'th mode.

3 TEST SETUP

For locating damages with the SEZ method, data is required from the undamaged and damaged state. This is, however, possible with the residential-sized wind turbine blade, which is designed specifically for damage identification purposes. The blade, which consist of two parts of polymer that are bolted together along the leading and trailing edge, has a length of approximately 800 mm and weighs 720 g, including the accelerometers and bolts. The bolts mounted on the blade allows one to introduce edge debondings of different sizes. The blade is fixed at the root and excited with a harmonic load of 75 Hz at the tip.

Figure 2: The residential-sized wind turbine blade. (a) The shaker exciter. (b) The connection between shaker and blade. (c) Accelerometers. (d) The fixed support.

The accelerations are captured by 14 uniaxial accelerometers, mounted close to the edges underneath the blade, hence providing measurements perpendicular to the surface.

4 LOCALIZATION RESULTS

The blade is modelled in ANSYS Workbench, using 3450 first-order shell elements. The FE-model compensates for the mass contribution from accelerometers and bolts in order to minimize the discrepancy between the FE- and actual model. In this case, three bolts are loosened along the trailing edge, spanning 7.5 % of the total length. The process for data acquisition is carried out by 49 experiments for the undamaged and damaged state, positioned as illustrated in figure 2.

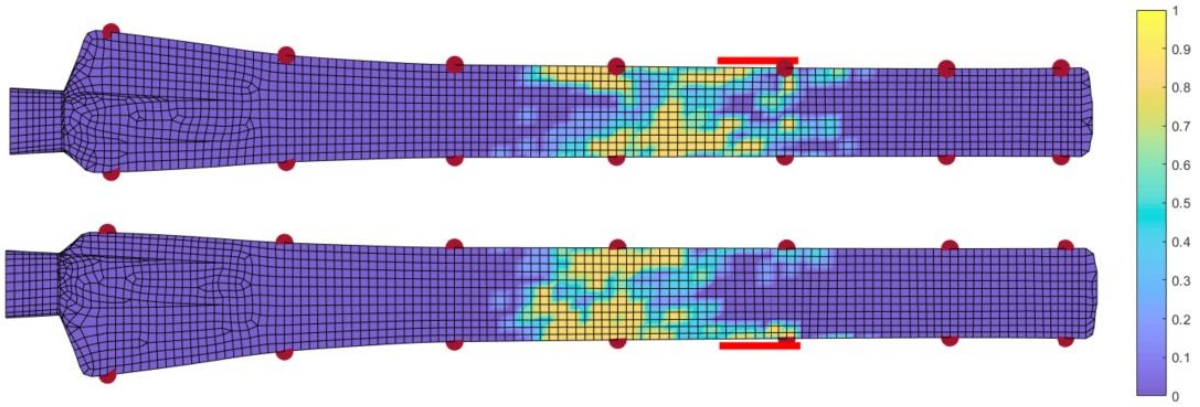

Figure 3: Residual, ϵ ,values for each element, associated with colours. The red dots mark the sensors and the red line is the location for the edge debonding.

The SEZ method is capable of locating the damaged area, although the resolution is low. As shown in figure 3, larger areas indicate damaged elements, which suggest for an implementation of a strategy to further improve the resolution. A solution for this could be a statistical evaluation of the results, implemented in the SEZ method.

5 CONCLUSIONS

The paper presents the SEZ method applied on a residential-sized wind turbine blade. The SEZ method constitutes a model-based approach, which relies heavily on a calibrated FE model. The damage was presented by loosening three bolts, allowing the damage length to be 7.5 % of the total length. One issue of measuring vibrations is the noise inherent in the signals. This could lead to a larger area being damaged, as shown in figure 3. However, the SEZ is capable of locating the damage but a further development is needed to increase the accuracy of the damage location. To improve the accuracy and robustness in the method, an implementation of a statistical evaluation is suggested in the SEZ method.

REFERENCES

[1] Rytter, A. Vibrational based inspection of civil engineering structures, *Ph.D. dissertation,* (1993).
[2] Ulriksen, M.D, Tcherniak D, and Damkilde L, “Damage Detection in an Operating Vestas V27 Wind Turbine Blade by use of Outlier Analysis”, IEEE Workshop on Environmental, Energy and Structural Monitoring Systems, (2015).
[3] Bernal, D. Ulriksen, M. D, Subspace Exclusion Zone Damage Localization, To be submitted to Mechanical Systems and Signal Processing (2017).
[4] Ulriksen, M. D, Damage Localization for Structural Health Monitoring: An Exploration of Three New Vibration-based Schemes, *Ph.D. dissertation.*

30th Nordic Seminar on Computational Mechanics
NSCM-30
J. Høgsberg. N.L. Pedersen (Eds.)
2017

NUMERICAL ANALYSIS OF ANISOTROPIC STIFFNESS OF THIN AL FOIL IN MULTIPLE MATERIAL DIRECTIONS BASED ON EXPERIMENTS

W. REHEMAN*, P. STÅHLE†, E. ANDREASSON* AND S. KAO-WALTER*

*Department of Mechanical Engineering
Blekinge Institute of Technology
Valhallavägen 1, 371 41 Karlskrona, Sweden
e-mail: wur@bth.se, web page: http://www.bth.se/

†Division of Solid Mechanics
Lund University (LTH)
Ole Römersväg 1,22100, Lund, Sweden
e-mail: per.stahle@solid.lth.se - Web page: http://www.solid.lth.se

Key words: Thin foil, Aluminium alloy, Anisotropy, Symmetry plane, Young's modulus

Summary. Numerical analysis have been performed on tensile test experiment data to evaluated the performances of a 9 microns thick aluminium foil. The identification of the anisotropic material properties is based on tensile tests performed in 11 different angles from 0° to 90° from the rolling direction. By least square fitting and extrapolation to zero load the elastic modulus is, as opposed to the general belief, proven to be very close to the expected bulk values for this specific material. The elastic modulus is shown to be anisotropic with a stiffness variation of aound 15%. Minimum stiffness is obtained in around 45° from the rolling direction.

1 INTRODUCTION

Thin foils and composite layers of aluminium are utilised in products for containers for beverage, food, medicine, etc.[1,2]. In these applications the thicknesses of the aluminium foil varies a lot and the thinnest are of the order of only a few microns. The application development and design depends increasingly on accurate predictive engineering methods. Thus, a thorough understanding of mechanical properties is required. Many experimental test and theoretical analyses have been performed to characterise the mechanical response[2,3,4]. A severe obstacle is that the mechanical response of thin samples are sensitive to geometrical effects, sample size and imperfections like wrinkles, weak grain, thickness variations etc. Therefore, the correct representation of mechanical properties and complete understanding of the mechanical behaviour involves delicate work of experimental test combined with theoretical studies. The numerical analysis is an important

part needed to make correct evaluation of test result.

The aim of this work is to thoroughly characterise aluminium foil by the use of physical testing and computational method. The earlier studies on this specific aluminium foil limited to uniaxial loading in the manufacturing direction i.e. Rolling Direction (RD). In this study, the anisotropic properties and material behaviour are investigated.

2 NUMERICAL APPROACH AND RESULTS BASED ON EXPERIMENT

The experimental measurements were performed on strips of this aluminium foil with the cross section dimensions of 15 x 100 mm^2 and a thickness of 9 microns, which is delivered from the production line at Tetra Pak. The samples were cut with incremental angles of 10° from the RD. An uniaxial tensile test were performed on the samples from different angles, see Fig. 1 for the result. Further details regarding the experiment is published in the work by Käck and Malmström[4].

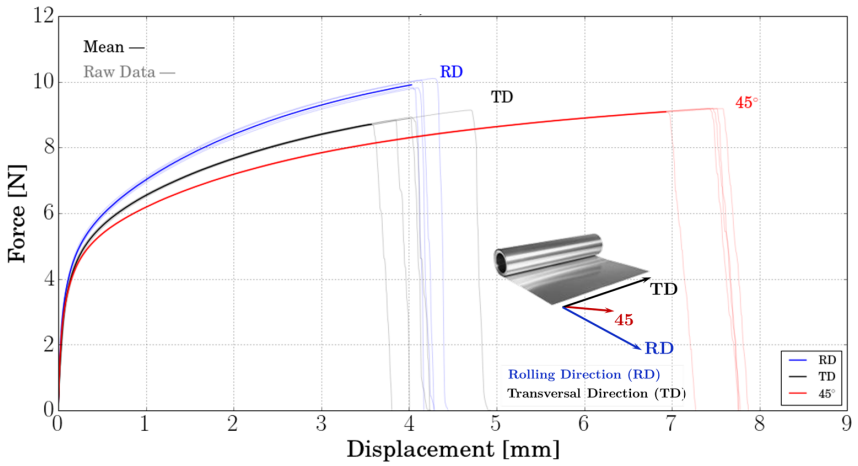

Figure 1: Experimental tensile test results for 0° (RD), 45° and 90° (TD)[4]

.

The handling of thin samples and correct performing during the test is quite challenging because of the extremely small thickness. Even though a very careful attention is paid to the test performing details, it is still difficult to correctly capture the initial elastic response. It is well know that Young's modulus for isotropic poly-crystalline aluminium is around 69 to 71 GPa, depending on the different alloying elements. In many engineering applications of thin aluminium foil Young's modulus is taken to be 40-45 GPa, referring to tensile test results performed on foils similar to the one tested by[1,5]. It is by us assumed that the rather low moduli are chosen as an engineering practicality and are deliberately including the plastic deformation that is initiated at very low load. It could also be caused by misalignment of the sample, slippage in the grips or devices used for measuring

the displacements or similar. The mere thinness of the foil as such does not seem as a reasonable argument. It is argued that as long as the material contains more than 10 to 20 atomic layers, e.g. more than 100nm, bulk properties may be assumed[6]. This motivates the present detailed exploration of the obtained data and its characterisation of the material properties.

From the performed test the force and elongation were measured for each direction, and the corresponding stress and strains are calculated. The stretching before the final rupture is rather homogeneous and below 10%. Further, the cross sectional area is unknown, which makes the, e.g. Cauchy stress unknown. Because of this, engineering stress and strain is used in this pilot study. The general stress and strain relationship on incremental form is written $\mathrm{d}\sigma_{ij} = C_{ijkl}\mathrm{d}\epsilon_{kl}$, where C_{ijkl} is the tangent stiffness of the material.

The stiffness tensor C_{ijkl}, being a rank 4 tensor, transforms according to the following

$$C'_{pqrs} = \beta_{pi}\beta_{qj}\beta_{rk}\beta_{ls}C_{ijkl}, \tag{1}$$

where the β_{ij} are the directional cosines. For the rotation in the x_1, x_2-plane all indices assume values 1 and 2. The Einstein summation rule applies.

Here the assumption is that the material is orthotropic and subjected to plane stress, thus the stiffness tensor is represented by the four relevant components, C_{1111}, C_{1122}, C_{2222} and C_{1212} in the principal coordinates x_1 and x_2. The components $C_{1112} = C_{1222} = 0$. In non-principal directions in the x_1, x_2-plane, the components C_{1112} and C_{1222} may be non-zero. The relation in Eq. (1), gives the uniaxial component as,

$$C'_{1111} = C_{1111}\cos^4(\theta_n) + (C_{1122} - 2C_{1212})\cos^2(\theta_n)\sin^2(\theta_n) + C_{2222}\sin^4(\theta_n), \tag{2}$$

where the angle $\theta_n = \theta_0 + n\Delta\theta$ with $n = 0, 1, ..., 10...$ The angle θ_0 is the anti-clockwise angle from the rolling direction to the principal direction of the material and $\Delta\theta = 10^\circ$. The least square set of constant parameters (A, B, C, θ_0) is implicitly given by Eq. (2), where $A = C_{1111}$, $B = C_{1122} - 2C_{1212}$, and $B = C_{2222}$.

Three linear equations allow elimination of A, B, and C from the least square requirements. A final non-linear equation is solved iteratively for θ_0. The solution for θ_0 is not unique and therefore the iterative procedure was locked into a small range of plausible angles. The range -20° to 20°, gave realistic solutions for all tensile test directions given by $n = 0, ..., 11$. The set (A, B, C, θ_0) represents the tangent stiffness and is a function of the strain. The result is displayed in Figs. 2 a) and b), where E' and C'_{1111} is shown.

3 CONCLUSIONS

1. Detailed analysis of tensile tests on a 9 micron thick aluminium foil show that the stiffness practically assume bulk values.

2. The material is slightly anisotropic with around a $\pm 7\%$ variation.

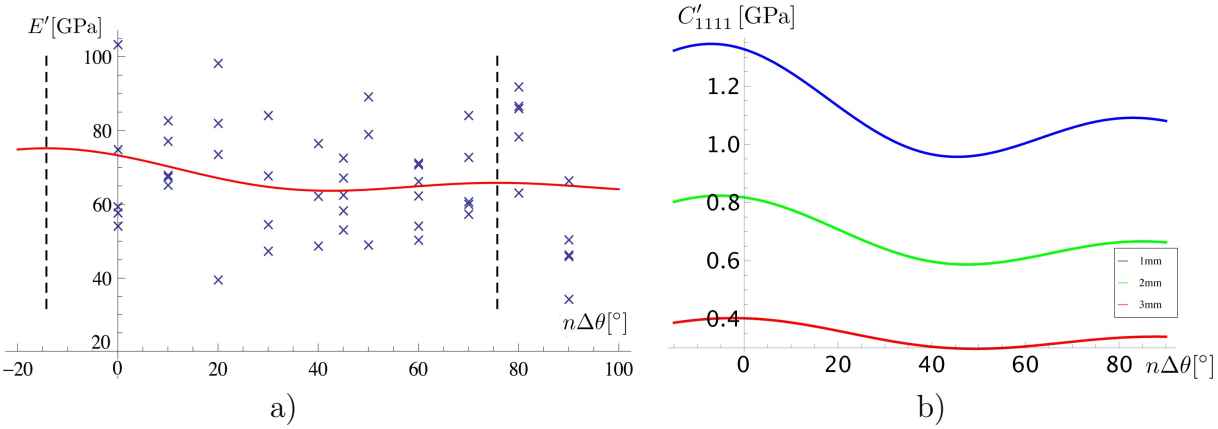

Figure 2: a) Elastic modulus $E' = C'_{1111}$ as $\delta \to 0$ for different loading directions vs the RD. The dashed vertical delimiters show the principal directions. b) Uniaxial tangent stiffness at different elongations, δ=1, 2 and 3 mm. Both are as a function of the angle $n\Delta\theta$. The angle θ_0 is visible on the left side of the diagram.

3. The primary principal direction is initially close to $-14°$ from the rolling direction and decreasing with increasing deformation to around $-2°$ at 3 mm elongation.

REFERENCES

[1] Kao-Walter, S., Dahlström, J., Karlsson, T. & Magnusson, A. A study of the relation between the mechanical properties and the adhesion level in a laminated packaging material. *Mechanics of Composite Materials* **40**, 29–36 (2004).

[2] Andreasson, E., Kao-Walter, S. & Ståhle, P. Micro-mechanisms of a laminated packaging material during fracture. *Engineering Fracture Mechanics* **127**, 313–326 (2014).

[3] Kao-Walter, S. & Ståhle, P. In-situ sem study of fracture of an ultrathin al-foil-modeling of the fracture processes. In *Proc. SPIE*, vol. 4537, 253–256 (2002).

[4] Malmberg, C. & Käck, B. Aluminium foil at multiple length scales, mechanical tests and numerical simulations in abaqus (2015).

[5] Bolzon, G. & Shahmardani, M. Macroscopic response and decohesion models of metal-polymer laminates. *Engineering Transactions* **65**, 53–59 (2017).

[6] Miller, R. E. & Shenoy, V. B. Size-dependent elastic properties of nanosized structural elements. *Nanotechnology* **11**, 139 (2000).

30th Nordic Seminar on Computational Mechanics
NSCM-30
J. Høgsberg. N.L. Pedersen (Eds.)
2017

LARGE-SCALE FORMING SIMULATION OF PAPERBOARD

K. ROBERTSSON*, E. BORGQVIST†, M. WALLIN*, M. RISTINMAA* AND J. TRYDING†

*Division of Solid Mechanics, Lund University, Sweden
e-mail: kristofer.robertsson@solid.lth.se, web page: http://www.solid.lth.se

†Tetra Pak Packaging Solutions AB, Lund, Sweden

Abstract. To allow for large scale forming applications, such as converting paperbaord into package containers, efficient and reliable numerical tools are needed. In finite element simulations of thin structures, structural elements are required to reduce the computational cost. Solid-shell elements based on reduced integration with hourglass stabilizations is an attractive choice. One advantage is the natural inclusion of the thickness direction, not present in standard degenerated shells, which is an advantage for many contact algorithms. Furthermore, no restrictions to the constitutive model is imposed for solid shell elements i.e. they can be used without enforcing the plane stress condition. To be able to simulate the converting process, the solid-shell element proposed by Schwarze and Reese[2] is implemented together with the state of the art continuum model for paperboard developed by Borgqvist et.al.[1]. This approach is validated by comparing the obtained results with those found from 3D continuum elements. Finally, to show the potential for this approach, a large scale forming simulation for paperboard is illustrated as proof of concept.

Keywords: Paperboard, Application, Solid-Shell Element, Constitutive Model, Forming

REFERENCES

[1] Borgqvist, E., Wallin, M., Ristinmaa, M. & Tryding, J. An anisotropic in-plane and out-of-plane elasto-plastic continuum model for paperboard. *Composite Structures* **126**, 184–195 (2015).

[2] Schwarze, M. & Reese, S. A reduced integration solid-shell finite element based on the EAS and the ANS concept – Large deformation problems. *International Journal for Numerical Methods in Engineering* **85**, 289–329 (2010).

30th Nordic Seminar on Computational Mechanics
NSCM-30
J. Høgsberg. N.L. Pedersen (Eds.)
2017

MOVING MESH AND IMAGE REGISTRATION IN FEniCS

J. LARSSON[a], A. LOGG[b], K. MODIN[b] AND A. SEHLSTRÖM[c]

[a]Department of Animal and Plant Sciences
University of Sheffield, Sheffield, UK

[b]Department of Mathematical Sciences
Chalmers University of Technology, Gothenburg, Sweden

[c]Department of Architecture and Civil Engineering
Chalmers University of Technology, Gothenburg, Sweden
e-mail: alexander.sehlstrom@chalmers.se - web page: http://www.chalmers.se

Key words: image registration, computational anatomy, FEM, FEniCS.

1 INTRODUCTION

Image registration is about finding a transformation that warps a source image into a target image, matching gross features. It is a critical task in medical imaging. Computational anatomy (CA) is a state-of-the-art framework for image registration, founded in the theory of fluid dynamics and PDE: one seeks a time-dependent vector field that generates a continuous warp of the source image into the target image.

Here we construct a finite element realisation of CA by representing the continuous warp by a moving mesh. The PDE governing the motion of the mesh is an infinite-dimensional nonlinear gradient flow[1]; a brief description is given in section 2. In essence, it is a time-stepping problem, where an elliptic PDE is solved in each time step using the FEniCS finite element package[2]. The solution process is summarised in fig. 1.

Although commonly used in medical contexts, we stress that CA has promising applications also in structural engineering, as discussed in section 4.

2 THEORY

In this section we give a brief account of the infinite-dimensional gradient flow equation by Bauer et. al.[1]. Our spatial domain is the n-dimensional unit square $\Omega = [0,1)^n \subset \mathbb{R}^n$. An *image* is a function $I\colon \Omega \to [0,1]$. A *warp* is an invertible smooth mapping $\varphi\colon \Omega \to \Omega$ (a diffeomorphism). Denote the source and target images by I_0 and I_1. The governing PDE is given in terms of a time-dependent vector field $\mathbf{u} = \mathbf{u}(t, \mathbf{x})$ and a time-dependent

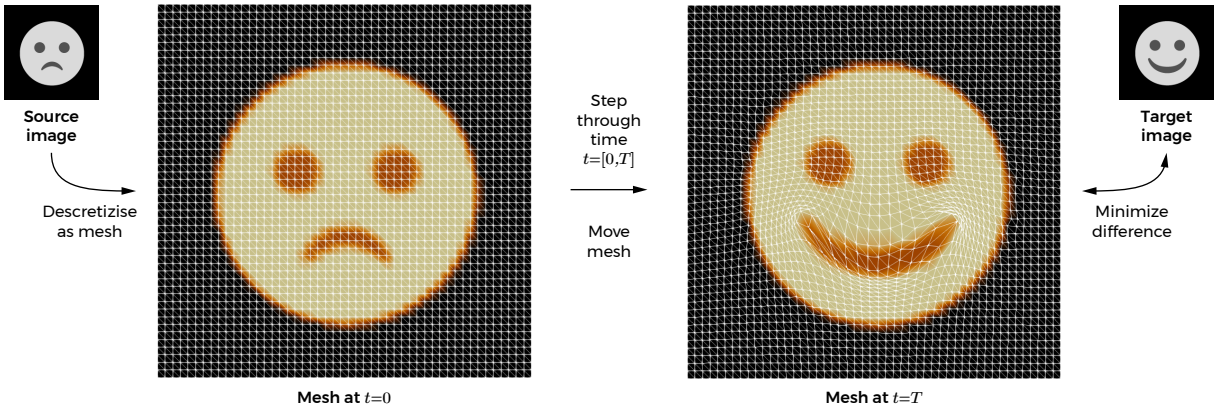

Figure 1: Solution method overview: Source and target images are discretized as FE meshes. By stepping through time, the nodes of the source mesh are moved in such a way that the intensity difference between the moved mesh and the target mesh is minimised.

warp $\varphi = \varphi(t, \mathbf{x})$ as

$$(1 - \alpha\Delta)^k \mathbf{u} = \left(I_0 \circ \varphi^{-1} - I_1\right) \nabla \left(I_0 \circ \varphi^{-1}\right), \tag{1}$$

$$\frac{\partial \varphi}{\partial t} = \mathbf{u} \circ \varphi, \tag{2}$$

where $k \in \{1, 2, \ldots\}$ and $\alpha > 0$ specify the order and scale of 'warp smoothing'. The compositions are with respect to the spatial variable: $I_0 \circ \varphi^{-1} = I_0(t, \varphi^{-1}(t, \mathbf{x}))$ and $\mathbf{u} \circ \varphi = \mathbf{u}(t, \varphi(t, \mathbf{x}))$.

3 IMPLEMENTATION

A spatial discretisation of the PDE system (1) is obtained by representing the velocity field $\mathbf{u}$ as a finite element vector field on a (fixed) mesh representation of Ω. The warp φ is represented as another (moving) mesh, who's nodal points are updated from $\mathbf{u}$ using the forward Euler time discretisation. The compositions are obtained by standard finite element interpolation. Thus, at each time-step we need to solve an elliptic, vector valued PDE of the strong form

$$(1 - \alpha\Delta)^k \mathbf{u} = (I - I_1) \nabla I, \tag{3}$$

where $I = I_0 \circ \varphi^{-1}$. We use periodic boundary conditions. Furthermore, at each time-step the nodal coordinates of the moving mesh are updated as $\mathbf{x}_i(t + h) = \mathbf{x}_i(t) + h\mathbf{u}(t, \mathbf{x}_i(t))$, where h is the time-step size.

The implementation is done using FEniCS via the Python interface[2] in a package called Narwhal. The pixel intensity values of the source and target images are read into arrays and mapped to the vertices of a mesh consisting of triangular Lagrange elements of order k. The strong form of all used PDE:s are then computed depending on the k parameter. A time stepping loop then solves the problem iteratively until the norm of the velocity field $\mathbf{u}$

is small enough. The system of linear equations can be solved using various methods and preconditioning. The full implementation along with the code needed for the following two examples is available via Bitbucket[1].

3.1 Example 1: Proof of concept using smileys

The implemented solver has been tested by transforming smileys (fig. 2). Using fig. 2a1 as source and fig. 2b as target, the result seen in fig. 1 is obtained. Similar results are obtained for figs. 2a2 and 2a3 and to some extend also for fig. 2a4 as source. Figure 2a5 has a different topology compared to the target—the existence of eyebrows—and, as expected, the solver can not handle this and the eyebrows remain when convergence is obtained. Figure 2a6 is exactly the same image as the target fig. 2b but for a 90° clockwise rotation. Here the solver reaches a local minimum and not a global; instead of twisting the mesh to reach global minimum, half of the mouth is merged with one of the eyes to form the target mouth and the other half forms a new eye. This issue can be handled by adding rigid motion to the warp model, as is a common technique in CA.

(a1) (a2) (a3) (a4) (a5) (a6) (b)

Figure 2: Source faces (a) and target face (b).

3.2 Example 2: The effect of the k parameter

The effect of the smoothness parameter k of eq. (1) has been investigated using images obtained from μ-CT scans of snail shells. Higher values of k force the transformations of the mesh to be smoother, thereby better preserving edges in the source image, see fig. 3.

4 FUTURE WORK

In order for the solver to be applicable to big scale problems, further enhancements are needed. Adding a volume change penalisation as well as ensuring global—rather than local—minimum may improve the quality of the result. It is also suggested that a parameter study is performed in order to find out reasonable choices for time-step h and smoothing parameters k and ϵ. To find costly computations, profiling of the code is suggested.

Regarding applications in structural mechanics and architecture, it may be possible to start with a uniform mesh and a source image with constant intensity and morph the image into a target image representing a stress plot. The outcome is expected to be a non-uniform mesh with densely packed elements in areas with high stresses and sparsely packed

[1] `https://bitbucket.org/sehlstrom/fenics-diffeomorphic/`

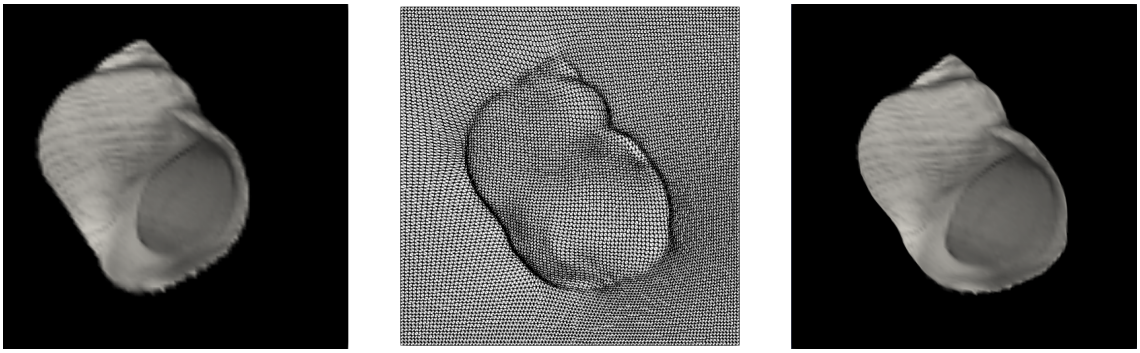

(a) Source image (b) Resulting mesh, $k = 1$ (c) Resulting image, $k = 1$

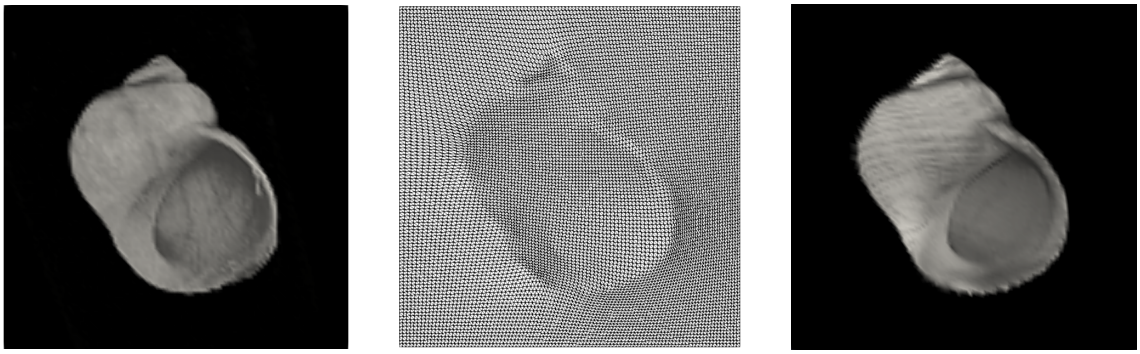

(d) Target image (e) Resulting mesh, $k = 4$ (f) Resulting image, $k = 4$

Figure 3: Source image, target image and resulting meshes and images for $k = 1$ and $k = 4$. A low value of k allows for more extreme deformations of the mesh compared to higher values.

elements in areas with low stresses. By adding members with equal cross section along the edges of all elements in the mesh, an effective configuration can be achieved yielding about the same utilisation of all elements. Another possibility is pattern matching, enabling e.g. a glass roof structure to cast shadows in a predetermined pattern on the floor of a covered courtyard.

REFERENCES

[1] Bauer, M., Joshi, S. & Modin, K. Diffeomorphic density matching by optimal information transport. *SIAM Journal on Imaging Sciences* **8**, 1718–1751 (2015).

[2] Logg, A., Mardal, K.-A., Wells, G. N. *et al. Automated Solution of Differential Equations by the Finite Element Method* (Springer, 2012).

30th Nordic Seminar on Computational Mechanics
NSCM-30
J. Høgsberg. N.L. Pedersen (Eds.)
2017

COMPOSITE THICKNESS OPTIMIZATION OF OFFSHORE WIND TURBINE BLADE WITH FIXED OUTER GEOMETRY

NSCM-30

JONAS SJØLUND[*] AND ERIK LUND[†]

Materials and Production
Aalborg University
Fibigerstraede 16, 9220 Aalborg East, Denmark
e-mail: [*]jhs@mp.aau.dk, [†]el@mp.aau.dk

Key words: Offshore Wind Turbine Blades, Composites, Structural Optimization.

Summary. With the objective of mass minimization, a 73-m offshore wind turbine blade is optimized using a gradient based approach on a Finite Element (FE) model. Constant loads and a fixed outer geometry are assumed. Plies of the same material and same orientation are grouped together in plygroups. The thicknesses of the plygroups are chosen as design variables. Manufacturing constraints such as ply-drops are taken into account using linear constraints. Structural constraints include buckling, tip displacement and max. strain failure indices.

1 INTRODUCTION

Offshore wind turbine blades are getting increasingly longer and heavier every year. These blades are often manufactured in big molds where the dry material is build up and solidified with resin using a vacuum process. The molds are relatively expensive, and a large number of blades needs to be manufactured in each mold before they are profitable. In the case of tailoring a blade for a new site with different loads, or simply redesigning a blade using improved design tools, changes to the outer geometry are not permitted as that would require changing the mold. In this work a proposed design method for minimizing the mass of an offshore wind turbine blade with a fixed outer geometry will be presented.

Mass minimization of wind turbine blades has been studied in a number of examples. In [1], a genetic optimization algorithm is used to find the optimal thickness of the shell and webs. However, the entire shell and web are assumed to have the same thickness. This is a consequence of genetic algorithms being very computationally expensive for many design variables. Another approach is used in [2] where a gradient based method called ‘Discrete Material and Thickness Optimization’ (DMTO) is used. In this method each layer has a density variable to determine if there should be material or not (topology). This is combined with multi-material optimization where each ply in addition also have material weight factors allowing it to ‘choose’ the best material. As this approach yields multiple design variables for each ply, it becomes computationally expensive for large structures.

In the following a parameterization with relatively few design variables will be presented. The parameterization approach will be demonstrated on a 73-m offshore wind turbine blade.

2 PARAMETERIZATION

The parameterization is done by first dividing the wind turbine blade into regions of similar layup. This can be seen on Figure 1 with the divisions marked using red dotted lines. Within these regions a constant layup is assumed.

Since wind turbine blades are often build up using many layers of the same material and same orientation, it is possible to group these together into plygroups. A sequence of these plygroups is assumed for each region. An example of a sequence of plygroups is shown on Figure 1 for the Main Laminate (MA) region. The thickness of the plygroups are the design variables used in the optimization problem.

The wind turbine blade is divided longitudinally into sections. In this work the sections have a length of 2 m. The thickness of a plygroup with unidirectional (UD) material located in the Main Laminate (MA) in longitudinal section no. j will be denoted $t_{MA,j,UD}$. The indices MA,j constitute what we denote as a patch: A group of finite elements with the same layup.

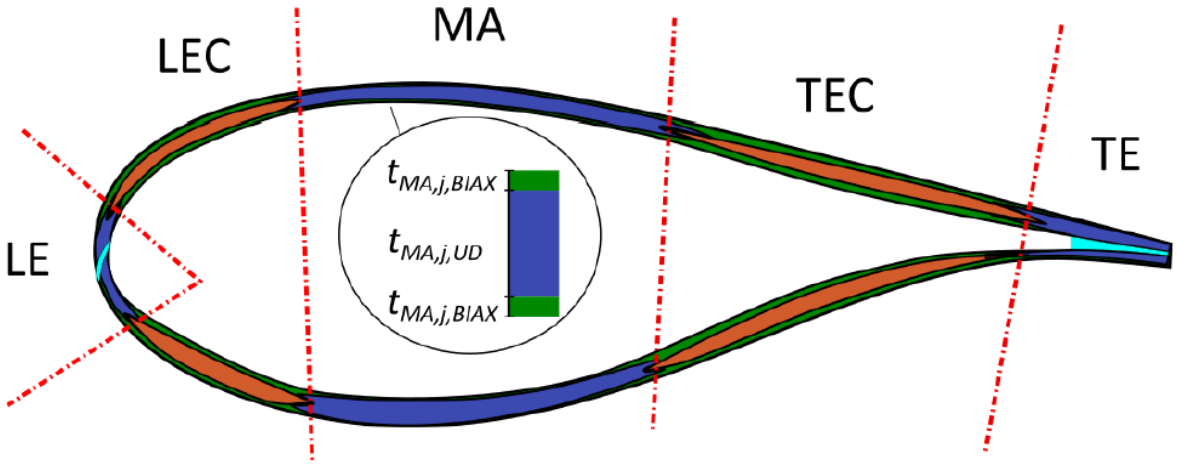

Figure 1 – Wind turbine blade cross section divided into regions of similar layup: Main Laminate (MA), Trailing Edge (TE), Trailing Edge Core (TEC), Leading Edge (LE), Leading Edge Core (LEC). Also shown is an example of the plygroups, and the sequence of plygroups, of the MA region.

2.1 Manufacturing Constraints

Plygroup thicknesses are allowed to vary independently as long as they are within manufacturing constraints. In this work ply-drop constraints are demonstrated. These are implemented by limiting the change in thickness in a plygroup from one patch to another. They are only applied in the longitudinal direction, and as an example they can for the MA UD plygroup be written as:

$$t_{MA,j,UD} - t_{MA,j+1,UD} \leq p \tag{1}$$

$$t_{MA,j+1,UD} - t_{MA,j,UD} \leq p \tag{2}$$

Here is p the allowable change in thickness per meter multiplied with the distance between the two longitudinal sections.

3 MODELLING AND METHOD

This work takes offset in the outer geometry of a 73-m offshore wind turbine blade. The full description of the layup is beyond this extended abstract, but is similar to what is seen on Figure 1. Design variables include the UD plygroup thicknesses in TE/LE/MA regions, and also the core thicknesses of the LEC/TEC regions are included.

3.1 Finite Element Model

The wind turbine blade is modelled using a FE model. The FE model is using layered solid-shell elements which is important in order to capture the correct stiffness in the trailing edge, see e.g. [3]. Furthermore solid-shell elements provide better results for the out-of-plane components. A cross-section of the FE model can be seen on Figure 2.

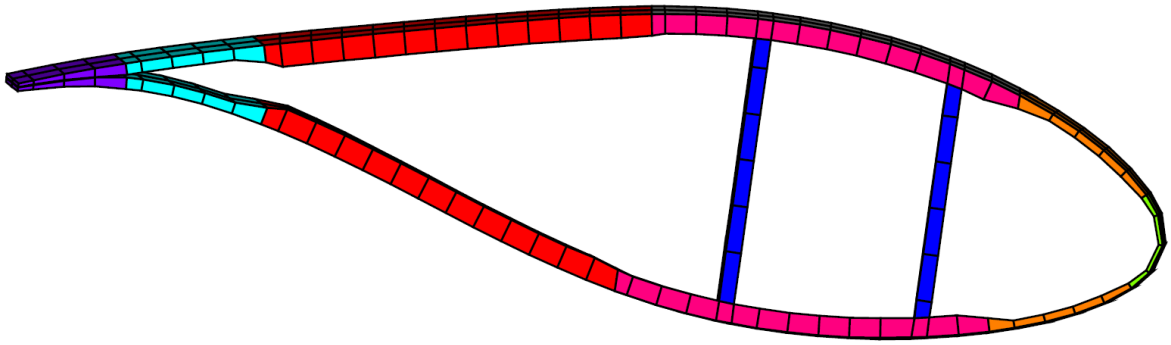

Figure 2 – A cross-section of the FE model. The blade is modelled using solid-shell elements, with one element through thickness. The different colors display the regions which the blade is divided into.

3.2 Optimization

The optimization problem is solved using a Sequential Linear Programming (SLP) approach. Sensitivities are found using a semi-analytic approach implemented in an in-house design and optimization tool called MUST [4]. The SLP approach is combined with merit functions, a global convergence filter and an adaptive move-limit strategy, see [2] for more details. The optimization objective is to minimize the mass of the blade using thickness design variables. Structural constraints are set up for both the edgewise and flapwise load cases and include linear buckling load factors, tip displacement and max. strain failure indices. Manufacturing constraints include plydrop constraints and upper/lower limits on thicknesses.

4 RESULTS

Optimization results are shown on Figure 3 where it can be seen that the mass of the blade is reduced from 30105 kg to 28825 kg. Normalized constraint values are also plotted and it can be seen that the buckling load factor and tip displacement in the flapwise load case are active constraints in the last iterations.

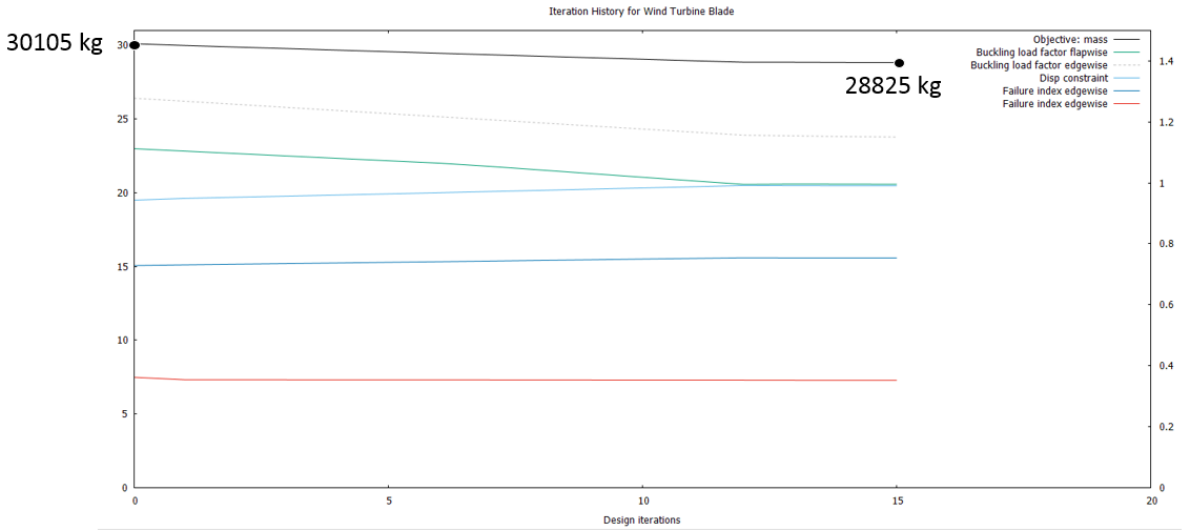

Figure 3 – Optimization results: On the left axis is the mass of the blade. On the right axis are normalised constraints.

5 CONCLUSIONS

A wind turbine blade design approach has been demonstrated. The design approach utilizes gradient based optimization to minimize the mass of the blade. Using two load cases and constraining linear buckling factors, tip displacement, failure indices and thickness changes, the mass of the blade is reduced from 30105 kg to 28825 kg.

REFERENCES

[1] M. Jureczko, M. Pawlak, and A. Mężyk, “Optimisation of wind turbine blades,” *J. Mater. Process. Technol.*, vol. 167, no. 2–3, pp. 463–471, 2005.

[2] S. N. Sørensen, R. Sørensen, and E. Lund, “DMTO – a method for Discrete Material and Thickness Optimization of laminated composite structures,” *Struct. Multidiscip. Optim.*, vol. 50, no. 1, pp. 25–47, Jul. 2014.

[3] P. U. Haselbach, “An advanced structural trailing edge modelling method for wind turbine blades,” *Compos. Struct.*, vol. 180, pp. 521–530, Nov. 2017.

[4] MUST, “The MUltidisciplinary Synthesis Tool,” *Dep. Mater. Prod. Aalborg Univ.*, 2017.

30th Nordic Seminar on Computational Mechanics
NSCM-30
J. Høgsberg. N.L. Pedersen (Eds.)
2017

DROPLET PENETRATION AND CHEMICAL DEGRADATION IN A POROUS MEDIUM

HANJUN YU* AND GIHUN SON*

*Department of Mechanical Engineering, Sogang University
35 Baekbeom-ro Mapo-gu, Seoul 04107, South Korea
e-mail: gihun@sogang.ac.kr, web page: http://htlab.sogang.ac.kr/

Key words: Chemical Degradation, Droplet, Level-set Method, Porous Medium.

Summary. The chemical degradation in a toxic droplet absorbed in a porous medium is numerically investigated by solving the conservation equations of mass, momentum and chemical concentration. A level-set method for tracking the liquid-gas interface is extended to computation of droplet penetration and chemical reaction in a porous medium. The effects of porosity and initial concentration on the droplet chemical degradation are quantified.

1 INTRODUCTION

The chemical degradation in a toxic droplet penetrated in a porous medium is important in treatment of chemical agents in soil. However, a numerical method for computing the droplet motion and chemical reaction in the porous medium has not yet been developed.

Recently, numerical simulations of droplet motion in a porous medium were performed using a marker-and-cell (MAC) method[1], the volume-of-fluid (VOF) method[2] and a level-set (LS) method[3]. However, the computations were not extended to the chemical reaction in a porous medium.

In this work, the LS method is extended to computation of droplet penetration and chemical degradation in a porous medium. The volume averaged conservation equations of mass, momentum and chemical concentration are employed for the porous medium including the effects of porosity and drag force caused by the porous solid matrix.

2 NUMERICAL ANALYSIS

The present numerical approach is based on the LS formulation developed by Choi et al.[3] for droplet motion in a porous medium. The droplet surface is tracked by the LS function ϕ, which is defined as a signed distance from the liquid-gas interface while the porous surface is described by another distance function ψ. In this work, the following assumptions are made: the flow is axisymmetric and isothermal; the chemical reaction occurs only in the liquid phase.

We consider the following irreversible chemical reaction between toxic contaminant (A) and decontaminant (B) components:

$$A + nB \rightarrow C \tag{1}$$

where n is the stoichiometric ratio. Using the matching conditions at the porous-fluid interface, the conservation equations of mass and momentum in the liquid and gas phases and the component mass fraction (Y) in the liquid phase can be expressed as

$$\begin{aligned}
\nabla \cdot \hat{\mathbf{u}} &= 0 && (2)\\
\hat{\rho}\frac{\partial \hat{\mathbf{u}}}{\partial t} &= -\hat{\epsilon}_2[\nabla p + \sigma\kappa\nabla\alpha_\phi + (1-\alpha_\psi)B\hat{\mathbf{u}}] + \nabla\cdot\frac{\hat{\mu}}{\hat{\epsilon}_3}\nabla\hat{\mathbf{u}} + \hat{\mathbf{f}} && (3)\\
\frac{\partial \hat{\epsilon}_1 Y_A}{\partial t} &= -\hat{\mathbf{u}}\cdot\nabla Y_A + \nabla\cdot\hat{\epsilon_2}\hat{D}_A\nabla Y_A - \hat{\epsilon}_1 k_r Y_A Y_B && (4)\\
\frac{\partial \hat{\epsilon}_1 Y_B}{\partial t} &= -\hat{\mathbf{u}}\cdot\nabla Y_B + \nabla\cdot\hat{\epsilon_2}\hat{D}_B\nabla Y_B - \hat{\epsilon}_1 n\frac{M_B}{M_A}k_r Y_A Y_B && (5)
\end{aligned}$$

where

$$\begin{aligned}
\alpha_{\phi,\psi} &= 1 \qquad \text{if } \phi,\psi > 0 && (6)\\
\alpha_{\phi,\psi} &= 0 \qquad \text{if } \phi,\psi \le 0 && (7)\\
\hat{\mathbf{u}} &= \mathbf{u}\alpha_\psi + \epsilon\mathbf{u}(1-\alpha_\psi) && (8)\\
\mathbf{n} &= \nabla\phi/|\nabla\phi| && (9)\\
\kappa &= \nabla\cdot\mathbf{n} && (10)\\
\hat{\rho} &= \rho_l F_\phi + \rho_g(1-F_\phi) && (11)\\
\hat{\mu}^{-1} &= \mu_l^{-1}F_\phi + \mu_g^{-1}(1-F_\phi) && (12)\\
\hat{\epsilon}_1 &= \alpha_\psi + \epsilon(1-\alpha_\psi) && (13)\\
\hat{\epsilon}_2^{-1} &= F_\psi + \epsilon^{-1}(1-F_\psi) && (14)\\
\hat{\epsilon}_3 &= F_\psi + \epsilon(1-F_\psi) && (15)\\
B &= \frac{150\hat{\mu}(1-\epsilon)^2}{\epsilon^3 d_p^2} + \hat{\rho}\frac{1.75(1-\epsilon)|\hat{\mathbf{u}}|}{\epsilon^3 d_p} && (16)\\
\hat{\mathbf{f}} &= -\hat{\rho}\hat{\mathbf{u}}\cdot\nabla\frac{\hat{\mathbf{u}}}{\hat{\epsilon}_1} + \hat{\epsilon}_2\hat{\rho}\mathbf{g} + \nabla\cdot\frac{\hat{\mu}}{\hat{\epsilon}_3}(\nabla\hat{\mathbf{u}})^T && (17)
\end{aligned}$$

Here, k_r is the chemical reaction rate constant and M is the molecular mass.

The LS function ϕ is advanced and reinitialized as

$$\frac{\partial\phi}{\partial t} + \frac{\hat{\mathbf{u}}}{\hat{\epsilon}_1}\cdot\nabla\phi = 0 \tag{18}$$

$$\frac{\partial\phi}{\partial\tau} = \frac{\phi}{\sqrt{\phi^2+h^2}}(1-|\nabla\phi|) \quad \text{if } |\phi| \ge h/2 \tag{19}$$

where h is a grid spacing.

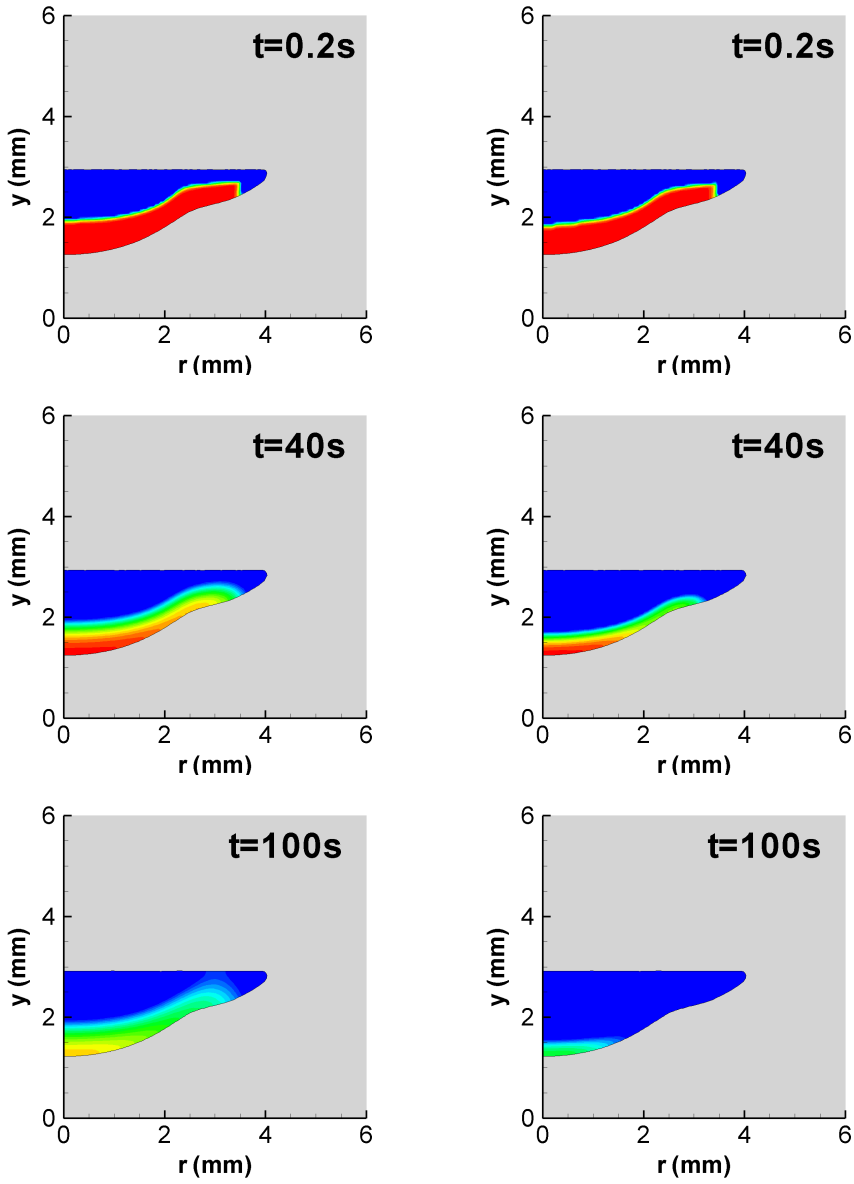

Figure 1: Concentration field of component A for $R_{B0} = 1mm$, $v_{B0} = 1m/s$, $k_r = 10^7(1/s)$ and $\epsilon = 0.2$ and different initial concentrations of component B: (a) $Y_{B0} = 0.1$ and (b) $Y_{B0} = 0.4$

3 RESULTS AND DISCUSSION

Computations are performed using the properties of water and air at 1 atm. In this work, we assume $n = 1$, $M_A = M_B$ and $D_A = D_B = 10^{-9}m^2/s$. The computational domain is chosen to be a cylindrical region of $0 \leq r \leq 9.6mm$ and $0 \leq y \leq 9.6mm$. The porous region is chosen to be $0 \leq y \leq 3mm$. Initially, a spherical droplet with a radius

of $1mm$ is impacted on the porous substrate. The droplet is assumed to have a toxic component (A) of $Y_{A0} = 0.1$. After the droplet is completely penetrated into the porous medium, a second droplet with a detoxifying component (B) is imposed on the porous substrate. We take the particle diameter of the porous medium as $d_p = 10\mu m$ and vary parametrically the initial concentration Y_{B0} of the second droplet and porosity ϵ.

Figure 1 shows the evolution of the liquid-gas interface and the associated concentration field of component A with different initial concentrations of component B. When the second droplet collides with the absorbed droplet, the concentration variations are localized near the droplet-droplet interface, and the mass of component A is sharply reduced. In the later period, when the droplet is completely embedded in the porous medium, the mass transfer occurs by diffusion and the chemical degradation of component A proceeds very slowly. The removal rate of component A is observed to significantly increase with the initial concentration of component B.

4 CONCLUSIONS

A level-set method was developed for computation of droplet penetration and chemical degradation in a porous medium by solving the conservation equations of mass, momentum and chemical concentration. The computations showed the time variation of the concentration field during the whole period of droplet penetration and chemical degradation. The removal rate of toxic component was observed significantly increase with the initial concentration of detoxifying component.

REFERENCES

[1] Reis, N.C., Griffiths, R.F. & Santos, J.M. Numerical simulation of the impact of liquid droplets on porous surfaces. *J. Comput. Phys.* **198**, 747–770 (2004).

[2] Kim, W.S. & Lee, S.Y. Behavior of a water drop impinging on porous substrates: examination of contact-line drag effect. *Atom. Sprays* **26**, 257–274 (2016).

[3] Choi, M., Son, G. & Shim, W. Numerical simulation of droplet impact and evaporation on a porous surface. *Int. Commun. Heat Mass Transf.* **80**, 18–29 (2017).

30th Nordic Seminar on Computational Mechanics
NSCM-30
J. Høgsberg. N.L. Pedersen (Eds.)
2017

THERMO-MECHANICAL ANALYSIS OF WIRE + ARC ADDITIVE MANUFACTURING PROCESS

LI SUN*, ZHILIANG ZHANG* XIAOBO REN† AND JIANYING HE*

* Department of Structural Engineering, Norwegian University of Science and Technology (NTNU), 7491 Trondheim, Norway
e-mail: li.sun@ntnu.no, web page: http://www.ntnu.edu/nml

† Materials and Chemistry, The Foundation for Scientific and Industrial Research (SINTEF), 7456 Trondheim, Norway
e-mail: xiaobo.ren@sintef.no, web page: http://www.sintef.no/sintef-materialer-og-kjemi

Abstract. Wire and Arc Additive Manufacture (WAAM) is widely used for the manufacture of large metal components due to its high deposition rate. However, residual stresses and distortion are introduced by the non-uniform expansion and contraction of the material during the rapid thermal cycle[1,2]. So studying the thermo-mechanical performance of the WAAM process and the effects of manufacturing parameters on residual stress are very important to predict the residual stresses.

In this work, the thermo-mechanical performance of the WAAM process was studied by the 2D/3D transient fully coupled thermo-mechanical FE models. Plastic deformation zone was then analyzed based on the temperature and stress's distribution and history. In addition, the effects of printing speed, heat flux input and mesh size of models on temperature and stress were evaluated and they showed sound effect on the thermo-mechanical performance. Finally, by comparison, the simulation results of sequential coupled thermo-mechanical model and fully coupled thermo-mechanical model are similar, but the latter is much efficient than the former.

Keywords: Thermal-mechanical analysis, Wire + arc additive manufacturing, Manufacturing parameters, Residual stress

REFERENCES

[1] Ding J, Colegrove P, Mehnen J, Ganguly S, Sequeira Almeida PM, Wang F, Williams S . Thermo-mechanical analysis of Wire and Arc Additive Layer Manufacturing process on large multi-layer parts. Comp Mater Sci 50, 3315-3322 (2011).

[2] D. H. Ding, Z. X. Pan, D. Cuiuri, and H. J. Li, "Wire-feed additive manufacturing of metal components: technologies, developments and future interests," International Journal of Advanced Manufacturing Technology, 81, 465-481, Oct 2015.

30th Nordic Seminar on Computational Mechanics
NSCM-30
J. Høgsberg. N.L. Pedersen (Eds.)
2017

FRACTURE SURFACE MORPHOLOGY UNDER DUCTILE TEARING OF METAL PLATES

MUHAMMET F. KAÇAR[*], CİHAN TEKOĞLU[*] AND KIM L. NIELSEN [†]

[*] Department of Mechanical Engineering, TOBB University of Economics and Technology,
Söğütözü, Ankara, 06560, Turkey
e-mail: c.tekoglu@etu.edu.tr, web page: http://cihantekoglu.etu.edu.tr

[†] Department of Mechanical Engineering, Solid Mechanics Section, Technical University of Denmark,
DK-2800 Kongens Lyngby, Denmark
Email: kin@mek.dtu.dk - Web page: http://www.mek.dtu.dk

Key words: Ductile plate tearing, Microstructure randomness, Void-by-Void, Multiple void interaction, Localization.

Summary. The present work takes as offset the hypothesis that microstructural parameters, related to particle size and distribution, govern the transition between crack surface morphologies observed in experiments. The key question is; why does tearing of a given metal plate leave a specific morphology on the fracture surface?

1 INTRODUCTION

The micro-mechanisms governing ductile plate tearing have been established through decades of research. Fracture of ductile metal plates, subject to mode I tearing, is known to depend heavily on the metal properties, microstructure and plate dimensions. Intermetallic inclusions are often responsible for the nucleation of the micro-voids that, upon loading, grow to coalesce and eventually form micro-cracks. However, distinct crack surface morphologies, such as cup-cup, cup-cone, and slanting are observed for extensive crack growth in metal plates and several investigators report that plates made of high strength age-hardened aluminum alloys, or high strength steels, exhibit slanted crack growth, whereas a cup-cup type fracture is observed for low strength alloys. Despite such insight, the interplay between tearing modes remains to be fully understood, e.g. nowhere is a conclusive answer found to; *why does a propagating crack choose one tearing mode over others?* In the present, work focus is turned to the effect of microstructure - in terms of void nucleation sites, number and distributions. The hypothesis is that; a population of small particle/void nucleation sites, distributed randomly in the material, gives rise to a very different fracture behavior in comparison to a population of randomly distributed large particle/void nucleation sites with the same overall volume fraction. Essentially, a shift in the governing mechanism from multiple void interactions, in a macroscopic deformation band, to a microscopic localization process that occurs as void-by-void interaction, is expected.

2 MODELLING FRAMEWORK

The present work adopts, and modifies, the simplified 2D plane strain model setup considered by Nielsen and Hutchinson (2012). Rather than restricting the analysis to a homogeneous Gurson-Tvergaard-Needleman (GTN) material (a continuum description), the present work focuses on the effect of introducing a population of "discrete" particles that act as discrete void nucleation sites. Thus, the model setup allows microstructural parameters such as the average initial porosity, the particle size (relative to plate thickness), number and distribution characteristics to enter the analysis. A number of void nucleation sites, N_p, are considered to be distributed randomly and modeled by locally introducing a high level of damage that locally follows a Gaussian bell (see Eq. (1)). Here, with the constraint that no overlapping between neighboring nucleation sites are allowed.

$$f_0(x_1, x_2) = f_0^M \exp\left(-\frac{(x_1 - x_1^M)^2 - (x_2 - x_2^M)^2}{2(R_p/4)^2}\right), \tag{1}$$

with f_0^M being the porosity at center of the nucleation site, x_i^M are the coordinates of the nucleation site center, and R_p is the radius of the nucleation site (with a minimum of 6 elements across each nucleation site). A background porosity is assumed to exist between nucleation sites, f_0^b, which allows neighboring sites to eventually coalesce. The GTN material model is employed to predict the porosity evolving from the nucleation sites as-well as the macroscopic material separation that develops across the plate thickness as voids link up. The employed version of the GTN model reads;

$$\Phi = \left(\frac{\sigma_e}{\sigma_y}\right)^2 + 2q_1 f^* \cosh\left(\frac{3}{2}\frac{q_2\sigma_{kk}}{\sigma_e}\right) - (1 + (q_1 f^*)^2), \tag{2}$$

and takes into account void coalescence by the phenomenological f^*-criterion introduced by Tvergaard and Needleman (1984). Thus, the analysis relies on two key void volume fractions; one to define the onset of void coalescence, f_c, and one to define the complete loss of load carrying capacity at a material point, f_f $(= f_0^M)$. The Tvergaard constants are; $q_1 = 1.5$ and $q_2 = 1.0$.

As plastic flow localizes ahead of the crack tip, the domain above and below the fracture process zone elastically unload. This enforces a constraint on the deformation along the x_3-direction that leads to a near tip plane strain condition (see Fig. 1). That is, a cross-sectional plane, assumed constraint to plane strain in the crack growth direction, is modeled by use of ABAQUS/Explicit and the section considered maintains an initial aspect ratio of $H/W = 3$. Figure 1 outlines the boundary value problem considered. The element size in the finely discretized section is; $L_e/W = 0.001$, with W being the plate thickness. Elements in that region are 4-node and square in the un-deformed configuration (employing reduced Gauss integration, CPE4R). ABAQUS/Explicit is employed to facilitate element erosion when a sufficient damage level is reached, but it is not the intention to enter a regime where inertia plays a role.

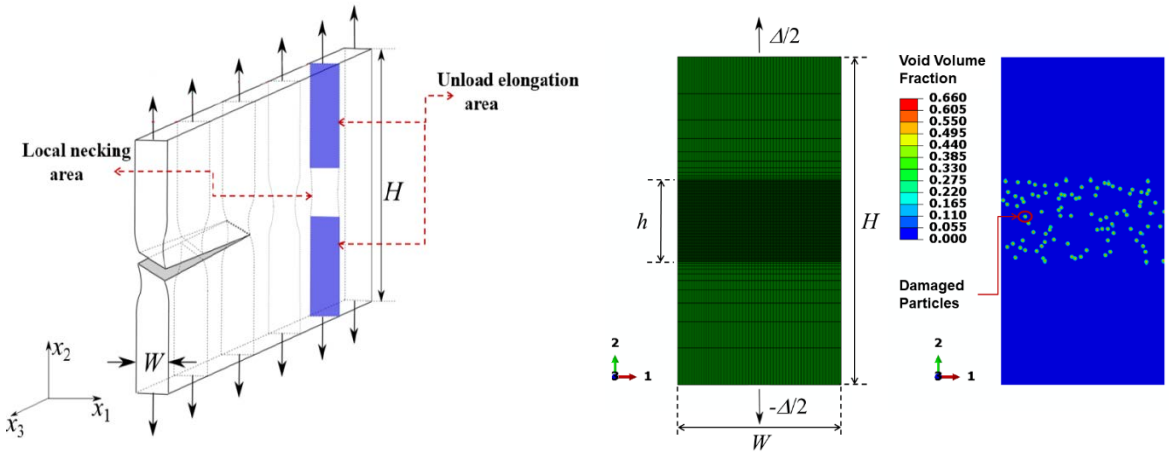

(a) (b)

Figure 1: (a) Schematic of the sequential fracture process governing ductile plate tearing under mode I loading, here identifying the domain height, H, and the plate thickness, W. (b) The FE mesh for the 2D plane strain plate section with imposed boundary conditions and illustrated damaged particle distribution.

3 RESULTS

The plate material is assumed to be a typical aluminum alloy in the calculations presented below (with a Young's modulus; $E = 70$ GPa, Poisson ratio; $\nu = 0.3$, density; $\varrho = 2700\ \mathrm{kg/m^3}$, initial yield stress; $\sigma_0 = 300$ MPa, and a power-low hardening exponent; $n \in [0.05,0.15]$). An extensive convergence study has been performed to adjust the model parameters; f_c, f_f, f_0^b, and the imposed macroscopic strain rate, $\dot{E}_{22}$, such that dynamic effects are eliminated from the results. Here, by ensuring a low kinetic energy and a rate-independent crack surface morphology (the latter proving to be a strict condition). The convergence study showed that with increasing initial porosity in the plate (which depends on f_f, f_0^b, and N_p), the $\dot{E}_{22}$ value required to provide quasi-static results decreases. This is in accordance with the physics of the problem: a larger initial porosity leads to several energetically (more or less) equivalent crack paths and even a small change in $\dot{E}_{22}$ results an alternative crack path to be activated. Also, for f_0^b values on the same order of magnitude as f_c, the crack path evolves through void-by-void coalescence and is rather insensitive to $\dot{E}_{22}$. Figure 2 shows preliminary results and, as expected, the crack path (here depicted in the un-deformed geometry) is indeed sensitive to the number, distribution and size of the damaged discretely modelled particles as well as to the strain hardening capacity of the plate.

4 CONCLUSIONS

A numerical framework is developed to investigate the effects of material/geometric parameters on the crack path morphology in ductile tearing of metal alloys. Although more calculations need to be performed to reach secure conclusions, the initial results suggest that a small (large) strain hardening exponent favors a slanted (cup-cup) crack, in accordance with the experimental results in the literature.

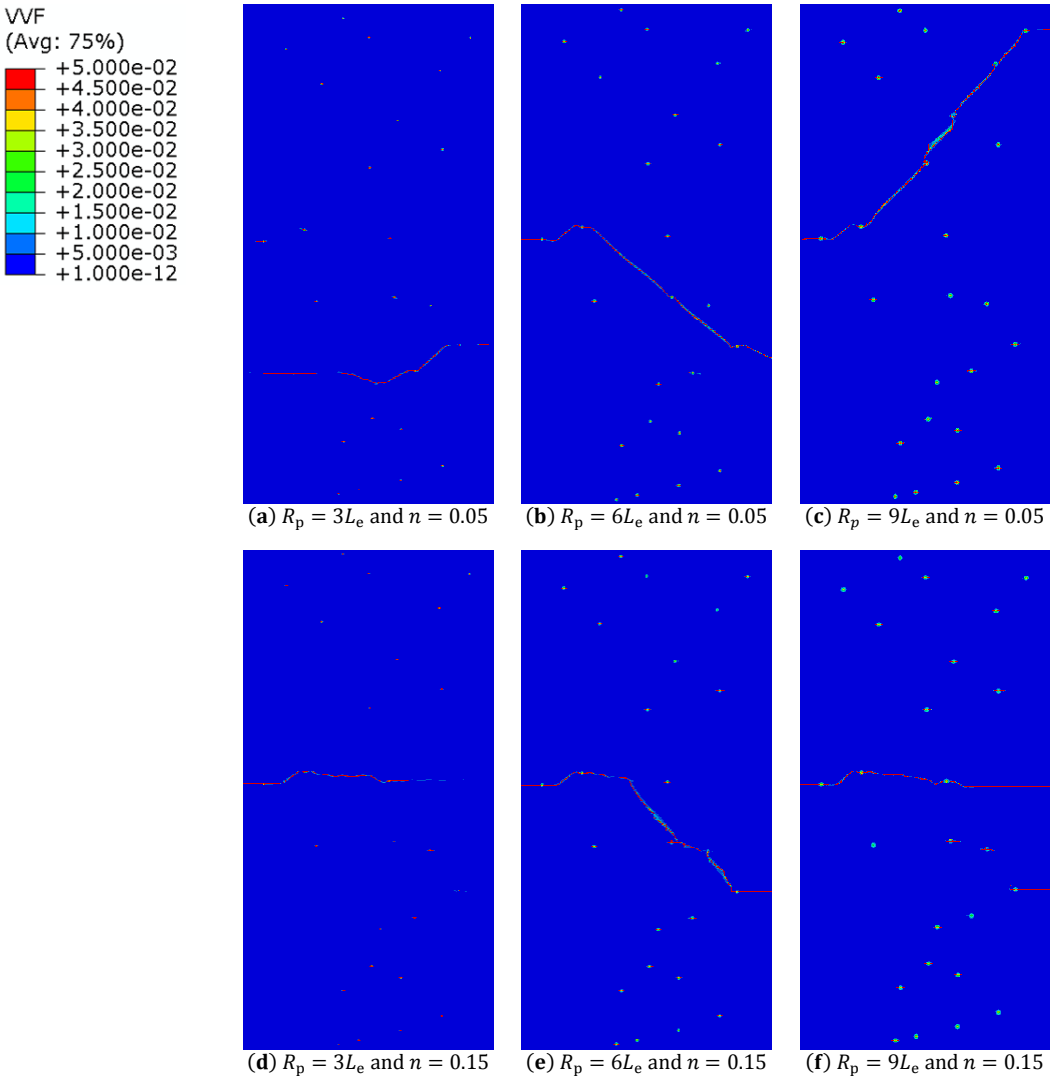

(**a**) $R_{\mathrm{p}} = 3L_{\mathrm{e}}$ and $n = 0.05$ (**b**) $R_{\mathrm{p}} = 6L_{\mathrm{e}}$ and $n = 0.05$ (**c**) $R_p = 9L_{\mathrm{e}}$ and $n = 0.05$

(**d**) $R_{\mathrm{p}} = 3L_{\mathrm{e}}$ and $n = 0.15$ (**e**) $R_{\mathrm{p}} = 6L_{\mathrm{e}}$ and $n = 0.15$ (**f**) $R_{\mathrm{p}} = 9L_{\mathrm{e}}$ and $n = 0.15$

Figure 2: (a-f) Crack path morphologies in the un-deforment geometry for $N_p = 25$, $f_c = 0.01$, $f_f = 0.05$, f_0^b=0.0001, and $\dot{E}_{22} = 0.0008\ \mathrm{s}^{-1}$. The particle radius, R_p, and strain hardening, n, are given below each figure.

ACKNOWLEDGEMENTS

The authors gratefully acknowledge the financial support by TÜBİTAK (project no: 315M133). KLN is financially supported by the VILLUM Foundation Young Investigator Programme, grant VKR023451.

REFERENCES

[1] K.L. Nielsen and J.W. Hutchinson, "Cohesive traction-separation laws for tearing of ductile metal plates", *Int. J. Impact. Eng.*, **48**, 15-23 (2012).

[2] V. Tvergaard and A. Needleman, "Analysis of the cup-cone fracture in a round tensile bar", *Acta Metall.*, **32**, 157-169 (1984).

30th Nordic Seminar on Computational Mechanics
NSCM-30
J. Høgsberg. N.L. Pedersen (Eds.)
2017

ROBUST RETURN ALGORITHM FOR ANISOTROPIC PLASTICITY MODELS

L. TIDEMANN*† AND S. KRENK*

*Department of Mechanical Engineering, Technical University of Denmark
DK-2800 Kongens Lyngby, Denmark

†Mærsk Olie & Gas
DK-6700 Esbjerg, Denmark
e-mail: lastid@mek.dtu.dk

Key words: Return algorithms, Computational methods, Cyclic plasticity.

1 INTRODUCTION

Plasticity models can be defined by an energy potential, a plastic flow potential and a yield surface. The energy potential defines the relation between the observable elastic strains $\boldsymbol{\gamma}_\mathrm{e}$ and the energy conjugate stresses $\boldsymbol{\tau}_\mathrm{e}$ and between the non-observable internal strains $\boldsymbol{\gamma}_\mathrm{i}$ and the energy conjugate internal stresses $\boldsymbol{\tau}_\mathrm{i}$, where the internal stresses control the various hardening mechanisms. Plasticity models may be defined either in terms of traditional stresses and strains $\boldsymbol{\tau} = [\sigma_{11}, \sigma_{22}, \cdots]^T$ and $\boldsymbol{\gamma} = [\varepsilon_{11}, \varepsilon_{22}, \cdots]^T$ or generalized stresses and strains, e.g. $\boldsymbol{\tau} = [N, M_y, \cdots]^T$ and $\boldsymbol{\gamma} = [\varepsilon, \kappa_y, \cdots]^T$, the latter typically used in plastic analysis of frame structures. To have a compact notation in the following $\boldsymbol{\tau}_\mathrm{e}$ and $\boldsymbol{\tau}_\mathrm{i}$ are arranged in a common vector $\tilde{\boldsymbol{\tau}}^T = [\boldsymbol{\tau}_\mathrm{e}^T, \boldsymbol{\tau}_\mathrm{i}^T]$ and correspondingly $\boldsymbol{\gamma}_\mathrm{e}$ and $\boldsymbol{\gamma}_\mathrm{i}$ are arranged in the common vector $\tilde{\boldsymbol{\gamma}}^T = [\boldsymbol{\gamma}_\mathrm{e}^T, \boldsymbol{\gamma}_\mathrm{i}^T]$.

In traditional stress-based analyses the stress is evaluated at a material point, where a single plastic mechanism may be active, whereas in the case of frame structures each beam may have two active plastic mechanisms, in the form of a yield hinge in each end as illustrated in Fig. 1. In general multiple plastic mechanisms may be active for different types of elements. Each plastic mechanism has a yield surface described by a yield function F_j and a flow potential G_j describing the plastic flow evolution by its gradient and these potentials are conveniently collected in the vectors $\mathbf{f}_y = [F_1(\tilde{\boldsymbol{\tau}}), \dots, F_n(\tilde{\boldsymbol{\tau}})]^T$ and $\mathbf{g} = [G_1(\tilde{\boldsymbol{\tau}}), \dots, G_n(\tilde{\boldsymbol{\tau}})]^T$ respectively.

The key to developing a general and robust return algorithm for anisotropic plasticity models is the strain evolution equation. The strain evolution equation is obtained from maximizing the dissipation rate under the assumption that the material is described by the flow potential[1,2]

$$\dot{\tilde{\gamma}} = \begin{bmatrix} \dot{\boldsymbol{\gamma}}_\mathrm{t} \\ \mathbf{0} \end{bmatrix} - \sum_j \partial_{\tilde{\boldsymbol{\tau}}} G_j \, \dot{\lambda}_j = \begin{bmatrix} \dot{\boldsymbol{\gamma}}_\mathrm{t} \\ \mathbf{0} \end{bmatrix} - \left(\partial_{\tilde{\boldsymbol{\tau}}}^T \mathbf{g}\right)^T \dot{\boldsymbol{\lambda}} \,, \tag{1}$$

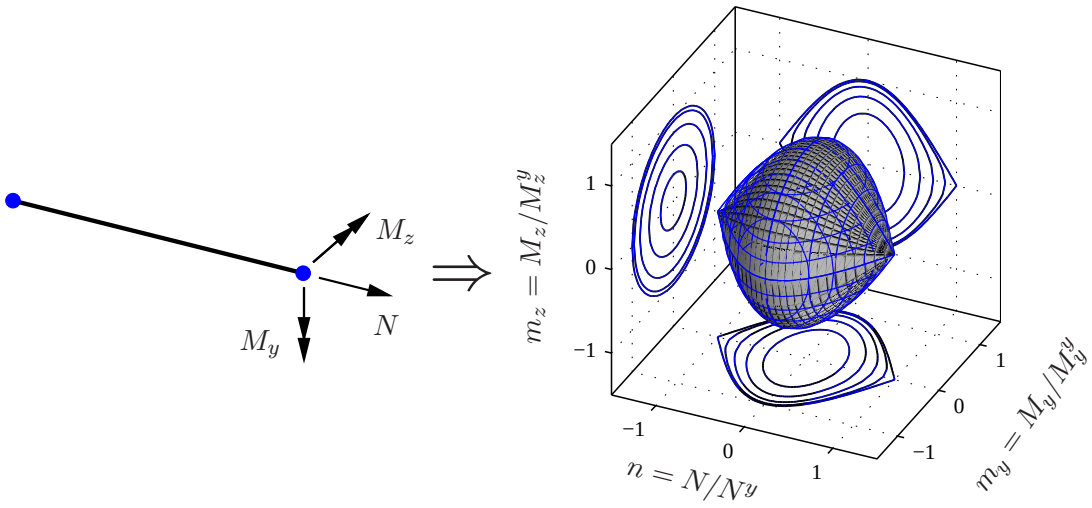

Figure 1: Beam with plastic hinges and corresponding yield surface.

where $\dot{\boldsymbol{\gamma}}_{\mathrm{t}}$ is the total increment in the observable strains. The plastic multipliers $\dot{\boldsymbol{\lambda}}$ are determined by the consistency condition that during plastic loading, the stress state $\boldsymbol{\tau}_{\mathrm{e}}$ must stay on the yield surfaces defined in $\mathbf{f}_y$.

2 RETURN ALGORITHM

The strain evolution equation (1) is reformulated to finite increments and is assumed to be satisfied in the final generalized stress state[3]. For non-trivial yield surfaces the strain evolution equation will not initially be satisfied and a residual is formed

$$\mathbf{r}_{\tilde{\gamma}} \;=\; \begin{bmatrix} \Delta\boldsymbol{\gamma}_{\mathrm{t}} \\ \mathbf{0} \end{bmatrix} - \Delta\tilde{\boldsymbol{\gamma}} - \left(\partial^T_{\tilde{\boldsymbol{\tau}}}\mathbf{g}\right)^T \Delta\boldsymbol{\lambda}\,. \tag{2}$$

The final state where $\mathbf{r}_{\tilde{\gamma}} = \mathbf{0}$ is obtained by a first order variation of the residual (2) combined with the consistency condition that the final stress state must be on the yield surface. The first order variation is formulated entirely in terms of $\delta\tilde{\boldsymbol{\tau}}$ and $\delta\boldsymbol{\lambda}$ with use of the constitutive relation

$$\delta\tilde{\boldsymbol{\tau}} \;=\; \tilde{\mathbf{K}}\,\delta\tilde{\boldsymbol{\gamma}}\,, \tag{3}$$

where the tangent stiffness matrix $\tilde{\mathbf{K}}$ contains the double derivatives of the energy potential. The resulting equation system to solve is

$$\begin{bmatrix} \tilde{\mathbf{K}}_A^{-1} & \left(\partial^T_{\tilde{\boldsymbol{\tau}}}\mathbf{g}\right)^T \\ \partial^T_{\tilde{\boldsymbol{\tau}}}\mathbf{f}_y & \mathbf{0} \end{bmatrix} \begin{bmatrix} \delta\tilde{\boldsymbol{\tau}} \\ \delta\boldsymbol{\lambda} \end{bmatrix} \;=\; \begin{bmatrix} \mathbf{r}_{\tilde{\gamma}} \\ -\mathbf{f}_y \end{bmatrix}\,, \quad \tilde{\mathbf{K}}_A^{-1} \;=\; \tilde{\mathbf{K}}^{-1} + \sum_j \frac{\partial^2 G_j}{\partial\tilde{\boldsymbol{\tau}}^T\partial\tilde{\boldsymbol{\tau}}}\Delta\lambda_j\,, \tag{4}$$

where $\tilde{\mathbf{K}}_A$ is the consistent algorithmic stiffness matrix. Instead of solving (4) directly it is solved sequentially by eliminating $\delta\tilde{\boldsymbol{\tau}}$ in the first equation and determining $\delta\boldsymbol{\lambda}$ from the second equation and back-substituting the result into the first equation. Anisotropic

plasticity models may have yield surfaces with regions with large curvature, Fig. 1, leading to large changes in the direction of the gradient of the yield surface and the plastic flow potential. Though $\delta\tilde{\boldsymbol{\tau}}$ is a linear function of the residual $\mathbf{r}_{\tilde{\gamma}}$ and the value of the yield function $\mathbf{f}_y$ according to (4) the function is non-linear as $\tilde{\mathbf{K}}_A^{-1}$, $\partial_{\tilde{\boldsymbol{\tau}}}^T\mathbf{g}$ and $\partial_{\tilde{\boldsymbol{\tau}}}^T\mathbf{f}_y$ in general are non-linear. The increment $\delta\tilde{\boldsymbol{\tau}} = \delta\tilde{\boldsymbol{\tau}}(\xi\mathbf{r}_{\tilde{\gamma}}, \xi\mathbf{f}_y)$ is therefore represented by a second order approximation

$$\delta\tilde{\boldsymbol{\tau}}(\xi) \;=\; \xi\,\frac{\partial(\delta\tilde{\boldsymbol{\tau}})}{\partial\xi}\bigg|_{\xi=0} + \tfrac{1}{2}\xi^2\frac{\partial^2(\delta\tilde{\boldsymbol{\tau}})}{\partial\xi^2}\bigg|_{\xi=0}, \tag{5}$$

where the constant term is zero for $\xi = 0$ and the two derivatives are given by

$$\frac{\partial(\delta\tilde{\boldsymbol{\tau}})}{\partial\xi} \;=\; \mathbf{K}_\mathbf{r}\mathbf{r}_{\tilde{\gamma}} - \mathbf{K}_\mathbf{f}\mathbf{f}_y\,, \quad \frac{\partial^2(\delta\tilde{\boldsymbol{\tau}})}{\partial^2\xi} \;=\; \frac{\partial}{\partial\xi}\Big(\mathbf{K}_\mathbf{r}\mathbf{r}_{\tilde{\gamma}} - \mathbf{K}_\mathbf{f}\mathbf{f}_y\Big) \;\simeq\; \frac{\Delta\mathbf{K}_\mathbf{r}}{\Delta\xi}\mathbf{r}_{\tilde{\gamma}} - \frac{\Delta\mathbf{K}_\mathbf{f}}{\Delta\xi}\mathbf{f}_y\,. \tag{6}$$

The differences $\Delta\mathbf{K}_\mathbf{r}$ and $\Delta\mathbf{K}_\mathbf{f}$ are determined by making half a step, i.e. setting $\xi = 1/2$ and determining the matrices in the updated state by the gradients $\partial_{\tilde{\boldsymbol{\tau}}}^T\mathbf{g}$ and $\partial_{\tilde{\boldsymbol{\tau}}}^T\mathbf{f}_y$ as well as the second order derivatives $\partial^2 G_j/(\partial\tilde{\boldsymbol{\tau}}^T\partial\tilde{\boldsymbol{\tau}})$. These are combined with the solution of the equation system (4) to form $\mathbf{K}_\mathbf{r}^{1/2}$ and $\mathbf{K}_\mathbf{f}^{1/2}$. Inserting the results into (6) and (5) with $\Delta\xi = 1/2$ and setting $\xi = 1$ gives the relation

$$\delta\tilde{\boldsymbol{\tau}} \;=\; \mathbf{K}_\mathbf{r}^{1/2}\mathbf{r}_{\tilde{\gamma}} - \mathbf{K}_\mathbf{f}^{1/2}\mathbf{f}_y\,. \tag{7}$$

This is analogous to a method used in explicit stress integration[3] where a midpoint is found and the elasto-plastic stiffness at the midpoint is used for a full step.

3 NUMERICAL EXAMPLES

The robustness of the return algorithm is illustrated by deformation of a beam with plastic hinges, Fig. 1, described by a cyclic plasticity model[1] in terms of the normalized section forces[2] $n = N/M^y$ and $m = M/M^y$. The yield surface is slightly rounded in comparison to the one shown in Fig. 1. The energy potential consists of two quadratic terms uncoupling $\boldsymbol{\tau}_\mathrm{e}$ and $\boldsymbol{\tau}_\mathrm{i}$ whereby $\tilde{\mathbf{K}}$ becomes a block diagonal matrix with $\mathbf{K}_\mathrm{e}$ and $\mathbf{K}_\mathrm{i}$ in the diagonals. The yield surface is kinematic hardening and is tailored for cyclic plasticity models with general hardening behaviour[1]. The beam is modelled with parameters representing ideal-plastic behaviour, Fig. 2(a) and (b), and parameters representing non-linear hardening plastic hinges, Fig. 2(c) and (d). Both beams are subjected to a large strain increment with an equivalent estimated elastic stress state with $n = 14$ and $m_y = 4$ at one hinge and $n = 14$ and $m_y = 0$ at the other hinge.

The estimated elastic stress state is located far away from the yield surface in a region with relatively large curvature of the yield surface and two plastic mechanisms. Nevertheless the algorithm returns the stress state to the yield surfaces in just 10 iterations in the ideal plasticity case as illustrated in Fig. 2(a) and (b). About half the number of iterations is used to get to the neighbourhood of the final state and the remaining half is

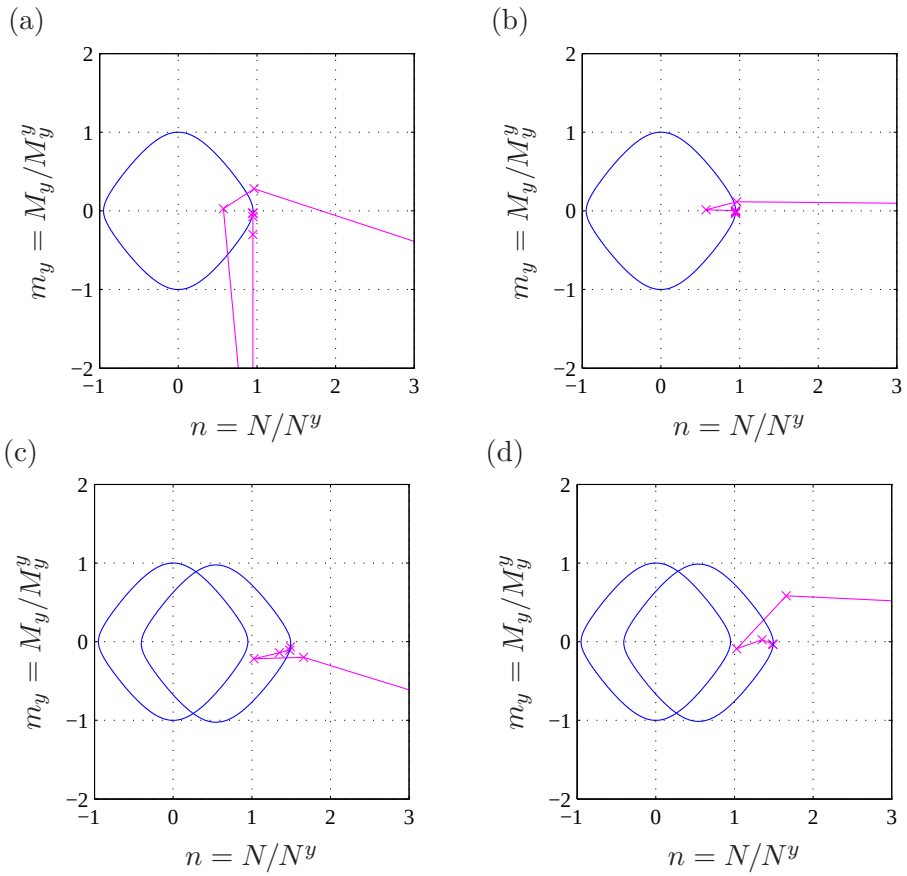

Figure 2: Return with ideal plasticity parameters (top) and hardening plasticity parameters (bottom). Left: Yield surface 1. Right: Yield surface 2.

to ensure $\mathbf{r}_{\tilde{\gamma}} = \mathbf{0}$. Hardening typically eases return and as shown in Fig. 2(c) and (d) it does in the present case as well, as the return is made in only 7 steps. It is noted that a traditional single-step return algorithm fails to converge for the predicted stress states shown in Fig. 2. In general the method presented here is more robust, e.g. if half the deformation increment used above is applied a traditional single-step return algorithm will converge in the ideal-plastic case but not in the hardening case.

REFERENCES

[1] Krenk, S. & Tidemann, L. A compact cyclic plasticity model with parameter evolution. *Mechanics of Materials* **113**, 57–68 (2017).

[2] Tidemann, L. & Krenk, S. Cyclic plastic hinges with degradation effects for frame structures. *Journal of Engineering Mechanics* (accepted for publication) (2017).

[3] Zienkiewicz, O. C., Taylor, R. L. & Zhu, J. Z. *The Finite Element Method* (Elsevier Butterworth–Heinemann, Oxford, 2005), 6 edn.

30th Nordic Seminar on Computational Mechanics
NSCM-30
J. Høgsberg. N.L. Pedersen (Eds.)
2017

A NEW CORRECTION METHOD TO MEASURE MATERIAL'S EQUIVALENT STRESS-STRAIN CURVE WITH AXISYMMETRIC NOTCHED TENSILE SPECIMEN

NSCM-30

SHENGWEN TU[*], XIAOBO REN[†], BÅRD NYHUS[†]; ODD MAGNE AKSELSEN[†], JIANYING HE[*], ZHILIANG ZHANG[*]

[*]Department of structure Engineering
Norwegian University of Science and Technology
Richard Birkelands vei 1a, NO-7491, Trondheim, Norway
e-mail: shengwen.tu@ntnu.no, web page: http://www.ntnu.edu/nml

[†]SINTEF Materials and Chemistry
Richard Birkelands vei 2b, NO-7456, Trondheim, Norway
Email: Xiaobo.Ren@sintef.no - Web page: http://www.sintef.no

Key words: Equivalent Stress-Strain Curve, Axisymmetric Notched Tensile Specimen, Bridgman Correction, Large Strain.

Summary. This study introduces a new correction method to obtain equivalent stress-strain curve in large strain by converting true stress-strain curve from axisymmetric notched tensile specimen. Experimental work were performed with a 420 MPa structural steel to verify the correction method. Equivalent stress-strain curves derived with the proposed correction method show good agreement with those from extensometer before diffuse necking and present lower stress-strain curves than those from Bridgman correction method in large strain.

1 INTRODUCTION

A good understanding of material's equivalent stress-strain behavior in large strain is very important for large deformation analysis. For example, for ductile fracture assessment with finite element method, material ahead of the crack tip deforms significantly and presents very complicate stress and strain field. The material's equivalent stress-strain curve should be given in large strain to characterize the stress state ahead of the crack tip accurately.

The well-known Bridgman correction is not very accurate when the strain is large[1,2]. This is mainly due to the assumption that the equivalent strain is uniform in the necked specimen minimum cross-section. Hybrid experimental-numerical method works elegantly, but it is time consuming to match the stress-strain curves[3] from test and from simulation iteratively. Recently, we proposed a new correction method to correct true stress-strain from any axisymmetric notched specimens[4,5] to material's equivalent stress-strain curve. This method was derived with numerical analyses with power-law hardening material. In this study, we

experimentally verified the proposed correction method with a 420 MPa structural steel by performing quasi-static tensile tests with axisymmetric notched specimens. True stress-strain curves from axisymmetric notched specimens are then corrected with the proposed correction method. Good agreement between the equivalent stress-strain curves from axisymmetric notched specimens and from smooth specimens with extensometer before diffuse necking are observed. By comparing the equivalent stress-strain curve from Bridgman correction, it infers that our proposed method presents good accuracy.

2 CORRECTION METHOD WITH AXISYMMETRIC NOTCHED SPECIMEN

By investigating true stress-strain curves from axisymmetric notched specimens with power-law hardening materials numerically, we proposed an empirical correction function. The correction function can be written in a general form:

$$\xi = g_{a_0/R_0}(\varepsilon) \cdot f(\varepsilon_{P_{\max}}) \cdot f_{\xi_{\varepsilon=0.8,n=0}}(a_0/R_0) \tag{1}$$

where a_0/R_0, ε, and $\varepsilon_{P_{\max}}$ are the initial notch radius ratio, strain and strain corresponding to the maximum load. The correction function consists of three parts. The first part depends on the deformation level of an axisymmetric notched tensile specimen, and behaviors linearly with the strain, as seen in Eq. (6).

$$\begin{aligned} &g_{a_0/R_0}(\varepsilon) = (b_1 * \varepsilon + b_2)_{a_0/R_0} \\ &b_1 = 0.02606 * (a_0/R_0)^2 - 0.2 * (a_0/R_0) + 0.2764 \\ &b_2 = -0.02215 * (a_0/R_0)^2 + 0.16264 * (a_0/R_0) + 0.7796 \end{aligned} \tag{2}$$

The second part is a function of the strain corresponding to the maximum load, see in Eq. (3).

$$f(\varepsilon_{p_{\max}}) = -0.5357 * \varepsilon_{P_{\max}} + 1 \tag{3}$$

The third part is used to calculate the reference values used for normalization of the perfectly plastic material. A second order polynomial function is used to establish the relation between the reference values and the initial notch radius ratio, as Eq. (4).

$$f_{\xi_{\varepsilon=0.8,n=0}}(a_0/R_0) = -0.01579 * (a_0/R_0)^2 + 0.1411 * (a_0/R_0) + 1.3647 \tag{4}$$

When a_0/R_0, ε, and $\varepsilon_{P_{\max}}$ are known, true stress, σ_T, calculated by dividing load by current minimum cross-section area can be converted to the equivalent stress, σ_{eq}, by Eq. (5):

$$\sigma_{eq} = \sigma_T / \xi \tag{5}$$

3 TESTING PROGRAM

To verify the proposed correction function, we performed quasi-static tensile tests with axisymmetric notched specimens machining from a 420 MPa structure steel. The geometry of the notched and smooth specimens is shown in Fig. 1. In this study, $a_0 = 6\ mm$ and $d_0 = 20\ mm$ are used for all the axisymmetric notched specimens. d_0 is the specimen outer diameter. By

varying initial notch curvature radius, R_0, a_0/R_0 ranges from 0.5 to 3. All the specimens were tested in a universal test machine Instron 5985 in displacement control with the crosshead speed of 0.3 *mm*/minute. The specimen deformation was recorded by a digital high speed camera and then analyzed with a so-called edge tracing method to calculate the strain, which is defined by the specimen minimum cross-section area reduction.

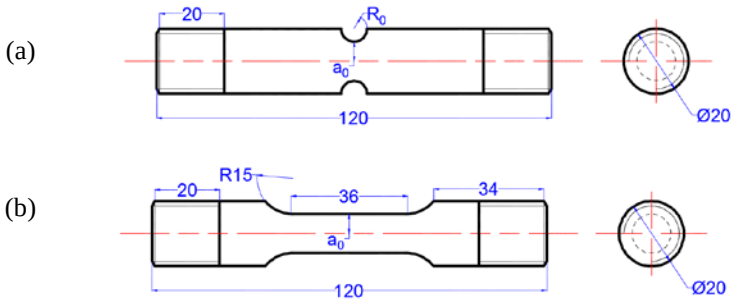

Figure 1: Sketches of the tensile specimens: (a) axisymmetric notched tensile specimen; (b) smooth round bar specimen.

4 RESULTS AND DISCUSSION

In the tests, the load was recorded with the same frequency as the camera framing rate. All the pictures taken in the tests were analyzed with the edge tracing method. The true stress-strain curves for all the axisymmetric notched specimens and smooth round bar specimen are presented in Fig. 2. It is evident that notched specimens with smaller a_0/R_0 corresponds to a higher true stress at the same strain and fails at larger true stress and smaller strain.

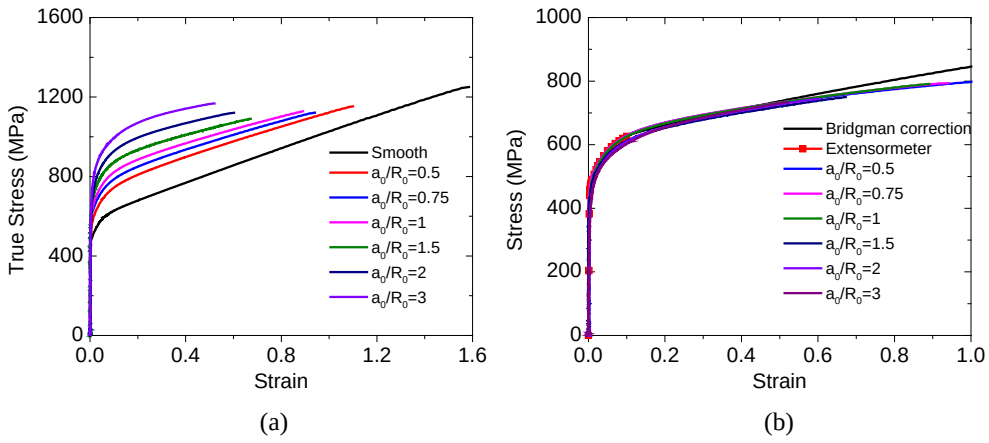

Figure 2: (a) True stress-strain curves from tests; (b) The equivalent stress-strain curves by correcting curves in Fig. 2 (a) with Eq. (1). True stress-strain curve from smooth round bar specimen is also shown.

$\varepsilon_{P_{max}}$ is determined from load-strain curves and equals to 0.1 for all the axisymmetric notched specimens. True stress-strain curves in Fig. 2 (a) are corrected by Eq. (1) and corresponding equivalent stress-strain curves are presented in Fig. 2 (b). Equivalent stress-

strain curves measured with extensometer and by correcting true stress-strain from smooth round bar specimen with Bridgman correction are also presented. All the curves in Fig. 2 (b) almost collapse into one, with small scatters. It indicates that equivalent stress-strain curve derived with the correction function is accurate. Difference between the equivalent stress-strain curves from Bridgman correction method and from our proposed correction method can be observed. Usually, the equivalent stress corrected by Bridgman correction method is still larger than the material's equivalent stress at large strain. We can infer that our method can present better accuracy than Bridgman correction method when the strain is large.

5 CONCLUSION

In this study, we introduced our recent proposed correction method, with which true stress-strain curve from any axisymmetric notched specimens can be converted to material's equivalent stress-strain curve in large strain. We experimentally verified the accuracy of our proposed correction method with a 420 MPa structural steel. Results show that our proposed correction method present accurate equivalent stress-strain curve when the strain is large. It should be noted that the specimen should fulfill the geometry requirements: $d_0 \geq 3.5a_0$. This correction method can also be used to determine the equivalent stress-strain curves of each individual material zone of weldments when the specimen minimum cross-section radius is smaller than the material zone length in the notch.

ACKNOWLEDGE

The Chinese Scholarship Council is greatly acknowledged for the financial support. The authors wish to thank the Research Council of Norway for funding through the Petromaks 2 Programme, Contract No.228513/E30.

REFERENCES

[1] P. W. Bridgman, *Studies in large plastic flow and fracture*, McGraw Hill, 1952.

[2] G. La Rosa, G. Mirone and A. Risitano, "Postnecking elastoplastic characterization degree of approximation in the bridgman method and properties of the flow stress true stress ratio", *Metall Mater Trans A*, **37**, 615-624 (2003).

[3] J. Peirs, P. Verleysen, W. Van Paepegem and J. Degrieck, "Determining the stress–strain behaviour at large strains from high strain rate tensile and shear experiments", *Int. J. Impact Eng*, **38**, 406-415 (2011).

[4] Z. Zhang, M. Hauge, C. Thaulow et al., "A notched cross weld tensile testing method for determining true stress–strain curves for weldments", *Eng. Fract. Mech*, 69, 353-366 (2002).

[5] S. Tu, X. Ren and Z. Zhang et al., "A special notched tensile specimen to determine the flow stress-strain curve of hardening materials without applying the Bridgman correction", *Eng. Fract. Mech*, 179, 225-239 (2017).

30th Nordic Seminar on Computational Mechanics
NSCM-30
J. Høgsberg. N.L. Pedersen (Eds.)
2017

ON MATHEMATICAL MORPHOLOGY, NON-LINEAR FILTERS, AND MINIMUM LENGTH SCALE CONTROL IN TOPOLOGY OPTIMIZATION

EDDIE WADBRO* AND LINUS HÄGG*

*Department of Computing Science, Umeå University, SE 901 87 Umeå, Sweden
e-mail: eddiew@cs.umu.se and linush@cs.umu.se

Key words: Topology optimization, Regularization, Nonlinear filters, Size control, Mathematical morphology

Summary. We propose a definition of the minimum length scale for subsets of a bounded convex design domain, and show that the length scale so defined is tightly linked to the operators of mathematical morphology. The numerical experiments use density based topology optimization with morphology mimicking fW-mean filters to impose minimum length scales on two material phases for a minimum compliance problem. The optimized designs are essentially binary and exhibit minimum length scales on both material phases.

1 INTRODUCTION TO FILTERS, MATHEMATICAL MORPHOLOGY, AND MINIMUM LENGTH SCALE CONTROL

Filters ensure existence of solutions to some continuous versions of the filtered penalized minimum compliance problem[1,2]. Filters also provide mesh-independent solutions and combat the so-called checkerboard problem for the discretized problem[3]. During the last decade, there has been an intense interest in developing new non-linear filtering strategies[4,5,6]. A vast majority of available filters for topology optimization can be written in the form of an fW-mean[7]; that is, the fitlered density is given by

$$\big(F(\rho)\big)(x) = g\left(\int_{\mathcal{N}_x} W(x,y) f\big(\rho(y)\big)\,\mathrm{d}y\right), \tag{1}$$

where $f\colon [0,1] \to [f_{\min}, f_{\max}] \subset \mathbb{R}$ and $g\colon [f_{\min}, f_{\max}] \to [0,1]$ are smooth and invertible functions, $\mathcal{N}_x$ is the neighborhood of x, and the kernel W satisfies $\int_{\mathcal{N}_x} W(x,y)\,\mathrm{d}y = 1$ for all x. Typically, $g = f^{-1}$ and $W(x,\cdot) = \chi_{\mathcal{N}_x}/|\mathcal{N}_x|$, where $\chi_{\mathcal{N}_x}$ and $|\mathcal{N}_x| > 0$ are the characteristic function and the measure (area or volume) of $\mathcal{N}_x$, respectively; these choices render $\big(F(\rho)\big)(x)$ to be the f-mean of ρ in $\mathcal{N}_x$.

The underlying idea of mathematical morphology is to gain information about a set $M \subset \mathbb{R}^d$ by probing it by another set $B \subset \mathbb{R}^d$, called the structuring element. Here, we restrict our attention to structuring elements that contain 0 and are open, bounded, symmetric, and convex. The standard morphological operators (see, for example, the review

by Heijmans[8]) are defined for subsets of $\mathbb{R}^d$. Often, design optimization problems are formulated for the case where the design domain Ω is a d-orthotope, or a hyperrectangle (or the union of finitely many d-orthotopes), while the structuring element B is an open Euclidean ball. To take the boundedness of the design domain into account, we define

$$\mathcal{D}_B^\Omega(M) = \mathcal{D}_B(M) \cap \Omega \text{ and } \mathcal{E}_B^\Omega(M) = \mathcal{E}_B(\Omega^\complement \cup M) \cap \Omega, \tag{2}$$

where $\mathcal{D}_B(M)$ and $\mathcal{E}_B(M)$ are the standard dilate and erode operators, respectively. As in standard mathematical morphology, we define the open and close operators on bounded domains to be the compositions $\mathcal{O}_B^\Omega = \mathcal{D}_B^\Omega \circ \mathcal{E}_B^\Omega$ and $\mathcal{C}_B^\Omega = \mathcal{E}_B^\Omega \circ \mathcal{D}_B^\Omega$, respectively. Note that by taking $\Omega = \mathbb{R}^d$, we obtain the standard morphological operators on $\mathbb{R}^d$. We define the local length scale relative B in Ω at $x \in M$ as

$$R_B^\Omega(M; x) = \sup\{r > 0 \mid E_{rB}^\Omega(M; x) \neq \emptyset\}, \tag{3}$$

where $E_{rB}^\Omega(M; x) = \{y \in M \mid x \in (y + rB) \cap \Omega \subset M\}$. By using this local length scale, we define the minimum length scale of M relative B in Ω as

$$R_B^\Omega(M) = \inf_{x \in M} R_B^\Omega(M; x). \tag{4}$$

If an open set $M = \mathcal{O}_{rB}^\Omega(M)$ for $r > 0$, then we say that the set M is rB-open relative Ω, or just rB-open if $\Omega = \mathbb{R}^d$. The following heorems relate sets that are rB-open relative Ω and length scale definition (4).

Theorem 1. *If $M \neq \emptyset$, then M is rB-open for any r satisfying $0 < r < R_B^\Omega(M)$.*

Theorem 2. *If $M \neq \emptyset$ and $R_B^\Omega(M) > 0$, then $R_B^\Omega(M) = \sup\{r > 0 \mid M = \mathcal{O}_{rB}^\Omega(M)\}$.*

The above theorems show that any non-empty set that has a positive minimum length scale relative B is rB-open for all $r > 0$ that are less than $R_B^\Omega(M)$, and not rB-open for any r greater than $R_B^\Omega(M)$. Thus, one way of obtaining independent size control of two materials, occupying regions M and $V = \Omega \setminus \overline{M}$, respectively, is to require that M is $r_M B$-open relative Ω and V is $r_V B$-open relative Ω, for some positive constants $r_M > 0$ and $r_V > 0$. Due to duality of the morphological operators, conditions $\mathcal{O}_{r_M B}^\Omega(M) = M$ and $\mathcal{O}_{r_V B}^\Omega(V) = V$ take the form

$$\mathcal{O}_{r_M B}^\Omega(M) = M \text{ and } \mathcal{C}_{r_V B}^\Omega(\Omega \cap \overline{M}) = \Omega \cap \overline{M}. \tag{5}$$

2 NUMERICAL EXPERIMENT—MINIMUM HEAT COMPLIANCE

Here, we aim to minimize the heat compliance of a square plate that occupies the computational domain Ω, illustrated on the left side of Figure 1, and is subject to uniform heating. The plate is held at zero temperature along the boundary portion Γ_D and is thermally insulated along the rest of the boundary Γ_N. For this problem, there are numerical evidence that an open–close filtering strategy (combined with adequate penalization of intermediate conductivities) fails to provide designs with minimum length scale on both

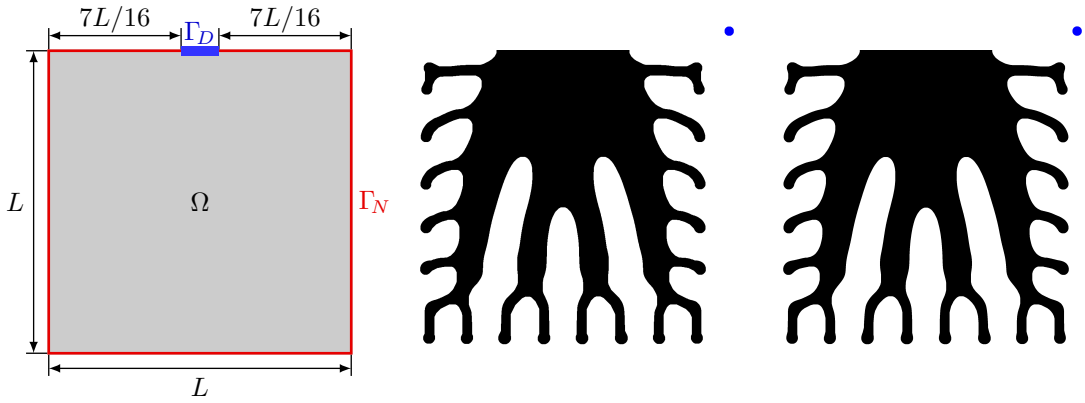

Figure 1: Left: Geometry for the minimum heat compliance problem. Middle: Optimized design on a resolution of 1024×1024 elements. Right: Middle: Optimized design on a resolution of 2048×2048 elements. For both optimized design, the neighborhood used to stipulate the minimum size for both material phases is displayed in the upper right corner.

material phases[2]. Thus, the minimum heat compliance problem, although its apparent simplicity, is rather challenging for methods that aim to impose minimum length scale in density based topology optimization.

To promote designs that satisfy condition (5), we modify the SIMP[9] method as follows: For a given design vector $\boldsymbol{\rho}$, we define the physical density

$$\tilde{\boldsymbol{\rho}}(\boldsymbol{\rho}) = \underline{\rho}\mathbf{1} + (1-\underline{\rho})\big(\boldsymbol{\mathcal{O}}_h(\boldsymbol{\rho})\big)^p, \tag{6}$$

where $\underline{\rho} = 10^{-3}$ is the relative conductivity of the low condictivity material, $p \geq 1$ is a SIMP penalty parameter, and $\boldsymbol{\mathcal{O}}_h(\boldsymbol{\rho})$ is a differentiable approximation of the discrete morphological opening. However, instead of using $\boldsymbol{\mathcal{O}}_h(\boldsymbol{\rho})$ in the volume constraint, we use a differentiable approximation of the discrete morphological closing $\boldsymbol{\mathcal{C}}_h(\boldsymbol{\rho})$. More precisely, we define the set of admissible designs $\mathcal{A}$ as

$$\mathcal{A} = \left\{\boldsymbol{\rho} \in \mathbb{R}^n \mid \mathbf{0} \leq \boldsymbol{\rho} \leq \mathbf{1} \text{ and } \boldsymbol{v}^T\boldsymbol{\mathcal{C}}_h(\boldsymbol{\rho}) \leq V^*\right\}, \tag{7}$$

where $\boldsymbol{v} \in \mathbb{R}^n$ is a vector that holds the fractional volume ($|E|/|\Omega|$) of the elements, and V^* is the maximum fractional volume of Ω allowed to be occupied by material.

We use $V^* = 0.5$ and optimize the material distribution by using the optimality criteria method[9] with damping parameter $\eta = 0.5$ together with the morphology mimicking filtering strategy based on harmonic averaging as introduced in topology optimization by Svanberg and Svärd[6]. (More precisely, we use a combination of filters of the form (1) with $f(x) = (x+\alpha)^{-1}$ or $f(x) = (1-x+\alpha)^{-1}$, and $g = f^{-1}$.) Here, we use a continuation approach for the SIMP parameter p as well as the non-linearity parameter α. The results in the middle and on the right side of Figure 1 was computed on a resolution of 1024×1024 and 2048×2048 elements, respectively. In both cases the neighborhood used to stipulate the minimum size for both material phases is displayed in the upper right corner of the

image showing the design. A closer analysis reveals these designs are essentially binary and that both the material phases satisfy the desired minimum size property; in particular, the achieved minimum size of the high conductivity phase equals the imposed minimum size.

REFERENCES

[1] Bourdin, B. Filters in topology optimization. *International Journal for Numerical Methods in Engineering* **50**, 2143–2158 (2001).

[2] Hägg, L. & Wadbro, E. Nonlinear filters in topology optimization: existence of solutions and efficient implementation for minimal compliance problems. *Structural and Multidisciplinary Optimization* **55**, 1017–1028 (2017).

[3] Sigmund, O. & Petersson, J. Numerical instabilities in topology optimization: a survey on procedures dealing with checkerboards, mesh-dependencies and local minima. *Structural Optimization* **16**, 68–75 (1998).

[4] Guest, J. K., Prévost, J. H. & Belytschko, T. Achieving minimum length scale in topology optimization using nodal design variables and projection functions. *International Journal for Numerical Methods in Engineering* **61**, 238–254 (2004).

[5] Sigmund, O. Morphology-based black and white filters for topology optimization. *Structural and Multidisciplinary Optimization* **33**, 401–424 (2007).

[6] Svanberg, K. & Svärd, H. Density filters for topology optimization based on the Pythagorean means. *Structural and Multidisciplinary Optimization* **48**, 859–875 (2013).

[7] Wadbro, E. & Hägg, L. On quasi-arithmetic mean based filters and their fast evaluation for large-scale topology optimization. *Structural and Multidisciplinary Optimization* **42**, 879–888 (2015).

[8] Heijmans, H. J. A. M. Mathematical morphology: A modern approach in image processing based on algebra and geometry. *SIAM Review* **37**, 1–36 (1995).

[9] Bendsøe, M. P. & Sigmund, O. *Topology Optimization. Theory, Methods, and Applications [SIMP § 1.1.2, Optimality criteria method § 1.2]* (Springer, 2003).

30th Nordic Seminar on Computational Mechanics
NSCM-30
J. Høgsberg. N.L. Pedersen (Eds.)
2017

NANOPARTICLES INFLUENCED ON TWO-PHASE DISPLCEMENT INTO NANOCAPILLARY BY MOLECULAR DYANIMC SIMULATION

XIAO WANG[1], ZHILIANG ZHANG[1] AND JIANYING HE[1*]

[*] NTNU Nanomechanical Lab, Department of Structural Engineering,
Norwegian Universtiy of Science and Technology(NTNU),
7491, Trondheim, Norway
Email: jianying.he@ntnu.no, Web page: http://www.ntnu.edu/nml

Key words: Nanoparticles, Displacement, Capillary, Molecular Dynamics Simulation

Summary. Molecular dynamics simulation has been carried out to investigate spontaneous two-phase displacement process into capillary influenced by the surface wettability of NPs. The dynamic displacement process and the motion behavior of nanoparticles are analyzed to reveal the microscopic displacement mechanism in confined channel.

1 INTRODUCTION

Now, most oil reservoirs around the world are experiencing their second half of life. With the growth in energy demand and decline in oil production from conventional oil reservoirs, the necessity of appropriate enhanced oil recovery (EOR) method as a more efficient technology gets further importance.

One of the emerging interest is the new generation fluid based on nanofluids and nanoparticles (NPs) transport in confined channel[1]. Nanofluids are a class of fluids engineered by dispersing NPs in base fluid, which are first known as its thermal properties [2]. Recently, a renewed interest arise in the application of nanofluid for enhanced oil recovery, such as changing the properties of fluid, wettability alternation of rock, advanced drag reduction, strengthening sand consolidation, reducing interfacial tension and increasing mobility of the capillary-trapped oil [3,4]. In this study, we focus on the fundamental understanding of the role of NPs on the spontaneous water-oil displacement into an ultra-confined capillary by molecular dynamic (MD) simulation using LAMMPS code.

2 COMPUTATION METHOD

The simulation system is shown in Figure 1, containing a water-based fluid with dispersed spherical NPs, oil fluid and a capillary. The solid capillary used in the system is face-centered cubic (fcc) crystal lattice structure of silicon. The fluid consists of 10000 water molecules and 16 nanoparticles with a diameter of 7.0 Å, so the volume fraction of NPs is about 5%. The standard pairwise 12-6 Lennard-Jones (L-J) potential is used to describe the van der Waals interaction between water and NPs, water and capillary, and NPs and capillary. For oil molecules, a cylindrical oil model composed by decane was built to be filled fully of cylindrical capillary completely. In order to ensure spontaneous water-oil displacement, the characteristic energy between capillary and water is chosen as 0.6, which means a hydrophilic

capillary. By tuning characteristic energy between NPs and water, different wettability of NPs can be obtained. Hydrophobic, mixed-wet, and hydrophilic NPs are applied in the water phase to explore the displacement mechanism of nanofluids into porous media.

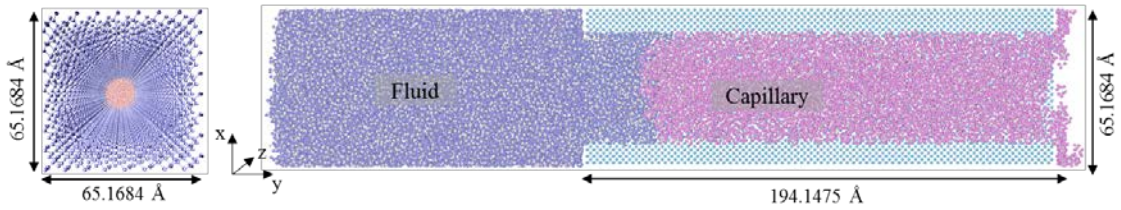

Figure 1. The simulation system contains a water-based nanofluid (red) laden with well-distributed spherical nanoparticles (light green) and a capillary (blue): (a) the 3D perspective of the top view; (b) the side view.

3 RESULTS AND DISCUSSION

The snapshots of oil displacement process by nanofluids into reservoir are summarized in Figure 2, which reveal the influence of wetting properties of NPs on displacing phase behaviour. It can be seen that water molecules can spontaneously diffuse into the capillary and displace the oil molecules in the referenced NP-free system. Once NPs are added into fluids, the transportation of displacing fluids is hindered. Compared with base fluid, the addition of nanoparticles would influence the speed of spontaneous capillary displacement process. For hydrophilic NPs, almost all of them are dispersed in water phase, and could displace all the oil molecules when the simulation time is 16.0 ns, which shows little difference compared with NP-free case. While for the mixed and hydrophobic NPs are added into base fluids, it is interesting to see that some NPs would move into the oil phase, and there is still some oil left in the capillary compared with base fluid and fluid with hydrophilic NPs.

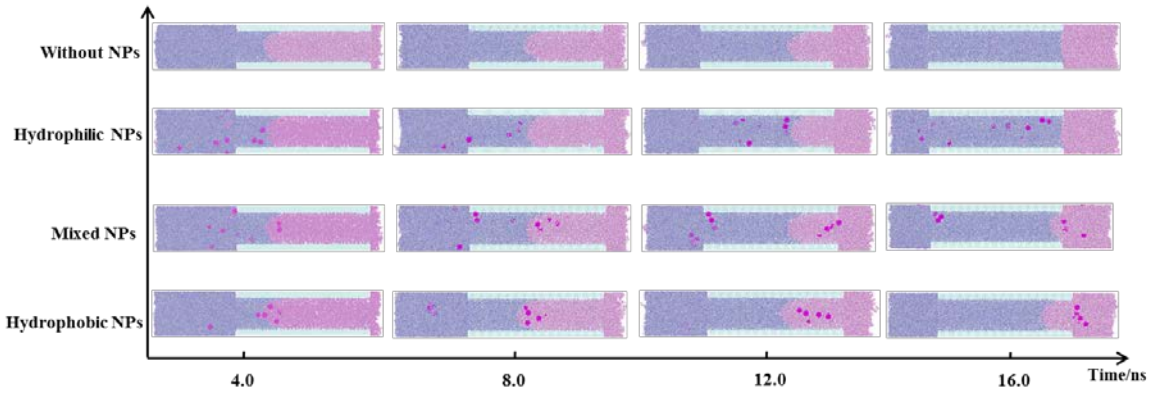

Figure 2. The snapshots of nanofluids with different type of NPs as time evolutions. Here *x*-axis shows the simulation time and *y*-axis the wettability of NPs changing via characteristic energy.

Then, the dynamic interfacial thickness is calculated to characterize the interfacial change during the displacement process, and illustrate the difference of displacement influenced by wettability of NPs. During the displacement process, three typical stages are observed for all the spontaneous water-oil displacement process, via, Developing Stage, Transition Stage and

Equilibrium Stage, respectively. For process with nanoparticles, the main difference is in the Transition Stage, which is closely related with the motion behavior of nanoparticles in this stage.

Therefore, the migration dynamics of NPs in fluids is analyzed to explore the dominating effects of water-oil mechanism. For hydrophilic NPs, three main motion behaviors are observed: (i) NPs dispersed in water, (ii) NPs adsorbed on the capillary, and (iii) NPs adsorbed on interface of fluid-fluid. While for hydrophobic and mixed NPs, phenomena that NPs diffuses into oil phase is also observed. The motion behaviour for NPs would have great influence on the properties of fluids, such as viscosity, and wettability of solid capillary.

4 CONCLUSION

Molecular dynamics simulation has been carried out to investigate spontaneous water-oil process of nanofluids into capillary influenced by the surface wettability of NPs. Ideal material model is adopted to tune the interactions between NPs, water and capillary. It is clear that adding NPs will influence the interfacial behavior and hence alternate the properties of nanofluids in the solid capillary. The displacement of the nanofluid is hindered compared with NP-free case, due to the confinement of nanochannels.

5 ACKNOWLEDGMENT

This work is financially supported by the Research Council of Norway via WINPA project No. 234626. The computational resources are provided by Norwegian Metacenter for Computational Science (NOTUR NN9110k and NN9391k).

REFERENCES

[1] J.Y. Wu, J.Y. He, O. Torsæter and Z.L. Zhang, *Effect of nanoparticles on oil-water flow in a confined nanochannels: a molecular dynamics study*. SPE 156995, (2012).

[2] S.U.S. Choi, and J.A. Eastman, *Enhancing Thermal Conductivity of Fluids with Nanoparticles*, in *The Proceedings of the 1995 ASME International Mechanical Engineering Congress and Exposition*. San Francisco, 1995, pp. 99 – 105.

[3] Z. Hu , S.M. Azmi, G. Raza, P.W.J. Glover and D. Wen, *Nanoparticle-Assisted Water-Flooding in Berea Sandstones*, *Energy & Fuels*, **30,** 2791-2804 (2016).

[4] X. Wang, S.B. Xiao, Z.L. Zhang and J.Y. He, *Effect of Nanoparticles on Spontaneous Imbibition of Water into Ultraconfined Reservoir Capillary by Molecular Dynamics Simulation. Energies*, **10,** 506 (2017).

30th Nordic Seminar on Computational Mechanics
NSCM-30
J. Høgsberg. N.L. Pedersen (Eds.)
2017

APPLICATION OF PERMANENT MAGNETIC RINGS TO REDUCING ENERGY LOSSES IN THE SUPPORTS OF VERTICAL FLYWHEELS

JAROSLAV ZAPOMĚL[*†], PETR FERFECKI[†] AND JAN KOZÁNEK[*]

[*] Institute of Thermomechanics
The Czech Academy of Sciences
Dolejškova 5, 180 00 Prague, Czech Republic
e-mail: zapomel@it.cas.cz, kozanek@it.cas.cz - web page: http://www.it.cas.cz

[†] Department of Applied Mechanics
VSB – Technical University of Ostrava
17. listopadu 15, 708 33 Ostrava – Poruba, Czech Republic
Email: jaroslav.zapomel@vsb.cz, petr.ferfecki@vsb.cz - web page: http://www.vsb.cz

Key words: High Speed Flywheels, Energy Losses Reduction, Permanent Magnet Modelling.

Summary. An important requirement put on operation of high speed vertical flywheels is minimizing energy losses generated in the flywheel supports. A simple technological solution that makes it possible consists in lifting the flywheel by a pair of permanent magnets. The carried out research was focused on implementation of the magnets in computational models, expressing the energy losses and on the study of efficiency of this design arrangement.

1 INTRODUCTION

High speed flywheels with vertical axis of rotation are frequently used as devices for energy storage[1]. One of the main requirements put on their operation is minimizing the energy losses. The ones generated in the flywheel supports depend on the forces transmitted between the flywheel and its frame. A possible technological solution consists in lifting the flywheel by permanent magnets[2]. The efficiency of this arrangement was studied by means of computer simulations. The research was focused on modelling the flywheel, implementation of the permanent magnets in the computational model and on expressing the energy losses generated in the flywheel supports. The carried out computational simulations confirmed reducing the power loss if the magnetic rings were applied.

2 THE INVESTIGATED FLYWHEEL DEVICE

The investigated vertical rotor (flywheel) consists of a flexible shaft and of one rigid disc (Fig. 1). The shaft is coupled with a rigid frame by two squeeze film dampers with rolling element bearings at both its ends. The oil is supplied into each damper by 4 oil inlets. The upper bearing is a ball bearing the lower one is a roller bearing. The rotor turns at constant angular speed, is loaded by its weight and is excited by the disc unbalance. Two magnetic rings are used to reduce the loading transmitted through the flywheel supports. The rings are attached to the disc the and to the stationary frame. The distance between the rings is adjusted in such a way that their mutual interaction compensates the gravity force acting on the rotor.

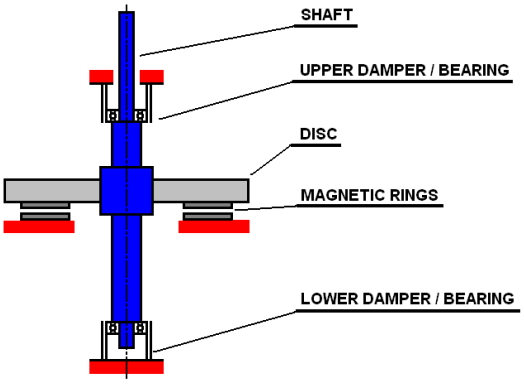

Figure 1: The studied flywheel system

3 THE COMPUTATIONAL MODEL

In the computational model the disc and the frame are considered as absolutely rigid bodies, the shaft is represented by a beam body discretized into finite elements, the squeeze film dampers by springs and force couplings and the magnetic rings by a force interaction between the disc and the frame.

The equation of motion of the system reads

$$\mathbf{M}\ddot{\mathbf{x}} + (\mathbf{B}_P + \mathbf{B}_M - \omega\mathbf{G})\dot{\mathbf{x}} + (\mathbf{K} + \omega\mathbf{K}_C)\mathbf{x} = \mathbf{f}_U + \mathbf{f}_H + \mathbf{f}_M \,. \tag{1}$$

M, **G**, **K**, $\mathbf{K}_C$ are the mass, gyroscopic, stiffness and circulation matrices, $\mathbf{B}_P$, $\mathbf{B}_M$ are the matrices of damping produced by the environment and the shaft material, $\mathbf{f}_U$, $\mathbf{f}_H$, $\mathbf{f}_M$ are the vectors of the unbalance, hydraulic and magnetic forces, **x** is the vector of the system general displacements, ω is angular speed of the rotor rotation, and $(\dot{\cdot})$, $(\ddot{\cdot})$ denote the first and second derivatives with respect to time.

The steady state solution of the motion equation was calculated by application of the trigonometric collocation method.

The squeeze film dampers[3,4] are considered as of finite length. The pressure distribution in the full oil film is governed by the Reynolds equation[3,4]. In areas where the pressure drops to a critical value, a cavitation is assumed. In accordance with the observations pressure of the medium in cavitated regions remains constant and equal to the pressure in the ambient space. Components of the hydraulic force acting on the rotor journal are calculated by integration of the pressure distribution around the damper circumference and along its length.

The determination of the magnetic force acting on the disc proceeds from the idea of mutual interaction of two magnetic dipoles[5]. If point magnetic dipole j finds itself in a magnetic field of dipole i, the dipole i acts on dipole j by force $\vec{F}_{MGji}$ and moment $\vec{M}_{MGji}$

$$\vec{M}_{MGji} = \vec{m}_{MGj} \times \vec{B}_i(\vec{r}_j) \,, \tag{2}$$

$$\vec{F}_{MGji} = \left(\vec{m}_{MGj}\vec{\nabla}\right)\vec{B}_i(\vec{r}_j) \,. \tag{3}$$

$\vec{m}_{MGi}$, $\vec{m}_{MGj}$ are the magnetic moments of point dipoles i, j, B_i is the magnetic induction of the

field of magnetic dipole i, $\vec{r}_i, \vec{r}_j$ are the position vectors of magnetic dipoles i, j, respectively.

The magnetic induction of the field of magnetic dipole i at location of dipole j is given

$$\vec{B}_i(\vec{r}_j) = \frac{\mu_0}{4\pi}\left\{\frac{3\left[\vec{m}_{MGi}\left(\vec{r}_j - \vec{r}_i\right)\right]}{\left|\vec{r}_j - \vec{r}_i\right|^5}\left(\vec{r}_j - \vec{r}_i\right) - \frac{\vec{m}_{MGi}}{\left|\vec{r}_j - \vec{r}_i\right|^3}\right\}. \tag{4}$$

μ_0 is the vacuum permeability.

To determine the magnetic force and moment by which the magnetic ring fixed to the stationary frame acts on the one attached to the disc both magnetic rings were divided into small volumes and each of them was considered as a point magnetic dipole. Then it holds

$$\vec{m}_{MG} = \vec{M}_{MG} V . \tag{5}$$

$\vec{m}_{MG}$ is the magnetic moment, $\vec{M}_{MG}$ is the magnetization and V denotes the volume.

The magnetic force and moment acting on the flywheel was obtained as a sum of magnetic forces and moments by which all magnetic dipoles related to the magnet coupled with the frame act on all dipoles related to the ring attached to the rotor.

The power losses in the bearings are given by product of the speed on the rotor rotation and the rolling resistance moment M_R [6]

$$M_R = \left(X\, F_R + Y\, F_A\right) f_B \frac{d_H}{2} . \tag{6}$$

d_H is the diameter of the shaft journal, f_B is the friction coefficient[6], F_R, F_A are the radial and axial components of the force transmitted through the bearing and X, Y are the loading coefficients, the value of which depends on the bearing type [6].

4 RESULTS OF THE COMPUTATIONAL SIMULATIONS

The main technological parametres of the system are: the flywheel mass is 139 kg, the speed of the flywheel rotation is 1000 rad/s, the outer/inner diametre/thickness of the magnetic rings is 320/200/20 mm and the magnets polarization is 0.9 T.

The dependence of the axial force by which the magnetic ring fixed to the stationary frame acts on the rotor disc on the width of the gap between the magnets is drawn in Fig. 2.

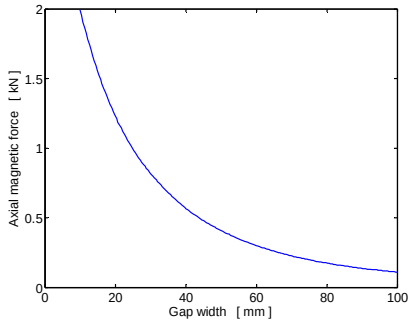

Figure 2: Dependence of the axial magnetic force on the gap between the permanent magnets

The results show that the gap of 18 mm compensates the weight of the flywheel rotor.

Fig. 3 shows the time history of the loss power in the lower and upper bearings during several rotor revolutions. As evident, applications of the magnetic rings has no influence on energy losses in the lower bearing (roller bearings) but reduces considerably the power loss in the upper bearing (ball bearing).

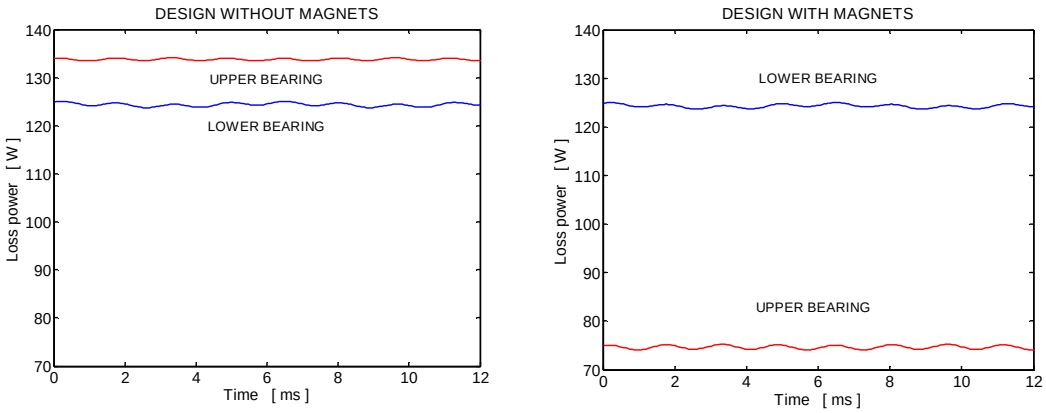

Figure 3: Loss power in the bearings for the arrangements without and with permanent magnets

5 CONCLUSIONS

One technological solution, which makes it possible to minimize energy losses in the supports of high speed vertical flywheels, consists in reducing the axial force caused by the flywheel weight by means of permanent magnets lifting the flywheel. The research work was focused on implementation of the permanent magnets in the computational models of high speed flywheels and on performing the study of efficiency of this design arrangement by means of computer simulations. The obtained results show that application of the properly adjusted magnetic rings contributes to reducing energy losses in the flywheel supports.

REFERENCES

[1] I. Hadjipaschalis, A. Poullikkas and V. Efthimiou, "Overview of current and future energy storage technologies for electric power applications", *Renewable and Sustainable Energy Reviews*, **13**(6-7), 1513-1522 (2009)

[2] S. Jiang, H. Wang and S. Wen, "Flywheel energy storage system with permanent magnet bearing and a pair of hybrid ceramic ball bearing", *Journal of Mechanical Science and Technology*, **28**(12), 5043-5053 (2014)

[3] J. Zapoměl, *Computer modelling of lateral vibration of rotors supported by hydrodynamical bearings and squeeze film dampers*, VSB-Technical University of Ostrava, Ostrava, 2007, (in Czech).

[4] A. Z. Szeri, *Tribology: Friction, Lubrication, and Wear*, Washington, New York, London: Hemisphere, Publishing Corporation, 1980.

[5] H. E. Knoepfel: *MAGNETIC FIELDS A Comprehensive Theoretical Treatise for Practical Use*, John Wiley & Sons, Inc., New York, 2000.

[6] A. Bolek and J. Kochman, *Machine parts*, SNTL Prague, Vol. I, 1989, (in Czech).

30th Nordic Seminar on Computational Mechanics
NSCM-30
J. Høgsberg. N.L. Pedersen (Eds.)
2017

DYNAMICS OF THE GYROSCOPIC POWER TAKE-OFF WAVE ENERGY ABSORBER IN IRREGULAR SEA STATES

ZILI ZHANG[*], SØREN R.K. NIELSEN[†] AND JAN OLSEN[‡]

[*] Department of Engineering, Aarhus University, Denmark
Email: zili_zhang@eng.au.dk

[†] Department of Civil Engineering, Aalborg University, Denmark
Email: srkn@civil.aau.dk

[‡] JOLTECH, Langbrogade 3, 6400 Sønderborg, Denmark
Email: JAO@joltech.dk

Key words: Gyroscopic wave energy absorber, nonlinear rigid body dynamics, irregular sea

Summary. Dynamic modelling and analysis of a newly proposed wave energy point absorber, the Gyroscopic power take-off (GyroPTO) absorber, is presented in this study. Inside the float of the GyroPTO, there is a mechanical system made up of a spinning flywheel with its spin axis in rolling contact to a ring. In order to improve the performance (stability) of GyroPTO in irregular sea states, a magnetic coupling mechanism is further added between the spin axis and the flywheel. Theoretical modeling of the GyroPTO is carried out using analytical rigid body dynamics, and a 4-DOF nonlinear model is established. Linear wave theory has been applied together with rational approximation of the radiation damping moments, leading to an extended state vector formulation of the coupled structure- wave system. Simulation results show that magnetic coupling successfully improves the stability of the flywheel in irregular sea states.

1 INTRODUCTION

A wave energy converter (WEC) is defined as a dynamic system for converting the energy in waves into mechanical energy stored in the oscillating system. Among different types of WECs, point absorbers are the most widely investigated WEC devices. A point absorber is a WEC that is capable of absorbing energy from waves propagating in any direction, and with horizontal dimensions much smaller than the dominating wave length[1]. For almost all point absorbers, the instantaneous absorbed energy varies significantly with time, making the expensive additional power electronics mandatory before the power can be supplied to the grid. This motivates a search for an alternative device which is able to deliver a more constant power to the grid without introducing power electronics.

The Gyroscopic power take-off (GyroPTO) wave energy point absorber is a possible solution[2]. The general idea is to use the gyroscopic moment on a spinning flywheel inside a floating structure, so that almost constant power output from the generator can be obtained

from the absorbed wave energy. As shown in Figure 1a), it consists of a float rigidly connected to a lever. In the other end the lever is supported by a hinge, which allows for rotations around a horizontal axis and a vertical axis. Inside the float is a mechanical system made up of a ring, a spinning flywheel and a generator. The ring is free to rotate in a plane orthogonal to the lever, while the spin axis of the flywheel is supported by a track in the ring with a width slightly larger than the diameter of the axis. This track forms a guidance for the precession of the spin axis, which is assumed to roll on the inner side of the track during rotations of the ring without slip. In operational conditions, the wave induced pitch and roll motions of the float produce a time-varying rotation of the ring, which combined with the spinning velocity of the flywheel creates a gyroscopic moment. This moment produces the necessary contact force between the spin axis and the inner side of the track, to provide the friction force making the rolling of the spin axis possible. Therefore, the gyroscopic moment enforces a kinematical constrain between the rotational velocities of the spin axis and the ring. When synchronization of the angular frequency of the ring to the peak frequency of the wave loading takes place, the responses of the ring and the flywheel become almost harmonic. This phenomenon is the basic reason for the functioning of the system. At synchronization, this means that the generated electric power becomes almost constant in time, making the need for additional power electronics unnecessary before the power can be supplied to the grid.

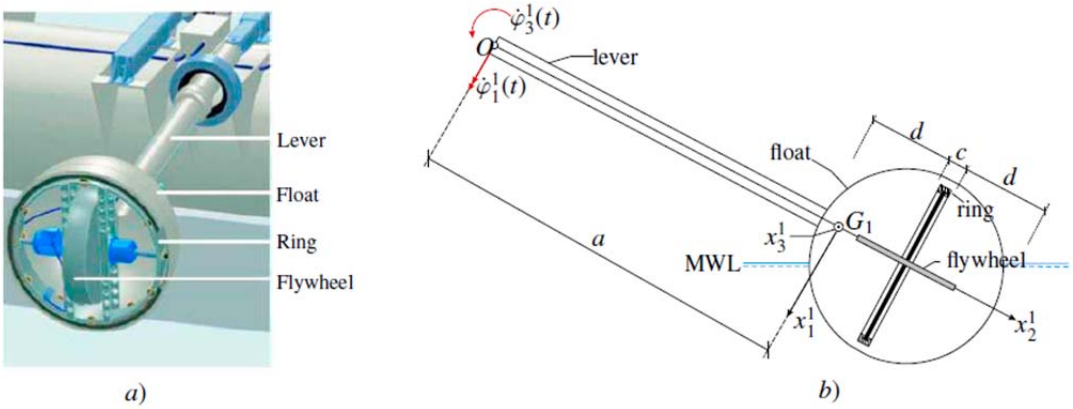

Figure 1: The GyroPTO point absorber. a) Schematic details. b) Geometry of the GyroPTO and the definition of the (x_1^1, x_2^1, x_3^1)- coordinate system fixed to the float.

2 DYNAMIC MODELLING

Based on rigid body dynamics, a 4-DOF nonlinear model is to be established for the GyroPTO device with magnetic coupling. The DOFs are $\varphi_1^1(t)$, $\varphi_3^1(t)$, $\Psi(t)$ and $\omega(t)$, where $\varphi_1^1(t)$ and $\varphi_3^1(t)$ represent the rotations of the lever and float (the external structure), $\Psi(t)$ represents the rotational angle of the ring and $\omega(t)$ represents the rotational angle of the flywheel.

Four different principal axes coordinate systems attached to four rigid bodies moving relative to each other are to be introduced for deriving the equations of motion of the device. The components of a vector defined with regard to the kth principal axes coordinate system (x_1^k, x_2^k, x_3^k) are indicated with an upper k, where k=1,2,3,4. As shown in Figure 1b), the

(x_1^1, x_2^1, x_3^1)- coordinate system is fixed to the float with origin at G_1, where G_1 is the mass center of gravity of the lever and float. As shown in Figure 2, the (x_1^2, x_2^2, x_3^2)- coordinate system is fixed to the precessing ring with the origin G_2, where G_2 is the mass center of gravity of the ring (G_2 is also the mass center of gravity of the sub-structure made up of the spin axis and the flywheel). The x_1^2- axis is rotated from x_1^1- axis by the angle $\Psi(t)$, which is one of the DOFs of the system. The kinetic energy T_1 of the lever and float and kinetic energy T_2 of the ring can thus be formulated using (x_1^2, x_2^2, x_3^2)- and (x_1^2, x_2^2, x_3^2)- coordinate systems, respectively.

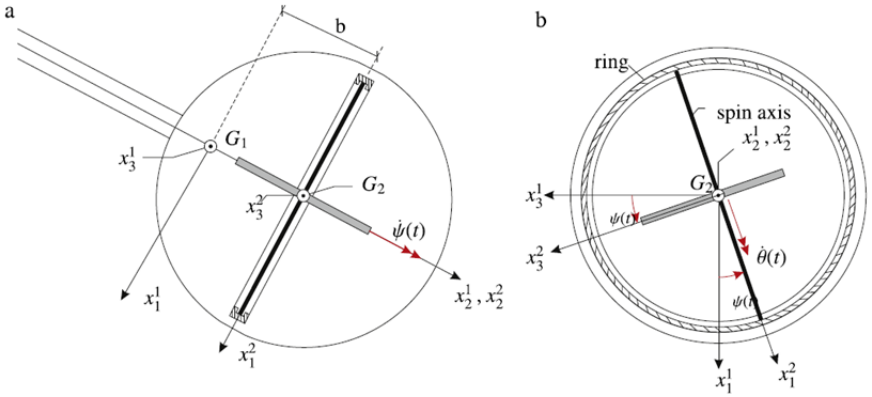

Figure 2: Definition of the (x_1^2, x_2^2, x_3^2)- coordinate system fixed to the ring.

Instead of a rigid connection, the spin axis is connected to the flywheel via a magnetic coupling mechanism allowing for a relative rotation between the spin axis and the flywheel, as shown in Figure 3. This coupling acts as a linear viscous damping mechanism on the flywheel, with the damping constant depending on the strength of the magnetic field.

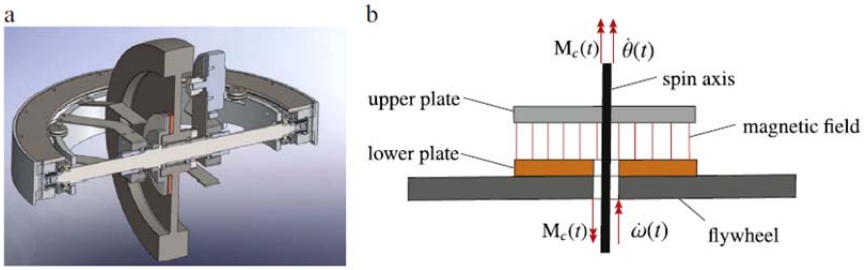

Figure 3: The magnetic coupling

As shown in Figure 4, the (x_1^3, x_2^3, x_3^3)- principal axes coordinate system and the (x_1^4, x_2^4, x_3^4)- principal axes coordinate system are fixed to the spin axis (with the upper plate) and the flywheel (with the lower plate), respectively. The total kinetic energy of the system can be obtained by summing up kinetic energies of the sub-structures, and nonlinear equations of motion of the 4-DOF model can be established using the Lagrange equation[2].

Linear wave theory is used for hydrodynamic loads modeling. The wave excitation moments are obtained using JONSWAP spectrum. The FRFs of the radiation damping moments are approximated using rational functions, and extended state vector formulation of the coupled structure- wave system is finally obtained[2].

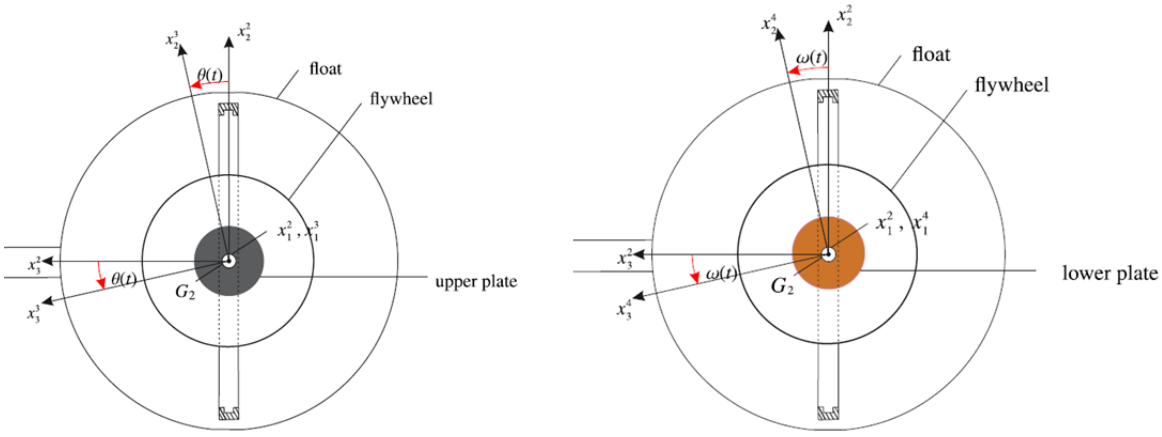

Figure 4: The (x_1^3, x_2^3, x_3^3)- coordinate system fixed to the spin axis, the (x_1^4, x_2^4, x_3^4)- coordinate system fixed to the flywheel

3 RESULTS

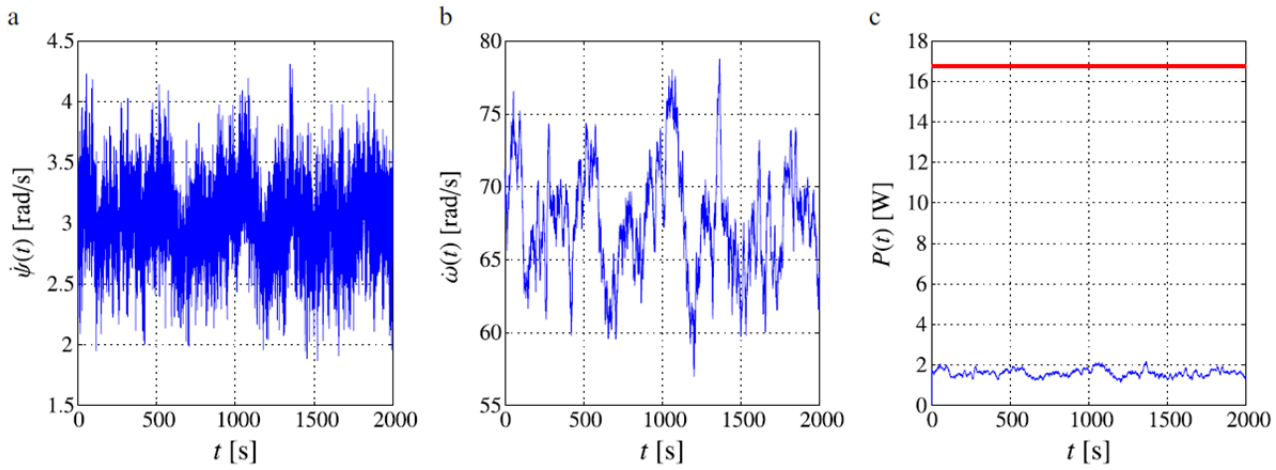

Figure 5: Responses of (a) the ring and (b) the flywheel, and (c) the power output. Synchronization maintained.

Figure 5 shows when the device is synchronized with the wave frequency, both the ring and flywheel are rotating around constant values. The power output (blue line) is almost constant as well. But comparing with the mean input wave energy (red line), the efficiency of the device is not very high, which might be improved by semi-active control.

REFERENCES

[1] S.R.K. Nielsen, Z. Qiang, M.M. Kramer, B. Basu and Z. Zhang, "Optimal control of nonlinear wave energy point converters", *Ocean Eng.*, **72**, 176-187 (2013).

[2] Z. Zhang, B. Chen, S.R.K. Nielsen and J. Olsen, "Gyroscopic power take-off wave energy point absorber in irregular sea states", *Ocean Eng.*, **143**, 113-124 (2017).

30th Nordic Seminar on Computational Mechanics
NSCM-30
J. Høgsberg, N.L. Pedersen (Eds.)
2017

GIGA-VOXEL STRUCTURAL OPTIMIZATION

NIELS AAGE*, ERIK ANDREASSEN*, BOYAN S. LAZAROV* AND OLE SIGMUND*

*Department of Mechanical Engineering, Solid Mechanics
Technical University of Denmark
2800 Lyngby, Denmark
e-mail: naage@mek.dtu.dk, web page: http://www.topopt.dtu.dk/

Abstract. The optimal topology of large structural systems has until now been concerned with the design of individual parts and not that of complete assemblies. However, due to recent advances in numerical algorithms tailored for large scale structural optimization this limitation can now be circumvented[1]. In this work we present several examples displaying how high resolution topology optimization can be used to obtain new, as well as already known[2], insight within the field of structural optimization. To demonstrate the capabilities of the developed framework we apply it to the design of the supporting structure of an entire wing from a Boeing 777 type aircraft[3]. In order to obtain a design that allows for details in the order of those found in existing wing structures, we discretize the wing with approximately 1.1 billion tri-linear hexahedral finite elements, yielding a maximum element size of $h = 0.8$cm. The design problem is solved using mathematical programming methods, filters from image processing and a multiple load case problem formulation. The results show how the topology of the wing structure has obvious similarities to nature's own light weight aviation design, i.e. bird bones, and how very fine resolution topology optimization provides new insight and possible weight savings for future aircraft designs.

Keywords: Topology optimization, giga resolution, high performance computing, finite element methods.

REFERENCES

[1] Aage, N., Andreassen, E. & Lazarov, B. S. Topology optimization using PETSc: An easy-to-use, fully parallel, open source topology optimization framework. *Structural and Multidisciplinary Optimization* **51**, 565–572 (2015).

[2] Sigmund, O., Aage, N. & Andreassen, E. On the (non-)optimality of Michell structures. *Structural and Multidisciplinary Optimization* **54**, 361–373 (2016).

[3] Aage, N., Andreassen, E., Lazarov, B. S. & Sigmund, O. Giga-voxel computational morphogenesis for structural design. *Nature,* **accepted** (2017).

30th Nordic Seminar on Computational Mechanics
NSCM-30
J. Høgsberg. N.L. Pedersen (Eds.)
2017

VIBRATION CONTROL IN PERIODIC STRUCTURES BY PIEZOELECTRIC RL SHUNTS

JAN HØGSBERG

Department of Mechanical Engineering - Technical University of Denmark (DTU)
Nils Koppels Allé, Building 404, DK-2800 Kongens Lyngby, Denmark, e-mail: jhg@mek.dtu.dk

Key words: Waves, Periodic structure, Damping, Piezoelectric shunt, Modal analysis.

Summary. Within the framework of periodic structures, the calibration of RL shunted piezoelectric inclusions is investigated with respect to maximum damping of a particular wave form. A finite element setting is assumed, with local shunted inclusions inside the unit cell. The effect of the shunts is represented for a targeted wave form, characterized by its short-circuited eigenvalue problem and two correction coefficients, representing the influence from residual modes, not addressed by the supplemental damping. Calibration formulae are finally derived for the shunt inductance L and resistance R. The presentation contains dispersion diagrams and vibration amplitude curves for the optimally calibrated RL shunt system in a 1-D periodic structure with local piezoelectric inclusions.

1 PERIODIC STRUCTURE

The equilibrium equation for a structure may be determined by vanishing virtual work in a finite element formulation with element displacements contained in the element displacement vector $\mathbf{u}_e$. The element virtual work can then be expressed as

$$\delta W_e = \delta \mathbf{u}_e^T \Big([-\omega^2 \mathbf{m}_e + \mathbf{k}_e] \mathbf{u}_e + \mathbf{b}_e f_e - \mathbf{f}_e \Big) \tag{1}$$

with element mass matrix $\mathbf{m}_e$, stiffness matrix $\mathbf{k}_e$, participation vector $\mathbf{b}_e$, piezoelectric force f_e and external load $\mathbf{f}_e$. Wave propagation for a periodic structure is commonly analyzed by representing the spatial dependence of the wave via the normalized wavenumber $\gamma \ell_e$ in the factorized form

$$\mathbf{u}_e = \mathbf{E}(\gamma \ell_e) \mathbf{A}_e \mathbf{u} \tag{2}$$

Here $\mathbf{A}_e$ extracts the element displacements from the global displacement vector $\mathbf{u}$, while the wavenumber dependent exponential matrix $\mathbf{E}(\gamma \ell_e)$ represents the spatial advancement of the wave through the element.

The total work is obtained by summation over the elements in the periodic structure

$$\delta W = \sum_e^{N_e} \delta W_e = \delta \mathbf{u}^T \Big((-\omega^2 \mathbf{M} + \mathbf{K}) \mathbf{u} - \mathbf{W} \mathbf{f} \Big) = 0 \tag{3}$$

introducing the global mass and stiffness matrices

$$\mathbf{M} = \sum_{e}^{N_e} (\mathbf{E}\mathbf{A}_e)^T \mathbf{m}_e (\mathbf{E}\mathbf{A}_e) \quad , \quad \mathbf{K} = \sum_{e}^{N_e} (\mathbf{E}\mathbf{A}_e)^T \mathbf{k}_e (\mathbf{E}\mathbf{A}_e) \tag{4}$$

while the piezoelectric forces are represented by the term

$$\mathbf{W}\mathbf{f} = \sum_{p}^{N_p} (\mathbf{E}\mathbf{A}_p)^T \mathbf{b}_p f_p = \sum_{p}^{N_p} \mathbf{w}_p f_p \,, \quad \mathbf{w}_p = (\mathbf{E}\mathbf{A}_p)^T \mathbf{b}_p \tag{5}$$

with summation over the reduced number of elements representing a piezoelectric inclusion. The equilibrium equation from (3) can then be written in homogeneous form[1]

$$(-\omega^2 \mathbf{M} + \mathbf{K})\mathbf{u} + \mathbf{W}\mathbf{f} = \mathbf{0} \tag{6}$$

The construction of the unit cell is shown in Fig. 1 for a unidirection rod-type structure, where the gray areas represent piezoelectric inclusions and (c) illustrates the periodicity.

2 PIEZOELECTRIC SHUNT FORCE

In (6) the vector $\mathbf{f}$ may contain electromechanical forces f_p from several piezoelectric elements within the unit cell. An electromechanical force is defined as

$$f_p = \theta V \qquad , \qquad p = 1, 2, \ldots N_p. \tag{7}$$

where V is the voltage across the element nodes, while θ represents the electromechanical coupling coefficient. The piezoelectric coupling is governed by the electrical balance equation,

$$Q = -\theta \mathbf{b}_p^T \mathbf{u}_p + CV \tag{8}$$

where Q is the charge in the element, while C is the capacitance of the piezoelectric element associated with blocked strain conditions.

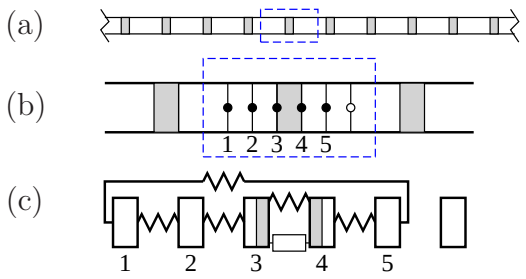

Figure 1: (a) Periodic bar with (b) unit cell and (c) representative spring-mass system.

The shunt properties are expressed by the impedance relation $V = -i\omega Z(\omega)Q$, whereby

$$\Big(1 + i\omega C Z(\omega)\Big)\mathbf{f} = \theta^2 C^{-1} i\omega C Z(\omega)\mathbf{v} \tag{9}$$

in which the piezoelectric forces are collected in the vector $\mathbf{f} = [f_1, f_2, \ldots, f_{N_p}]^T$, while

$$\mathbf{v} = \mathbf{W}^T\mathbf{u} \qquad , \qquad \mathbf{W} = \big[\mathbf{w}_1, \mathbf{w}_2, \ldots, \mathbf{w}_{N_p}\big] \tag{10}$$

represents the displacement vector for the piezoelectric inclusions.

3 MODAL EQUATION

The free vibration properties (ω_j and $\mathbf{u}_j$) for the unit cell structure with piezoelectric inclusions, periodic boundary conditions and short-circuited electrodes is governed by

$$\big(\mathbf{K} - \omega_j^2\mathbf{M}\big)\mathbf{u}_j = \mathbf{0} \tag{11}$$

The piezoelectric displacement vector $\mathbf{v}$ is approximated by the contribution $\mathbf{v}_r q_r$ from the targeted mode $j = r$ and supplemental flexibility from the non-resonant modes ($j \neq r$). This augmented modal representation can be written as[2,3]

$$\mathbf{v} = \mathbf{v}_r q_r - \Big(\frac{1}{k_r\kappa_r'} - \frac{1}{\omega^2 m_r \mu_r'}\Big)\mathbf{f} \tag{12}$$

where $\mathbf{v}_r = \mathbf{W}^T\mathbf{u}_r$, while κ_r' and μ_r' represent apparent flexibility and inertance ratios associated with the influence of residual modes. Elimination of $\mathbf{v}$ in (9) gives

$$\Big[1 + \frac{\theta^2}{Ck_r}\frac{1}{\kappa_r'} + \frac{1}{i\omega C Z(\omega)} - \frac{\theta^2}{Ck_r}\frac{\omega_r^2}{\omega^2}\frac{1}{\mu_r'}\Big]\mathbf{v}_r^T\mathbf{f} = \frac{\theta^2}{Ck_r}k_r\nu_r^2 q_r \tag{13}$$

in which the modal participation factor is $\nu_r = \sqrt{\mathbf{v}_r^T\mathbf{v}_r}$. In (13) the flexibility correction modifies the apparent electromechanical coupling, while the inertance correction in the last term represents an artificial inductance that alters the shunt frequency. The corresponding structural equation of motion follows from a modal representation of (6),

$$(-\omega^2 m_r + k_r)q_r + \mathbf{v}_r^T\mathbf{f} = 0 \tag{14}$$

The two coupled equations (13) and (14) comprise an eigenvalue problem, governing the wave propagation in the unit cell. The residual mode correction coefficients κ_r' and μ_r' can be determined by introducing a pure inductive shunt $Z(\omega) = i\omega L$ for each of the n_p inclusions. Hereby, the structural frequency ω_r splits into $n_p + 1$ frequencies around ω_r, of which ω_A and ω_B are associated with structural vibration modes, while the remaining modes are highly damped. The two frequencies determine intermediate coefficients

$$\kappa_* = \Big[1 - \Big(\frac{\omega_A}{\omega_r}\Big)^2\Big]\Big[\Big(\frac{\omega_B}{\omega_r}\Big)^2 - 1\Big] \quad , \quad \mu_* = \Big[1 - \Big(\frac{\omega_r}{\omega_B}\Big)^2\Big]\Big[\Big(\frac{\omega_r}{\omega_A}\Big)^2 - 1\Big] \tag{15}$$

which are subsequently used to determine the actual correction coefficients

$$\frac{1}{\kappa_r'} = \frac{1}{\kappa_*} - \frac{k_r}{\theta^2 C^{-1}} \quad , \quad \frac{1}{\mu_r'} = \frac{1}{\mu_*} - \frac{k_r}{\theta^2\omega_r^2 L} \tag{16}$$

4 CALIBRATION

The desired resonant vibration damping is obtained by shunts with a resistor R and an inductor L placed in parallel in the shunt, whereby the impedance is given as

$$\frac{1}{Z(\omega)} = \frac{1}{R} + \frac{1}{i\omega L} \tag{17}$$

Upon substitution, the flexibility relation (13) can be expressed in short form as

$$\Big[\frac{1}{\kappa_r} + \frac{\omega_r}{i\omega\beta_r} - \frac{\omega_r^2}{\omega^2\mu_r}\Big]\mathbf{v}_r^T\mathbf{f} = k_r\nu_r^2 q_r \tag{18}$$

in which the resulting stiffness, damper and inertance ratios are defined as

$$\frac{1}{\kappa_r} = \frac{k_r}{\theta^2 C^{-1}} + \frac{1}{\kappa_r'} \quad , \quad \frac{1}{\beta_r} = \frac{k_r}{\theta^2\omega_r R} \quad , \quad \frac{1}{\mu_r} = \frac{k_r}{\theta^2\omega_r^2 L} + \frac{1}{\mu_r'} \tag{19}$$

with correction coefficients κ_r' and μ_r' determined in (16).

Effective vibration control of the targeted mode $j = r$ is obtained by initially requiring that the damping should be identical in the two non-redundant wave forms. This is for the parallel RL shunt secured by the simple relation

$$\mu_r = \kappa_r \quad \Rightarrow \quad \frac{1}{\omega_r^2 CL} = 1 + \frac{\theta^2}{k_r C}\Big(\frac{1}{\kappa_r'} - \frac{1}{\mu_r'}\Big) \tag{20}$$

which determines the shunt inductance L. The maximum damping is then obtained at the bifurcation point in a complex root locus diagram, associated with

$$\beta_r = \sqrt{\tfrac{1}{4}\kappa_r} \quad \Rightarrow \quad \frac{1}{\omega_r CR} = \sqrt{4\frac{\theta^2}{k_r C}\Big(1 + \frac{\theta^2}{k_r C}\frac{1}{\kappa_r'}\Big)} \tag{21}$$

explicitly calibrating the shunt resistance R. Alternatively, the factor $\frac{1}{4}$ can be increased to $\frac{1}{2}$, whereby optimal vibration amplitude mitigation is instead obtained[2,3].

REFERENCES

[1] Høgsberg J (2017) Vibration damping in periodic 1d-structures by R-shunted piezoelectric elements. *Proceedings of SMART 2017*, 5-8 June, 2017, Madrid.

[2] Krenk S and Høgsberg J (2016) Tuned resonant mass or inerter-based absorbers: unified calibration with quasi-dynamic flexibility and inertia correction. *Proceedings of the Royal Society A - Mathematical, Physical and Engineering Sciences* 472: 20150718 (23pp). DOI: 10.1098/rspa.2015.0718.

[3] Høgsberg J and Krenk S (2017) Calibration of piezoelectric RL shunts with explicit residual mode correction. *Journal of Sound and Vibration* 386: 65-81.

30th Nordic Seminar on Computational Mechanics
NSCM-30
J. Høgsberg. N.L. Pedersen (Eds.)
2017

A FAILURE LOCUS FOR HYDROGEN ASSISTED FAILURE

SANDRA FUENTES-ALONSO*, ZACH D. HARRIS†, JAMES T. BURNS† AND EMILIO MARTÍNEZ-PAÑEDA††

*Department of Construction and Manufacturing Engineering
Universidad de Oviedo
Campus de Viesques, 33203 Gijón, Spain

†Center for Electrochemical Science and Engineering
Department of Materials Science and Engineering, University of Virginia
395 McCormick Road, Charlottesville, VA 22904, USA

††Department of Mechanical Engineering
Technical University of Denmark
2800 Kgs. Lyngby, Denmark
e-mail: mail@empaneda.com - Web page: http://www.empaneda.com

Abstract. We investigate cracking in the presence of hydrogen by means of a hybrid experimental-numerical approach. Slow strain rate tests are conducted in a Nickel superalloy under different environmental conditions. Finite element analysis of crack initiation and subsequent growth is modeled by means of a hydrogen-dependent traction separation law. A special control algorithm is employed to overcome numerical instabilities intrinsically associated with cohesive zone formulations. The fracture energy is degraded by means of an experimentally-motivated hydrogen degradation relation. Numerical results provide important insight into the failure process, enabling to identify critical values of hydrogen concentration and remote stresses that trigger cracking. The work builds upon previous works by the authors[1,2] and brings important insight into the technologically important problem of hydrogen assisted cracking.

Keywords: Hydrogen embrittlement, Cohesive zone models, Fracture, Finite element analysis.

REFERENCES

[1] E. Martínez-Pañeda, C.F. Niordson and R.P. Gangloff. Strain gradient plasticity-based modeling of hydrogen environment assisted cracking. *Acta Mater.*, **117**, 321–322, (2016).

[2] B.C. Rincon Troconis, Z.D. Harris, H. Ha, J.T. Burns and J.R. Scully. The effect of heat-to-heat variations in metallurgy and hydrogen-metal interactions on the hydrogen embrittlement of Monel K-500. *Mater. Sci. Eng., A*, **703**, 533–550, (2017).

30th Nordic Seminar on Computational
Mechanics NSCM-30
J. Høgsberg. N.L. Pedersen (Eds.)
2017

MOLECULAR DYNAMIC SIMULATION OF SHOCK-WAVE COMPACTION OF NANOPOWDER IN OPEN AND CONSTRAINED CONDITIONS

ALEXANDER E. MAYER[*], ANDREI A. EBEL[*] AND MOHAMMAD K.A. AL-SANDOQACHI[†]

[*] Chelyabinsk State University
Bratiev Kashirinykh 129, 454001, Chelyabinsk, Russia
e-mail: mayer@csu.ru, web page: http://www.csu.ru

[†] South Ural State University (National Research University)
Lenin Prospect 76, 454080 Chelyabinsk, Russia

Key words: Shock-wave compaction, Nanoparticles, Severe Plastic Deformation, Nanostructured Coating, Molecular Dynamics.

1 INTRODUCTION

Application of shock loading for consolidation of powders of metals and other materials has a long history[1,2]. This process can lead to the formation of micro- or nanostructured metals. Specific feature of the dynamic compression by a shock wave consists in the localization of the zone of high temperatures along the particle surface that preserves the microstructure of the internal parts of the particles. The shock wave can be generated by different ways, but in all cases, the powder is placed in a container inside a shock-loaded assembly. The assembly design is selected for minimization of the tensile stresses in the resulting compact, because these stresses can cause cracking of the compact.

Our previous molecular dynamic (MD) simulations[3] showed that the exit of a shock wave from substrate to a free surface with nanoprotrusions leads to severe plastic deformation of them. A part of the shock energy is spent on plastic deformation, and the reflected tension wave weakens that leads to an increase in the spallation threshold in comparison with a flat surface. The nanoprojections are flattened into a continuous layer. The further investigation shows that the same situation takes place for nanopowder distributed along the substrate surface. It opens an opportunity to perform the shock-wave compaction of nanopowders in the open conditions, without the constraining wall. This process is investigated here by means of MD simulations in comparison with the more traditional compaction in the constrained conditions, when the nanopowder placed inside the container between the walls.

2 PROBLEM STATEMENT

MD simulation is performed using the LAMMPS[4]. For the pure Al and the Al-Cu system we use both the interatomic potential[5] based on the embedded atom method (EAM) and the more complex potential[6] with accounting of the angular dependences (ADP). Visualization and analysis of data are carried out using the OVITO[7]. Defective structure is revealed by the centro-symmetry parameter, which value indicates the degree of defectiveness of the lattice.

We consider both the nonopowder constrained between two walls and the nanopowder lying on the substrate without second wall (open conditions). Periodic boundary conditions are used in the directions along the substrate (wall) surface. The shock compression pulses are created on the external surface of substrate (or one of walls) by both the high-velocity impact of a flat impactor and the pressure pulse imitating the laser irradiation.

3 RESULTS

Compaction of nonopowder with the free surface can be performed by a single shock wave in the case of the same material of the substrate and the nanoparticles (Figure 1). Multiple short pulses of shock compression are more appropriate in the case of different materials (Figure 2), because a long single pulse can leads to the spall fracture in this case.

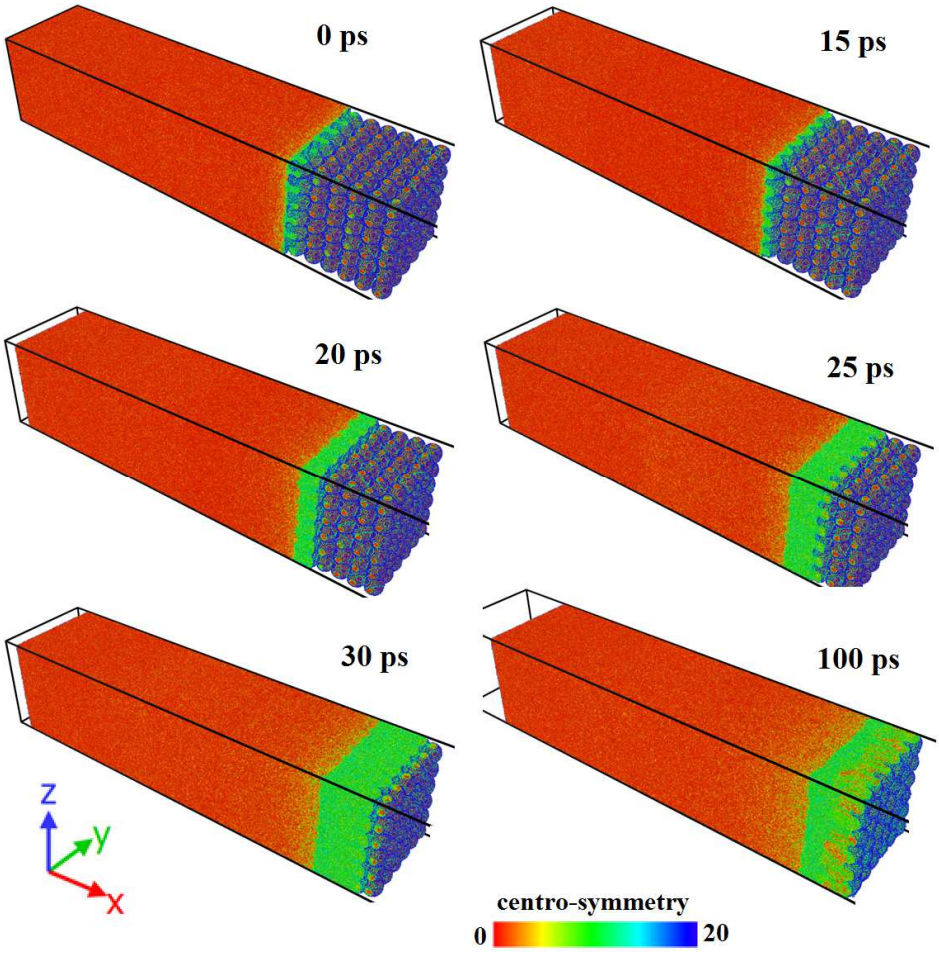

Figure 1: Compaction of Al nanoparticles on Al substrate into a monolitic coating under the action of the compression pulse initiated by the impact with velocity of 800 m/s. The flat impactor has the thickness of 40 nm, the substrate has the thickness of 85 nm. Nanoparticles with diameters of 6 nm are placed in 6 layers. The MD system contains 13.3 milion atoms. Time from the begining of impact is indicated from the right-hand side. Color scale corresponts to the centro-symmetry parameter : red colour (around zero) corresponds to perfect lattice, green color (about 5) corresponds to lattice defects, blue color (about 20) corresponds to free surfaces.

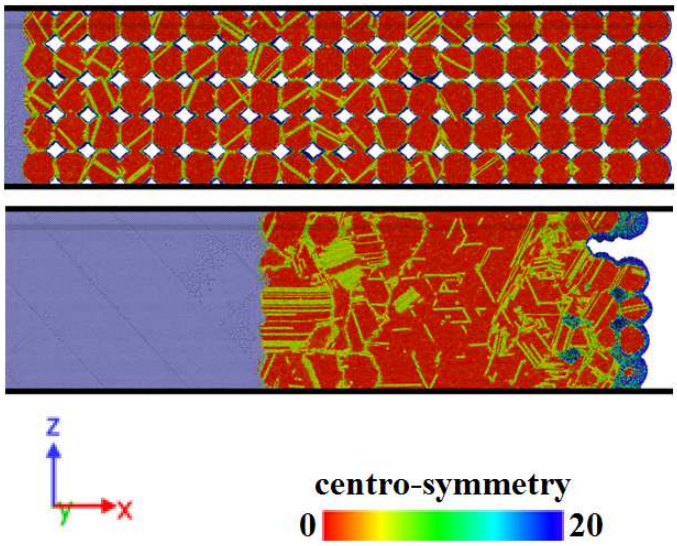

Figure 2: Compaction of Cu nanoparticles (6 nm in diameter, 20 layers) on Al substrate into a monolitic coating under the action of the compression pulses with the amplitude of 12 GPa and duration of 3 ps initiated by the pressure applied to the opposite surface. The substrate thickness is 122 nm. The MD system contains 11.7 milion atoms. Central cross-section of the MD system : initial state (from above) and the state after 15 pulses (from below). Color scale for Cu atoms corresponts to the centro-symmetry parameter, see caption to Figure 1 for description of colors. Al atoms from the left have one color.

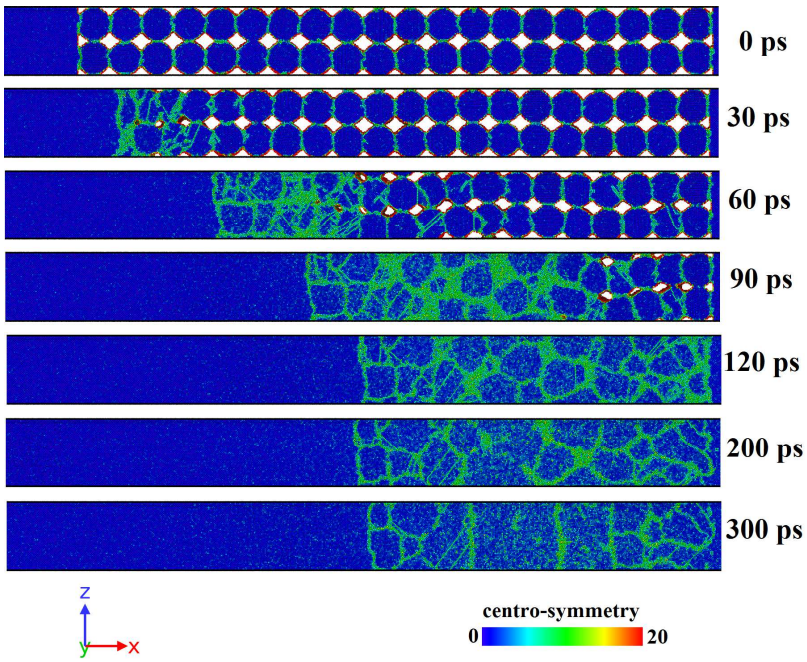

Figure 3: Compaction of Al nanoparticles (6 nm in diameter, 20 layers) placed between Al walls of container under the action of one compression pulse with the amplitude of 5 GPa and duration of 50 ps initiated by the pressure applied to the external side of the left wall. The wall thickness is 122 nm. The color scale for centro-symmetry parameter is inverted in comparison with that is used in Figures 1 and 2.

The dynamics of compaction is quite similar in both the open conditions (Figures 1 and 2) and the constrained conditions (Figure 3). The shock wave initiates the collapse of voids between the nanoparticles accompanying by severe plastic deformation and change of the particle shape. The only difference is in the further dynamics of shock and tension waves, which act on the second wall in the case of constrained system. The formed nanocrystalline structure is due to various initial orientations of the crystalline lattice in different particles. The formed grain boundaries are the former particle surfaces. The coarsening of grains takes place in the course of time after compaction that is the most obvious from Figure 3.

4 CONCLUSIONS

- The nanopowder lying on the substrate surface and having the free rear surface (open conditions) can be compacted into a nanocrystalline coating by plane ultra-short shock waves propagating from the substrate onto the interface with nanoparticles.
- Multiple shock compression pulses with the width of about several nanoparticle diameters are well-suited for sequential layerwise compaction of the nanopowder on the surface of substrate made of different material.
- The dynamics and regularities of compaction is quite similar in both the open conditions and the constrained conditions of shock loading.

The work was supported by the Ministry of Education and Science of the Russian Federation, state tasks of NIR CSU 3.1334.2014/K and 3.2510.2017/PP, and by the grant from the President of the Russian Federation, project MD-7481.2016.1.

REFERENCES

[1] W.H. Gourdin, “Dynamic consolidation of metal powders”, *Prog. Mater. Sci.* **30**, 39–80 (1986).
[2] M.A. Meyers, D.J. Benson and E.A. Olevsky, “Shock consolidation: microstructurally-based analysis and computational modelling”, *Acta mater.* **47**, 2089–2108 (1999).
[3] A.E. Mayer and A.A. Ebel, “Influence of free surface nanorelief on the rear spallation threshold: Molecular dynamics investigation”, *J. Appl. Phys.* **120**, 165903 (2016).
[4] S. Plimpton, “Fast parallel algorithms for short-range molecular dynamics”, *J. Comp. Phys.* **117**, 1-19 (1995).
[5] J. Cai and Y.Y. Ye, “Simple analytical embedded-atom-potential model including a long-range force for fcc metals and their alloys”, *Phys. Rev. B* **54**, 8398 (1996).
[6] F. Apostol and Y. Mishin, “Interatomic potential for the Al-Cu system”, *Phys. Rev. B.* **83**, 054116 (2011).
[7] A. Stukowski, “Visualization and analysis of atomistic simulation data with OVITO–the Open Visualization Tool”, *Modell. Simul. Mater. Sci. Eng.* **18**, 015012 (2010).

30th Nordic Seminar on Computational Mechanics
NSCM-30
J. Høgsberg. N.L. Pedersen (Eds.)
2017

FORMATION OF FOAMED STRUCTURE IN METAL MELTS AT EXPANSION BY INERTIA

POLINA N. MAYER AND ALEXANDER E. MAYER

Department of Physics
Chelyabinsk State University (CSU)
Bratiev Kashirinykh 129, 454001, Chelyabinsk, Russia
e-mail: polina.nik@mail.ru, web page: http://www.csu.ru

Abstract. Metals can be subjected to isochoric heating under the action of ultra-short laser or electron irradiation. In these conditions, the initially solid substance melts and expands, due to the pressure gradients at first and due to inertia thereafter. The ablation of molten metal within the energy deposition area goes similar to the spall fracture in solids. Both the complete fracture of melt on droplets and the melt solidification as a foamed structure at some intermediate stage of tension are of practical interest.

In the present work, we investigate by means of molecular dynamics (MD) simulations the regularities of formation of the foamed metal melts at the high-rate tension. Melt fracture includes several stages[1]: growth of large and collapse of small pores; destruction of walls between pores with formation of jets; fragmentation of jets on droplets. The foamed melt retains till the void volume fraction exceeds 0.9 at least. The foamed structure evolution is controlled by surface tension. Analytical estimations for the time evolution of the mean radius, pressure in the system and the work on the melt tension are proposed[1] basing on the dimensional consideration. The void size grows in time even after termination of further melt extension, while the pore number decreases due to collapse of the smallest ones. Simulation of the foamed melt cooling down to room temperature shows the formation of an amorphous foamed structure, which persists over time. Mechanical properties of this structure are tested by means of MD simulations.

This work is supported by the grant from the President of the Russian Federation, Project No. MK-9111.2016.8.

Keywords: Foamed Aluminum, Foamed Iron, High-Rate Tension, Amorphous Metal, Molecular Dynamics.

REFERENCES

[1] P. N. Mayer and A. E. Mayer, “Late stages of high rate tension of aluminum melt: molecular dynamic simulation”, *J. Appl. Phys.*, **120**, 075901 (2016).

30th Nordic Seminar on Computational Mechanics
NSCM-30
J. Høgsberg. N.L. Pedersen (Eds.)
2017

DISCUSSION ON PROBLEMS IN BUCKLING ANALYSIS OF A CONTINUA

P. PEDERSEN AND N. L. PEDERSEN

Dept. of Mechanical Engineering, Solid Mechanics
Technical University of Denmark
Nils Koppels Allé, Building 404, DK-2800 Kgs. Lyngby, Denmark
e-mail: pauli@mek.dtu.dk

Abstract. In linear buckling analysis the eigenvalue problem, that constitutes the background for estimating critical buckling load, is

$$([S_0] + \lambda[S_\sigma])\{\Delta\} = \{0\} \tag{1}$$

where $[S_0]$ is the initial global stiffness matrix and $[S_\sigma]$ is the stress stiffness matrix that is part of the tangential stiffness matrix, both obtained based on linear elasticity. The matrix $[S_\sigma]$ is obtained by a reference load vector $\{\bar{A}\}$ and a factor on $\{\bar{A}\}$ implies the same factor on $[S_\sigma]$. The estimated critical buckling load vector is $\{A\}_C = \lambda_1\{\bar{A}\}$ where λ_1 is the lowest eigenvalue for the eigenvalue problem (1). From the assumption of linearity between $\{\bar{A}\}$ and $[S_\sigma]$ follows directly, that the critical buckling load vector $\{A\}_C$ is independent of the size(norm) of $\{\bar{A}\}$. This implies uncertainty in linear buckling analysis, and this is illustrated by applying geometrical non-linear displacement analysis, that shows that buckling load also depends on the norm of $\{\bar{A}\}$. The relations between the individual stress components in a finite element are unchanged for linear buckling analysis. However, with geometrical non-linear displacement analysis this is not the case, even assuming material linear elasticity. This also give doubts to the estimated buckling load, obtained by linear buckling analysis. The geometrical non-linear buckling analysis is based on the full tangential stiffness matrix $[\bar{S}_t]$ that is separated in a gamma stiffness matrix $[\bar{S}_\gamma]$ and a stress stiffness matrix $[\bar{S}_\sigma]$. These matrices depend on a reference load $\{\bar{A}\}$ and therefore the stiffness matrices contain a bar notation and must be determined by iteration. The eigenvalue problem for non-linear buckling analysis is interpreted as an extrapolation along the tangential stiffness matrix

$$([\bar{S}_\gamma] + \lambda[\bar{S}_\sigma])\{\Delta\} = \{0\} \tag{2}$$

Applying this approach for estimating non-linear buckling analysis, comparison to (1) is used to show errors from linear buckling analysis, i.e., for initial uniform and unchanged design the buckling load as a function of the size(norm) of reference load $\{\bar{A}\}$ is shown not to be constant. A cantilever beam-column and a frame of two beam-columns are used as examples.

List of authors